NASA Technical Memorandum 85779

Analysis of Normalized Radar Cross Section (σ^o) Signature of Amazon Rain Forest Using Seasat Scatterometer Data

Emedio M. Bracalente and Jon L. Sweet

AUGUST 1984

NASA

NASA Technical Memorandum 85779

Analysis of Normalized Radar Cross Section (σ^o) Signature of Amazon Rain Forest Using Seasat Scatterometer Data

Emedio M. Bracalente
Langley Research Center
Hampton, Virginia

Jon L. Sweet
Kentron International, Inc.
Hampton, Virginia

National Aeronautics
and Space Administration

Scientific and Technical
Information Branch

1984

CONTENTS

ABBREVIATIONS AND SYMBOLS

AV	average
a	y-intercept, dB
B_N, BN	Doppler filter noise bandwidth
b	slope, dB/deg
DG	= (Average NKT across cells 1 to 12) - (Cell NKT)
DPN	noise power measurement, NP - PSN
dBW	decibels below 1 W
GDR	Geophysical Data Record
JPL	Jet Propulsion Laboratory
max	maximum
min	minimum
NKT	noise spectral density measured during T_N
NP	noise power measured during T_N
NRCS	normalized radar cross section (or σ^o), dB
NSD	normalized standard deviation, SD/Mean
PSN	noise power measured during T_G
pol	polarization
RR	$= \frac{T_G/T_N}{V_{SN}/V_N}$
R^2	coefficient of determination
SD	standard deviation of measurement
SNKT	noise spectral density measured during T_G
SNR	signal-to-noise ratio
T	integration time over which voltage is determined
TA	equivalent antenna noise temperature, K
TAM	mean value of antenna noise temperature, K
TEV	equivalent system noise temperature, K

TEVM	mean value of system noise temperature, K
T_G,TG	range-gate integration period, sec
T_{GC},TGC	corrected range-gate integration period, sec
T_N,TN	noise integration period, sec
V_N,VN	noise voltage
V_{SN},VSN	signal plus noise voltage
θ_i	incidence angle, deg
$\bar{\theta}_i$	mean incidence angle, deg
σ^o	normalized radar cross section (or NRCS), dB
$\overline{\sigma^o}$	mean normalized radar cross section, dB

SUMMARY

A detailed analysis of the normalized radar cross section (NRCS) signature of the Amazon rain forest was conducted with the Seasat scatterometer data. The response of NRCS (σ^o) as a function of incidence angle was determined for each orbit that passed over the Amazon rain forest. For each orbit, the mean value of σ^o was determined for each Doppler channel by averaging the measurements from the 5 to 18 rain forest hits obtained during a pass. A coded map, developed by the University of Kansas (NASA CR-165921), was used to determine which measurements were viewing the Amazon rain forest. Plots of σ^o against incidence angle were made for each orbit pass for which the major portion of the beam covered the rain forest. These plots are included in the appendixes. Measurements from multiple orbits were combined, in which the measurement of σ^o for each channel of the same beam and polarization were averaged together. These combined statistics were determined for three separate time periods. These time periods correspond to the local Sun time when the subsatellite point crosses the equator. The three periods were 0500 to 0730 (sunrise), 0800 to 1145 (morning), and 1730 to 2330 (evening). The sunrise and morning periods occurred during all the ascending passes, whereas the evening period occurred during the descending passes. Plots of $\overline{\sigma^o}$ against incidence angle for these combined time periods, as a function of beam and polarization, show that a relative bias of less than 0.3 dB exists between all beams over a range of incidence angle from 30° to 53°. At lower and higher incidence angles, relative biases of 0.5 to 0.75 resulted. These larger gain biases are caused by a combination of uncertainty of yaw attitude and errors in antenna gain pattern. Variation of $\overline{\sigma^o}$ with respect to incidence angle can be adequately modeled (over a range of incidence angle from 30° to 53°) with a straight line of $\overline{\sigma^o}_{(dB)} = a + b\theta_i$, where θ_i is the incidence angle. Values calculated for the slope b varied from 0.08 to 0.13 dB/deg and for the intercept a from 1.97 to 4.75 dB, depending on the beam and the time of day. A comparison between time periods of the response of σ^o as a function of incidence angle shows that on the average, the values of σ^o for the sunrise period (0500 to 0730) were about 0.75 dB higher than for the morning and evening periods.

The backscattered measurements analyzed show the Amazon rain forest to be relatively homogeneous, azimuthally isotropic, and insensitive to polarization. The return from the rain forest target appears to be relatively consistent and stable, except for the small diurnal variation that occurs at sunrise. Because of the relative stability of the rain forest target and of the scatterometer instrument calibration, the response of $\overline{\sigma^o}$ as a function of incidence angle allowed detection of errors in the measured or estimated yaw attitude angle. Also, small instrument gain biases in some of the processing channels were detected. This detection led to the development of an improved σ^o algorithm, which uses a more accurate processing method for estimating the system noise power, and a method for correcting the small gain bias errors. This correction algorithm can be applied to the Seasat sensor data record; thus, a better estimate of σ^o is provided, especially at low signal-to-noise ratios. The study of the Amazon rain forest backscatter signature shows that it is a suitable target for calibrating spaceborne scatterometers.

INTRODUCTION

During the Seasat program, the need for in-flight calibration of multibeam scatterometers became apparent. The absolute calibration or bias in the measurement of the normalized radar cross section (NRCS or σ^o) can be determined to within 1 to 1.7 dB by prelaunch calibration. These bias errors are due mainly to uncertainties in the absolute gain of the antenna and its relative gain pattern and in the true value of the transmitter output power. These biases in the measured σ^o must be removed in order to avoid a bias in the derived wind speed and direction. The use of aircraft underflight data proved to be inadequate for this purpose. It was suggested (by R. K. Moore of the University of Kansas Center for Research) that the Amazon rain forest, because of its heavy foliage with its random orientation and homogeneity, could make a suitable target for calibrating spaceborne scatterometers. Although the absolute NRCS of the Amazon forest is not known and an absolute bias calibration cannot be determined, a relative bias calibration between the 8 scatterometer beams (4 antennas, 2 polarizations) on Seasat can be made. This relative calibration is important since measurements from multiple beams are used to derive wind vector solutions. Significant errors in wind speed and direction would result if significant biases existed between antennas. The absolute bias calibration was performed by adjusting the G and H coefficients, that relate σ^o to the surface wind vector (ref. 1) by using in situ wind vector measurements.

The relative bias calibration was performed with data from a limited number of passes (11) over the Amazon region. Small corrections to the antenna pattern gain table and the addition of small bias corrections were incorporated in the final σ^o algorithm as a result of this analysis. The discussion of this calibration analysis can be found in reference 2. A further study of the Amazon rain forest σ^o signature by using Seasat data was performed by the University of Kansas (refs. 3 and 4). The results of that study confirmed the suitability of the Amazon rain forest as a calibration source and relative accuracy of the calibration results with the limited number of orbit passes. Data from 60 orbit passes were analyzed in the University of Kansas study (only data available at that time). Only seven of these passes contain horizontal polarization data since most of the passes (56) were from the end of the Seasat mission when the instrument was in mode 1 (beams 1 to 4 for vertical polarization). To complete the analysis of the rain forest response and to obtain more horizontal polarization data, a study of the data from the remaining orbit passes was conducted.

An additional 89 orbits were processed and analyzed. In addition, the previous 60 orbits were reprocessed so that they could be combined with the new orbits in order to provide overall statistics of the Amazon rain forest σ^o response for the time period corresponding to the Seasat mission. Although the previous study provides a good overall picture of the rain forest σ^o response characteristics and how well the antennas are cross calibrated, a number of data anomalies showed up during the processing of the 149 orbits which were not recognized during the previous study. The anomalies included bad data points due to bit errors, bad data on a number of Geophysical Data Record (GDR) tapes at the time of the Amazon overpass, large yaw angle determination errors on a number of orbits, and small instrument gain biases on a number of Doppler channels. Since the number of these anomalies is small in comparison with the total number of points processed during the previous study, the general results of that study are still valid. Some of these anomalies, however, help to explain discrepancies observed during the previous study.

A brief discussion of the various anomalies discovered during this latest study is presented in this report. All anomalous data were deleted or corrected so as not to affect the overall statistics. A σ^o correction algorithm was developed which provides a better estimate of the communication noise and a technique for correcting the small instrument gain biases. A brief discussion of this algorithm is presented. The data for all the orbit passes processed were corrected by using this algorithm prior to compiling the overall combined statistics. Overall statistics of σ^o plotted against incidence angle are presented as a function of beam number, polarization, and time of day. Various intercomparisons between beams, polarizations, time of day, and Amazon location are also presented. Linear regression analysis of the response of σ^o against incidence angle is presented for each beam and polarization as a function of time of day.

During 10-min periods at different times of the Seasat mission the transmitter was turned off. During these time periods, the instrument measures the system noise power. An analysis of this noise is presented. The results of this analysis show that incorrect range-gate times were specified for channels 13, 14, and 15 (nadir channels). Finally, a brief discussion of the Amazon rain forest response for the three nadir channels is presented. Also, plots of mean NRCS ($\overline{\sigma^o}$) against incidence angle are shown in appendixes A and B for all ascending and descending orbits processed, respectively, and a description of the σ^o correction algorithm is presented in appendix C.

For those unfamiliar with the basic operation of the Seasat scatterometer, a review of references 2 and 4 would be appropriate prior to reading the remainder of this report. These references give information on the technique used in the scatterometer for measuring σ^o and information on previous analysis of some Amazon rain forest data.

DESCRIPTION OF DATA PROCESSED

Amazon Map

Coded land-water and vegetation classification maps were developed by the University of Kansas. With source maps that were produced by the Department of Cartography of the Brazilian Institute of Geography, a digitized land-water map was created with a 0.25° by 0.25° grid overlay. Each grid box was assigned a code using the following convention:

0 - flatland only (no significant rivers)
1 - some small rivers but mostly land
2 - large rivers through grid box
3 - rough terrain

To further classify the Brazilian land, a vegetation map for the Amazon basin was produced with a 0.5° by 0.5° grid. Codes were assigned to each grid box according to the conventions listed in table 1. Codes 1 and 2 of table 1 were the forests which are suitable for use as a standard target. Combination codes designated 7, 8, 9, and 10 were also suitable since the dominant vegetation was either 1 or 2. The results of the land, water, and vegetation classification were encoded into a computer algorithm. Details of this algorithm, and further discussion of the Amazon map, are given in reference 1.

The code is retrieved for the grid box containing the latitude and longitude location for the center of each Doppler cell which falls inside the Amazon map. All orbits processed were passed through the map classification algorithm so that each

Doppler cell location could be classified. Those cell locations which were classified as either 0 or 1 from the land-water map and also classified as either 1, 2, 7, 8, 9, or 10 from the vegetation map were considered rain forest targets and collected for data analysis. All the remaining cells were deleted from the analyzed data set. Figures 1(a) and (b) are copies of Brazilian maps used as the source for the classifications. The dashed outline shown in figure 1(a) represents the area of the Amazon region over which the classification was performed.

Orbit Passes Processed

The Amazon region orbits processed were grouped by either ascending or descending orbit. The ascending orbits passed over the Amazon rain forest between 0500 and 1145 local Sun time. The descending orbits passed over the Amazon rain forest between about 1730 and 2330 local Sun time. For each period, the earliest times occurred at the beginning of the mission and the latest times at the end of the mission. In general each pass (whether ascending or descending) crossed the equator (ascending or descending node) at approximately one of three longitudes. The three longitudes are 289.5°, 297.9°, and 306.2°. In the earlier part of the mission, when the spacecraft was not in a frozen orbit, the nodes occurred at other longitudes near these values. After day 238 the spacecraft was placed into a frozen orbit. From this time on, each Amazon orbit crossed one of the above nodes once a day for each orbit direction. Each of these node longitudes was crossed, for both the ascending and descending directions, once every third day.

The Seasat scatterometer measurement geometry and the basic characteristics of the instrument are given in figure 2. The instrument consists of four dual polarized antennas, which are oriented 45° to the satellite subtrack. Since the antenna beam pattern cuts across constant Doppler lines (shown in the figure), narrow band Doppler filters are used to separate the 15 Doppler cell measurements along the beam. The first 12 Doppler channels obtain measurements over an incidence range of approximately 25° to 55°. Three additional Doppler filters obtain measurements in a nadir swath (0°, 4°, and 8° incidence angles). Because of Earth rotation effects, the constant Doppler lines rotate slightly ($\approx \pm 3.5°$) throughout the orbit with respect to the antenna orientation. In an ascending orbit, this effect causes the cells from beams 1 and 3 to shift outward, covering a range of incidence angle from approximately 26° to 65°, whereas the cells from beams 2 and 4 shift inward, covering a range of incidence angle from approximately 22° to 53°. The opposite effect occurs during a descending orbit. The shaded area shown in figure 2 represents the common overlap between the forward and aft beams, the area in which both wind speed and direction over the ocean can be determined.

The antenna numbering scheme is shown in figure 2. During instrument operation, only one antenna and polarization is sampled during the 1.89-sec sample period. Four beams, for various combinations of antenna number and polarization, are sequenced during any particular operating mode. Table 2 lists the antennas and polarizations sequence for each operating mode. Only modes 1 and 2 provide both side coverage. The remaining modes provide coverage on either one side or the other, for various polarization combinations. The orbit subtracks for the three node crossings are shown in figures 3(a) and (b) for the ascending and descending orbits, respectively. The swath coverage, on either side of the middle node crossing subtrack, is indicated in these figures. This is the common overlap coverage (between fore and aft beams) provided in either mode 1 or 2. Only one-side coverage is provided by the two outside node crossing tracks, regardless of the operating mode, since one side of the subtrack is looking away from the Amazon in these node crossings. The swaths from these outside node crossings overlap approximately with one of the swaths of the middle node crossing as seen from figure 3.

Two hundred and two orbits with nodes which fell between longitudes 286° and 309° passed over or in the vicinity of the Amazon rain forest so that all or a significant portion of the swath coverage fell within the classified map. However, only 149 orbits provided suitable data for analysis. The remaining orbits did not provide suitable data because of data gaps, a significant number of bad data frames occurring during that portion of the orbit, or the instrument was in a one-side mode which looked away from the Amazon. Each orbit pass that was analyzed is given in tables 3 and 4 for the ascending and descending nodes, respectively. Included in the table are the orbit number, the beams and polarization that were operating, the longitude of the subtrack as it crosses the equator, the local Sun time at the node crossing, and some comments which are discussed in the section "Anomalies Encountered."

Arrangement of Data and Analysis Procedure

As seen from tables 3 and 4, only 15 orbits provided horizontal polarization data. Most of the remaining orbit passes were in mode 1, which provided vertical polarization data from all four antennas. There also were a few passes in modes 5 and 6, which are one-side vertical polarization only modes. The data analyzed were grouped by orbit direction (ascending or descending) and by three node crossing longitudes. The arrangement by orbit direction provides data for three different time periods; those occurring for the sunrise and morning hours (ascending orbits) and those occurring for the evening hours (descending orbits). Comparisons of data between the sunrise, morning, and evening time periods were made to show the effects of time of day on the NRCS response. Comparison of data from different node crossing longitudes provided information on the NRCS response for different Amazon rain forest locations.

For each orbit pass, the mean NRCS ($\overline{\sigma^o}$) for each Doppler cell (different incidence angle) that was classified as a suitable rain forest hit was computed from the number of samples obtained for the pass. On the order of 8 to 15 samples were obtained for each Doppler cell from each pass. For a few passes, the instrument was in a one-side single polarization mode; for these passes, 20 to 30 samples were obtained. Data from multiple orbits were combined in three time-of-day periods. The three periods were 0500 to 0730 (sunrise), 0800 to 1145 (morning), and 1730 to 2330 (evening). Plots of $\overline{\sigma^o}$ against incidence angle θ_i were produced for each orbit pass as a function of beam number and polarization. Overall statistics on the variation of σ^o as a function of incidence angle were computed. Linear regression curves of σ^o against incidence angle were also computed for each beam and polarization for the three time periods analyzed.

RESULTS OF INITIAL DATA ANALYSIS

Typical Results of NRCS Against Incidence Angle

Prior to processing the Amazon data, an improved method for estimating the channel noise power was developed. This improved method of noise estimation allows for a more accurate estimate of σ^o, especially at low signal-to-noise ratio. The original method of noise estimation used in the JPL processing determined the channel noise power by averaging 10 successive measurements of noise power for each channel. This was done separately for each beam and polarization. This method is acceptable over the open ocean, since for the time period of the 10 measurements, the system noise power is essentially constant. This is not quite true in the vicinity of land. Since the noise power from the land is higher than over water, an error in the average noise power would result when the antenna beam was moving from land to water (or vice versa) during the 10 sample periods. The noise power measured by each channel is different since each channel has a different bandwidth. However, if the noise power measured by each channel is divided by the channel bandwidth, the resulting noise spectral density should be the same for each channel. Thus by averaging the noise spectral density level across all channels, a more accurate measurement of the spectral density will be obtained, and, therefore, a more accurate estimate of the channel noise power, when the new spectral density value is multiplied by the channel bandwidth. This technique was incorporated in the initial processing of the Amazon data during this latest study (the Kansas University study (ref. 1) used the original JPL processed data). The average noise power was determined with channels 1 through 12, since it was first recognized that a small error was occurring in the noise power measurement on nadir channels 13, 14, and 15. This problem is further discussed in the section "Noise Analysis and Range-Gate Time Evaluation."

Figures 4 to 6 show plots of the mean NRCS versus incidence angle, obtained after this initial processing, for a sample number of orbit passes. Representative responses for each beam and polarization are included for each time period among these plots. Each symbol on these plots represents the mean σ^o ($\overline{\sigma^o}$) value computed from the sample values measured during the Amazon pass for each off-nadir cell of each beam and polarization operating during the pass. Cell 1 is the lowest incidence angle symbol for the beam represented and cell 12 is the highest incidence angle symbol. Because of Earth rotation effects, as discussed earlier, the channel incidence angles for two of the antennas cover a nominal range of approximately 22° to 55°, whereas the incidence angles from the other two antennas cover a range of approximately 25° to 65°. These ranges of angles can expand or shrink depending on the value of the roll, pitch, and yaw control angles. For an ascending orbit, antennas 1 and 3 are the expanded beams and antennas 2 and 4 are the compressed beams. The opposite arrangement is true for the descending orbits. The expanded and compressed beams can be seen in each of these plots. In many cases the value of $\overline{\sigma^o}$ for the higher cell is not shown, since values for incidence angles above 65° were not plotted. The time shown, in days, hours, and minutes, on each of these plots and on all subsequent plots, corresponds to the local Sun time of the subsatellite point as it crosses the equator. The actual local time at the location of the Doppler cell varies ±10 to ±20 min around this time, depending on which side swath and orbit direction are being considered. Note that all the ascending passes occur during the sunrise and morning hours (0500 to 1145), and the descending passes occur in the late afternoon and evening hours (1730 to 2345).

Figure 4 represents data from the sunrise period (0500 to 0730); figure 5, from the morning time period (0800 to 1145); and figure 6, from the evening time period (1730 to 2345). The relative responses between antennas and polarizations appear to agree very well over incidence angle ranges of 30° to 55°. Beam 4H appears to be biased slightly low on orbit 399 (fig. 6(b)). At incidence angles below 30°, there seems to be a greater separation in the NRCS responses among the various beams. Also in orbits 205, 535, 908, 1123, 1252, and 1281 (figs. 4 and 5), there is a noticeable dip in the NRCS value on cell 9 of some of the beams.

Anomalies Encountered

A number of data anomalies were uncovered during this study. These included bad data points due to bit errors on the signal plus noise voltage or the gain status channel, bad data frames or repeats of data frames, large errors in yaw angle determination on a number of orbits, and small instrument gain biases on a number of Doppler channels.

The bad data frames or repeats of data frames were detected by noticing the unusually large standard deviation on the value of NRCS during the orbit pass. An investigation of individual frames of data revealed these discrepancies. These bad data frames were subsequently removed from the data set. Similarly, bit errors were detected by observing the anomalous values of mean NRCS in plots of $\overline{\sigma^0}$ against incidence angle, such as in figure 7. In orbit 822 (fig. 7(a)), cell 12 ($\theta_i \approx 55°$) of beam 4 has an unusually high value of $\overline{\sigma^0}$. One of the samples had a value of σ^0 of +12.1 dB, which is obviously an erroneous result. It was found upon investigation that the gain status channel had (by a bit error) indicated that the channel was in gain step 3, when actually it was in gain step 1 (since the integrated noise voltage had a value corresponding to step 1). Since there is approximately 21 dB difference between these two gain steps, the actual value of σ^0 was about -9 dB. Orbit 1080 (fig. 7(b)) shows a slightly high value of $\overline{\sigma^0}$ on cell 7 of beam 3. In this case, the value of the integrated signal plus noise voltage (6.8 V) on one of the samples, used for computing the mean value, was significantly above the threshold value (4.7 V) at which the gain in the processor is switched to the next lowest gain step. This high voltage produced a value for σ^0 of -2.75 dB for this sample. This value raised the mean value for this cell from -8.8 dB to -8 dB. A similar situation occurred on cell 6 of beam 2 in orbit 1195 except in this case the signal plus noise voltage was unusually low on one of the samples, producing a value of σ^0 of -14 dB instead of a nominal value of -7.8 dB. This reduced value of σ^0 could have been caused by the presence of an unusually heavy rain cell at the Doppler cell location. In general, rain attenuation was not a problem in the processing of the Amazon data since the period of the Seasat mission occurred during the Amazon's dry season. Although it is certain that a number of sample measurements from all the Amazon passes processed were probably corrupted by rain attenuation, it is believed that they were few in number compared with the total number of samples averaged.

Reference 5 discusses the measurement accuracy of the Seasat attitude control system. As detailed in this report, large yaw angle (as much as 5° or 6°) excursions occurred during the early part of the mission because of Sun glint interference on the horizon scanners. This interference occurred during a small portion of the orbit. For some orbits, this interference occurred over the Amazon. If a large yaw angle exists, the Doppler cell locations will be shifted; this causes large changes in the incidence angle for each cell. A positive yaw excursion during an ascending orbit will cause the incidence angles of the expanded beams (1 and 3) to increase significantly, whereas the incidence angles of the compressed beams (2 and 4) will decrease. Orbit 650 (fig. 8(a)) is a situation where the yaw angle was between 5° and 6°; the outer cells of the expanded beam (1 and 3) did not intercept the Earth. When this occurs, footprint location data from the expanded beams are not computed. The two compressed beams (2 and 4) shown plotted for orbit 650 (fig. 8(a)) covered an incidence angle range of approximately 19° to 51°. Orbit 664 (fig. 8(b)) shows another case where the yaw angle was between 2° and 3°. As noted in the figure, cell 8 of beam 3 had an incidence angle of 60° instead of a normal angle of about 53°. As pointed out in reference 5, when the Sun glint interference occurs, the accuracy of yaw determination is greatly degraded. Errors in the specified yaw angle can cause significant errors in the measurement of σ^0 for the Doppler cells with low and high incidence angles. For this reason, the data for those orbits which had large yaw angles were not included in the combined statistics.

A Sun sensor was used to determine the yaw control angle. After day 230, no Sun sensor information was available over a major portion of the orbit due to the eclipse of the Sun by the Earth. This occurred on all the descending orbits over the Amazon. For this situation, the yaw angle is determined by extrapolating from the last Sun sensor measurement. The accuracy of yaw determination for this situation is 1° to 2° ±3 standard deviations (ref. 5), instead of a normal accuracy of about 0.2°. When large errors in yaw determination occur, significant errors in the specified antenna gain will result for the inner and outer Doppler cells; thus, an error in the measured σ^0 results. The σ^0 error sensitivity, in dB/(deg yaw angle), for each incidence angle is given in table 5. The largest sensitivity occurs at the highest incidence angle (outer Doppler cells), since the cells at these incidence angles shift the farthest in angular position for a given yaw angle change. The lowest incidence angles (inner Doppler cells) also have large sensitivities, since the cells for these angles lie on the steepest portion of the antenna gain pattern. The middle incidence angles lie near the peak of the antenna gain where the pattern is relatively flat, and therefore are essentially insensitive to yaw uncertainty errors or any other attitude uncertainty errors. The peak of the antenna gain is located at an incidence angle of about 45°. If a yaw determination error is present, the gain on the incidence angles below 45° will be estimated low and those above 45° will be estimated high, or vice versa depending on the direction of the error. In addition, the estimated gains for the forward and aft antennas will be in the opposite sense. The net result of all this is that the response of NRCS against incidence angle appears to be rotated about the 45° incidence angle point. The plot from orbit 607, shown in figure 8(c) is a very clear illustration of this effect. Reference 4 indicated that the yaw determination was difficult on this particular orbit due to the Sun glint interference, probably resulting in a large determination error. Orbit 607 of figure 8(c) appears to verify this situation. A number of other orbits such as orbits 1030, 1059, 1102, 1245, 1417, and 1460 shown in the figures of appendix B also show what appear to be significant yaw determination errors. All these orbits were descending passes occurring during the Sun occultation period when the yaw determination accuracy was 1° to 2°. It appears, in general, that all the descending orbits that occurred during the occultation period (after day 230) were subject to some yaw determination errors. However, only those orbits with obvious large yaw determination errors, as indicated in tables 3 and 4, were deleted from the combined statistics.

A dip in the NRCS response occurred for cell 9 of the aft beams (2 and 3) for a number of orbit passes. This dip can be seen in figures 4 and 5 for orbits 205, 535, 908, 1123, 1252, and 1281. The decrease in response was about 0.5 to 0.75 dB. This decrease was first attributed to the effects of rain attenuation. However, this was shortly ruled out since it occurred consistently for a large number of orbits. Further investigation of this problem revealed that a small instrument gain bias was present. This bias was not necessarily present during all orbit passes or on all beams processed during a pass. In general the instrument is calibrated to an accuracy of better than 0.1 dB. However, because of the technique used to calibrate all gain steps and the slight nonlinear square-law detector characteristics, a gain bias can sometimes occur because of the calibration process. This problem is most prevalent on channels 1 and 9 of the aft beams. It can occur on other channels and beams but to a lesser degree. Without going into a lot of detail here, this problem occurs on channel 9 mainly because the integrated voltage from the high calibration signal lies near the threshold level between gain steps 2 and 3. If the processor picks step 2 then the integrated calibration voltage will be at about the threshold value

(≈4.8 V). If step 3 is picked, the voltage falls to about 0.5 V since gain step 3 is approximately 10 dB lower than gain step 2. This integrated voltage is used to calculate the receiver gain. If step 2 is picked by the threshold detector, the integrated voltage determines the gain for step 2. The gain for step 3 is then determined by subtracting a fixed attenuation value (≈10 dB), incorporated in the processor, from the gain calculated for step 2. If the threshold detector picks step 3, then the integrated voltage determines the gain for step 3, and the gain of step 2 is determined by adding the fixed attenuation value to the gain of step 3. There appears to be a small relative bias between these two methods for establishing the gains for steps 2 and 3. The problem is partially caused by the small nonlinearity in the square-law detector characteristics and by a possible error in the prelaunch measurement of the fixed attenuation value. A similar situation occurs on channel 1, for the aft beams, when the highest gain step (step 1) is being calibrated. In this case, the integrated voltage from a low calibration signal lies near the threshold between gain steps 1 and 2; thus sometimes as on channel 9, a small bias is produced between the two methods for determining the gains for steps 1 and 2. Depending on which gain steps happen to be picked by the threshold detector, during calibration prior to an Amazon pass, a gain bias may or may not be present. An algorithm was developed, by using the average noise spectral density calculated across all the channels, for correcting these small gain biases.

Noise Analysis and Range-Gate Time Evaluation

As discussed in reference 1, an accurate measurement of the noise power is required in order to minimize the error on σ^o caused by the effects of communication noise. A more accurate measurement of the channel noise power can be made, as pointed out earlier, by averaging the noise spectral density measurement obtained by each Doppler channel. To evaluate the validity of this procedure an analysis was conducted of the noise power measurements made during the range-gate integration period and the noise integration period when the instrument was in the standby mode. Throughout the mission (approximately every 7 days) the instrument was placed in the standby mode for a 10-min period. In this mode, the transmitter is turned off but the receiver is still operating in a normal fashion making both a signal plus noise measurement (range-gate integration period) and a separate noise measurement (noise integration period). With the transmitter turned off, no backscattered signal is present; therefore, the measurements obtained from each integration period are a measure of the system noise power. The noise spectral density of each channel is obtained by dividing the measured noise power of the channel by its respective filter bandwidth. By comparing the noise spectral density made by each integration period for each Doppler channel, an evaluation of the consistency of the noise power measurement across all channels can be made. Also, an evaluation of the accuracy of the range-gate integration period, noise integration period, and Doppler filter bandwidths used in the σ^o algorithm processing can also be made.

As discussed in reference 1, the signal processor produces two voltages for each of the 15 Doppler channels. One voltage (V_{SN}) represents the integrated output of the square-law detector which is proportional to the mean signal plus noise power; the other voltage (V_N) is the integrated output which is proportional to the mean system noise power. When the transmitter is operating, the noise power, determined from V_N (incorporating the correct gain and integration time), is subtracted from the signal plus noise power, determined from V_{SN} (incorporating the correct gain and integration time), to obtain the signal power backscattered from the surface. When the transmitter is turned off, in the standby mode, V_{SN} processed during this time period is proportional to the system noise power, since there is no backscattered signal present. The level of V_{SN} and V_N will be different for a particular channel and system noise power, since the integration times for each voltage are different. Since the same bandwidth and system gains are used in the generation of these voltages, the ratio of these two voltages (V_{SN}/V_N) should be the same as the ratio of the integration times (T_G/T_N), where T_G is the range-gate integration time over which V_{SN} is determined and T_N is the noise integration time over which V_N is determined. For a constant system noise power, the normalized standard deviation of the value of these voltages is equal to $1/\sqrt{B_N T}$ where B_N is the Doppler filter noise bandwidth and T is the integration time over which the voltage is determined. Table 6 lists the noise bandwidth, noise integration period, range-gate integration period, and the NSD value for the V_{SN} and V_N measurements. As seen from this table, the NSD of both the V_{SN} and V_N measurements is less than 2 percent on most of the channels, and for many of the wider bandwidth channels (1 to 3 and 13, 14, and 15), less than 1 percent; thus, an accurate measurement of the system noise power is provided. The noise integration period is the same on all the channels, whereas the range-gate integration period is different for each channel, since the variation in the two-way range time, caused by orbit and attitude pointing angle variations, is greater on those cells which are farther from the subtrack (highest incidence angles). By evaluating the ratio of measured V_{SN} and V_N to the ratio of the integration times for each channel, the accuracies of the integration times listed in the table can be evaluated.

A statistical analysis was conducted on the V_{SN} and V_N measurements obtained when the instrument was operating in the standby mode (mode 10). The noise power and noise spectral densities for each channel were computed from these voltages. The ratio V_{SN}/V_N was computed and divided into the ratio T_G/T_N. This new ratio, averaged over a large number of data frames, should be equal to 1, if the integration times shown in table 6 and used in the computation are correct. The difference in the spectral densities computed from each voltage was determined. An average spectral density, across channels 1 through 12, was computed for each of the integration times. The difference between the average spectral density (computed from T_N) and the densities computed from T_N of each individual channel was also determined.

In between each set of four calibration frames, 124 science frames are processed. When operating in the standby mode the instrument samples antennas 4V and 3V. Each antenna is sampled for 1.89 seconds, with antenna 4V being sampled twice in a row followed by two samples of antenna 3V. This procedure continues for the 124 science frames. For each 124 science frame sequence analyzed, the means and standard deviations or normalized standard deviations of various parameters were determined for the 62 samples of each channel of each antenna. A total of 20 science sequences were analyzed in this manner from day 218 to day 281. Both ocean-viewing noise data and land-viewing noise data were analyzed. Tables 7 and 8 are samples of the resulting statistics for two 124 science frame sequences viewing water and land, respectively. A definition of all the parameters listed in these tables is given in the list of symbols and abbreviations. Included in these tables for each channel (cell) are the mean noise power and noise spectral density (SNKT and NKT) determined by each integrated voltage (V_{SN} and V_N), the difference between these two noise power measurements (DPN), and the difference (DG) between the average spectral density (AV NKT) of channels 1 through 12 and the individual noise spectral density (NKT) of each channel.

As seen from these tables, the measured noise spectral density values are relatively consistent across all channels. For channels 1 through 12 the difference (DPN) in the spectral density values measured by each integration period is less than about 0.03 dB, and in some cases less than 0.01 dB. For nadir channels 13, 14, and 15, the difference, however, is over 0.12 dB. This difference is a result of a small error in one of the integration periods, either T_G or T_N, and can be seen by the value of RR shown in the tables, where RR is the ratio T_G/T_N divided by the ratio V_{SN}/V_N, which, as pointed out previously, should be equal to 1 if the correct integration times are known. For the nadir channels, the RR value is consistently about 3 percent high. It is difficult to determine for sure which integration period is in error, since correcting either period and recomputing SNKT and NKT results in the same value for these parameters. However, analysis of the control timing design used in the instrument data processor indicates that the T_G value for each of the nadir channels is most likely in error. The corrected value of T_G for each of the nadir channels is listed in table 9. This value was determined by dividing the original value of T_G by the mean value of RR averaged over the 20 science sequences analyzed. The total number of samples averaged is listed in the table. These new values for T_G are incorporated in the σ^o correction algorithm.

The effective system noise temperature (TEV), determined by dividing the noise spectral density (NKT) by Boltzmann constant, is also listed in tables 7 and 8 for each of the channels, as well as the effective antenna noise temperature (TA) for each channel. Antenna noise temperature TA is determined by subtracting an estimate of the receiver noise temperature, determined by the receiver noise figure measured prior to launch, from the measured system noise temperature TEV. The antenna noise temperature is primarily a function of the brightness temperature of the surface viewed by the main lobe of the antenna pattern. The peak of the antenna gain is pointed at an incidence angle of about 45°. At this incidence angle over cloud-free water, with a physical temperature of about 298 K and an emissivity of about 0.54, the antenna noise temperature (TA) is in the range of 155 K to 165 K. Over land where the emissivity is about 0.85 to 0.90, the antenna temperature is in the range of 240 K to 260 K. The mean value of the antenna temperature (TAM), averaged over channels 1 to 12, as shown in tables 7 and 8, resulted in approximately these values. The water and land data shown in these tables were taken over the equator and over central Russia, respectively. The average system temperature (TEVM) shown for beam 4V is always slightly higher than beam 3V. This difference is expected since the antenna switching matrix loss for beam 4V is 0.1 dB higher than beam 3V, resulting in a system noise temperature that is about 30° higher on beam 4V. Note that the resultant TAM for both beams agrees fairly well. The slightly different values shown for each beam are probably because each beam views a slightly different surface area during the 124 science frame periods over which the mean values are obtained (beam 4V is looking forward and beam 3V is looking aft).

The sample NSD values listed for each channel spectral density measurement agree very closely with the predicted values listed in table 6. The average spectral densities (averaged across channels 1 to 12) for each integration period agree very well with each other. Also the NSD values for these average spectral densities are significantly lower than any individual channel NSD, showing that the average value of NKT provides a more accurate measurement of the true noise power existing in each channel. In this analysis, the average noise spectral density was computed across the first 12 channels. This computation was done since it was suspected beforehand that a small error was occurring in the noise power measurements of the three nadir channels. Since the error in the range-gate integration period (T_G) has been determined, a correction to the noise spectral density measurement NKT can be made. This correction must be made to reflect the small error in the channel gain that results during the calibration period from using an incorrect value of T_G. The amount of correction required for each channel is listed in table 9, as the factor $(T_N + T_{GC})/(T_N + T_G)$, where T_{GC} is the corrected value of T_G. This factor represents the error in gain that results. Incorporating this small correction now allows the average noise spectral density to be computed across all 15 channels. The results of these analyses show the consistency of the noise measurements, the stability of the instrument, and the accuracy of the measurements.

σ^o Correction Algorithm

A σ^o correction algorithm was developed which incorporates the average of the noise spectral density across all channels to provide a more accurate measurement of the channel noise power and to provide a means to correct for instrument gain biases. The more accurate measurement of the noise power produces a more accurate measurement of σ^o, especially at low signal-to-noise ratios.

As discussed earlier and shown in figures 4 and 5, a significant dip in the NRCS response sometimes occurs on various channels because of a bias error in the gain calibration period. This bias can easily be corrected by comparing the individual channel noise power measurement with the average value computed across all channels. Normally, when little or no bias error exists, the difference between the individual channel noise power measurement and the average noise power measurement is less than 0.1 dB, well within the normal measurement variability (see the DG values listed in tables 7 and 8). However, when a bias error occurs, this difference can amount to as much as 0.75 dB. In the σ^o correction algorithm, this difference is used to correct the instrument gain. Appendix C lists the equations and procedure used in the σ^o correction algorithm. All the Amazon σ^o signature data were reprocessed using this algorithm.

FINAL OVERALL RESULTS AND STATISTICS FOR ALL ORBITS ANALYZED

Off-Nadir Swath (Cells 1 to 12)

All 149 Amazon orbit passes were reprocessed by using the new σ^o correction algorithm. Figures 9 and 10 show plots of $\overline{\sigma^o}$ against incidence angle, after this reprocessing, for a sample number of orbits. Similar plots for these orbits were also shown in previous figures (figs. 4, 5, and 6) for the initial processing scheme which did not correct for instrument bias errors. An intercomparison of these sets of plots shows the significant improvement resulting on the channels most affected by the gain bias errors, especially for orbits 162, 205, 535, 908, and 1080. Plots of $\overline{\sigma^o}$ against incidence angle are shown in appendixes A and B for all the ascending and descending orbits processed, respectively. These plots are computer generated. Because of the lack of time, new plots using the reprocessed data were not made for all the orbits shown in these appendixes. The plots with the word "corrected" after the orbit number were made by using the σ^o correction algorithm.

As discussed earlier, the σ^o values in the plots are the mean values (averaged in ratio form) obtained for each Doppler cell during the Amazon pass. To see how much scatter existed in the data points averaged, sample scatter plots were made for a number of orbits. Figures 11 to 14 are samples of these scatter plots. Each plot shows, for a single beam, the σ^o value of each sample used in computing the mean values for each Doppler cell. It can be seen in general that the data points are tightly grouped and that the scatter is greater for the lower and higher incidence angles where the signal-to-noise ratio is lower; therefore, a higher normalized standard deviation (NSD) is produced on the measurement accuracy. In a number of cases, such as cell 7 of beam 1V, orbit 205 (fig. 11(a), data values fell significantly below the mean value and the values of the remaining group of data for that cell.

Cell 11 of beam 2V, orbit 205 also shows one point which is significantly below the other points. These low values are probably caused by one of two reasons: A rain cloud was present, causing rain attenuation, or that particular Amazon location was misclassified and did not contain a significant amount of rain forest. Also, it should be noted, the cell classification was determined by the latitude and longitude location of the center of the cell. Since the cells extend over an approximate 16- by 60-km area, parts of the cell area could encompass adjacent non-rain forest areas. Cell 7 of beam 3V, orbit 434 (fig. 12(c)) shows five measurements which are significantly below the mean value and the other group of 23 values. These five measurements were all located as a successive group of measurements along 175 km of the cell track. In these cases, it is most likely that a rain area caused attenuation on these measurements, since it is not likely that this total area would have been misclassified. Further analysis of measurements with the same incidence angle, from other orbits hitting this area, could be analyzed to determine if this is true. This type analysis was beyond the scope and allowable time of this study. The overall results of this study, however, are minimally affected by these outlier points, since the number of these points are few in comparison with the total measurements analyzed. Dropping these five low points, for example, only changes the mean value by about 0.2 dB.

If all the Doppler cell measurements were collected and separated into each of the Amazon classified grid points, the classification assigned to the grid point could be evaluated for its suitability as a rain forest target. This analysis was also beyond the scope of this study. However, in the process of identifying obvious outlier points from evaluating the statistical results of each orbit processed, a number of possibly misclassified grid points were identified. Later in the mission, when the satellite was in a frozen orbit, the subsatellite traversed approximately over the same track every 3 days. As discussed earlier, three different tracks were traversed for both the ascending and descending nodes. One of these tracks from each orbit direction was traversed each day. For each repeat pass (every 3 days), corresponding Doppler cells for each corresponding beam were located at approximately the same location, within 25 to 50 km, depending on the attitude pointing angles, and the exact synchronism of the measurement timing. A set of locations from five successive ascending orbit passes, crossing the 297.9° node, were found to lie within 3 to 25 km of each other over these five orbits. Figures 15 and 16 are scatter plots of beam 1V of these five orbits, orbits 1209, 1252, 1295, 1338, and 1381. Figures 17 and 18 are similar plots for beam 2V of these orbits. Considerable correspondence in σ^o value and similarity in response can be seen by comparing the plots from each orbit for each beam. Particularly, note the one low value that occurs on cell 8 of beam 1V (figs. 15 and 16) in comparison with the other points on that cell. This point was identified on each orbit and found to be at the approximate same location. The values of σ^o for these points were about the same for each of the orbits. A similar set of low values of σ^o can also be seen on cell 12 of beam 2V for each of these orbits (figs. 17 and 18). The locations of these outlier points along with their σ^o values are given in table 10. The minimum separation distance is about 3 km and the maximum about 25 km. The average separation is around 10 km. The points of cell 8 (beam 1V) lie near an Amazon river tributary in a mountainous region (see fig. 3(a)), and the points for cell 12 (beam 2V) lie near the main Amazon river. It is most likely that the locations of these points are misclassified. All outlier points of this type that could be identified were removed from all the individual orbit files before the combined statistics from multiple orbits were computed.

Statistics on the variation of σ^o were computed for each Doppler cell of each beam for all the orbits processed. Tables 11 to 16 are samples of these statistics for a number of orbits shown in the previous response and scatter plots. Included in the tables are the mean, standard deviation, minimum and maximum values, and the sample NSD of σ^o and the estimated NSD of a single σ^o measurement. The sample NSD is determined by dividing the standard deviation of σ^o by the mean of σ^o, with σ^o expressed in ratio form. The standard deviation in dB and the NSD are approximately related by the following expression:

$$(SD)_{dB} = 10\left(\log e\right)\frac{NSD}{100}$$

The estimated NSD is determined with the known values of the bandwidth and integration time, the measured SNR, and the estimate of attitude uncertainty errors.

The statistics show that the rain forest response is relatively stable. The standard deviation of σ^o varies from about 0.25 to about 0.75 dB over a range of incidence angle from 25° to 55°. The highest deviations occur at the low and high incidence angles, as would be expected, since the SNR is lowest at these angles and the attitude uncertainty errors are the highest. In almost all cases, the sample NSD is always slightly higher than the estimated NSD. This should be the case, since the sample NSD includes variability in the rain forest target response. The estimated NSD includes only measurement accuracy variability. The root mean square difference between these two NSD values provides an estimate of the surface response variability. Sometimes, the sample NSD is unusually high compared with the estimated NSD. This comparison indicates that a few of the sample values were significantly different from the remaining sample values in the group, as seen in the scatter plots. In general, these outlier values are low compared with the mean. They are caused, as discussed earlier, by either rain attenuation or a misclassification. In either event, since there is only one or two of them in a sample set, the mean value is not affected significantly by their presence. In a few rare instances, such as in cell 6 of beams 4H and 4V of orbit 428 (figs. 13(c) and (d)), a few points are much higher than the mean value. The statistics for this cell of these two beams (table 14) shows a high sample NSD value. Removing these outlier values reduces the sample NSD value to the more normal value of 5 to 6 percent. The mean value of σ^o is reduced by about 0.25 dB, smoothing out the response plot, which shows a slight rise in the curve at the incidence angle for cell 6, as seen in figure 9. An investigation of these high points on cell 6 revealed that an erroneous noise voltage (V_N) was received that was about 1.5 dB below the normal expected value for that cell. The noise voltage is used, as discussed earlier in the section "Noise Analysis and Range-Gate Time Evaluation," to compute the system noise power. Since the system noise power is relatively constant from measurement to measurement, the noise voltage should also stay constant. With the new correction algorithm technique, discussed earlier, an erroneous correction of about 1.5 dB was added to σ^o. This problem can be avoided in the instrument gain correction process, used in the σ^o correction algorithm, by setting a limit on the range of channel measured noise power (or system noise temperature TEV, see appendix C) over which a gain correction would be applied. The values of σ^o for the high points that showed up on cell 6 of orbit 428 would have been closer to the mean value had the gain correction (1.5 dB) not been applied. These erroneous values of V_N were probably caused by random bit errors. Fortunately, bit errors were rare and therefore had little effect on the results of the overall statistics.

After analyzing the response of $\overline{\sigma^o}$ against incidence angle for each individual orbit pass, a set of response plots and statistics were generated by combining the data from multiple orbit passes in the three time periods mentioned earlier (sunrise, morning, and evening). The data from multiple orbits were first combined according to their node crossing, so that response comparisons could be made between Amazon locations. Figure 19(a) is a plot showing a comparison of the response of $\overline{\sigma^0}$ against incidence angle for beams 1V and 2V for two different ascending node tracks. The mean σ^0 value was computed from all the data collected from all the orbits that fell in the morning time period. Figure 19(b) is a similar plot for beams 3V and 4V. As seen from these plots, the responses for both node tracks are very close; this closeness shows that the response for the Amazon rain forest is essentially constant for different locations. Similar plots for other time periods and polarizations also show consistent responses for different Amazon locations.

Since the response from any part of the Amazon rain forest for any specific time period was essentially constant, the data from all orbits within each time period were combined and a set of overall statistics were computed and plotted for each beam and polarization. Figures 20 to 22 are plots of $\overline{\sigma^0}$ against incidence angle of the combined data for each time period for various beam and polarization combinations. Figure 20 shows the vertical polarization response of each beam for the three time periods. Figure 21 shows the horizontal polarization response of each beam for the sunrise and evening time periods (no horizontal polarization data were taken during the morning hours). Figure 22 shows combined vertical and horizontal polarization plots for each beam for the sunrise and evening time periods. A study of these plots shows that the responses from all the beams compare very well, with small relative biases between beams and polarizations, especially antennas on the same side of the spacecraft (1 and 2 or 3 and 4). This agreement is particularly important since measurements from fore and aft beams on the same side of the spacecraft are combined to obtain wind vector data. The response between beams is more closely matched - within about 0.3 dB - over a range of incidence angle from about 30° to 53° than at incidence angles lower or higher than this range, where the deviation is 0.5 to 0.75 dB. Note the slight turning or rotation between the fore and aft beam responses in the evening time period (figs. 20 and 21). This effect was most likely caused by the larger yaw determination errors that may have existed on most of the descending orbits (evening passes) due to Sun occultation. (See earlier discussion on the effects of yaw determination error in section "Anomalies Encountered.")

Table 17 shows the σ^0 statistics computed for each Doppler cell of each beam and polarization, from the combining of all the sunrise (0500 to 0730) passes. Similarly, the statistics for the morning passes (0800 to 1145) are shown in table 18 and for the evening passes (1730 to 2330) are shown in table 19. The largest number of samples, used for computing the statistics, occurs in the vertical polarization beams during the morning and evening time periods. A total of 18 orbits were combined from the sunrise period, 54 orbits from the morning period, and 52 orbits from the evening period. Only 7 orbits each were available during the sunrise and evening periods for the horizontal polarization beams. As in the statistics for the individual orbits, the standard deviation of σ^0 varies from about 0.3 dB to about 0.7 dB over a range of incidence angle from 30° to 53°. At the lower and higher incidence angles, the standard deviation increases to about 0.75 dB to 1.0 dB. A few incidence angles above 60° have standard deviations of about 1.5 to 1.75 dB. This is not unexpected since these angles generally have low SNR and are more sensitive to attitude determination errors. The standard deviation of σ^0, or sample NSD, is generally a little larger for the evening passes (table 19), probably because of the higher yaw determination errors that existed during these orbits.

As seen from the combined statistics tables, the σ^0 response from the Amazon rain forest is relatively constant for a given incidence angle for each time period.

The most stable response occurs during the morning time period (0800 to 1145). A sample set of scatter plots for this time period is shown in figure 23(a) and (b) for beams 1V and 2V, respectively. Each Doppler cell contains on the order of 300 to 500 sample measurements. For the middle range of incidence angle, the data samples are fairly well concentrated. A larger spread in the data occurs at the lower and higher incidence angles, as expected. A few outlier points can be noted on some of the cells. Also note that there is a spread in the value of the incidence angle for each cell. This effect is caused by the variation in the attitude angles from orbit to orbit, which changes the pointing direction of the antenna and, therefore, the positional location of each Doppler cell. The sensitivity of incidence angle variation is greater for the higher incidence angles, which can be seen from the figure. For a given incidence angle, the incidence angle variation is larger on the expanded beam (beam 1V, fig. 23(a)) than on the compressed beam (fig. 23(b). This is because the expanded beam lies along a more sensitive portion of the hyperbolic Doppler lines, since these lines are rotated about 3.5° counterclockwise from the orientation shown in figure 2. Figures 23(c) and (d) are scatter plots of beams 1V and 2V from the evening time period. Since these data come from descending orbits, the expanded and compressed beams are reversed. Note in these cases that even though the incidence angle spread is slightly reduced, the spread in the σ^o is slightly larger and there is a greater number of outlier points.

A comparison of the NRCS response for each time period shows a definite change in the response curve between the sunrise data and the data from the other two periods. Figures 24 and 25 are response plots showing an intercomparison of the responses from each time period for each beam and polarization. It can be seen from these plots that the response from the sunrise period is on the order of 0.75 dB higher than the responses from the other two time periods. Note that the sunrise and morning responses run almost parallel to each other, whereas the evening responses appear slightly rotated with respect to the other two responses. Also the responses from the forward and aft beams on the same side of the spacecraft are rotated in the opposite direction. This effect is almost certainly caused by the higher yaw determination error that existed on most of the descending orbits. It appears that a slight yaw determination bias was present during all these orbits, causing a slight bias error in the computed antenna pointing angle. This resulted in a slight bias error in the retrieved antenna gain used to compute σ^o.

There is yet no clear explanation for the higher σ^o response during the sunrise period. The most logical explanation proposed so far is that a large quantity of water (early morning dew) is present on the upper foliage of the rain forest canopy, and this causes the increase in σ^o. The backscatter from trees and vegetation is, in general, a combination of volume scattering from dielectric discontinuities within the vegetation volume and surface roughness scattering from the soil under the trees and vegetation. However, for the Amazon rain forest, the vegetation canopy of the trees is so dense and, in general, high in moisture content, that little or no signal energy, at the scatterometer frequency, can penetrate to the surface. In fact, since the foliage is so dense and moist, the signal does not penetrate very far into the canopy volume, so that a large part of the scattering comes from surface roughness scattering at the air-canopy interface. The upper canopy of the rain forest foliage could be analogous to rough surface soil where the amount of volume penetration is a function of moisture content, and the backscatter is a function of the soil roughness and dielectric constant which determines the Fresnel reflection coefficient. The moisture content determines the magnitude of the reflection coefficient at the air-soil (or in this case the air-canopy) interface and the penetration depth of the signal. The additional moisture from the early morning dew further reduces the signal penetration into the canopy and increases the dielectric constant (increased reflection coefficient) at the air-foliage interface. It is known that backscatter measurements from soil with a rough surface have a higher σ^o for soil with a high moisture content than for dry soil (ref. 6, page 832), due to the increased dielectric constant and reduced soil penetration. It is this phenomenon that is the most likely explanation for the observed shift in the response of $\overline{\sigma^o}$ against incidence angle. Comparisons of the responses from the early evening orbits (sunset) with the late evening orbits were made. No observable shifts in response could be detected. As seen from the last set of figures of the response intercomparisons, the evening orbit responses appear consistent with the late morning responses. If moisture is forming on the upper canopy it must be forming in the early morning hours. A comparison of the responses for early sunrise (0500 to 0600) with those for late sunrise (0630 to 0730) shows a slight shift, indicating a slight drying out is occurring. The shift appears in general, however, to be relatively sudden, since by 0800 the response shift of 0.5 to 0.75 dB has occurred.

Linear regression curves, of $\overline{\sigma^o}$ as a function of incidence angle, were computed for each beam and polarization of each time period. The linear function is of the following form:

$$\overline{\sigma^o}_{(\mathrm{dB})} = a + b\theta_i$$

where a is the Y-intercept in dB, b is the slope in dB/deg, and θ_i is the incidence angle in degrees. The regression coefficients were computed over a range of incidence angle from 30° to 53° with the mean values of σ^o and incidence angles listed in tables 17 to 19. This range of incidence angle was used, since above $\theta_i = 53°$ the response begins to roll off at a larger slope and below $\theta_i = 30°$ the response appears to be leveling off towards a peak value that occurs somewhere between incidence angles of 0° and 20°. Table 20 lists the regression parameters for each of the beams and time periods. The table includes the coefficient of determination (R^2) and the value of $\overline{\sigma^o}$ at $\theta_i = 45°$, using the above function. An intercomparison of the $\overline{\sigma^o}$ value at $\theta_i = 45°$, for a particular time period, shows that little relative bias - less than 0.3 dB - exists between beams. Also a comparison of the value of $\overline{\sigma^o}$ at $\theta_i = 45°$ for the sunrise orbits with the other time periods, on a beam-by-beam basis, shows that a decrease of about 0.6 to 1.0 dB occurs between the sunrise period and the other two periods, with an average of 0.73 dB. The slope coefficient b varies from about 0.08 to 0.13. The slopes for the sunrise and morning passes are almost the same on a beam-to-beam basis. In the evening orbits the slopes on beams 1 and 3 decrease slightly from their sunset and morning values, whereas the slopes for beams 2 and 4 increase, showing the effects of the yaw determination error. Sample plots of the linear regression curves are shown in figure 24(a) for beam 1V. The vertical lines shown in this figure and figure 24(b) represent the ±1 standard deviation variation about the mean.

Nadir Cells (Cells 13, 14, and 15)

An analysis of the nadir cell response from the Amazon rain forest was performed on a limited set of orbits. The data were processed through the correction algorithm, incorporating the corrected range-gate times determined from the noise analysis described earlier. The statistical results from the processing of these data are shown in table 21. The nadir measurements are received through a side lobe of the antenna gain pattern that is located 40° from the peak of the antenna gain. The gain response at this point on the antenna pattern is anywhere from 10 to 22 dB down from the peak gain of the antenna. In general, the horizontal polarization beams have the highest response and therefore provide the largest SNR. These beams therefore will produce the smallest measurement error as seen by the estimated NSD value shown in table 21 for the horizontal polarization beams. The data shown in these tables include data from all three time periods. The statistics from each time period were analyzed separately. Because of the large deviations in the values of σ^o, as seen in table 21, no distinctive difference in the responses could be seen between time periods. For this reason, data from all time periods were combined.

The results of the statistical analysis show that σ^o varies over a wide range of values at these low incidence angles, especially the nadir cell (cell 15). This variation can be seen by the large sample NSD values which occur on all the beams, even those with the good side lobes which produce a more accurate measurement of σ^o, that is, low estimated NSD shown listed in the tables (beams 1H, 2H, and 4H). The scattering return from near or at nadir is very sensitive to small changes in surface roughness. The minimum and maximum values listed in the tables extend over a wide range of values, much greater than would be expected for measurement accuracy variation; thus, the variation in surface conditions that exists from sample to sample is shown. The nadir cell shows the widest variation, and the 8° cell (cell 13), the least variation, showing that as incidence angle increases, the sensitivity to surface roughness variation begins to decrease. From the analysis of the other 12 Doppler cells, the data near 20° had a greater spread than the data from higher incidence angles. Although this variation was caused primarily by higher NSD on the measurement due to lower SNR and attitude errors, part of the variation could be due to sensitivity to surface roughness variation. The nadir cell values on the better side lobe beams had values that varied from about -7 dB to 30.7 dB. The high value of 30.7 dB is approaching the pure specular return value which, for the nadir cells equivalent beamwidth over the cell dimensions, is on the order of 36 to 38 dB. This high value indicates that some large open relatively flat smooth areas existed in the canopy within the Doppler cell area. Unless these open areas are a large percent of the total Doppler cell area, they would have a small affect on the value of σ^o at the higher incidence angles. At nadir this is not the case, since the return from these specularlike areas are large compared with the return from the rough canopy surface.

With higher resolution nadir measurements, an evaluation of the Amazon map classification could probably be made by identifying as unsuitable rain forest targets those classification bins which produce high σ^o values. It is believed that for a solid rain forest canopy, over the total Doppler cell area, the σ^o value for a nadir measurement should be less than 0 dB. Since the value of σ^o near nadir varies so widely over the Amazon rain forest, little information can be obtained on the relative bias between the various beams at the portion of the antenna pattern corresponding to the three near nadir cells (cells 13, 14, and 15). This type of calibration is more suited to σ^o data obtained over the ocean, where the return is more constant for light to medium windspeeds.

CONCLUDING REMARKS

The results of a detailed study of the normalized radar cross section (NRCS or σ^o) response from the Amazon rain forest were presented. NRCS data from 149 Seasat orbits which passed over the Amazon rain forest were processed and analyzed. Statistics of the variation of σ^o data were computed, and response plots of $\overline{\sigma^o}$ against incidence angle were generated for each orbit. Statistics were generated for data combined from multiple orbits in three different time periods. Various anomalies, such as attitude determination errors, bit errors, and instrument channel gain biases, were detected. As a result of the analysis, a correction algorithm was developed, with the mean noise spectral density averaged across all channels, to correct for the gain bias and to improve the accuracy of the noise power measurement.

The analysis of the NRCS measurements obtained by the Seasat scatterometer shows the Amazon rain forest to be a homogeneous, azimuthally isotropic radar target which is insensitive to polarization. A small diurnal variation in the $\overline{\sigma^o}$ value was detected. The values obtained during the sunrise period were 0.5 to 1.0 dB higher than the morning and evening time periods. A theory is presented which indicates that the presence of moisture from early morning dew on the rain forest canopy increases the reflectivity and reduces signal penetration causing an increase in the NRCS. The variation of $\overline{\sigma^o}$ with incidence angle is adequately modeled by $\overline{\sigma^o}_{(dB)} = a + b\theta_i$, over a range of incidence angle θ_i from 30° to 53°, where a is y-intercept. The mean slope value b for all beams is about 0.1 dB. The maximum relative bias between antennas is shown to be about 0.3 dB over a range of incidence angle from 30° to 53°. At higher and lower incidence angles, the relative bias between beams increases to as much as 1 dB because of attitude determination errors (mostly on the yaw angle); small errors in the measured antenna pattern; and at the low incidence angles, a slightly higher sensitivity to roughness variation in the rain forest canopy.

This detailed study of the NRCS response from the Amazon rain forest has confirmed its suitability for use as a standard calibration target. Future spacecraft scatterometers can utilize the rain forest as a target for determining relative bias between antennas, detecting anomalies such as attitude determination errors, channel gain biases, and various bit errors. As described in NASA CR-165921, the NRCS measurements from the Amazon rain forest can also be used to correct pointing direction errors in the antenna gain tables. NASA CR-165921 develops a set of processing algorithms which can be used to analyze the rain forest data and determine antenna pointing errors and relative bias between antennas.

Although this present knowledge of the Amazon rain forest response appears suitable for use as a calibration source, further studies should be conducted to better classify the Amazon rain forest map and to obtain information on the absolute σ^o response so that an absolute calibration can be obtained. Further studies of the Seasat data could help to improve the map classification by collecting and analyzing all the σ^o hits that fall within each of the map grid points, including the nadir measurements. Aircraft flights over the Amazon, with a well calibrated scatterometer, could be helpful in obtaining absolute response characteristics of the rain forest. Analysis of higher resolution photographs of the rain forest, such as from Landsat spacecraft, may be helpful in providing information for better map classification.

Langley Research Center
National Aeronautics and Space Administration
Hampton, VA 23665
June 8, 1984

APPENDIX A

RESPONSE PLOTS OF $\overline{\sigma^o}$ AGAINST INCIDENCE ANGLE FOR ALL ASCENDING ORBITS

This appendix contains response plots of $\overline{\sigma^o}$ against incidence angle for all the ascending orbits. These orbits cover all the sunrise and morning time periods over the Amazon rain forest. A number of orbits are missing because of data gaps, bad frames of data, or an operating mode which looked away from the Amazon rain forest. The times shown on each plot correspond to the local Sun time of the subsatellite as it crosses the equator. The time is given in days, hours, and minutes. Each plot lists the orbit number, the beams, and the polarization of the data plotted. Each symbol represents the mean value of σ^o computed from the number of measurements obtained during the pass for each of the 12 off-nadir cells. The word "corrected" after the orbit number indicates that the data on that plot were processed through the σ^o correction algorithm. The plots shown in this appendix are computer generated. Time did not allow the plots from all orbits to be regenerated with the corrected version of σ^o. Therefore, many of the plots shown in this appendix are those generated from the initially processed σ^o data.

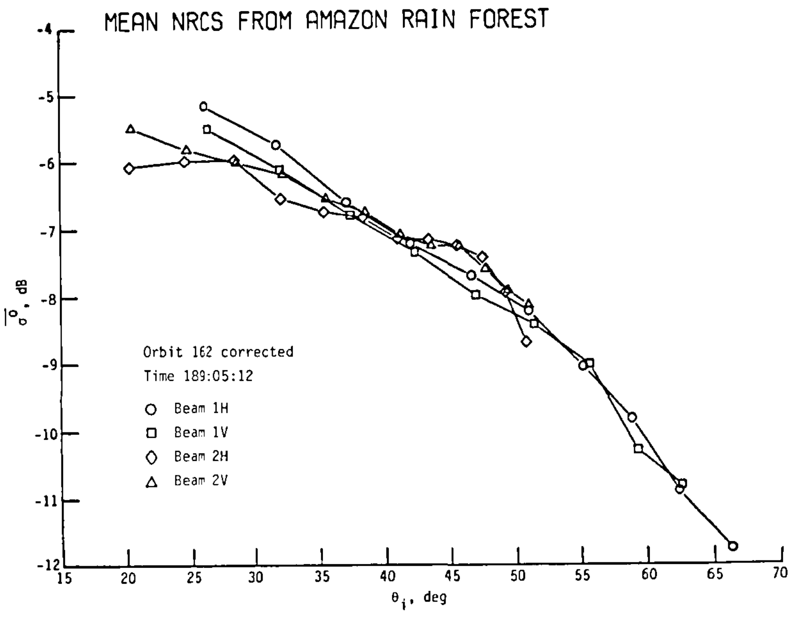
MEAN NRCS FROM AMAZON RAIN FOREST

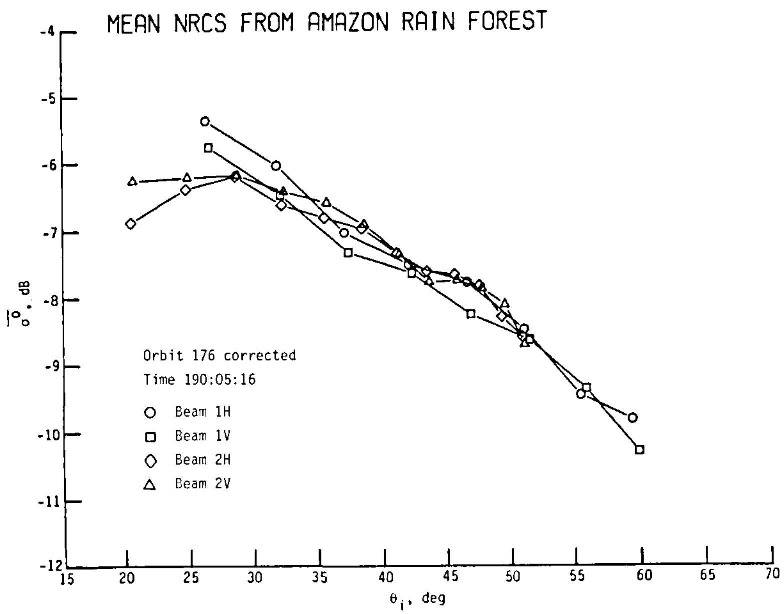
MEAN NRCS FROM AMAZON RAIN FOREST

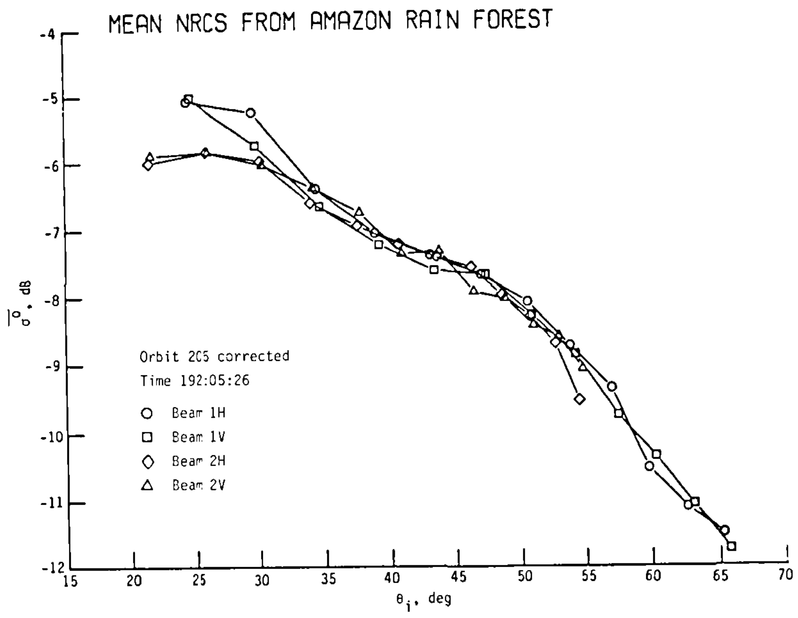
MEAN NRCS FROM AMAZON RAIN FOREST

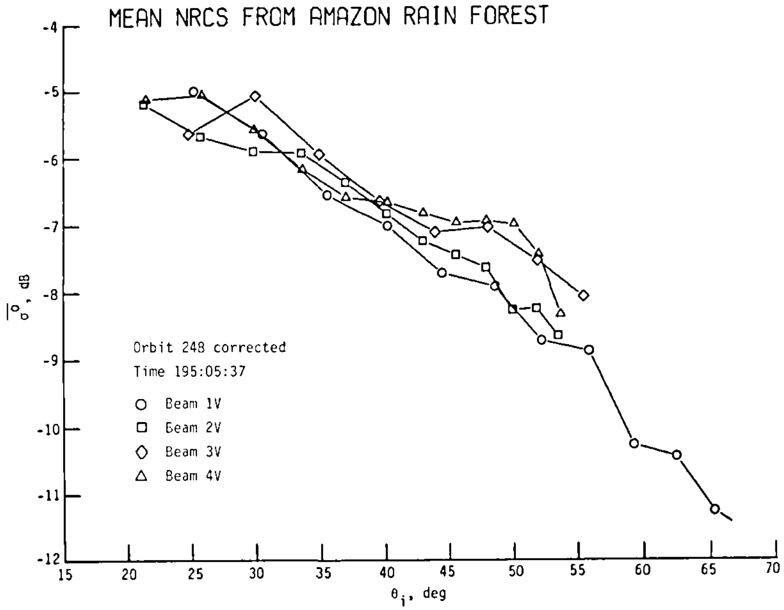
MEAN NRCS FROM AMAZON RAIN FOREST

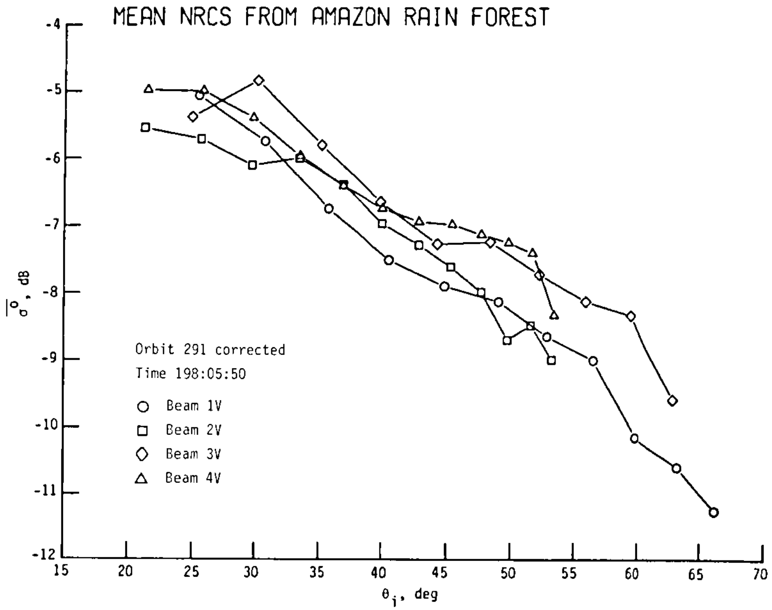
MEAN NRCS FROM AMAZON RAIN FOREST

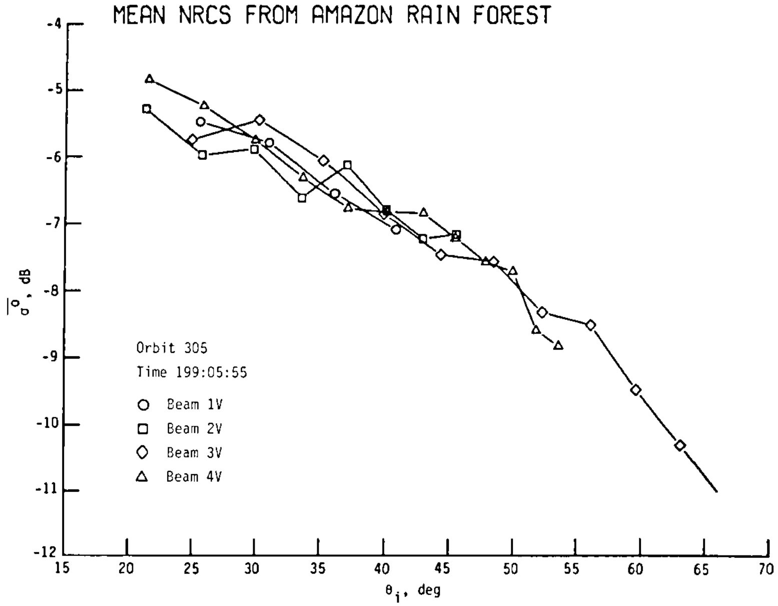
MEAN NRCS FROM AMAZON RAIN FOREST

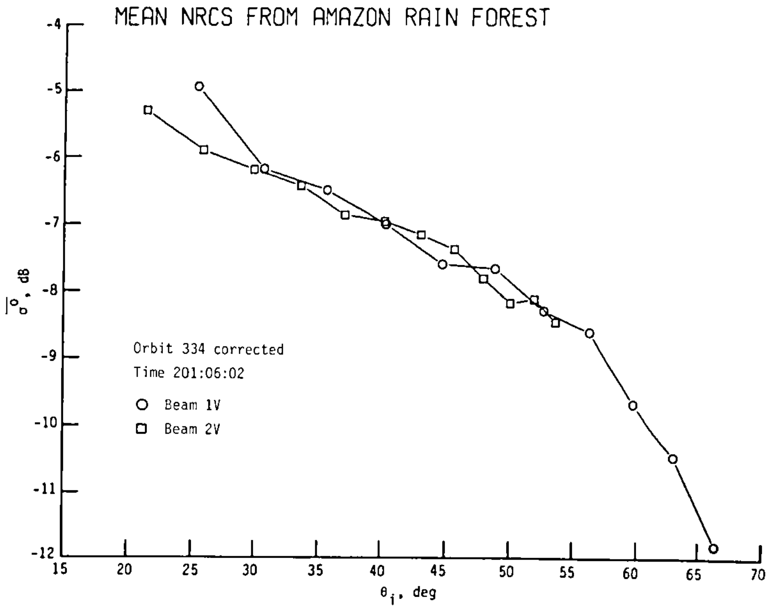
MEAN NRCS FROM AMAZON RAIN FOREST

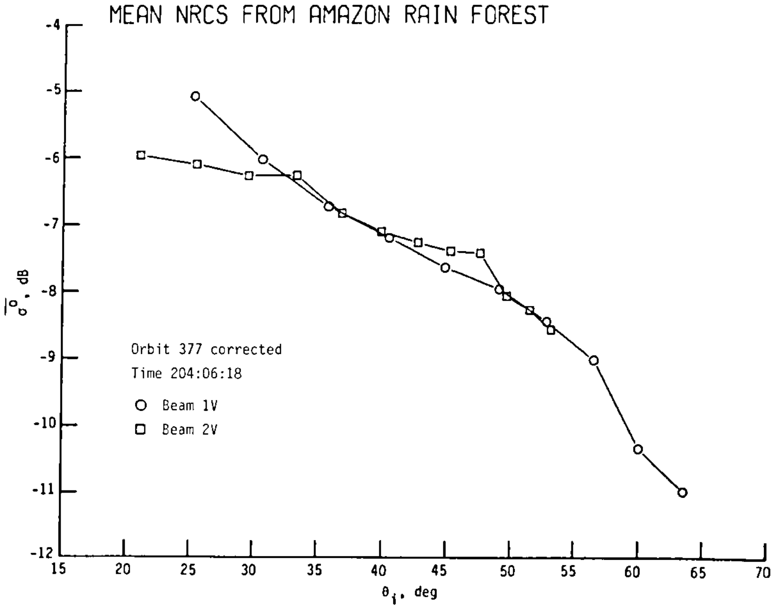
MEAN NRCS FROM AMAZON RAIN FOREST

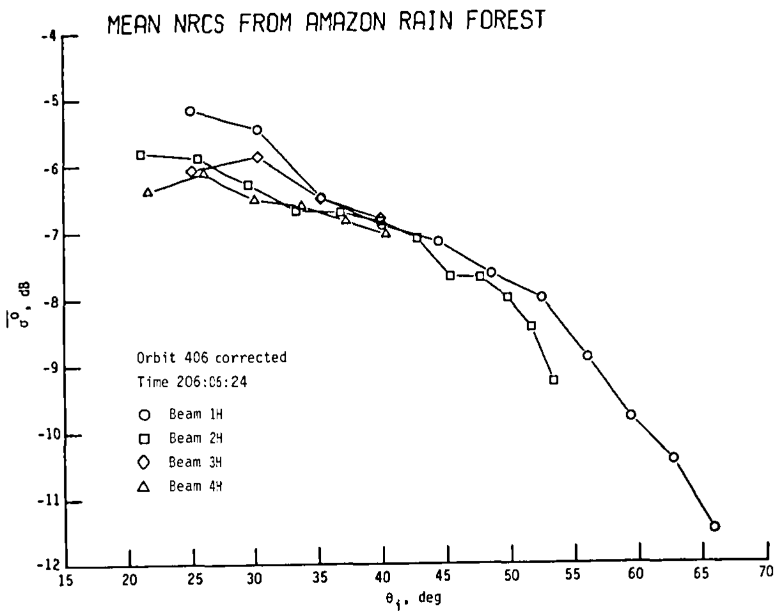
MEAN NRCS FROM AMAZON RAIN FOREST
Orbit 406 corrected
Time 206:06:24
○ Beam 1H
□ Beam 2H
◇ Beam 3H
△ Beam 4H
$\overline{\sigma^o}$, dB
-4
-5
-6
-7
-8
-9
-10
-11
-12
15
20
25
30
35
40
45
50
55
60
65
70
θ_i, deg

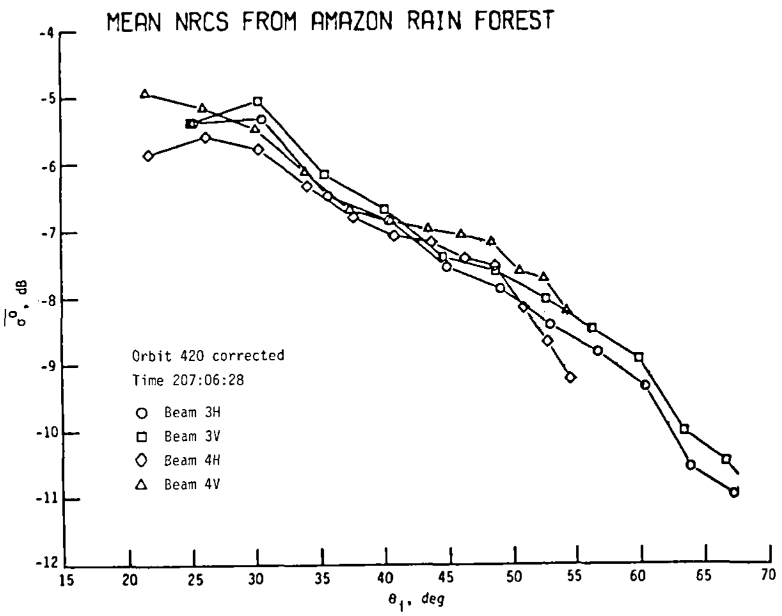
MEAN NRCS FROM AMAZON RAIN FOREST
Orbit 420 corrected
Time 207:06:28
○ Beam 3H
□ Beam 3V
◇ Beam 4H
△ Beam 4V
$\overline{\sigma^o}$, dB
-4
-5
-6
-7
-8
-9
-10
-11
-12
15
20
25
30
35
40
45
50
55
60
65
70
θ_i, deg

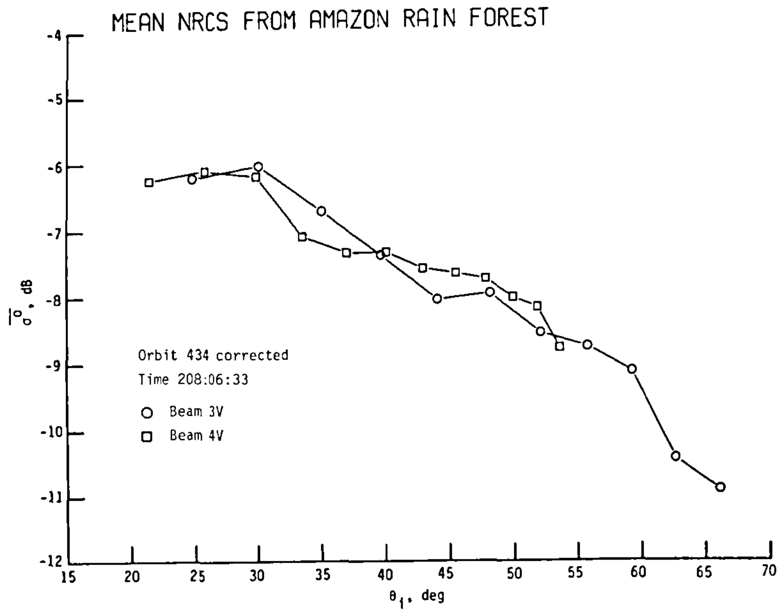
MEAN NRCS FROM AMAZON RAIN FOREST
Orbit 434 corrected
Time 208:06:33
○ Beam 3V
□ Beam 4V
$\overline{\sigma^o}$, dB
-4
-5
-6
-7
-8
-9
-10
-11
-12
15
20
25
30
35
40
45
50
55
60
65
70
θ_i, deg

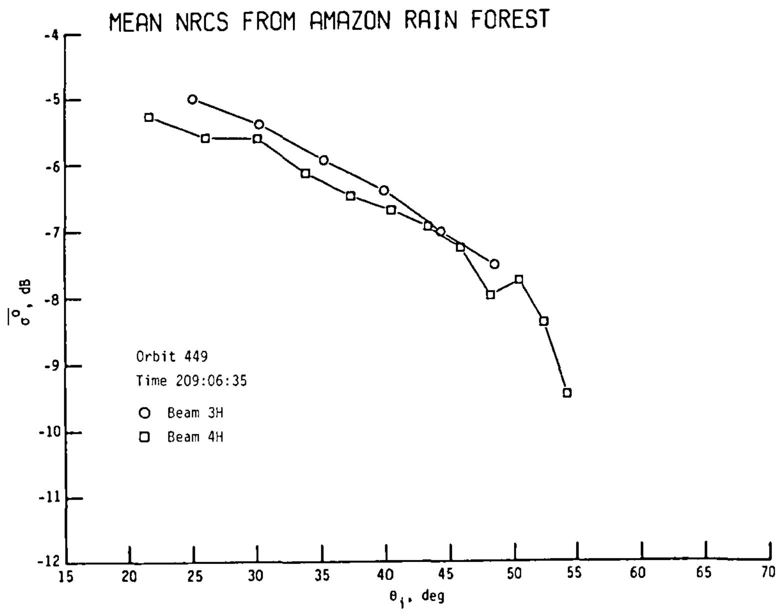
MEAN NRCS FROM AMAZON RAIN FOREST
Orbit 449
Time 209:06:35
○ Beam 3H
□ Beam 4H
$\overline{\sigma^o}$, dB
-4
-5
-6
-7
-8
-9
-10
-11
-12
15
20
25
30
35
40
45
50
55
60
65
70
θ_i, deg

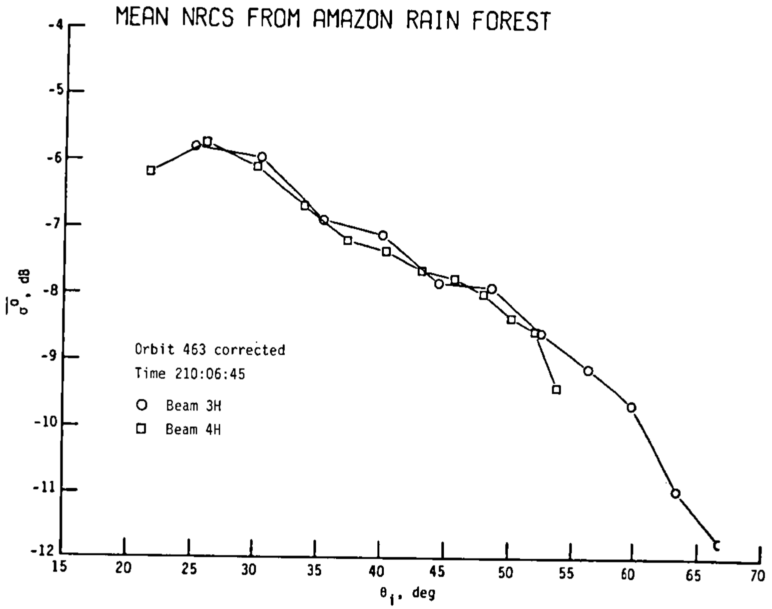
MEAN NRCS FROM AMAZON RAIN FOREST
$\overline{\sigma}_o$, dB
-4
-5
-6
-7
-8
-9
-10
-11
-12
15
20
25
30
35
40
45
50
55
60
65
70
θ_i, deg
Orbit 463 corrected
Time 210:06:45
○ Beam 3H
□ Beam 4H

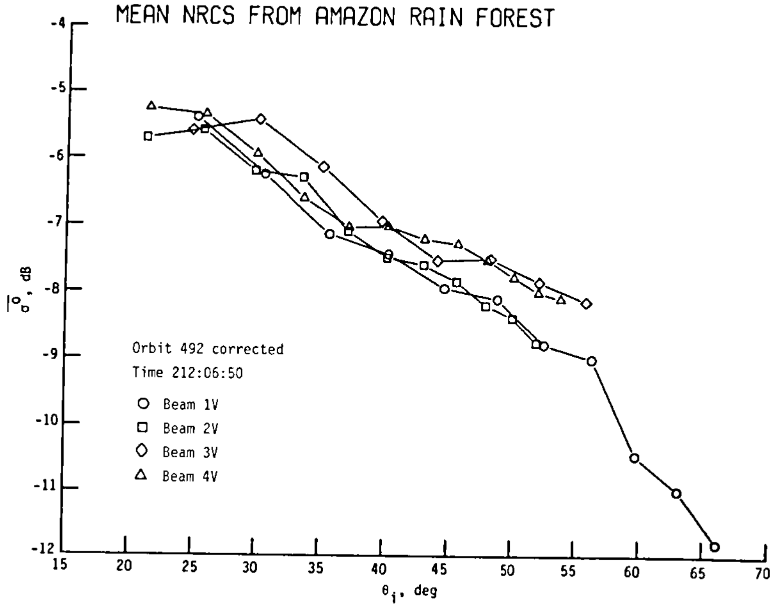
MEAN NRCS FROM AMAZON RAIN FOREST
$\overline{\sigma}_o$, dB
-4
-5
-6
-7
-8
-9
-10
-11
-12
15
20
25
30
35
40
45
50
55
60
65
70
θ_i, deg
Orbit 492 corrected
Time 212:06:50
○ Beam 1V
□ Beam 2V
◇ Beam 3V
△ Beam 4V

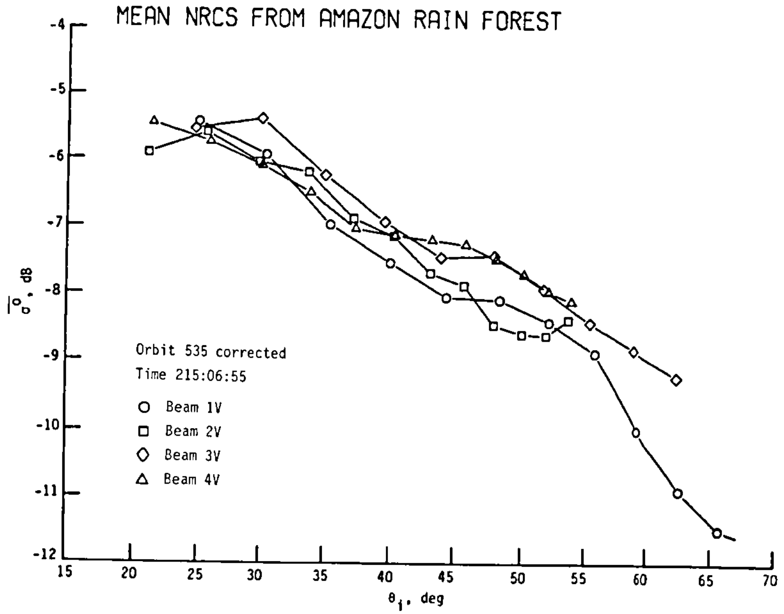
MEAN NRCS FROM AMAZON RAIN FOREST
$\overline{\sigma}_o$, dB
-4
-5
-6
-7
-8
-9
-10
-11
-12
15
20
25
30
35
40
45
50
55
60
65
70
θ_i, deg
Orbit 535 corrected
Time 215:06:55
○ Beam 1V
□ Beam 2V
◇ Beam 3V
△ Beam 4V

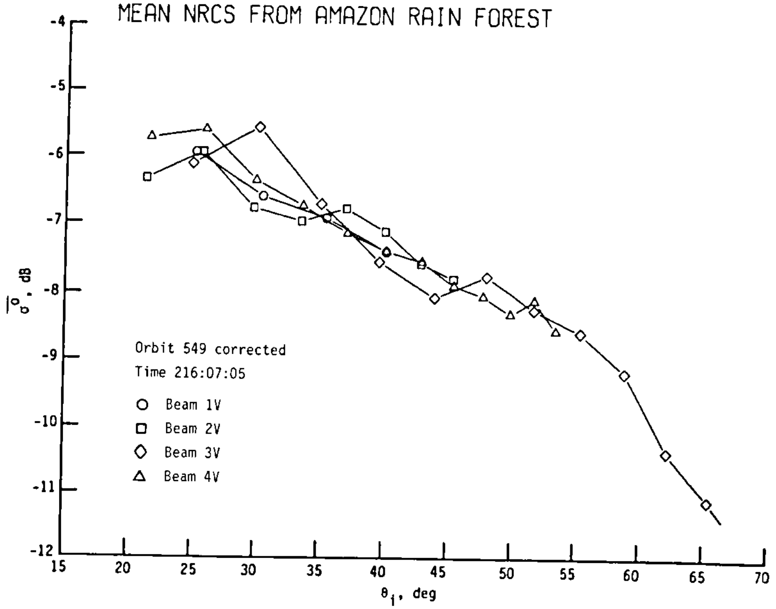
MEAN NRCS FROM AMAZON RAIN FOREST
$\overline{\sigma}_o$, dB
-4
-5
-6
-7
-8
-9
-10
-11
-12
15
20
25
30
35
40
45
50
55
60
65
70
θ_i, deg
Orbit 549 corrected
Time 216:07:05
○ Beam 1V
□ Beam 2V
◇ Beam 3V
△ Beam 4V

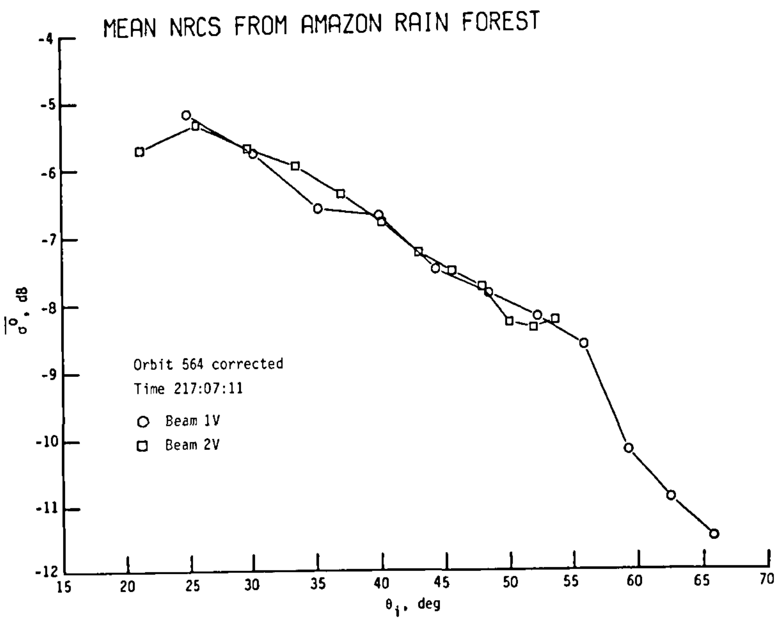

MEAN NRCS FROM AMAZON RAIN FOREST

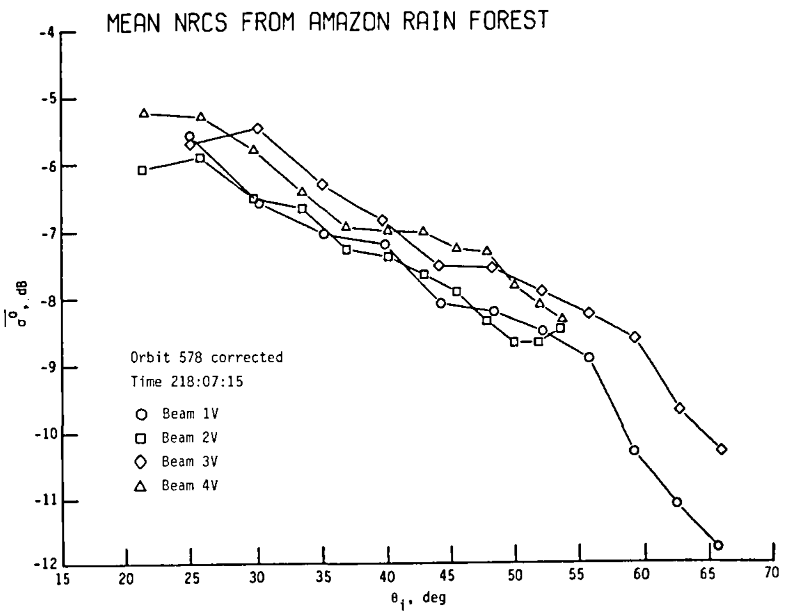

MEAN NRCS FROM AMAZON RAIN FOREST

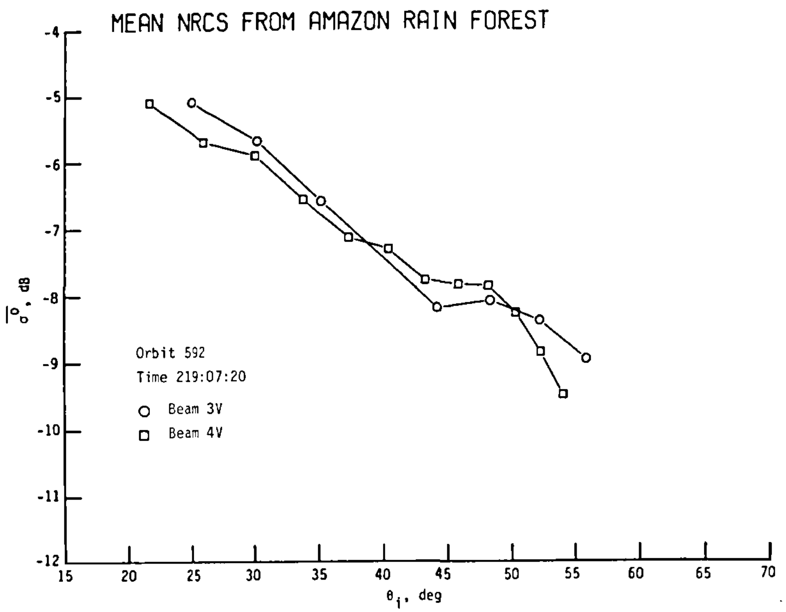

MEAN NRCS FROM AMAZON RAIN FOREST

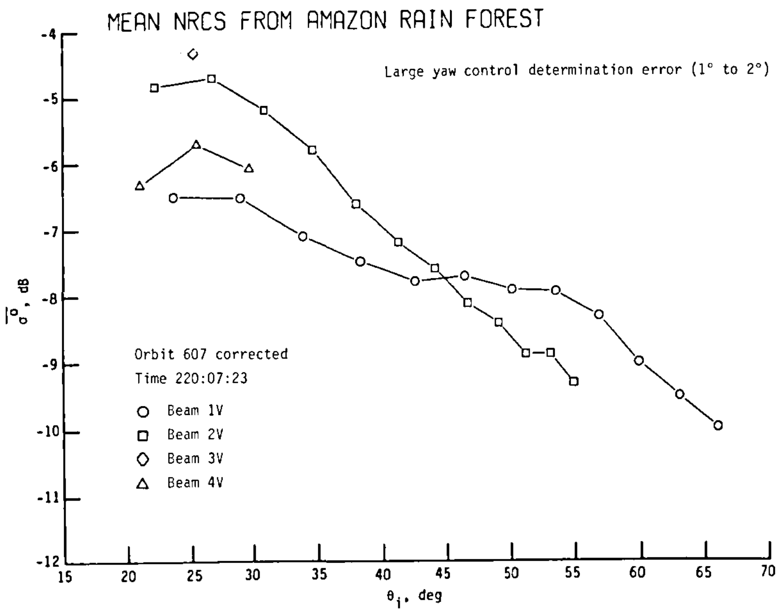

MEAN NRCS FROM AMAZON RAIN FOREST

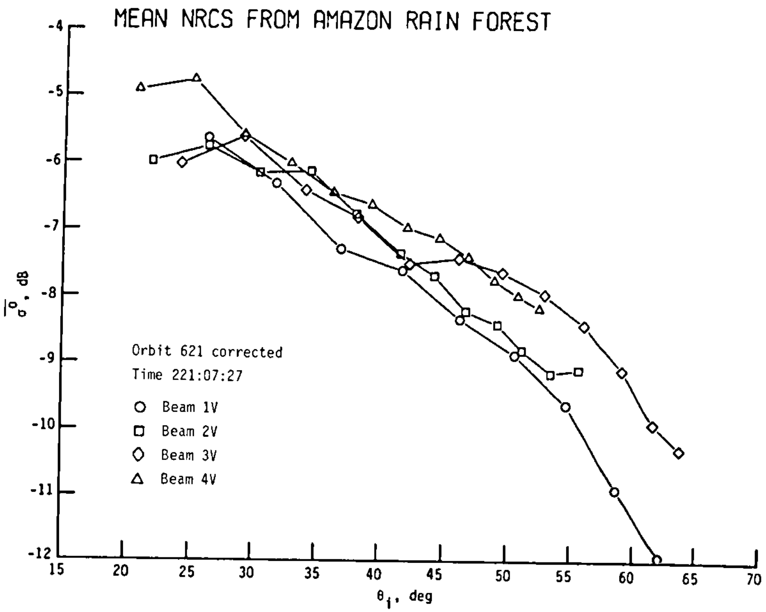
MEAN NRCS FROM AMAZON RAIN FOREST
$\overline{\sigma_o}$, dB
-4
-5
-6
-7
-8
-9
-10
-11
-12
15
20
25
30
35
40
45
50
55
60
65
70
θ_i, deg
Orbit 621 corrected
Time 221:07:27
○ Beam 1V
□ Beam 2V
◇ Beam 3V
△ Beam 4V

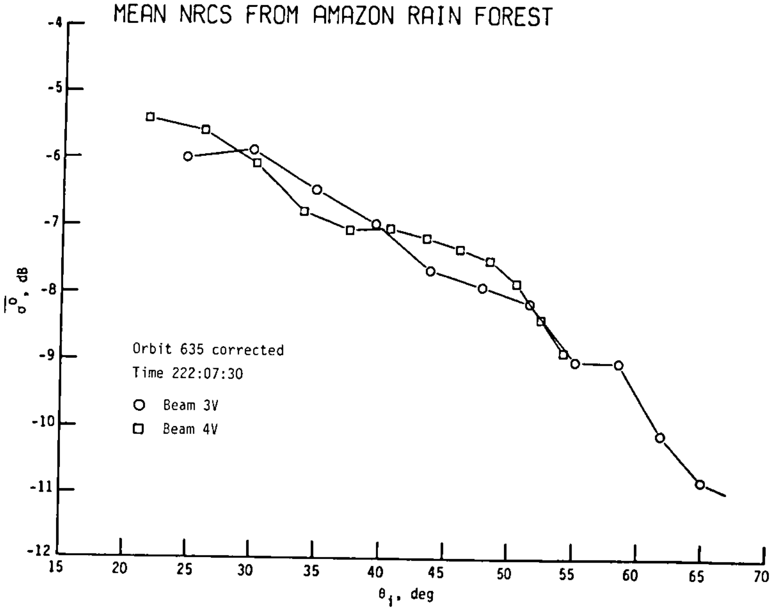
MEAN NRCS FROM AMAZON RAIN FOREST
$\overline{\sigma_o}$, dB
-4
-5
-6
-7
-8
-9
-10
-11
-12
15
20
25
30
35
40
45
50
55
60
65
70
θ_i, deg
Orbit 635 corrected
Time 222:07:30
○ Beam 3V
□ Beam 4V

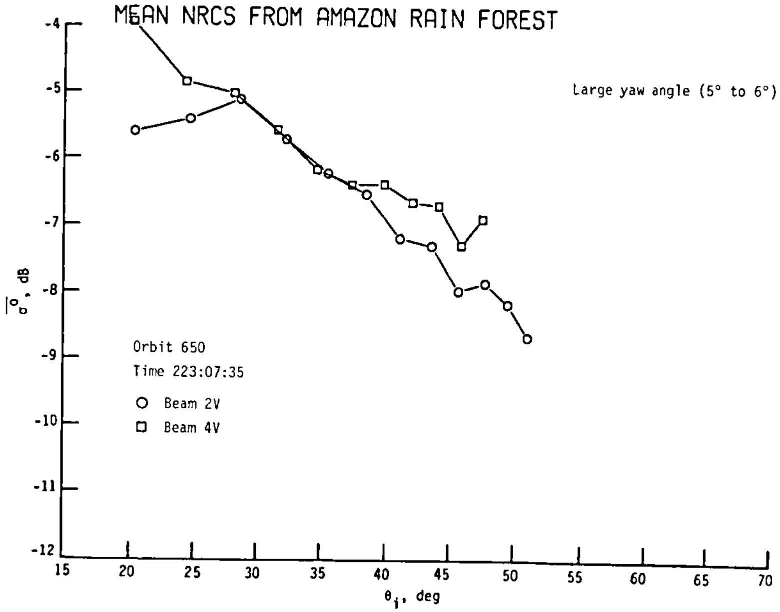
MEAN NRCS FROM AMAZON RAIN FOREST
Large yaw angle (5° to 6°)
$\overline{\sigma_o}$, dB
-4
-5
-6
-7
-8
-9
-10
-11
-12
15
20
25
30
35
40
45
50
55
60
65
70
θ_i, deg
Orbit 650
Time 223:07:35
○ Beam 2V
□ Beam 4V

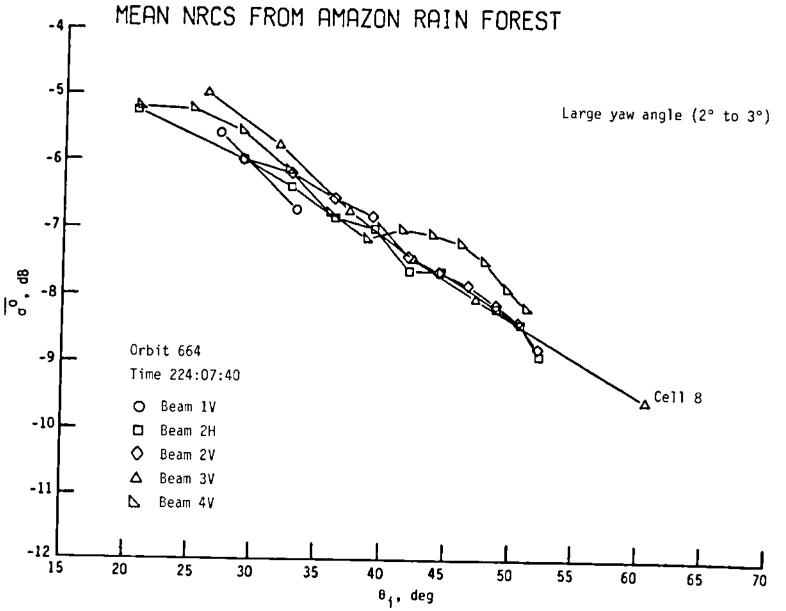
MEAN NRCS FROM AMAZON RAIN FOREST
Large yaw angle (2° to 3°)
$\overline{\sigma_o}$, dB
-4
-5
-6
-7
-8
-9
-10
-11
-12
15
20
25
30
35
40
45
50
55
60
65
70
θ_i, deg
Cell 8
Orbit 664
Time 224:07:40
○ Beam 1V
□ Beam 2H
◇ Beam 2V
△ Beam 3V
◺ Beam 4V

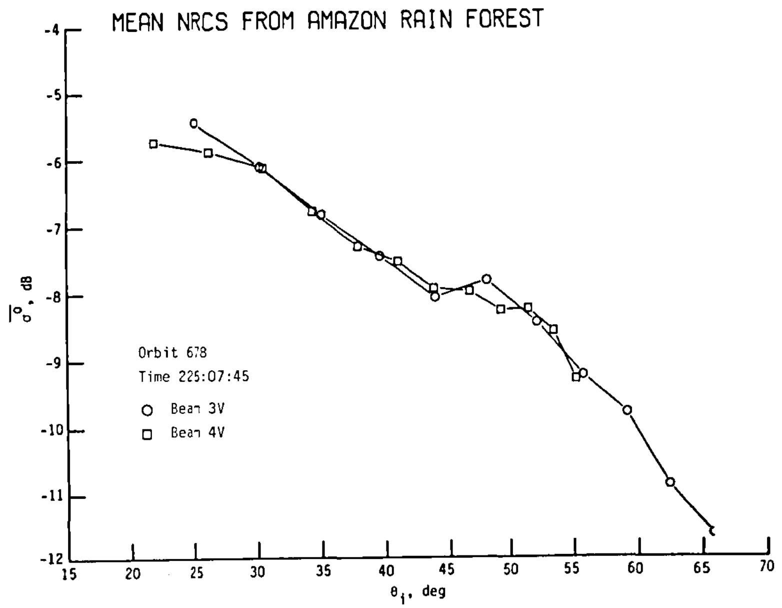
MEAN NRCS FROM AMAZON RAIN FOREST

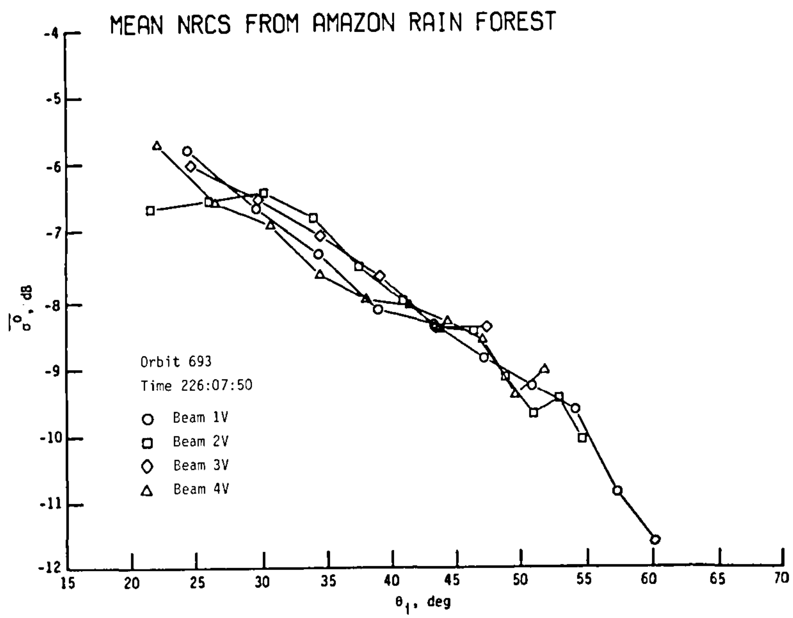
MEAN NRCS FROM AMAZON RAIN FOREST

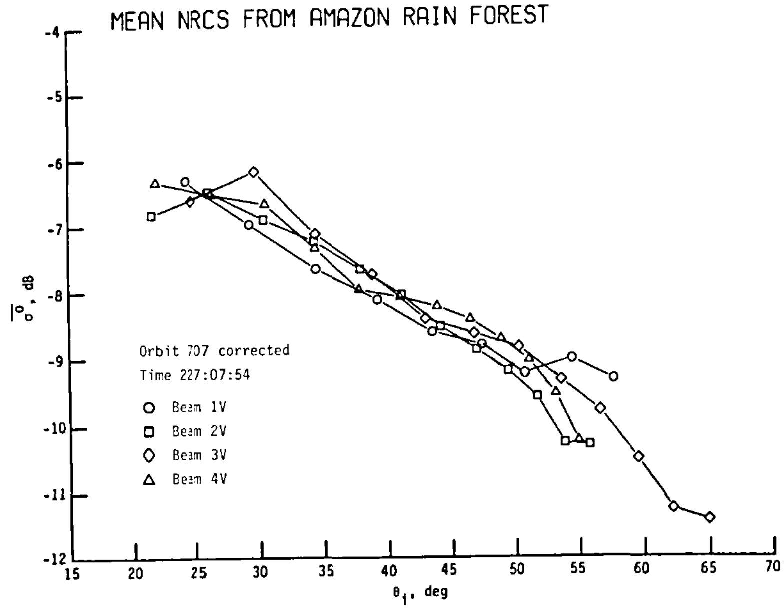
MEAN NRCS FROM AMAZON RAIN FOREST

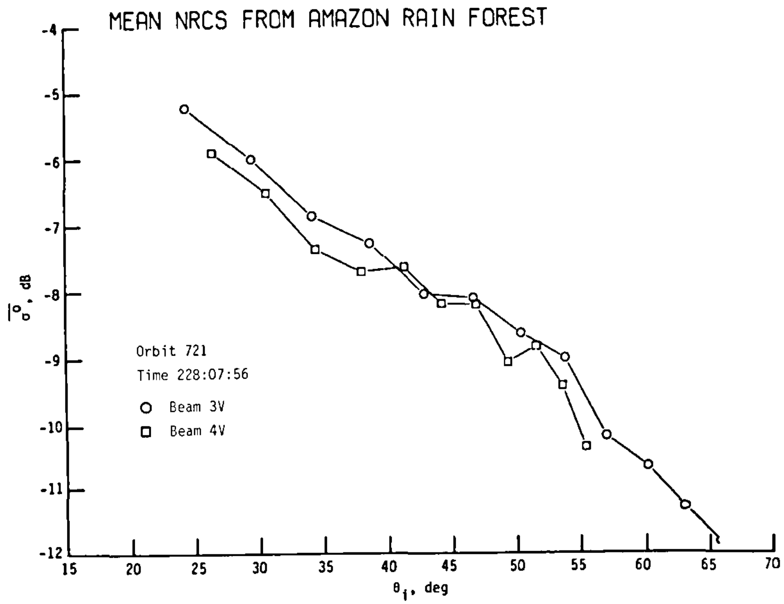
MEAN NRCS FROM AMAZON RAIN FOREST

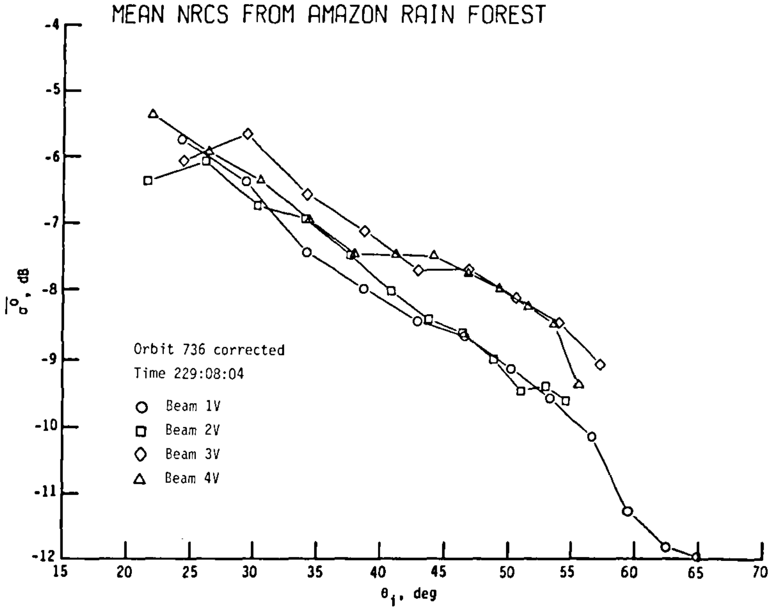
MEAN NRCS FROM AMAZON RAIN FOREST
$\overline{\sigma}_o$, dB
-4
-5
-6
-7
-8
-9
-10
-11
-12
15
20
25
30
35
40
45
50
55
60
65
70
θ_i, deg
Orbit 736 corrected
Time 229:08:04
○ Beam 1V
□ Beam 2V
◇ Beam 3V
△ Beam 4V

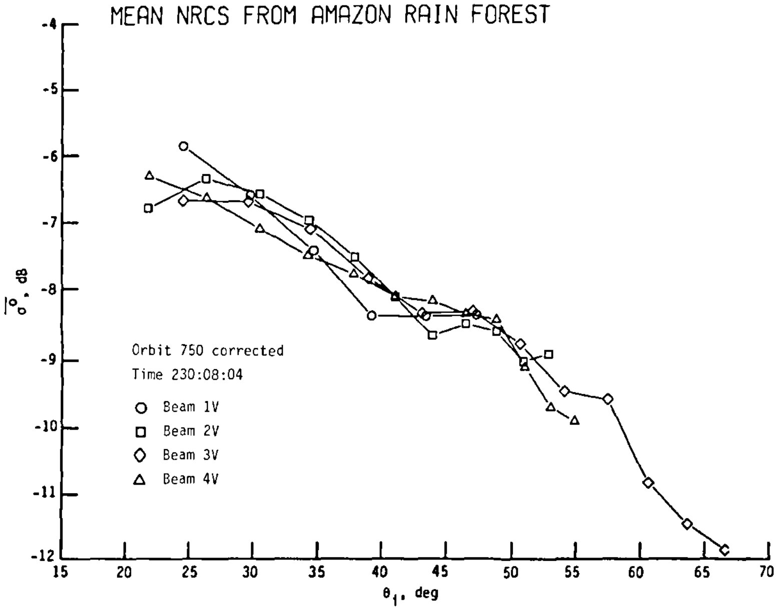
MEAN NRCS FROM AMAZON RAIN FOREST
$\overline{\sigma}_o$, dB
-4
-5
-6
-7
-8
-9
-10
-11
-12
15
20
25
30
35
40
45
50
55
60
65
70
θ_i, deg
Orbit 750 corrected
Time 230:08:04
○ Beam 1V
□ Beam 2V
◇ Beam 3V
△ Beam 4V

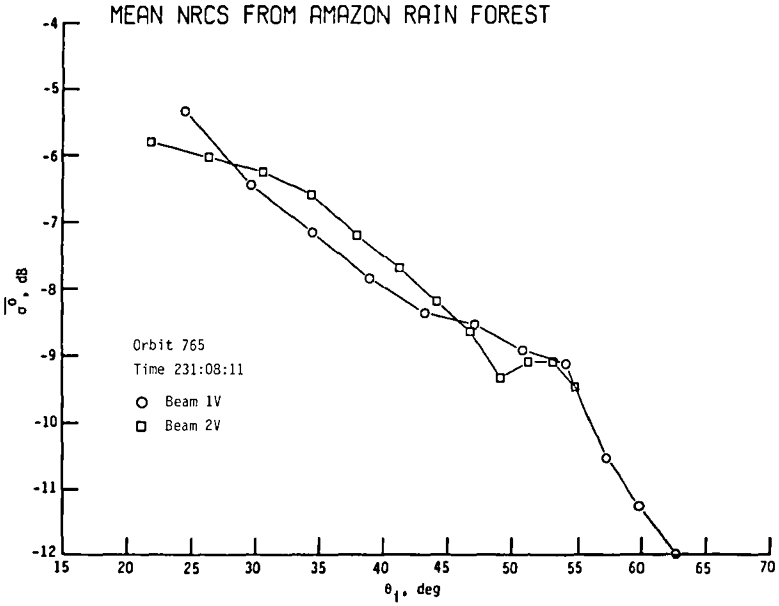
MEAN NRCS FROM AMAZON RAIN FOREST
$\overline{\sigma}_o$, dB
-4
-5
-6
-7
-8
-9
-10
-11
-12
15
20
25
30
35
40
45
50
55
60
65
70
θ_i, deg
Orbit 765
Time 231:08:11
○ Beam 1V
□ Beam 2V

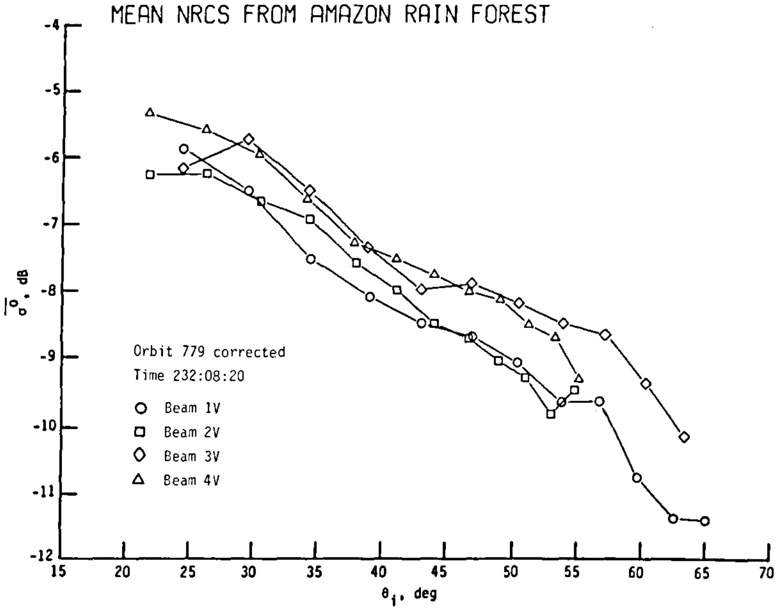
MEAN NRCS FROM AMAZON RAIN FOREST
$\overline{\sigma}_o$, dB
-4
-5
-6
-7
-8
-9
-10
-11
-12
15
20
25
30
35
40
45
50
55
60
65
70
θ_i, deg
Orbit 779 corrected
Time 232:08:20
○ Beam 1V
□ Beam 2V
◇ Beam 3V
△ Beam 4V

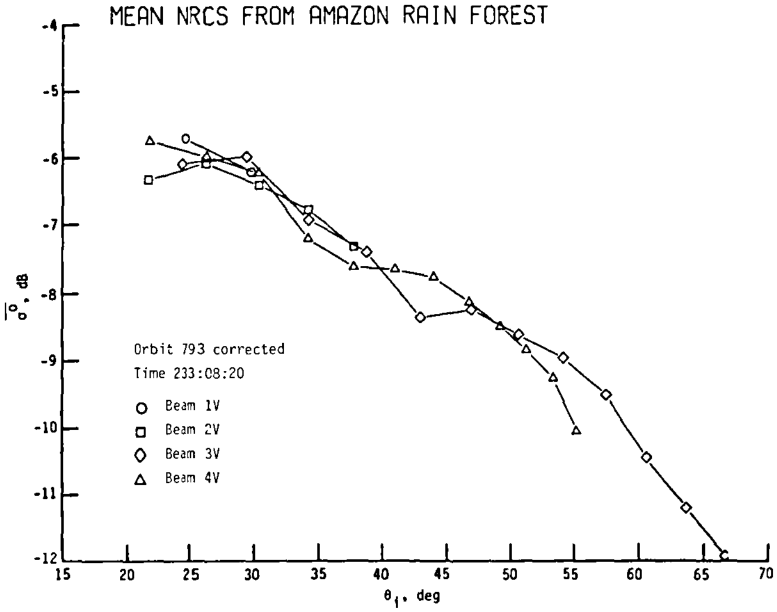
MEAN NRCS FROM AMAZON RAIN FOREST

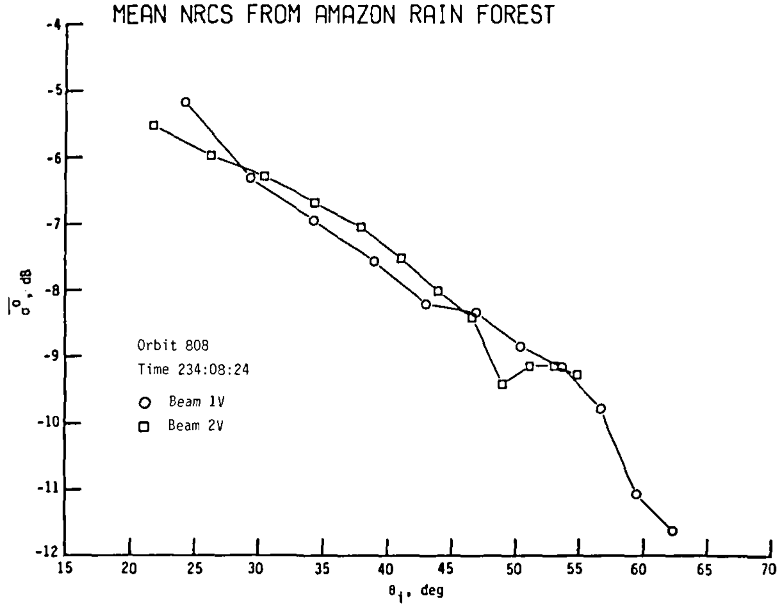
MEAN NRCS FROM AMAZON RAIN FOREST

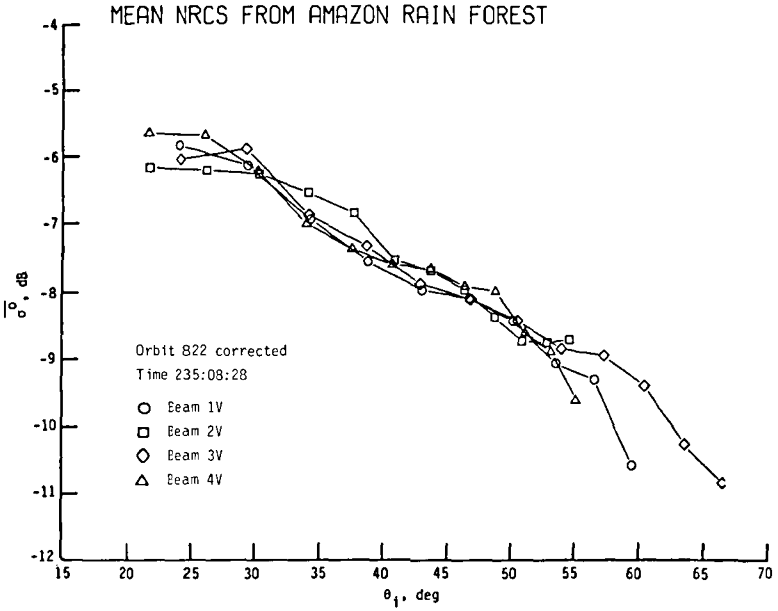
MEAN NRCS FROM AMAZON RAIN FOREST

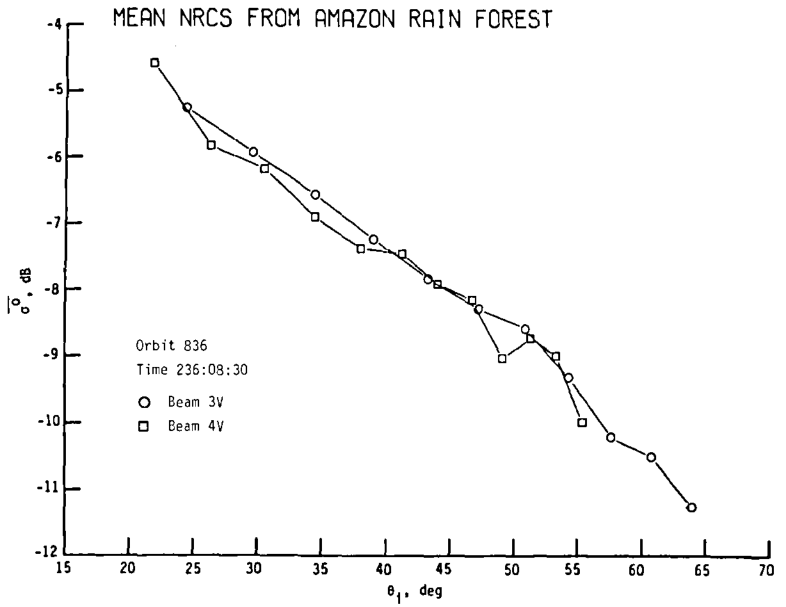
MEAN NRCS FROM AMAZON RAIN FOREST

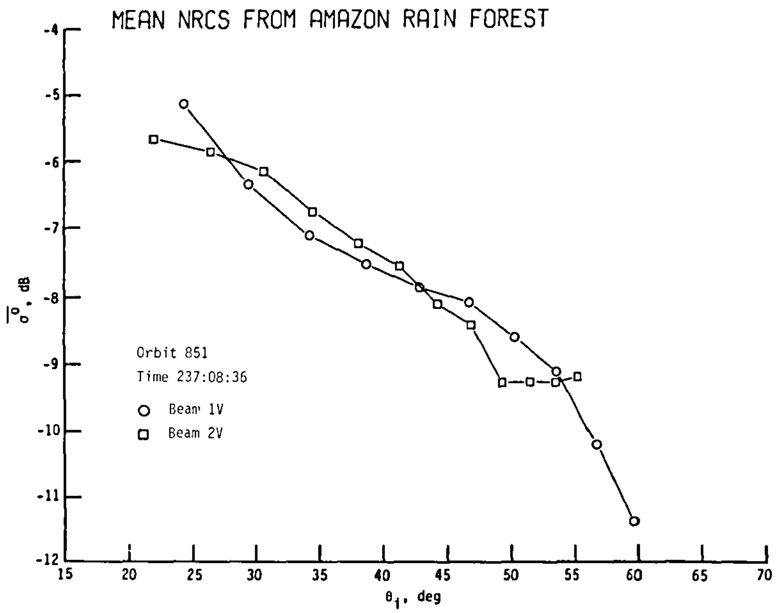
MEAN NRCS FROM AMAZON RAIN FOREST
$\overline{\sigma_o}$, dB
-4
-5
-6
-7
-8
-9
-10
-11
-12
15
20
25
30
35
40
45
50
55
60
65
70
θ_i, deg
Orbit 851
Time 237:08:36
○ Beam 1V
□ Beam 2V

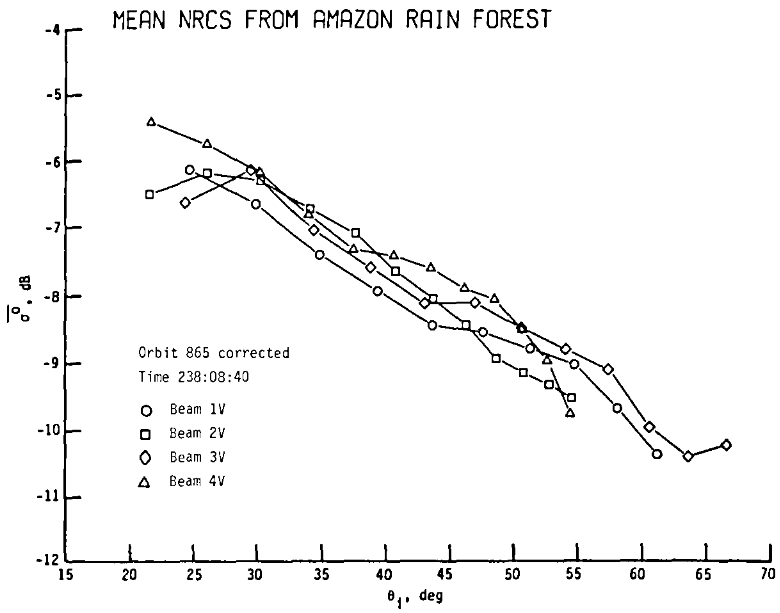
MEAN NRCS FROM AMAZON RAIN FOREST
$\overline{\sigma_o}$, dB
-4
-5
-6
-7
-8
-9
-10
-11
-12
15
20
25
30
35
40
45
50
55
60
65
70
θ_i, deg
Orbit 865 corrected
Time 238:08:40
○ Beam 1V
□ Beam 2V
◇ Beam 3V
△ Beam 4V

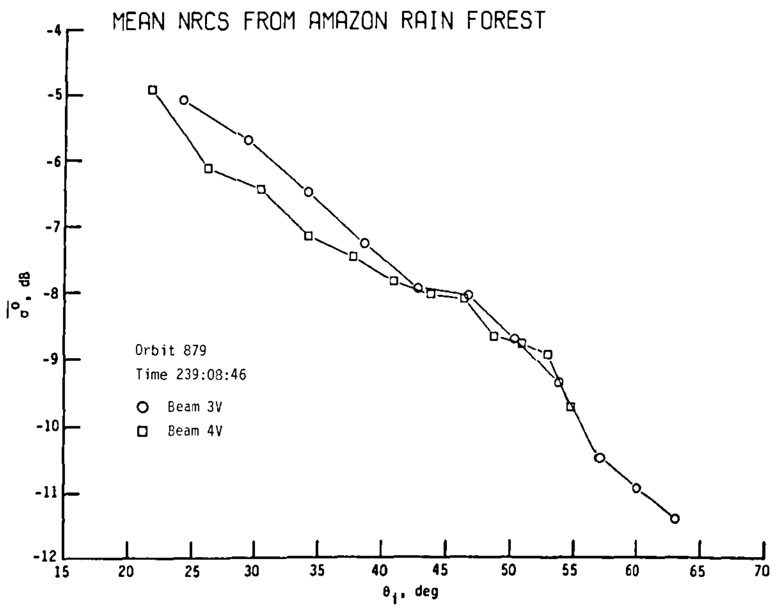
MEAN NRCS FROM AMAZON RAIN FOREST
$\overline{\sigma_o}$, dB
-4
-5
-6
-7
-8
-9
-10
-11
-12
15
20
25
30
35
40
45
50
55
60
65
70
θ_i, deg
Orbit 879
Time 239:08:46
○ Beam 3V
□ Beam 4V

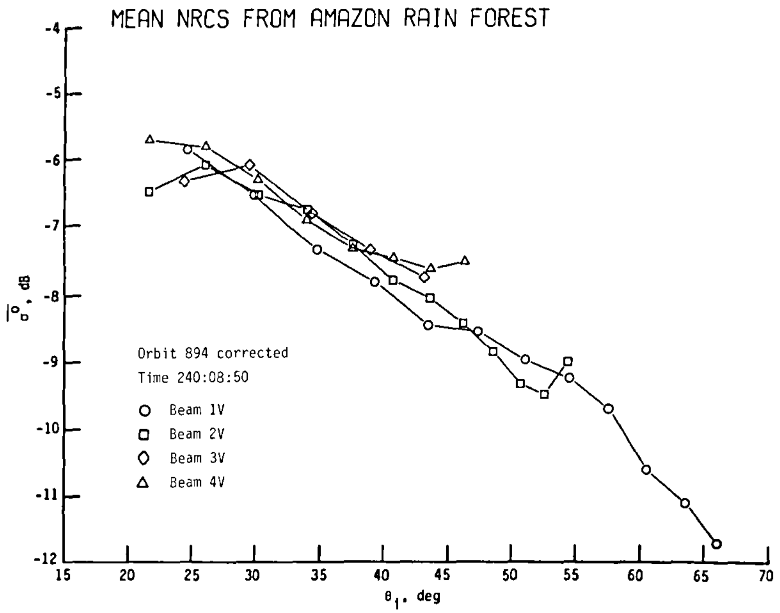
MEAN NRCS FROM AMAZON RAIN FOREST
$\overline{\sigma_o}$, dB
-4
-5
-6
-7
-8
-9
-10
-11
-12
15
20
25
30
35
40
45
50
55
60
65
70
θ_i, deg
Orbit 894 corrected
Time 240:08:50
○ Beam 1V
□ Beam 2V
◇ Beam 3V
△ Beam 4V

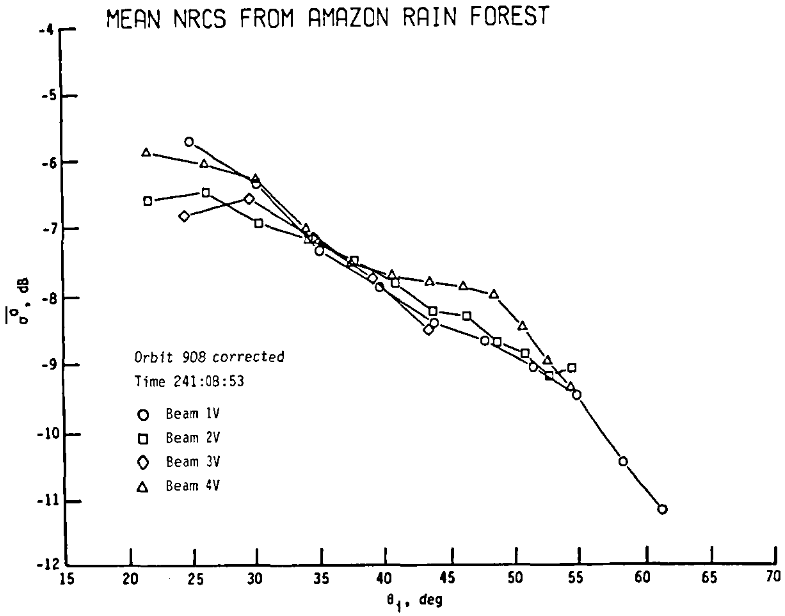
MEAN NRCS FROM AMAZON RAIN FOREST

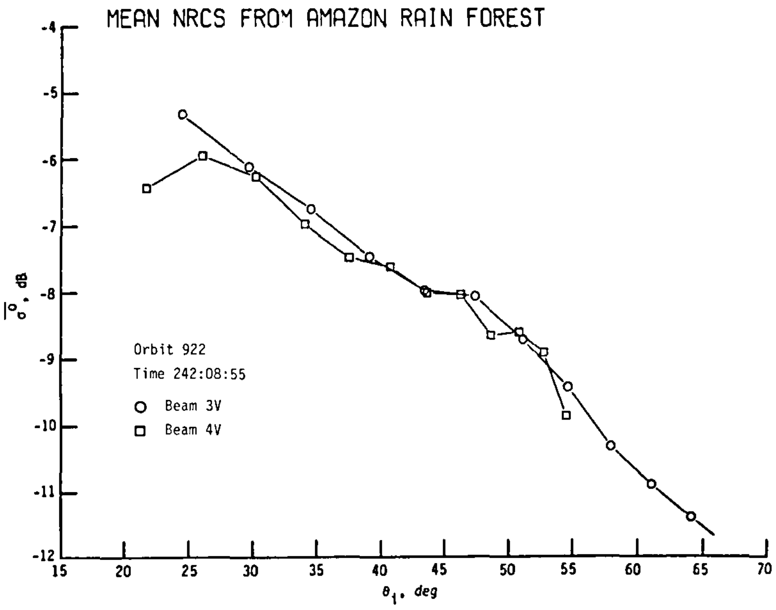
MEAN NRCS FROM AMAZON RAIN FOREST

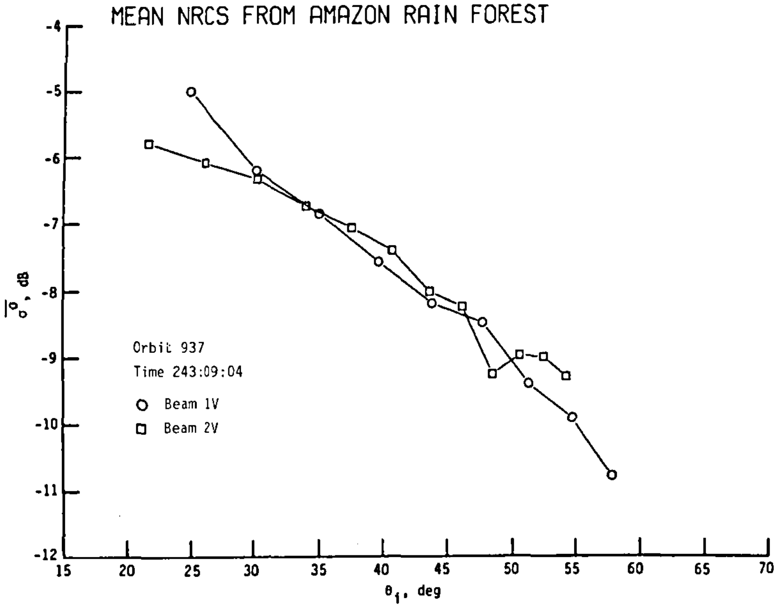
MEAN NRCS FROM AMAZON RAIN FOREST

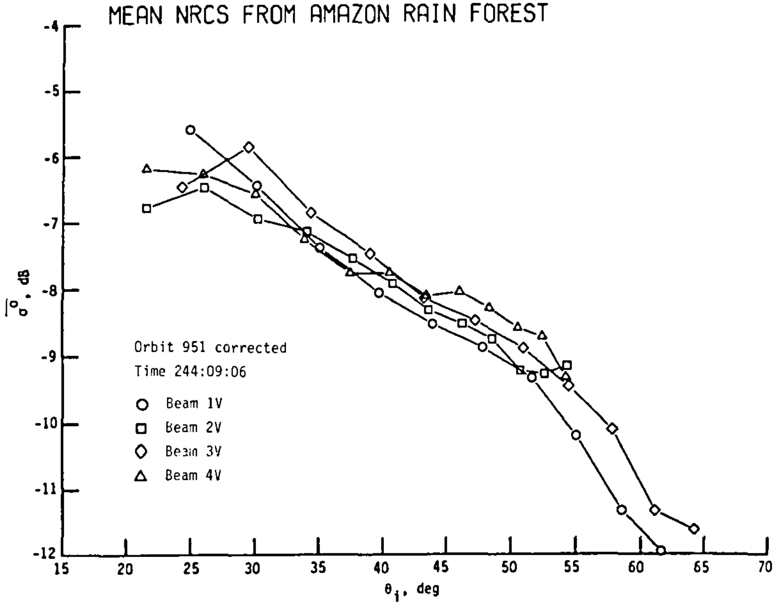
MEAN NRCS FROM AMAZON RAIN FOREST

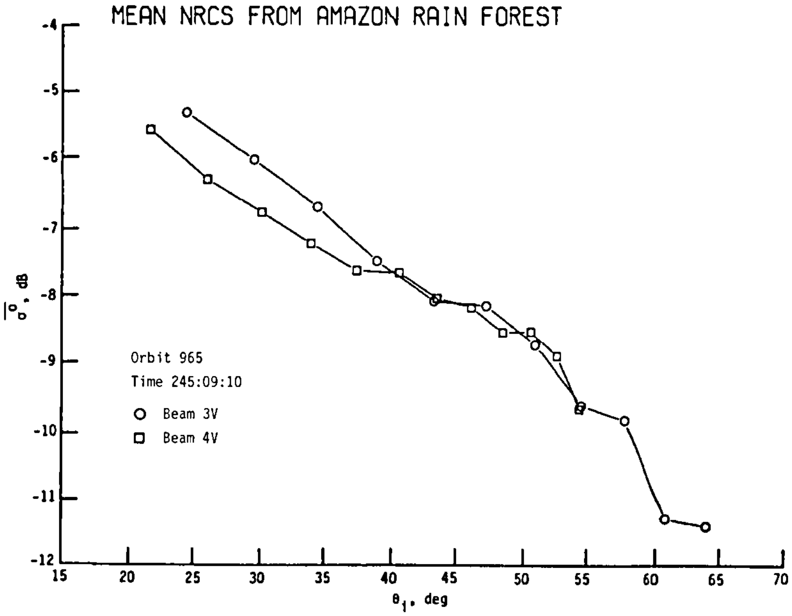

MEAN NRCS FROM AMAZON RAIN FOREST

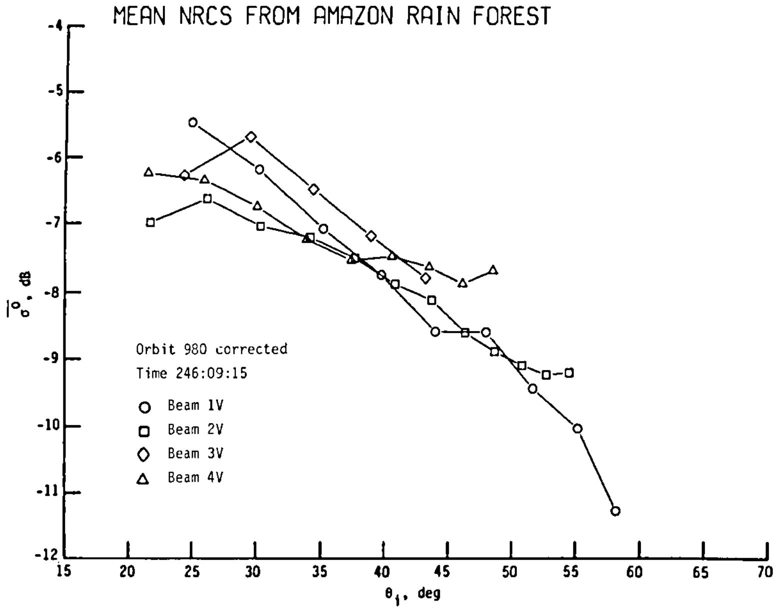

MEAN NRCS FROM AMAZON RAIN FOREST

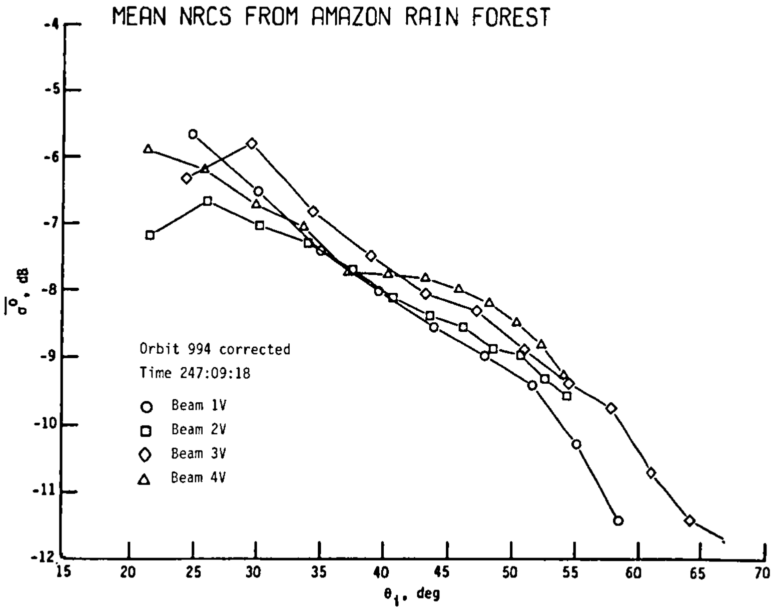

MEAN NRCS FROM AMAZON RAIN FOREST

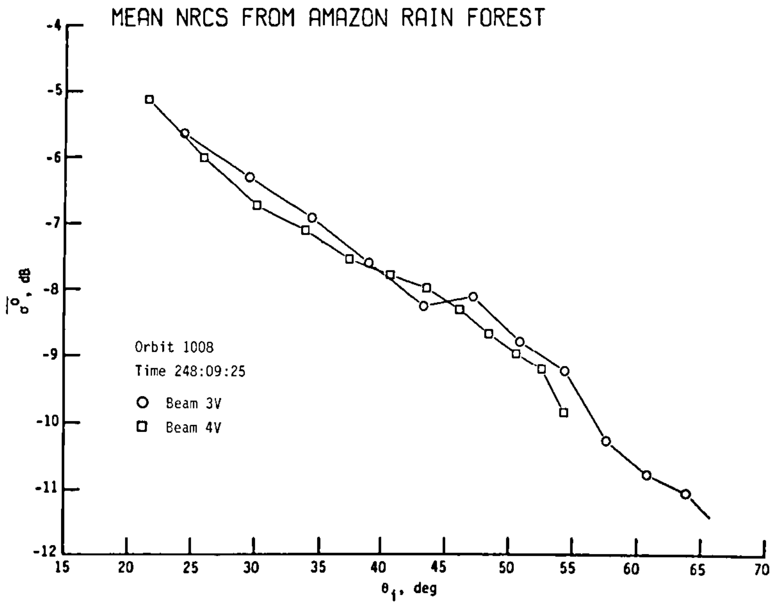

MEAN NRCS FROM AMAZON RAIN FOREST

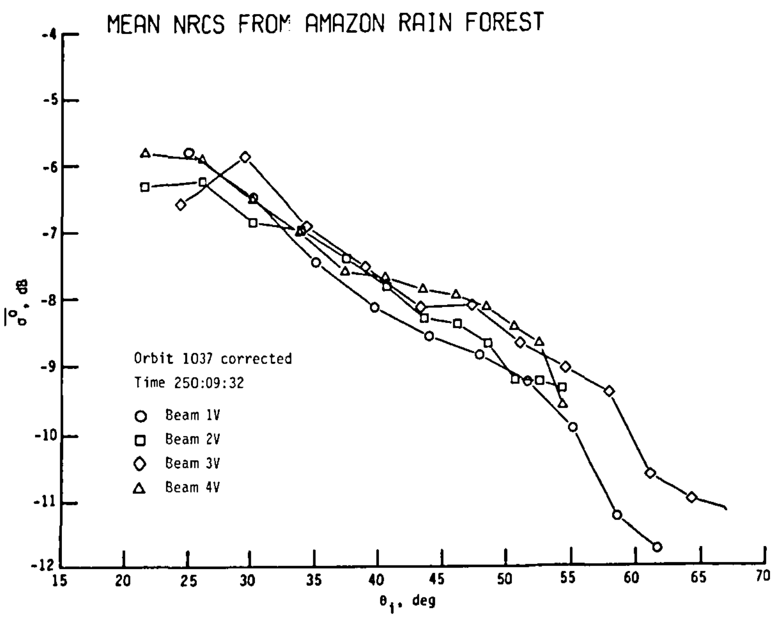

MEAN NRCS FROM AMAZON RAIN FOREST

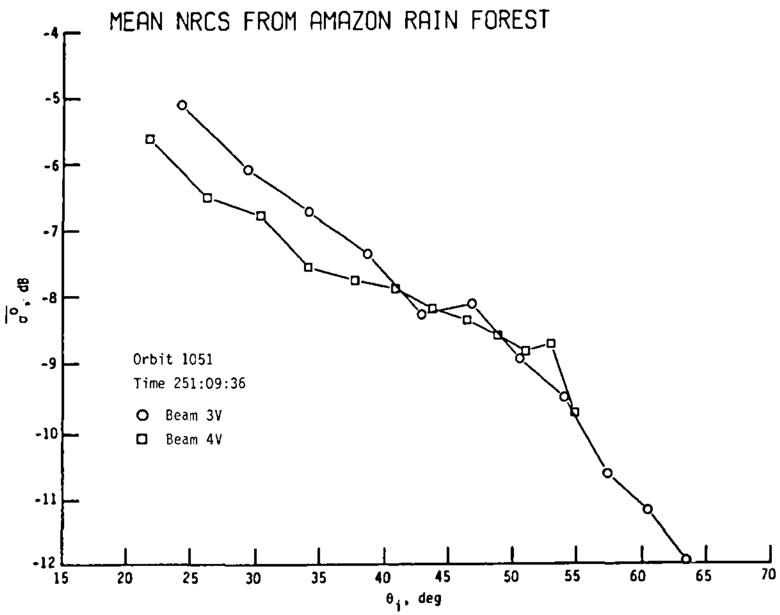

MEAN NRCS FROM AMAZON RAIN FOREST

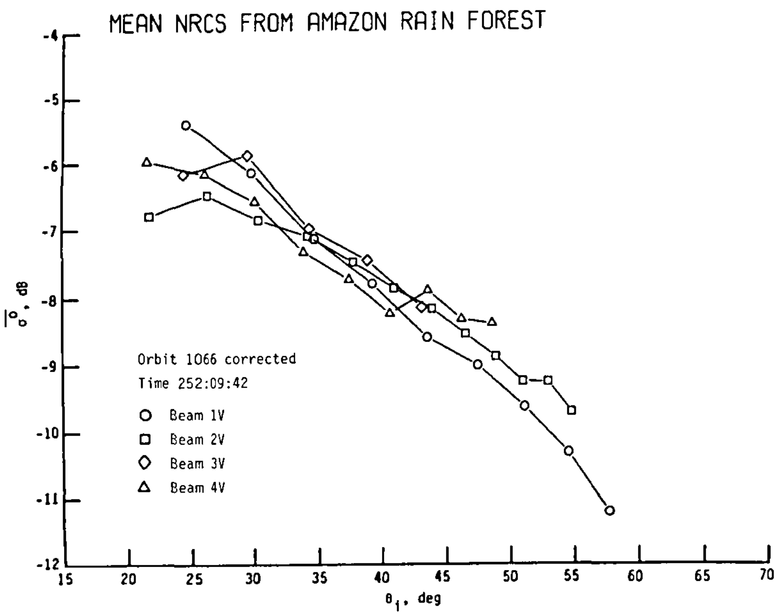

MEAN NRCS FROM AMAZON RAIN FOREST

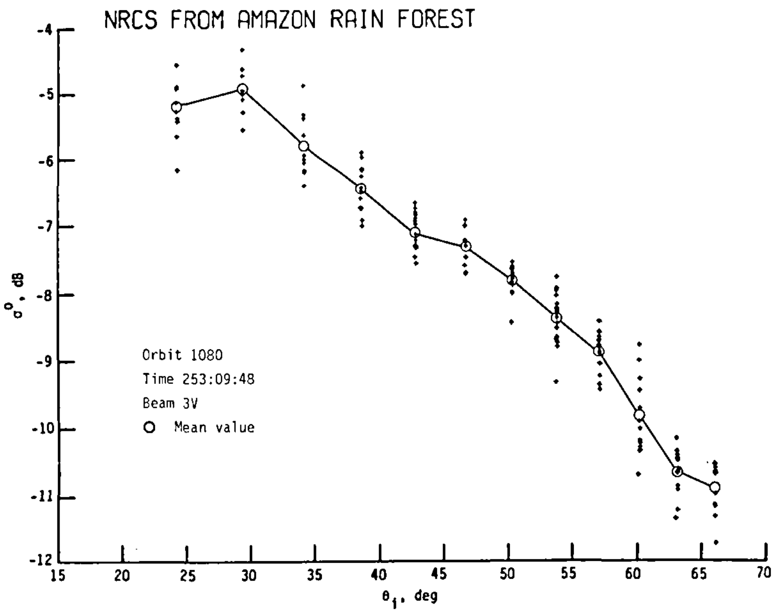

NRCS FROM AMAZON RAIN FOREST

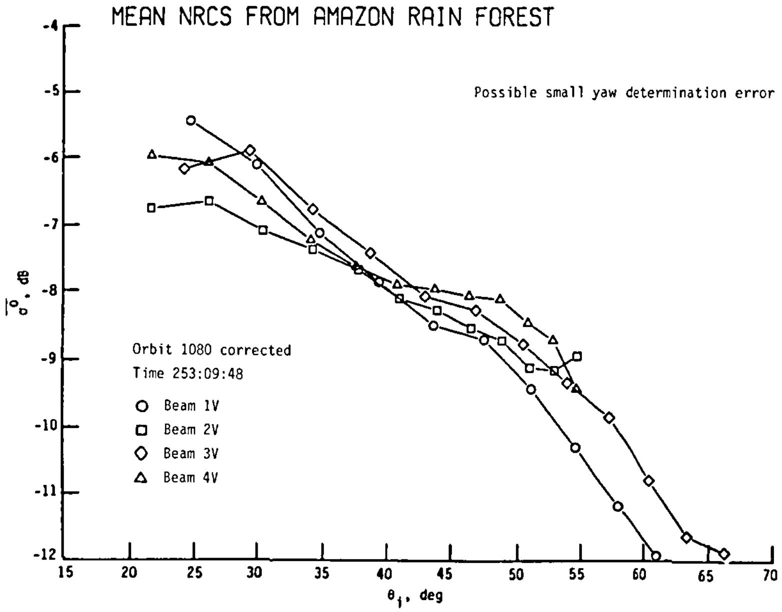
MEAN NRCS FROM AMAZON RAIN FOREST

Possible small yaw determination error

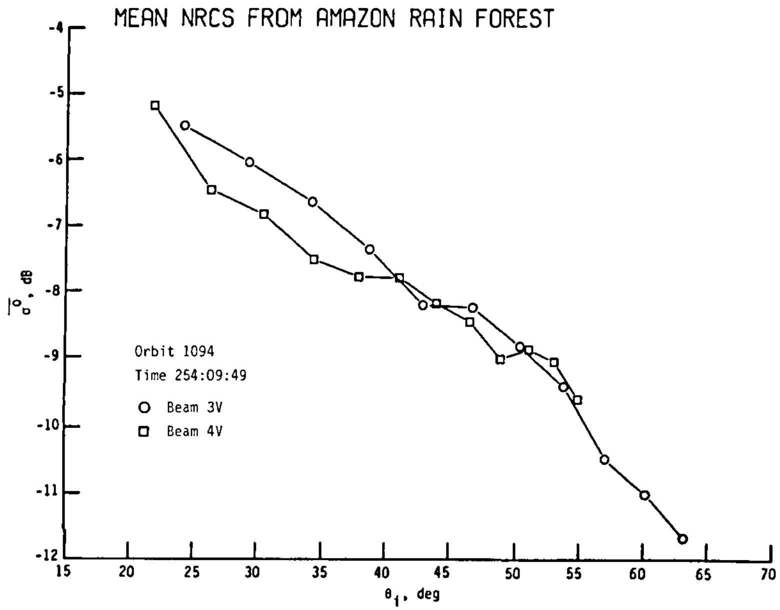
MEAN NRCS FROM AMAZON RAIN FOREST

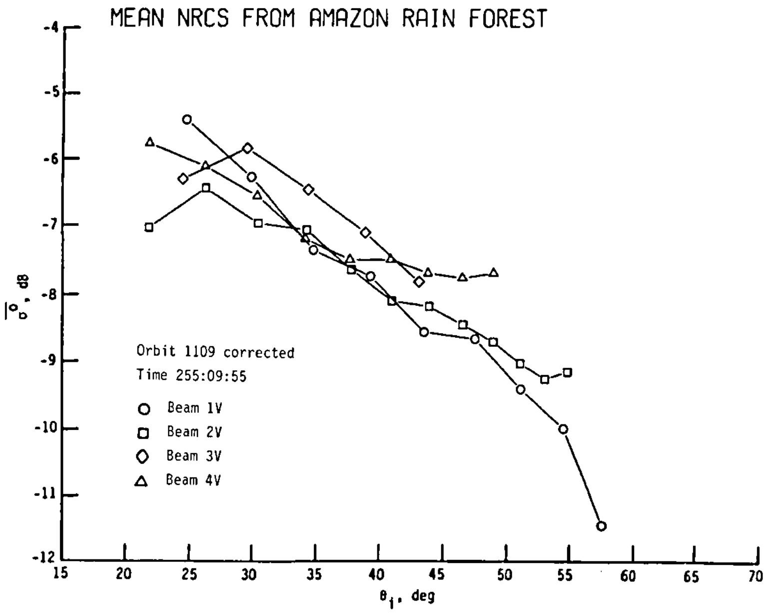
MEAN NRCS FROM AMAZON RAIN FOREST

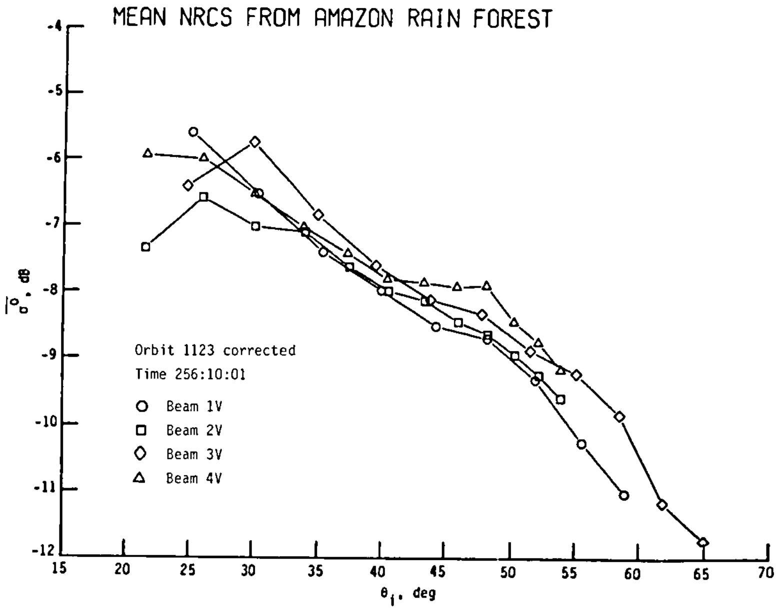
MEAN NRCS FROM AMAZON RAIN FOREST

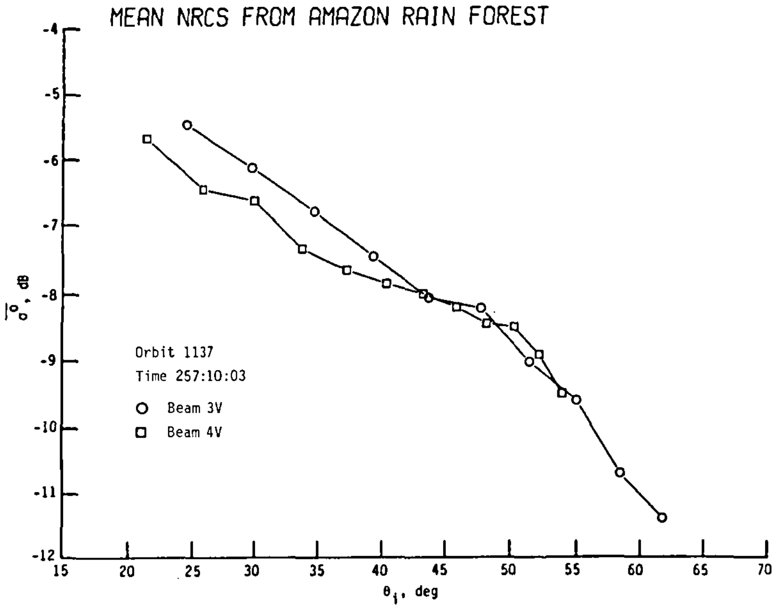
MEAN NRCS FROM AMAZON RAIN FOREST

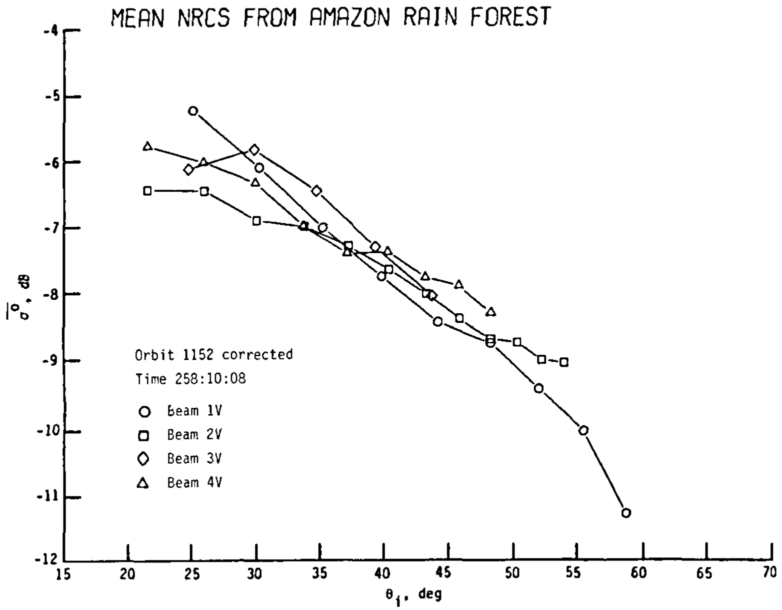
MEAN NRCS FROM AMAZON RAIN FOREST

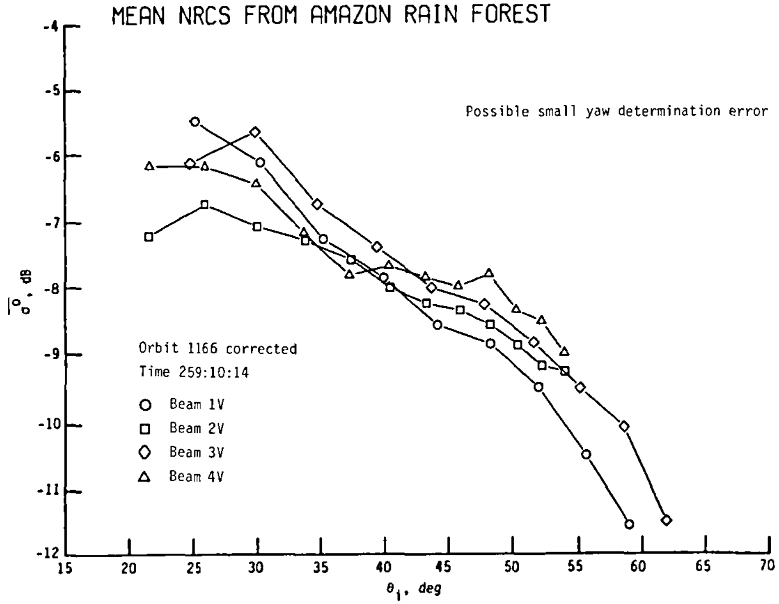
MEAN NRCS FROM AMAZON RAIN FOREST

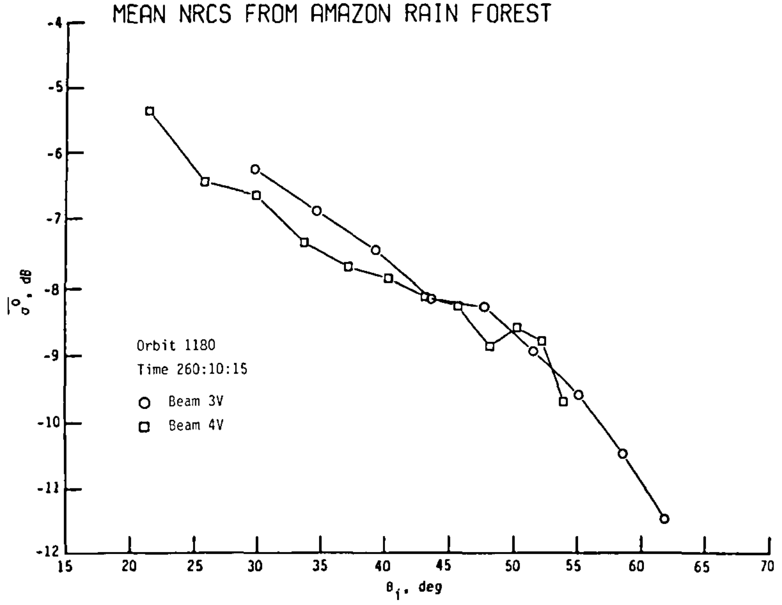
MEAN NRCS FROM AMAZON RAIN FOREST

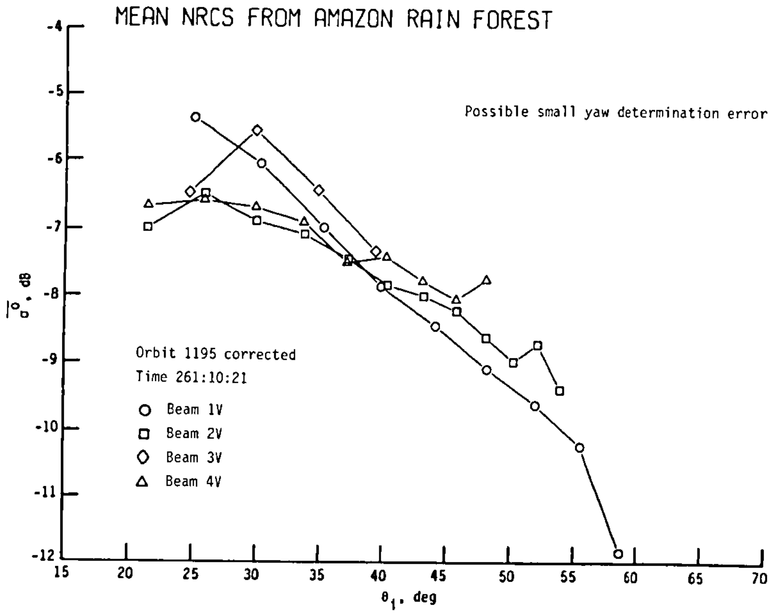
MEAN NRCS FROM AMAZON RAIN FOREST
Possible small yaw determination error
Orbit 1195 corrected
Time 261:10:21
○ Beam 1V
□ Beam 2V
◇ Beam 3V
△ Beam 4V
$\overline{\sigma_o}$, dB
-4
-5
-6
-7
-8
-9
-10
-11
-12
15
20
25
30
35
40
45
50
55
60
65
70
θ_i, deg

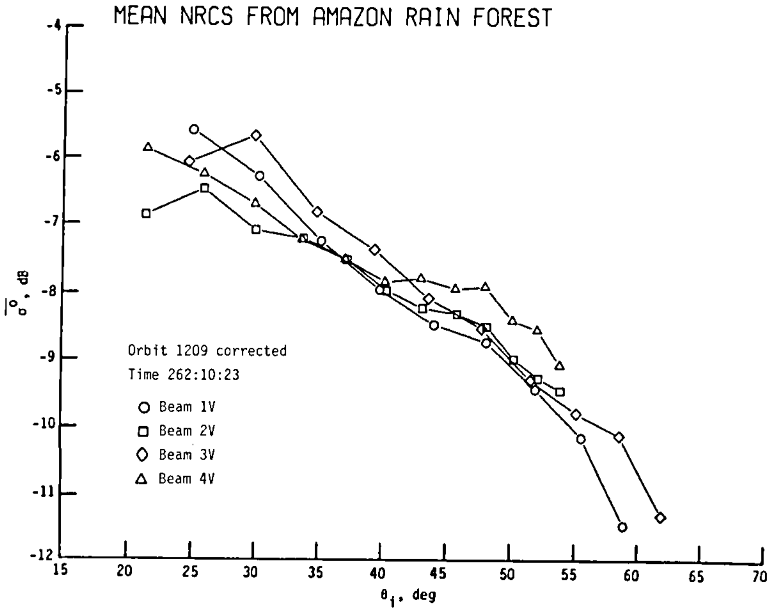
MEAN NRCS FROM AMAZON RAIN FOREST
Orbit 1209 corrected
Time 262:10:23
○ Beam 1V
□ Beam 2V
◇ Beam 3V
△ Beam 4V
$\overline{\sigma_o}$, dB
-4
-5
-6
-7
-8
-9
-10
-11
-12
15
20
25
30
35
40
45
50
55
60
65
70
θ_i, deg

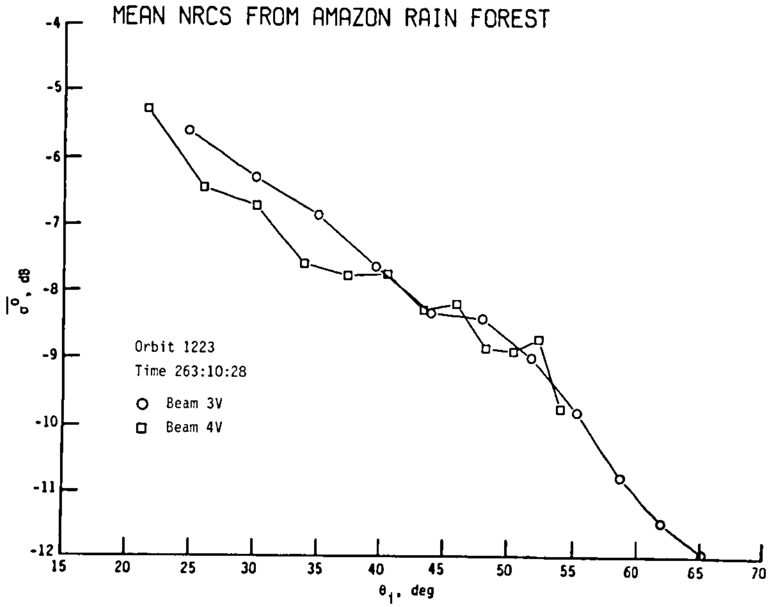
MEAN NRCS FROM AMAZON RAIN FOREST
Orbit 1223
Time 263:10:28
○ Beam 3V
□ Beam 4V
$\overline{\sigma_o}$, dB
-4
-5
-6
-7
-8
-9
-10
-11
-12
15
20
25
30
35
40
45
50
55
60
65
70
θ_i, deg

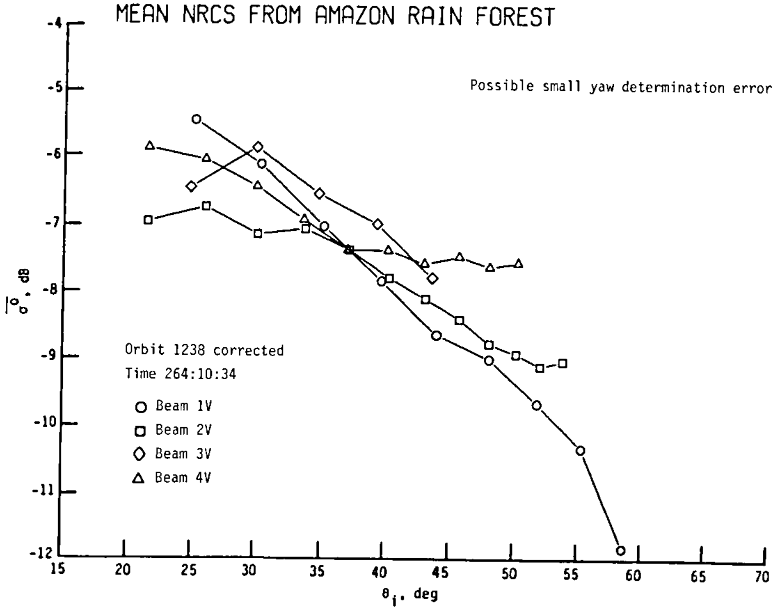
MEAN NRCS FROM AMAZON RAIN FOREST
Possible small yaw determination error
Orbit 1238 corrected
Time 264:10:34
○ Beam 1V
□ Beam 2V
◇ Beam 3V
△ Beam 4V
$\overline{\sigma_o}$, dB
-4
-5
-6
-7
-8
-9
-10
-11
-12
15
20
25
30
35
40
45
50
55
60
65
70
θ_i, deg

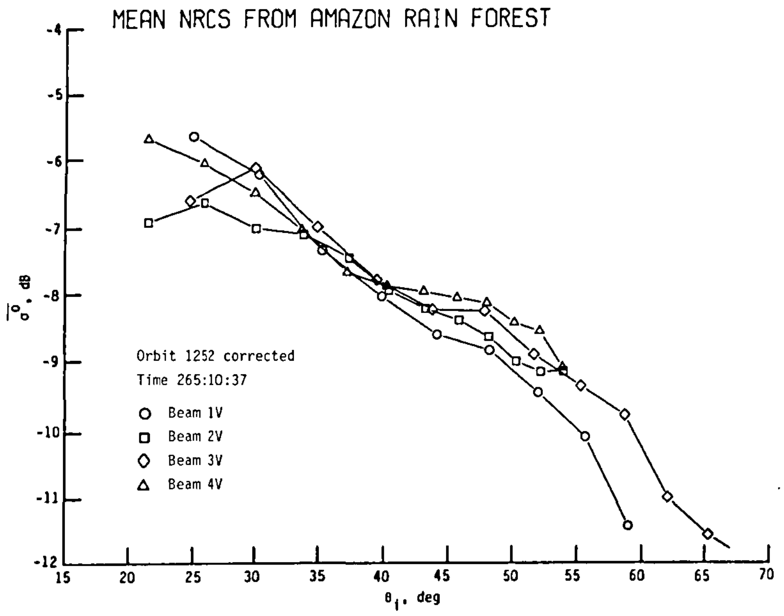
MEAN NRCS FROM AMAZON RAIN FOREST
σ̄o, dB
-4
-5
-6
-7
-8
-9
-10
-11
-12
15
20
25
30
35
40
45
50
55
60
65
70
θi, deg
Orbit 1252 corrected
Time 265:10:37
○ Beam 1V
□ Beam 2V
◇ Beam 3V
△ Beam 4V

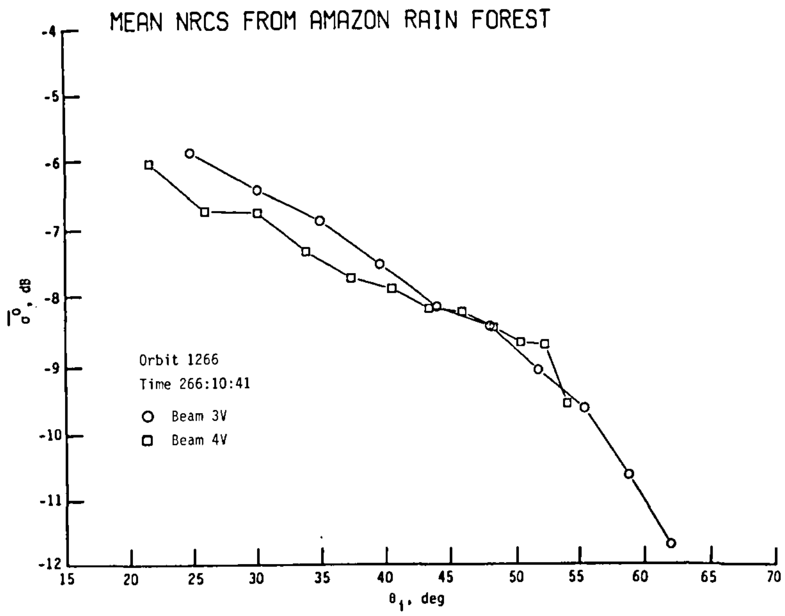
MEAN NRCS FROM AMAZON RAIN FOREST
σ̄o, dB
-4
-5
-6
-7
-8
-9
-10
-11
-12
15
20
25
30
35
40
45
50
55
60
65
70
θi, deg
Orbit 1266
Time 266:10:41
○ Beam 3V
□ Beam 4V

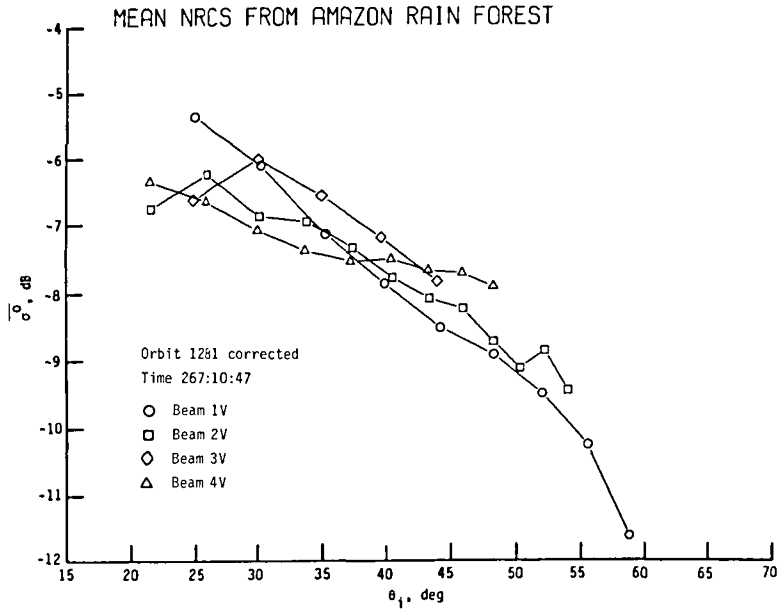
MEAN NRCS FROM AMAZON RAIN FOREST
σ̄o, dB
-4
-5
-6
-7
-8
-9
-10
-11
-12
15
20
25
30
35
40
45
50
55
60
65
70
θi, deg
Orbit 1281 corrected
Time 267:10:47
○ Beam 1V
□ Beam 2V
◇ Beam 3V
△ Beam 4V

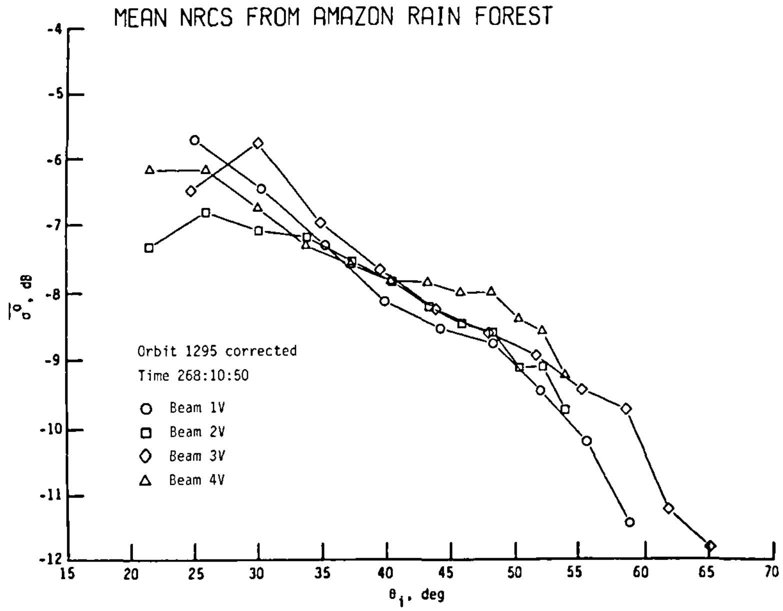
MEAN NRCS FROM AMAZON RAIN FOREST
σ̄o, dB
-4
-5
-6
-7
-8
-9
-10
-11
-12
15
20
25
30
35
40
45
50
55
60
65
70
θi, deg
Orbit 1295 corrected
Time 268:10:50
○ Beam 1V
□ Beam 2V
◇ Beam 3V
△ Beam 4V

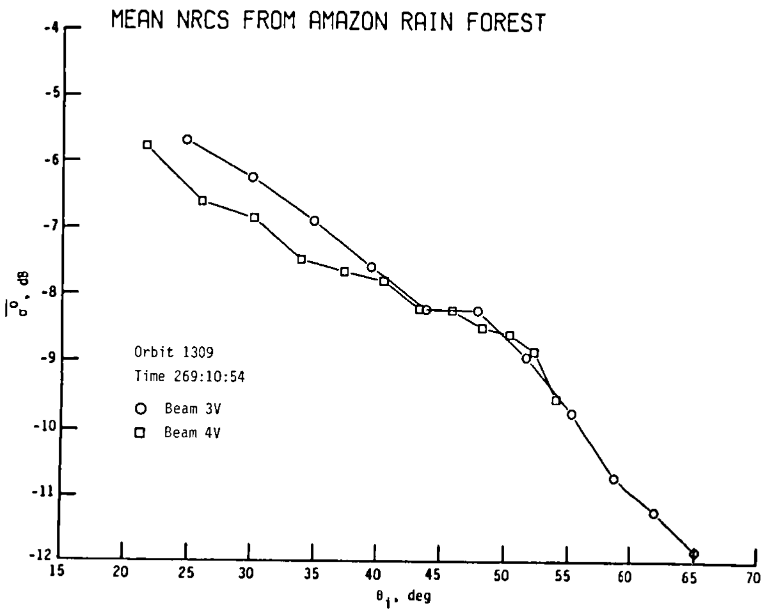
MEAN NRCS FROM AMAZON RAIN FOREST
Orbit 1309
Time 269:10:54
○ Beam 3V
□ Beam 4V
$\bar{\sigma}_o$, dB
-4
-5
-6
-7
-8
-9
-10
-11
-12
15
20
25
30
35
40
45
50
55
60
65
70
θ_i, deg

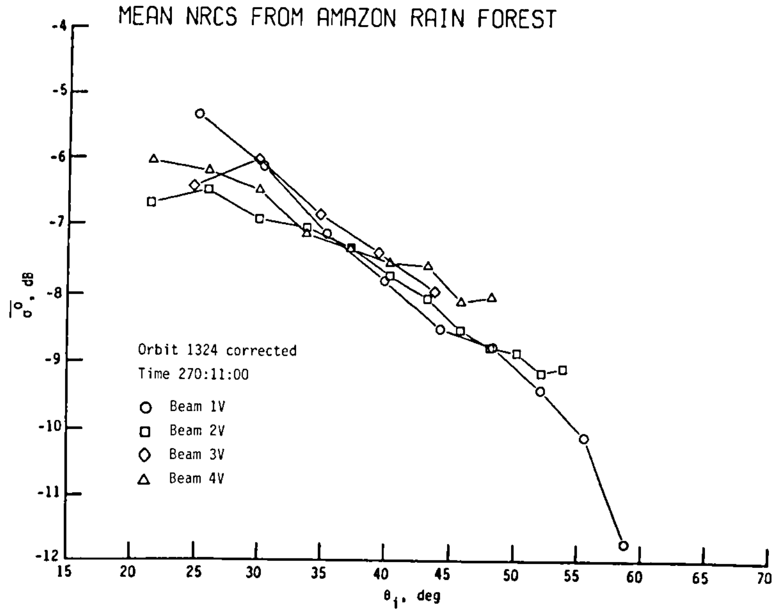
MEAN NRCS FROM AMAZON RAIN FOREST
Orbit 1324 corrected
Time 270:11:00
○ Beam 1V
□ Beam 2V
◇ Beam 3V
△ Beam 4V
$\bar{\sigma}_o$, dB
-4
-5
-6
-7
-8
-9
-10
-11
-12
15
20
25
30
35
40
45
50
55
60
65
70
θ_i, deg

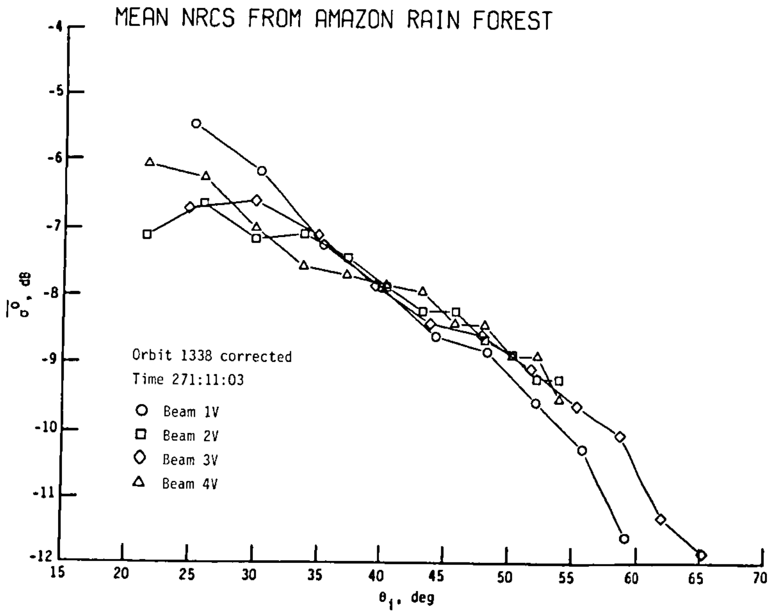
MEAN NRCS FROM AMAZON RAIN FOREST
Orbit 1338 corrected
Time 271:11:03
○ Beam 1V
□ Beam 2V
◇ Beam 3V
△ Beam 4V
$\bar{\sigma}_o$, dB
-4
-5
-6
-7
-8
-9
-10
-11
-12
15
20
25
30
35
40
45
50
55
60
65
70
θ_i, deg

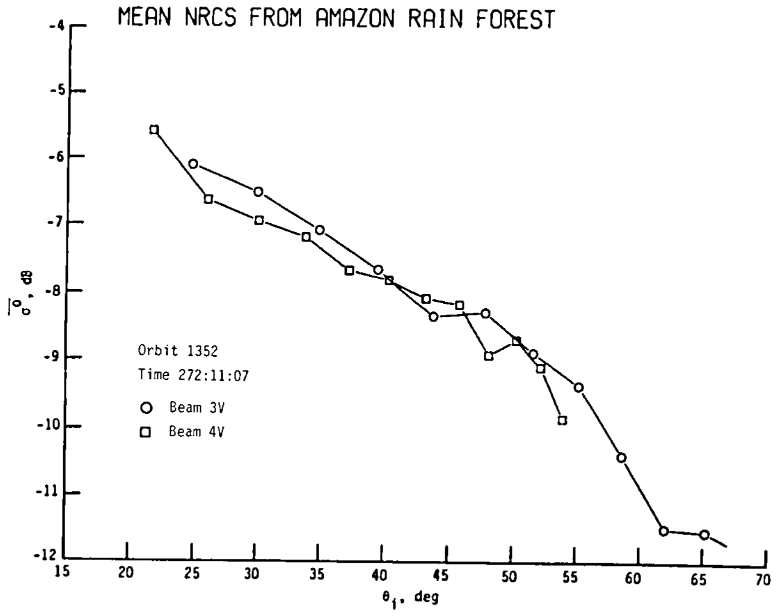
MEAN NRCS FROM AMAZON RAIN FOREST
Orbit 1352
Time 272:11:07
○ Beam 3V
□ Beam 4V
$\bar{\sigma}_o$, dB
-4
-5
-6
-7
-8
-9
-10
-11
-12
15
20
25
30
35
40
45
50
55
60
65
70
θ_i, deg

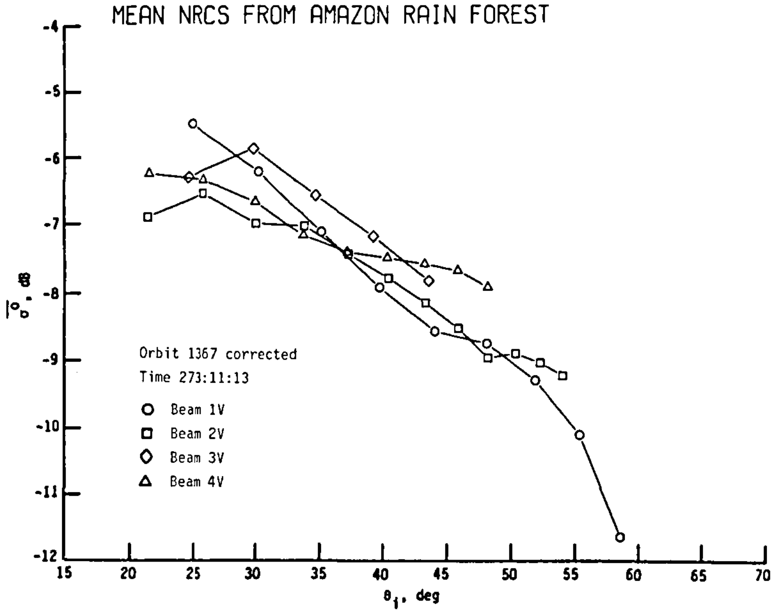
MEAN NRCS FROM AMAZON RAIN FOREST

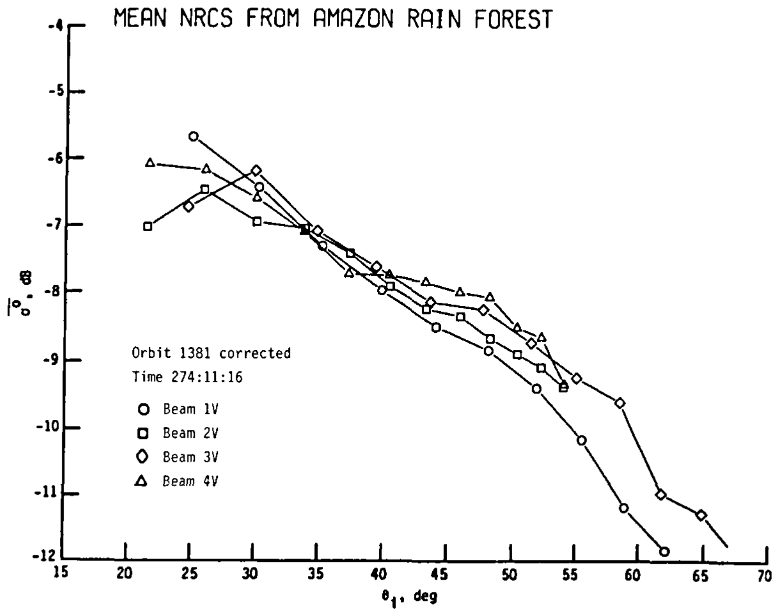
MEAN NRCS FROM AMAZON RAIN FOREST

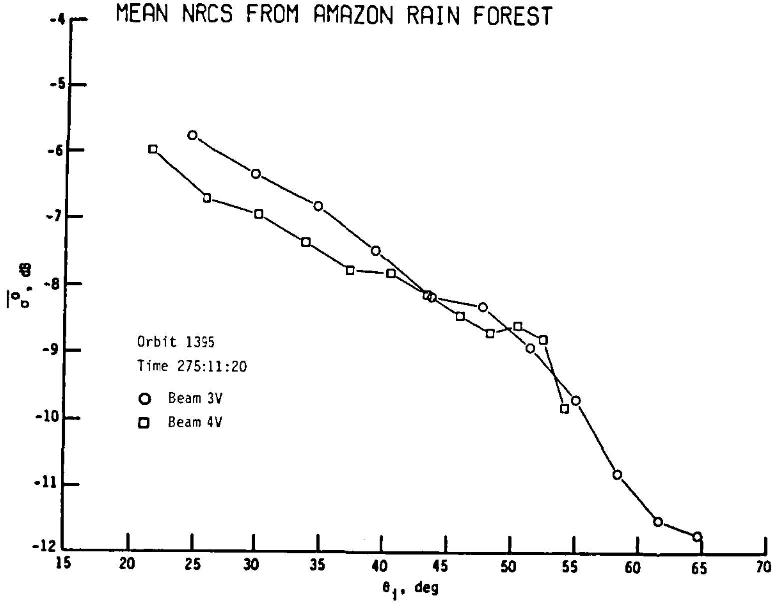
MEAN NRCS FROM AMAZON RAIN FOREST

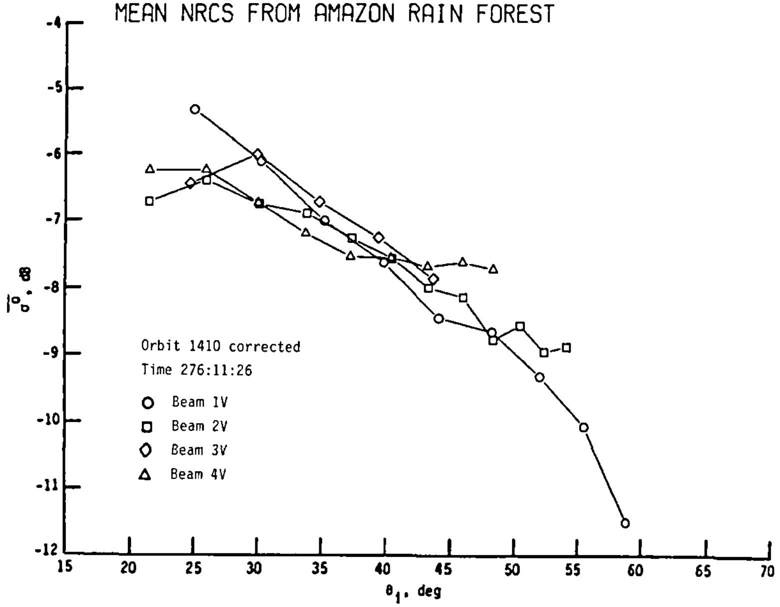
MEAN NRCS FROM AMAZON RAIN FOREST

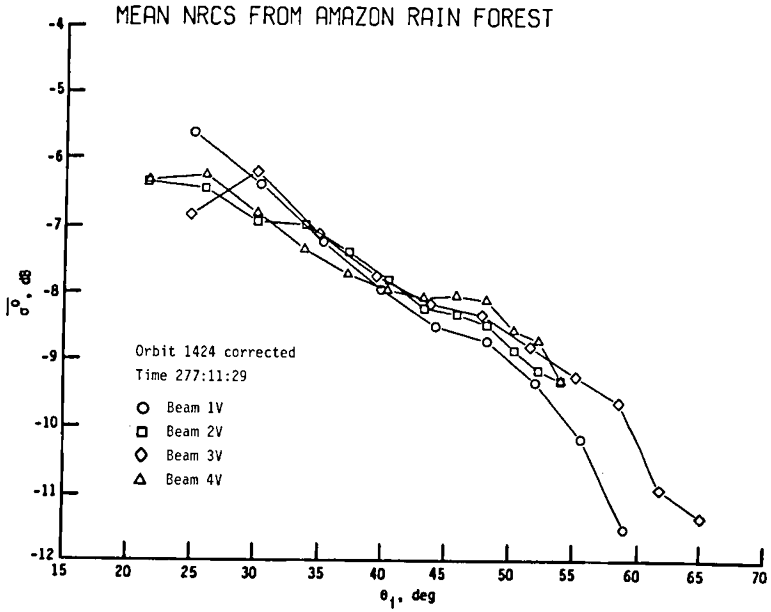

MEAN NRCS FROM AMAZON RAIN FOREST

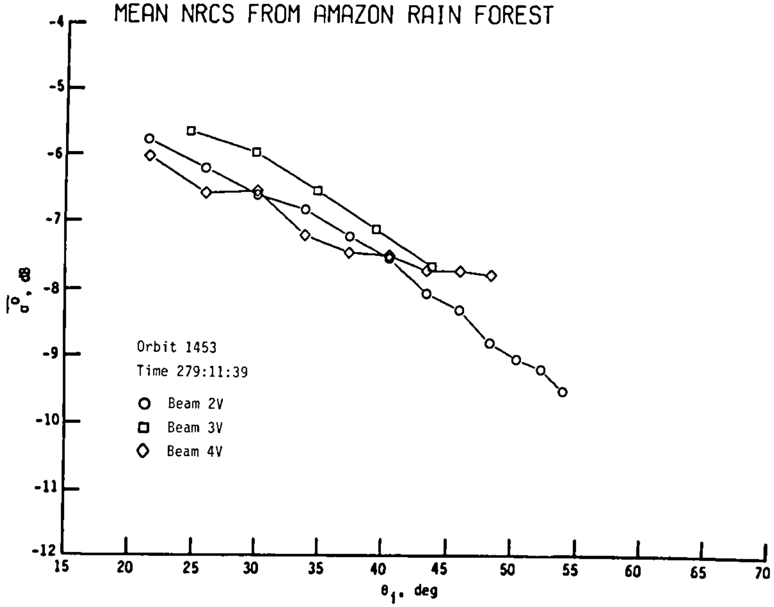

MEAN NRCS FROM AMAZON RAIN FOREST

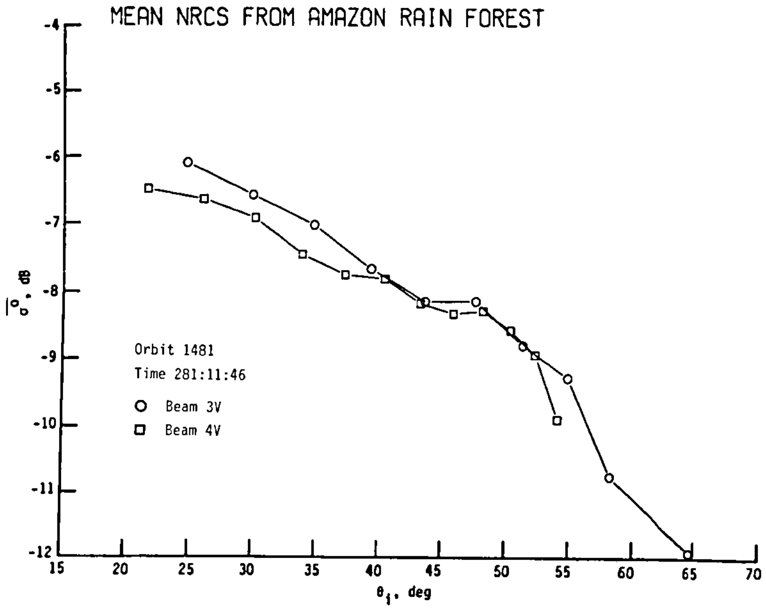

MEAN NRCS FROM AMAZON RAIN FOREST

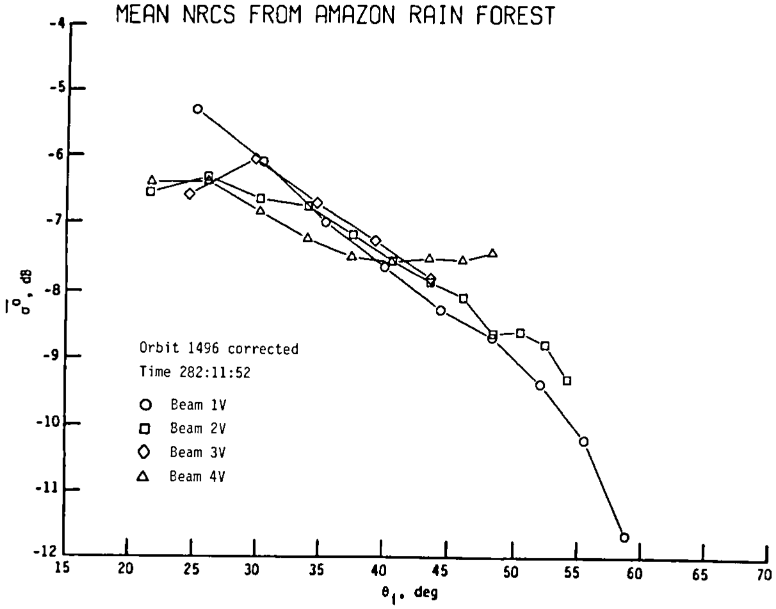

MEAN NRCS FROM AMAZON RAIN FOREST

APPENDIX B

RESPONSE PLOTS OF $\overline{\sigma^{o}}$ AGAINST INCIDENCE ANGLE FOR ALL DESCENDING ORBITS

This appendix contains response plots of $\overline{\sigma^{o}}$ against incidence angle for all the descending orbits. These orbits cover all the evening time periods that passed over the Amazon rain forest. See appendix A for further description of information shown in the plots.

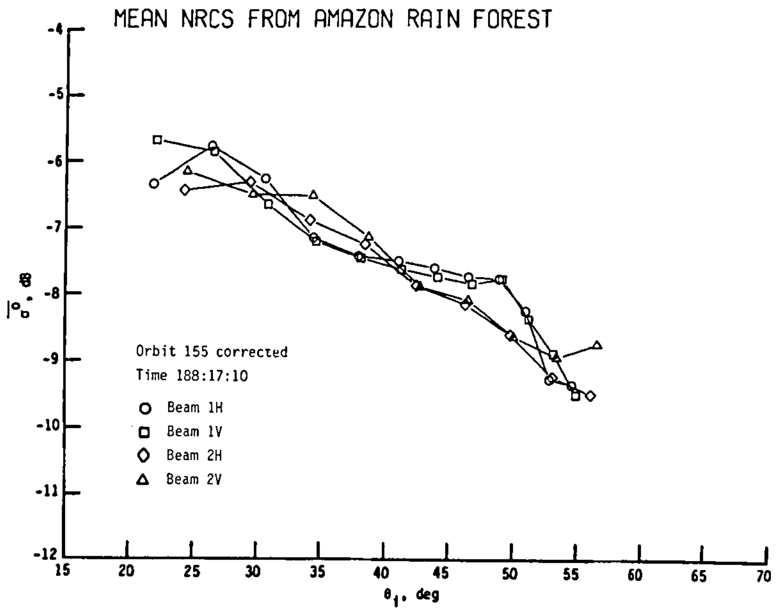
MEAN NRCS FROM AMAZON RAIN FOREST
-4
-5
-6
-7
-8
-9
-10
-11
-12
$\overline{\sigma}_o$, dB
15
20
25
30
35
40
45
50
55
60
65
70
θ_i, deg
Orbit 155 corrected
Time 188:17:10
○ Beam 1H
□ Beam 1V
◇ Beam 2H
△ Beam 2V

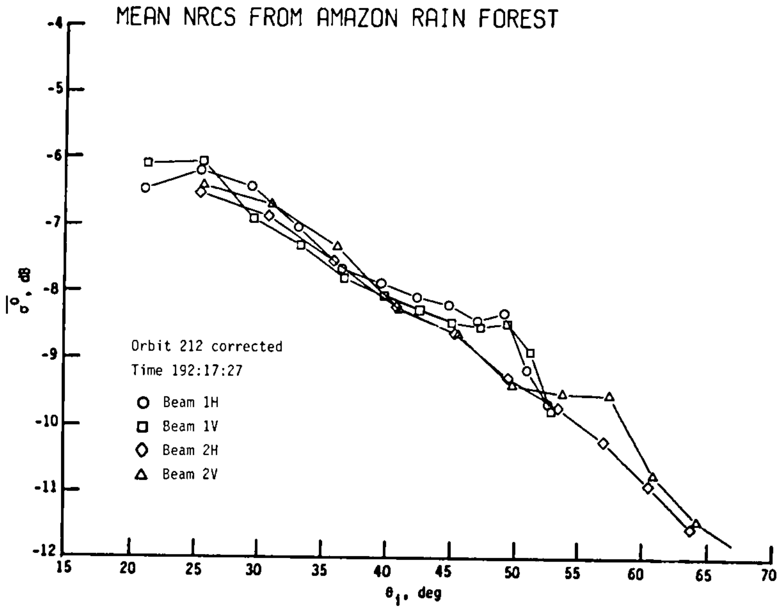
MEAN NRCS FROM AMAZON RAIN FOREST
-4
-5
-6
-7
-8
-9
-10
-11
-12
$\overline{\sigma}_o$, dB
15
20
25
30
35
40
45
50
55
60
65
70
θ_i, deg
Orbit 212 corrected
Time 192:17:27
○ Beam 1H
□ Beam 1V
◇ Beam 2H
△ Beam 2V

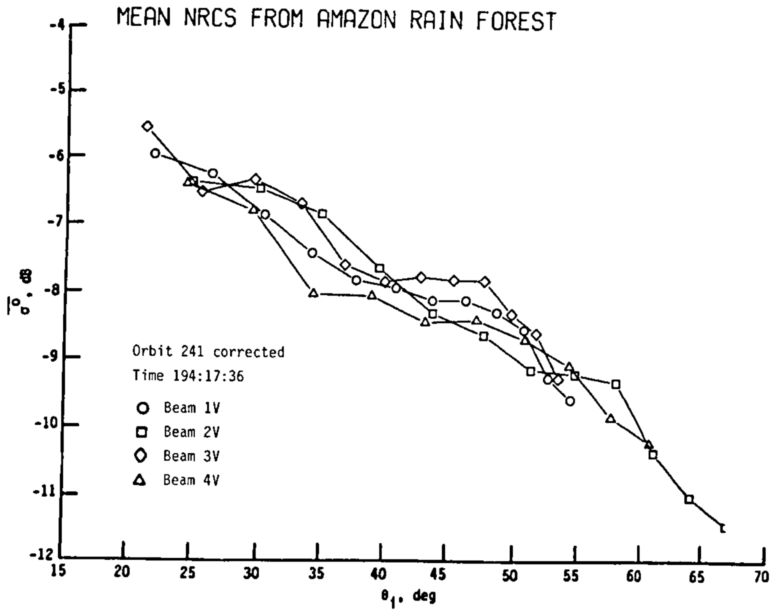
MEAN NRCS FROM AMAZON RAIN FOREST
-4
-5
-6
-7
-8
-9
-10
-11
-12
$\overline{\sigma}_o$, dB
15
20
25
30
35
40
45
50
55
60
65
70
θ_i, deg
Orbit 241 corrected
Time 194:17:36
○ Beam 1V
□ Beam 2V
◇ Beam 3V
△ Beam 4V

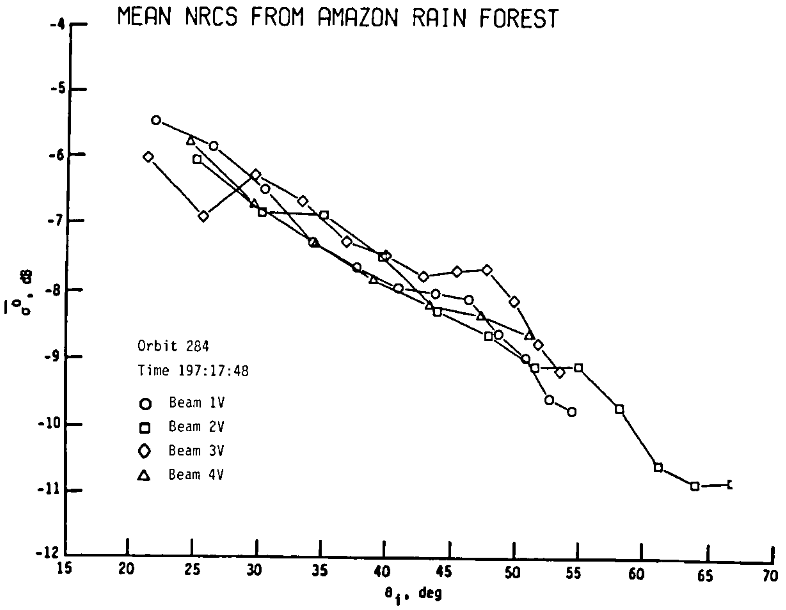
MEAN NRCS FROM AMAZON RAIN FOREST
-4
-5
-6
-7
-8
-9
-10
-11
-12
$\overline{\sigma}_o$, dB
15
20
25
30
35
40
45
50
55
60
65
70
θ_i, deg
Orbit 284
Time 197:17:48
○ Beam 1V
□ Beam 2V
◇ Beam 3V
△ Beam 4V

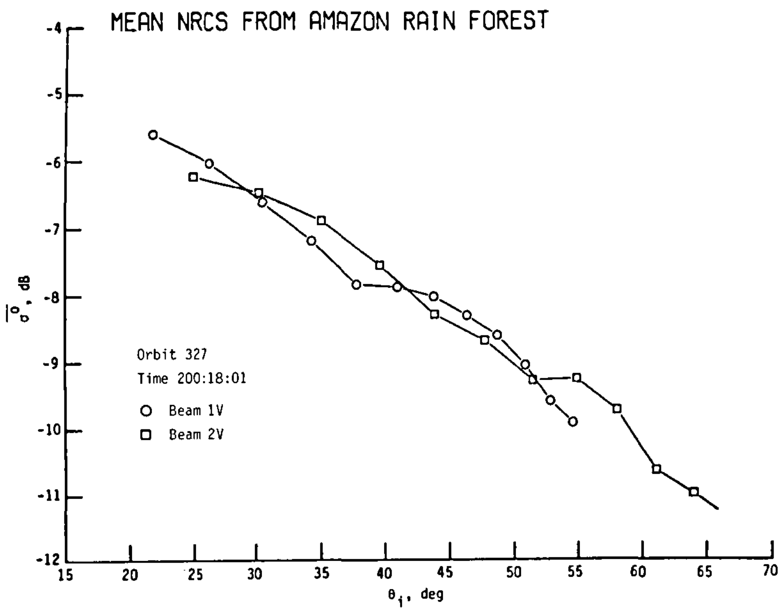
MEAN NRCS FROM AMAZON RAIN FOREST
$\overline{\sigma}^o$, dB
-4
-5
-6
-7
-8
-9
-10
-11
-12
15
20
25
30
35
40
45
50
55
60
65
70
θ_i, deg
Orbit 327
Time 200:18:01
○ Beam 1V
□ Beam 2V

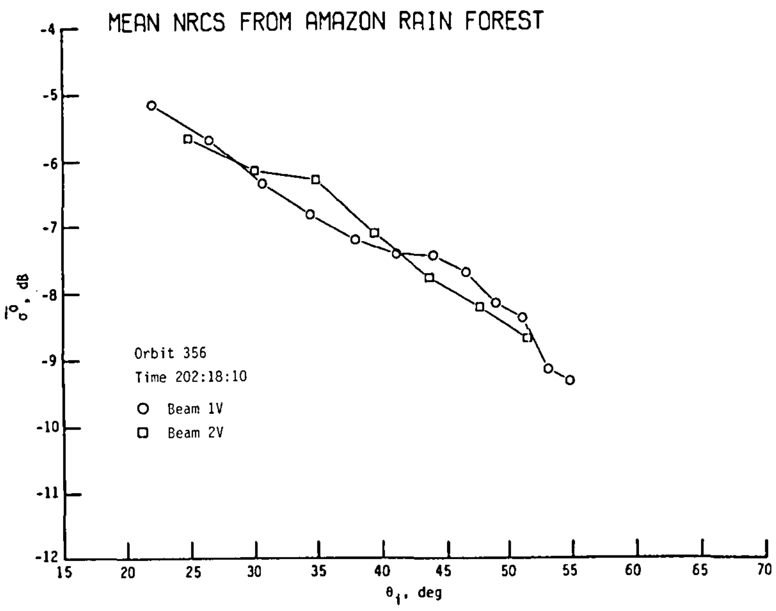
MEAN NRCS FROM AMAZON RAIN FOREST
$\overline{\sigma}^o$, dB
-4
-5
-6
-7
-8
-9
-10
-11
-12
15
20
25
30
35
40
45
50
55
60
65
70
θ_i, deg
Orbit 356
Time 202:18:10
○ Beam 1V
□ Beam 2V

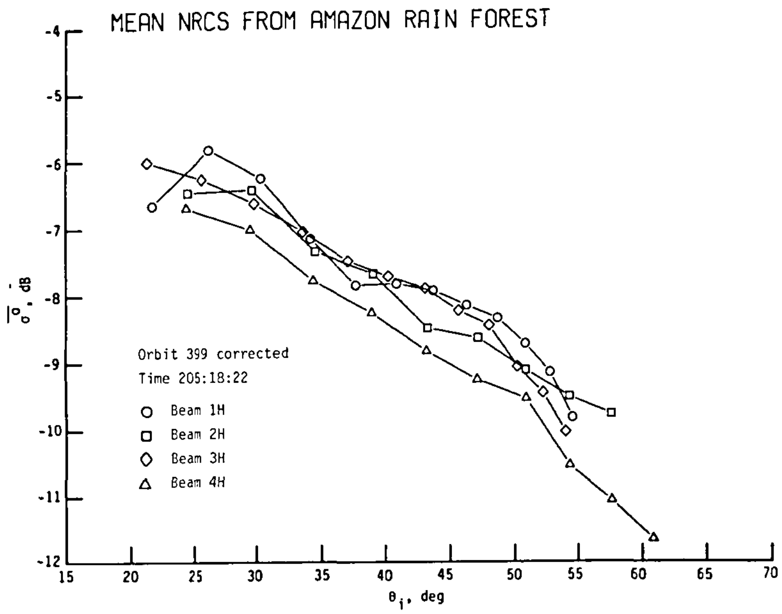
MEAN NRCS FROM AMAZON RAIN FOREST
$\overline{\sigma}^o$, dB
-4
-5
-6
-7
-8
-9
-10
-11
-12
15
20
25
30
35
40
45
50
55
60
65
70
θ_i, deg
Orbit 399 corrected
Time 205:18:22
○ Beam 1H
□ Beam 2H
◇ Beam 3H
△ Beam 4H

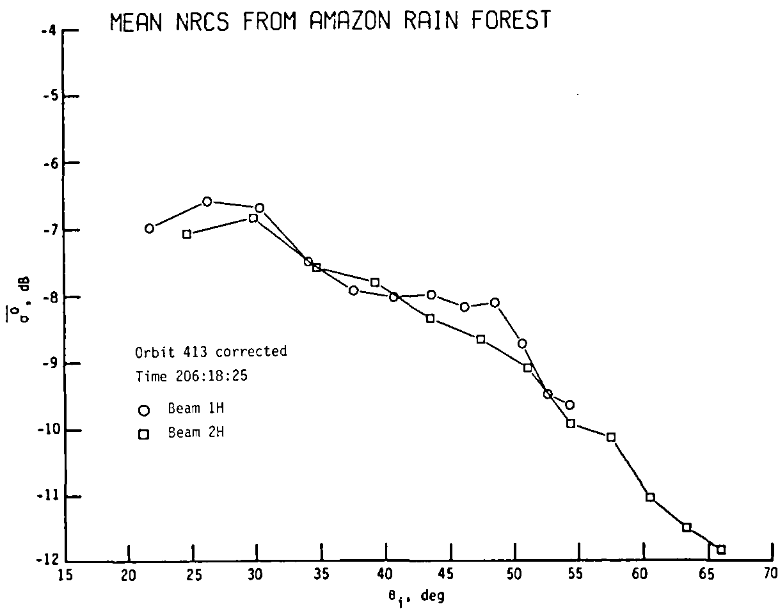
MEAN NRCS FROM AMAZON RAIN FOREST
$\overline{\sigma}^o$, dB
-4
-5
-6
-7
-8
-9
-10
-11
-12
15
20
25
30
35
40
45
50
55
60
65
70
θ_i, deg
Orbit 413 corrected
Time 206:18:25
○ Beam 1H
□ Beam 2H

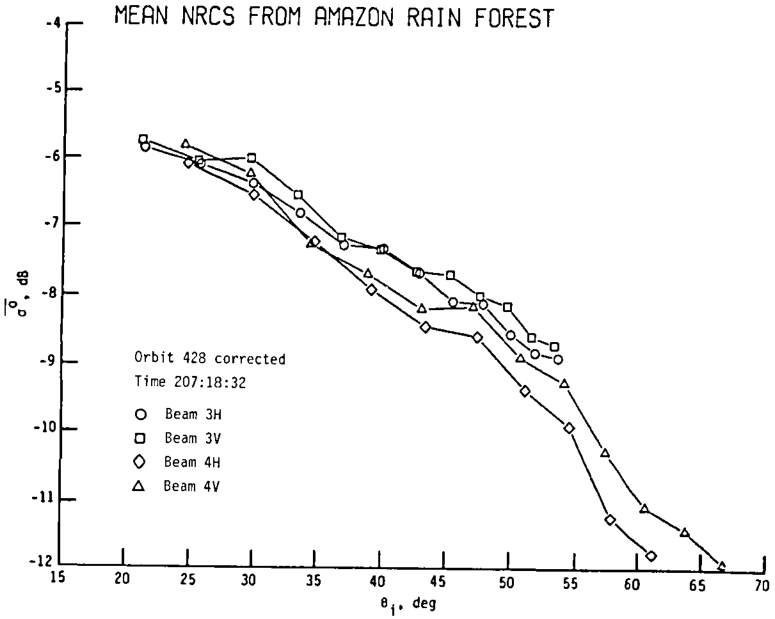
MEAN NRCS FROM AMAZON RAIN FOREST

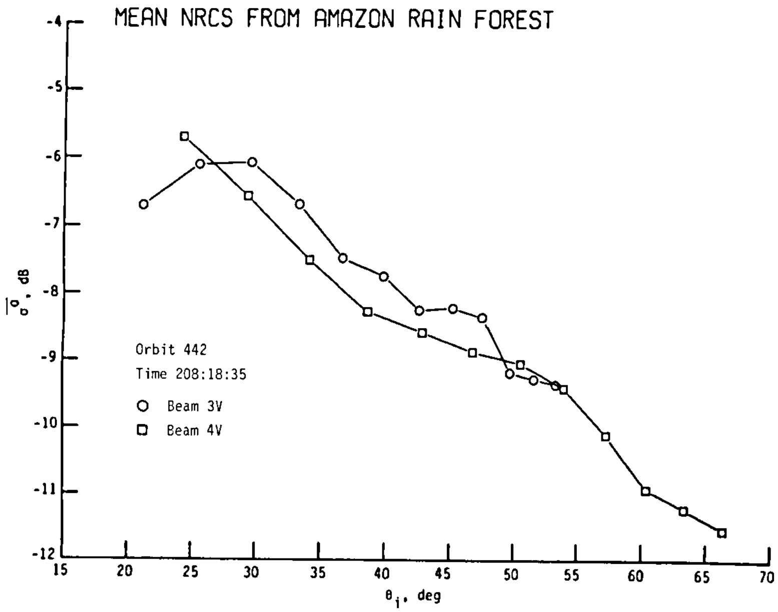
MEAN NRCS FROM AMAZON RAIN FOREST

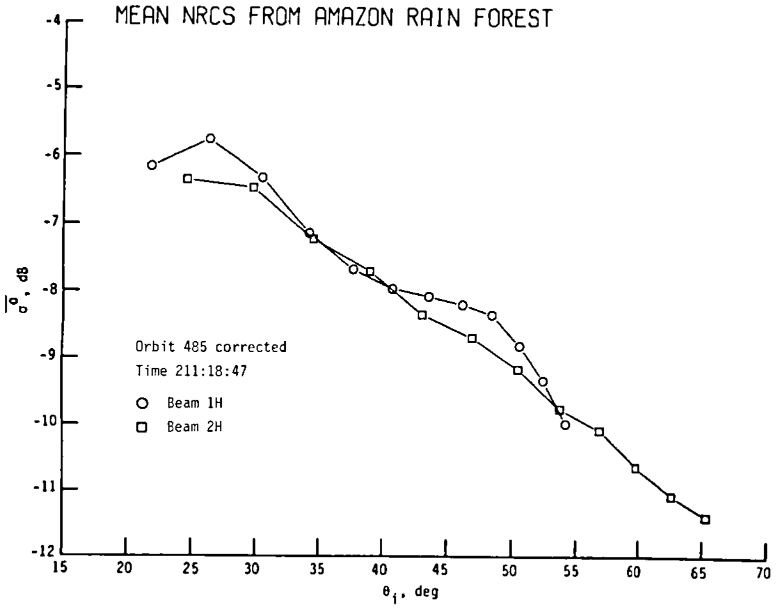
MEAN NRCS FROM AMAZON RAIN FOREST

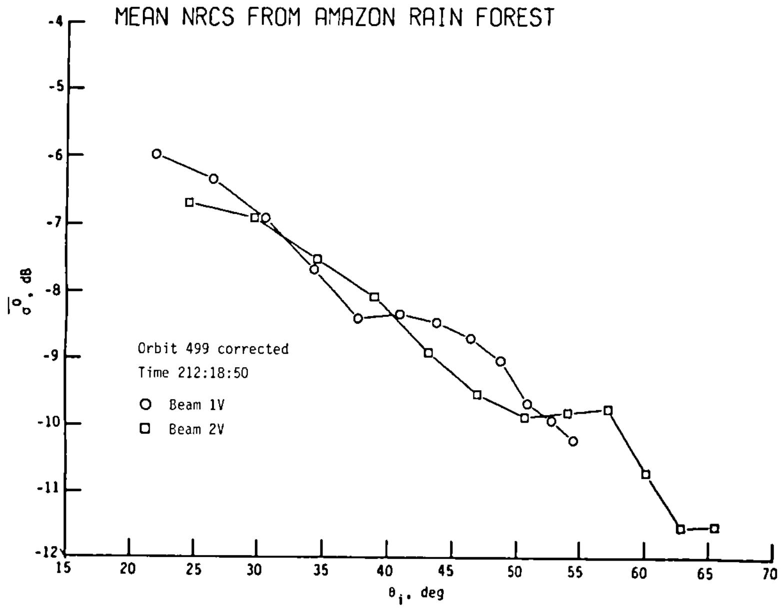
MEAN NRCS FROM AMAZON RAIN FOREST

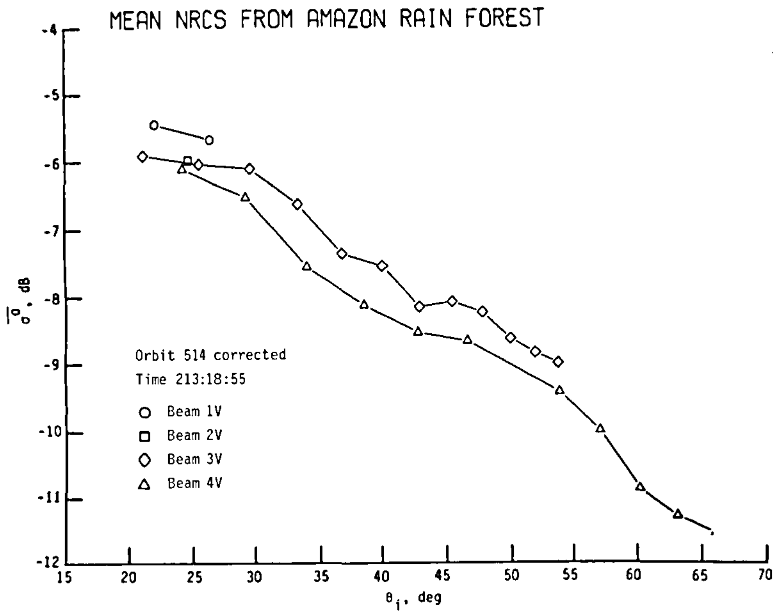
MEAN NRCS FROM AMAZON RAIN FOREST
σ°, dB
-4
-5
-6
-7
-8
-9
-10
-11
-12
θi, deg
15
20
25
30
35
40
45
50
55
60
65
70
Orbit 514 corrected
Time 213:18:55
○ Beam 1V
□ Beam 2V
◇ Beam 3V
△ Beam 4V

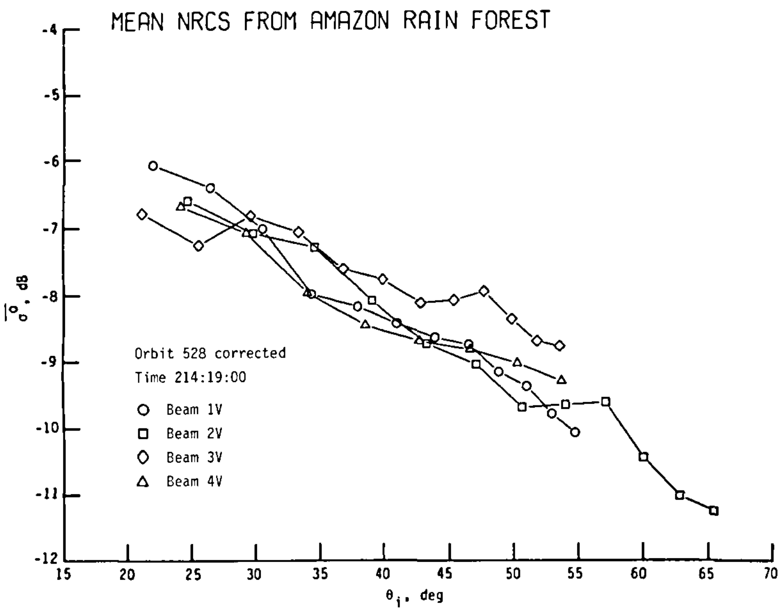
MEAN NRCS FROM AMAZON RAIN FOREST
σ°, dB
-4
-5
-6
-7
-8
-9
-10
-11
-12
θi, deg
15
20
25
30
35
40
45
50
55
60
65
70
Orbit 528 corrected
Time 214:19:00
○ Beam 1V
□ Beam 2V
◇ Beam 3V
△ Beam 4V

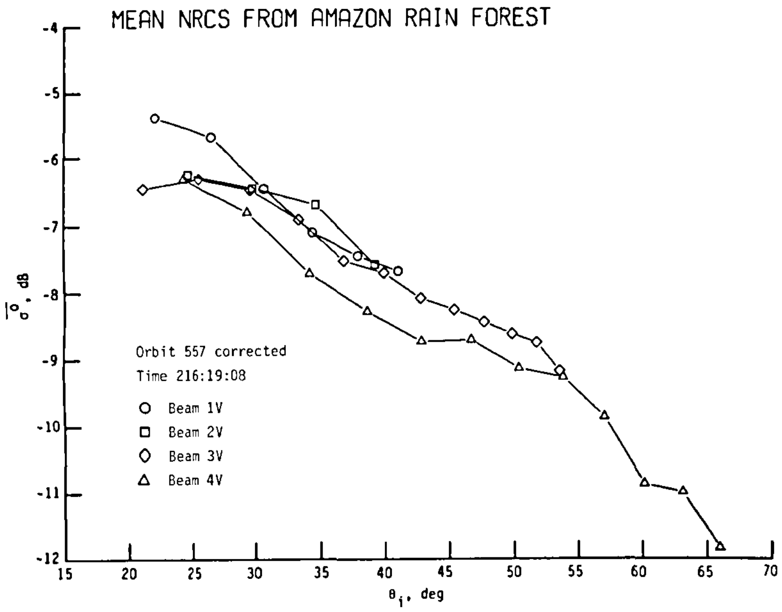
MEAN NRCS FROM AMAZON RAIN FOREST
σ°, dB
-4
-5
-6
-7
-8
-9
-10
-11
-12
θi, deg
15
20
25
30
35
40
45
50
55
60
65
70
Orbit 557 corrected
Time 216:19:08
○ Beam 1V
□ Beam 2V
◇ Beam 3V
△ Beam 4V

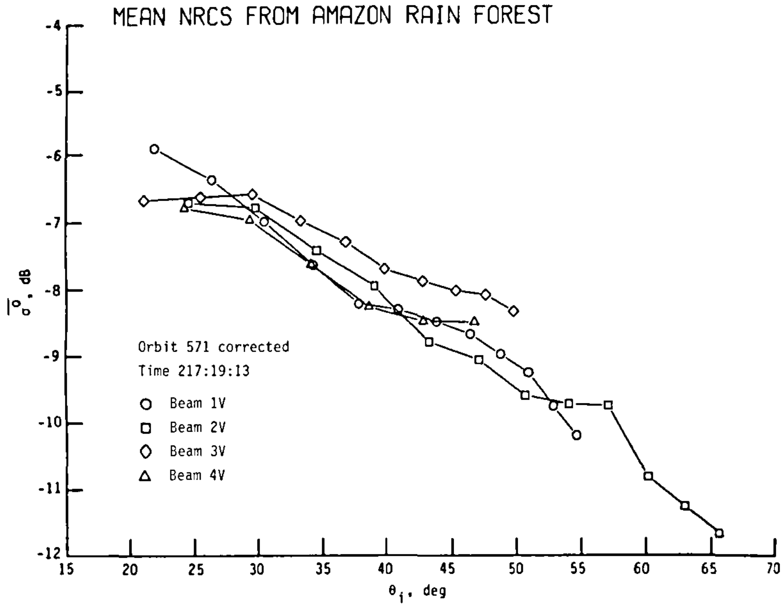
MEAN NRCS FROM AMAZON RAIN FOREST
σ°, dB
-4
-5
-6
-7
-8
-9
-10
-11
-12
θi, deg
15
20
25
30
35
40
45
50
55
60
65
70
Orbit 571 corrected
Time 217:19:13
○ Beam 1V
□ Beam 2V
◇ Beam 3V
△ Beam 4V

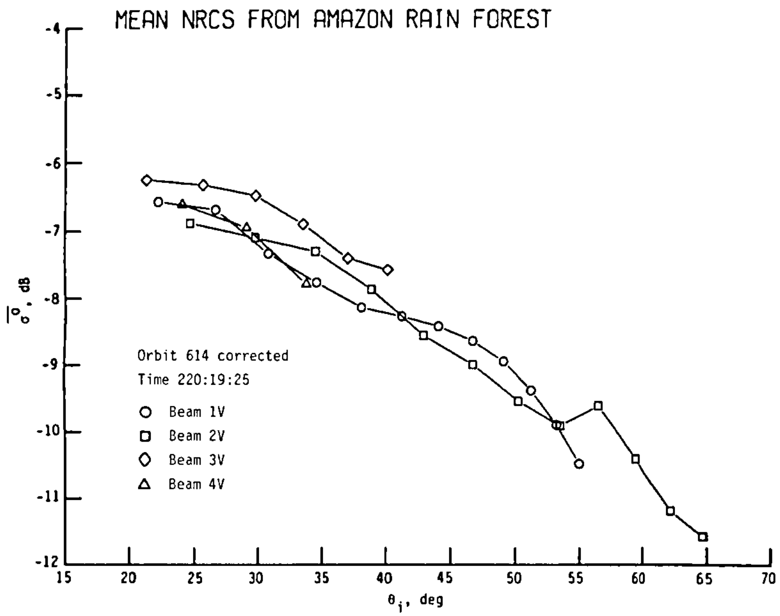
MEAN NRCS FROM AMAZON RAIN FOREST

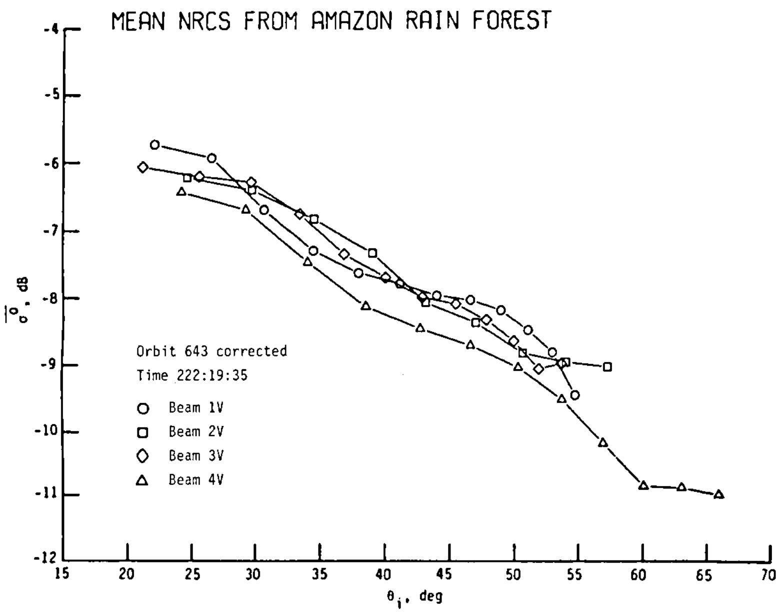
MEAN NRCS FROM AMAZON RAIN FOREST

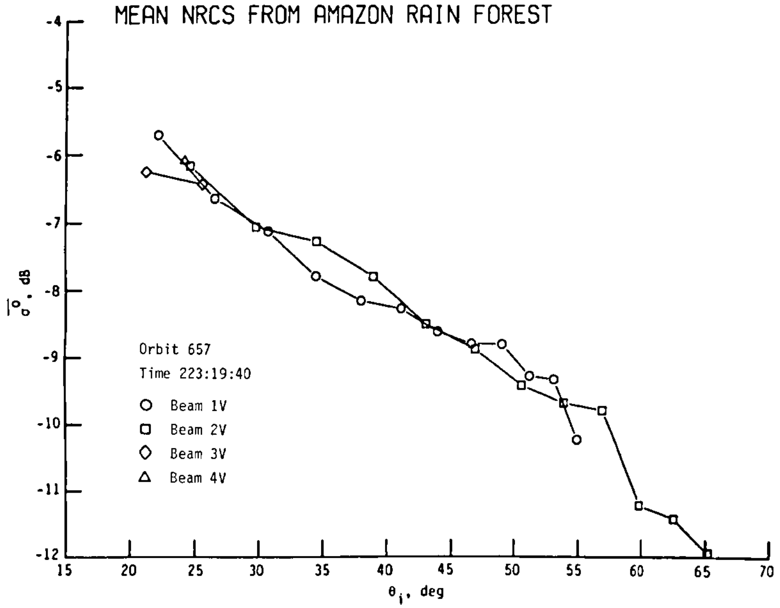
MEAN NRCS FROM AMAZON RAIN FOREST

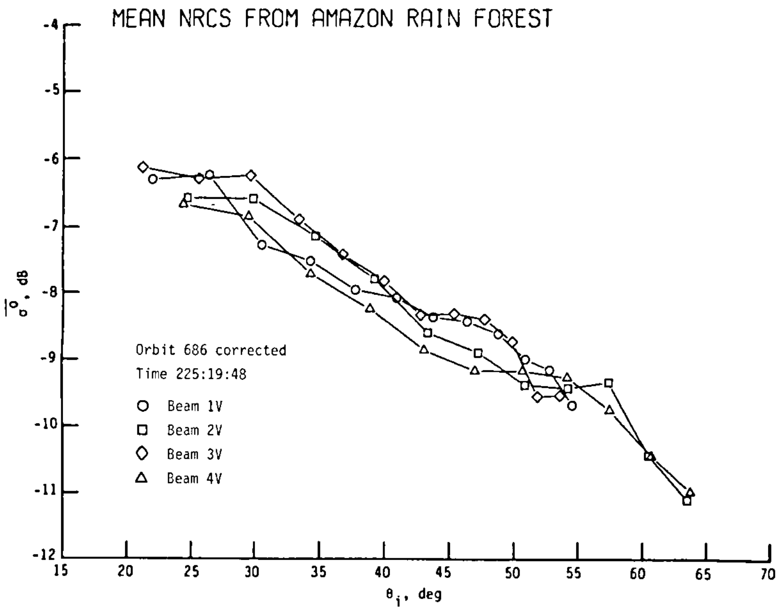
MEAN NRCS FROM AMAZON RAIN FOREST

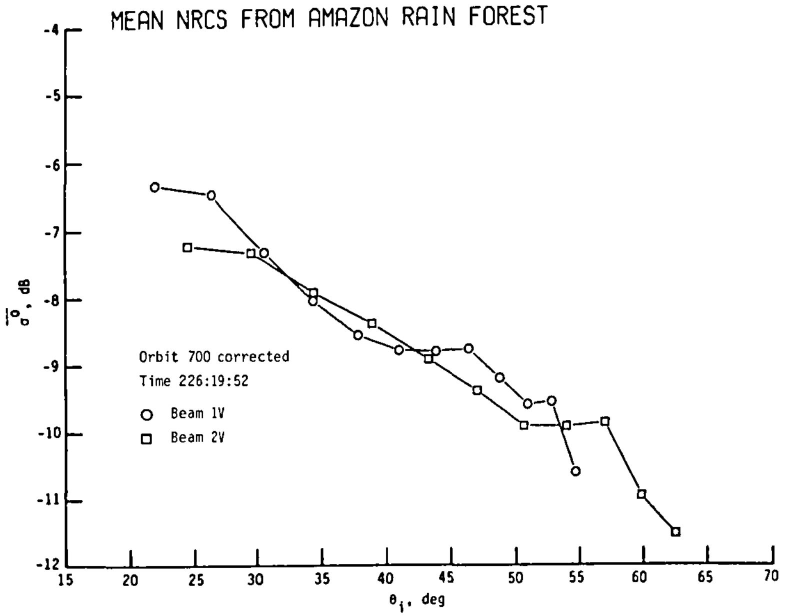
MEAN NRCS FROM AMAZON RAIN FOREST
$\overline{\sigma}^0$, dB
-4
-5
-6
-7
-8
-9
-10
-11
-12
15
20
25
30
35
40
45
50
55
60
65
70
θ_i, deg
Orbit 700 corrected
Time 226:19:52
○ Beam 1V
□ Beam 2V

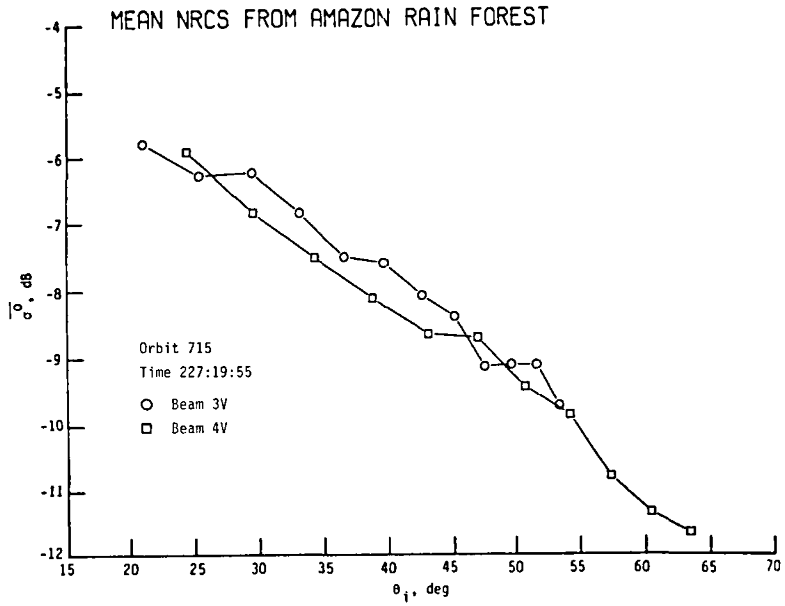
MEAN NRCS FROM AMAZON RAIN FOREST
$\overline{\sigma}^0$, dB
-4
-5
-6
-7
-8
-9
-10
-11
-12
15
20
25
30
35
40
45
50
55
60
65
70
θ_i, deg
Orbit 715
Time 227:19:55
○ Beam 3V
□ Beam 4V

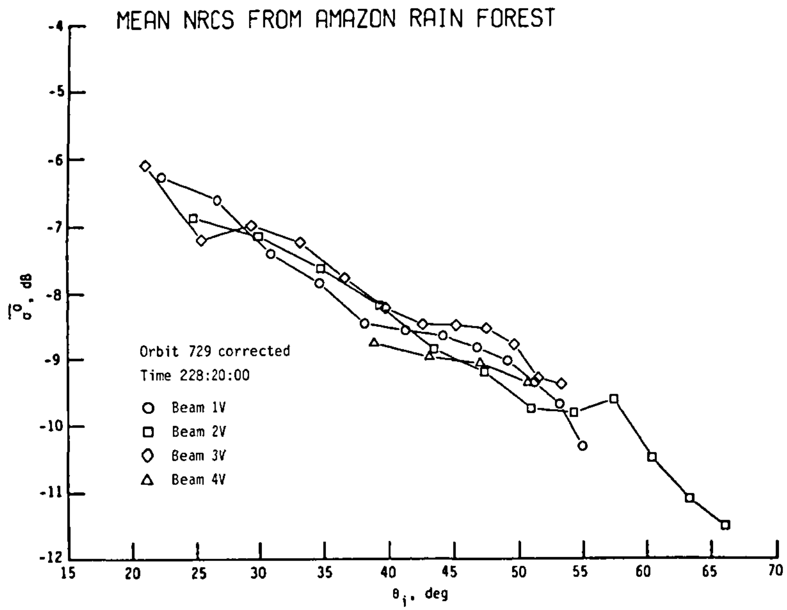
MEAN NRCS FROM AMAZON RAIN FOREST
$\overline{\sigma}^0$, dB
-4
-5
-6
-7
-8
-9
-10
-11
-12
15
20
25
30
35
40
45
50
55
60
65
70
θ_i, deg
Orbit 729 corrected
Time 228:20:00
○ Beam 1V
□ Beam 2V
◇ Beam 3V
△ Beam 4V

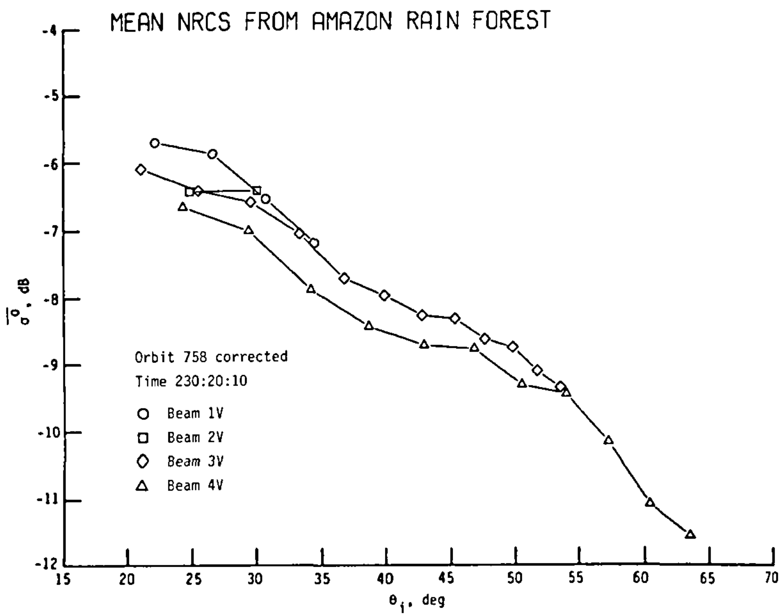
MEAN NRCS FROM AMAZON RAIN FOREST
$\overline{\sigma}^0$, dB
-4
-5
-6
-7
-8
-9
-10
-11
-12
15
20
25
30
35
40
45
50
55
60
65
70
θ_i, deg
Orbit 758 corrected
Time 230:20:10
○ Beam 1V
□ Beam 2V
◇ Beam 3V
△ Beam 4V

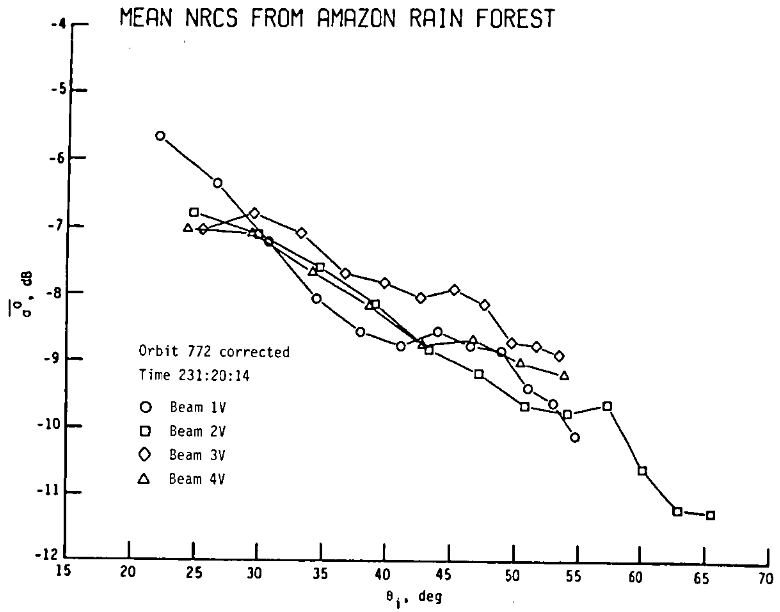
MEAN NRCS FROM AMAZON RAIN FOREST

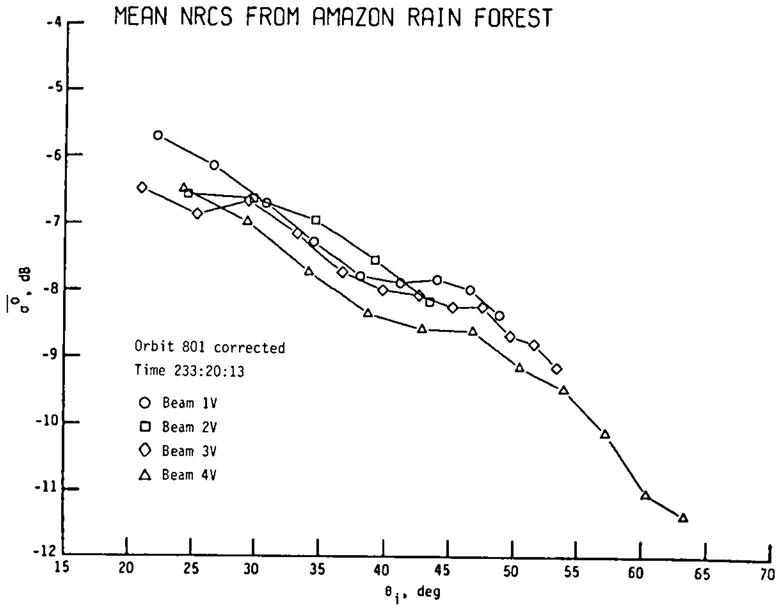
MEAN NRCS FROM AMAZON RAIN FOREST

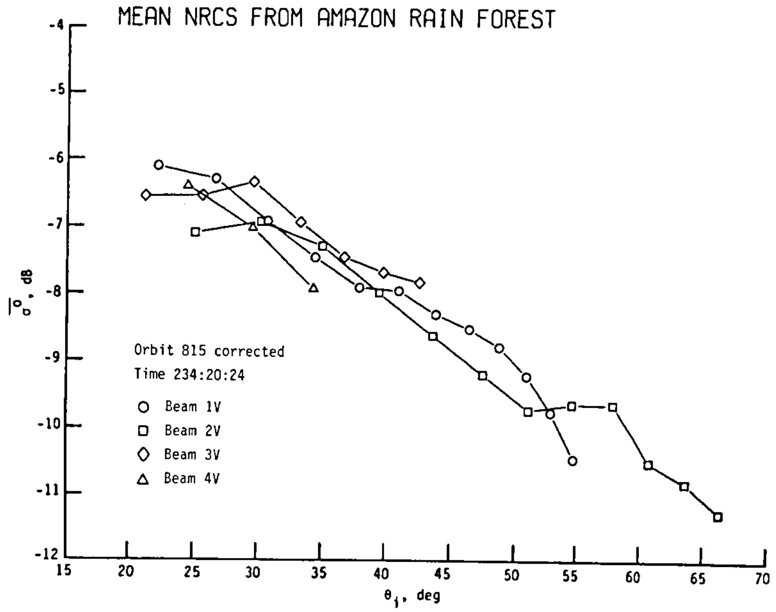
MEAN NRCS FROM AMAZON RAIN FOREST

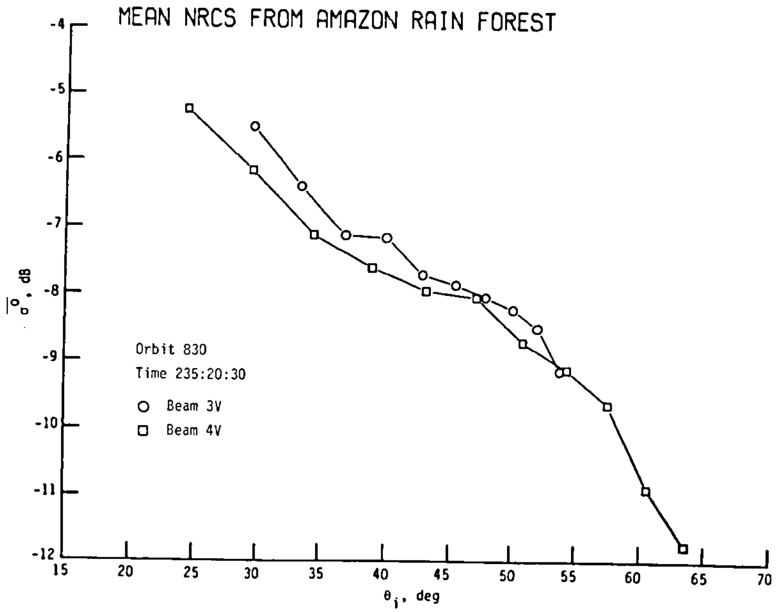
MEAN NRCS FROM AMAZON RAIN FOREST

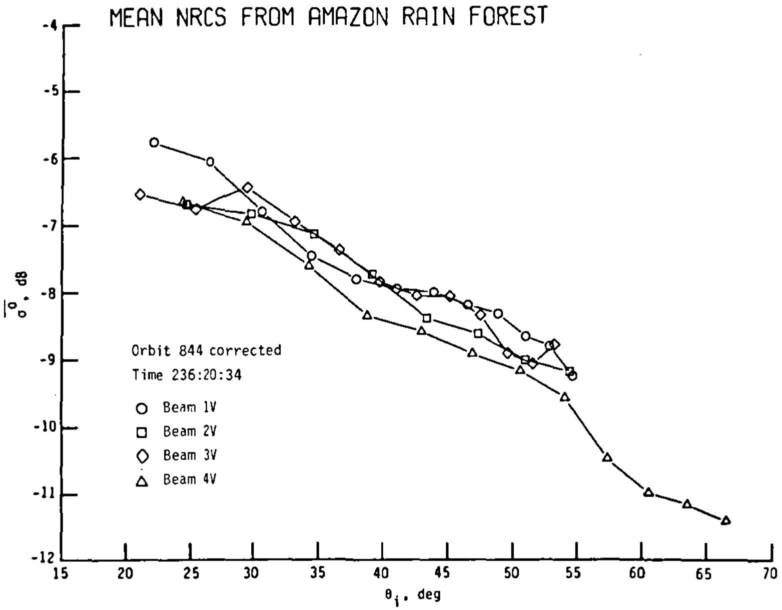
MEAN NRCS FROM AMAZON RAIN FOREST

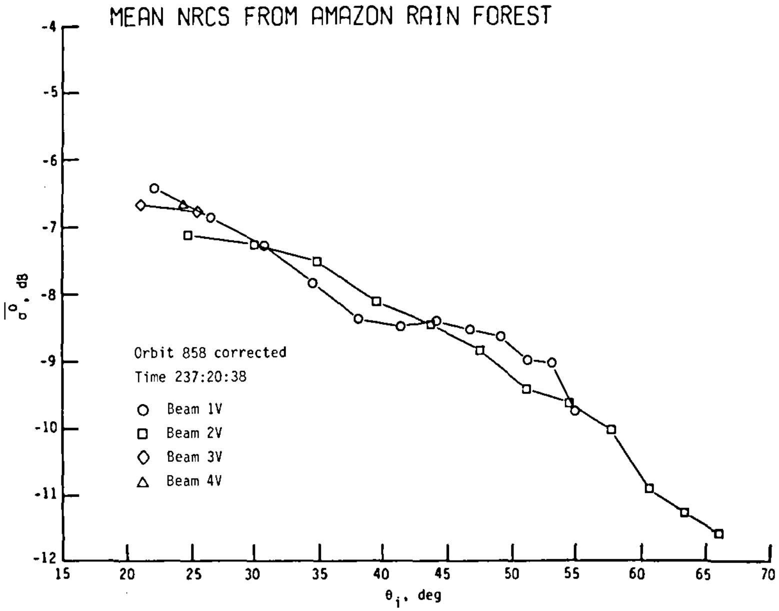
MEAN NRCS FROM AMAZON RAIN FOREST

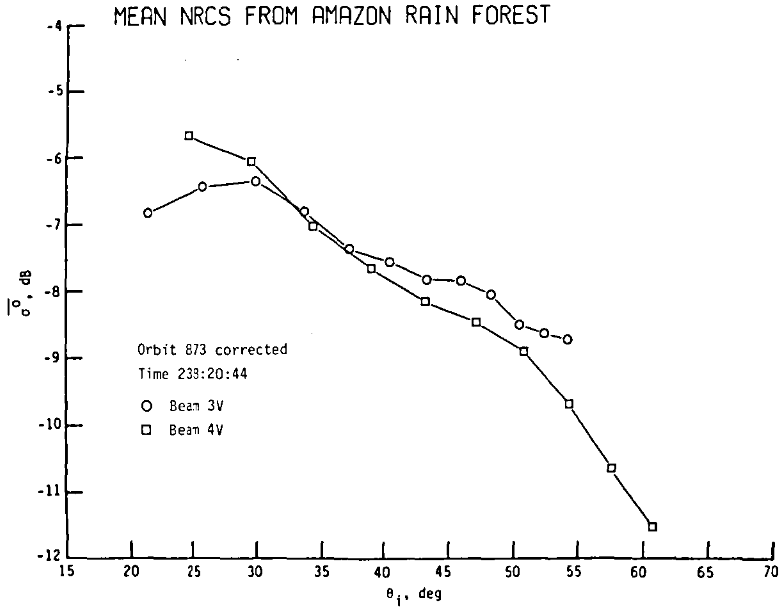
MEAN NRCS FROM AMAZON RAIN FOREST

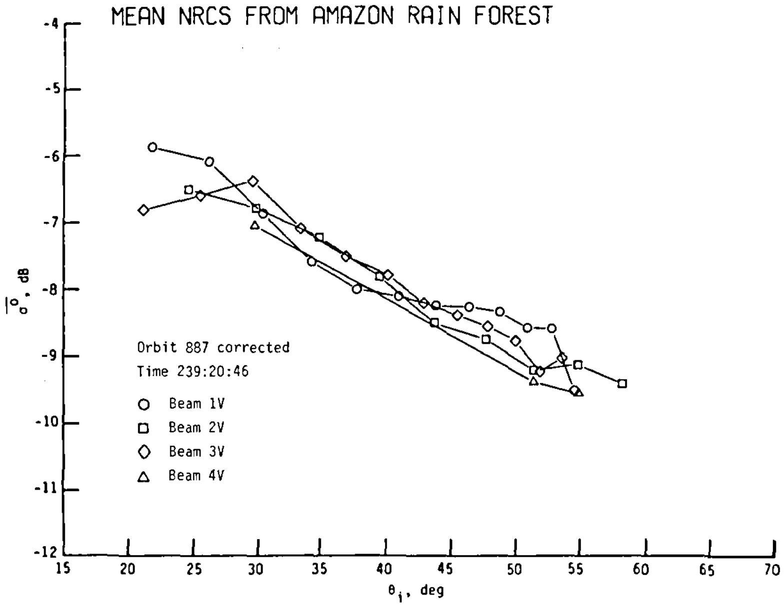
MEAN NRCS FROM AMAZON RAIN FOREST

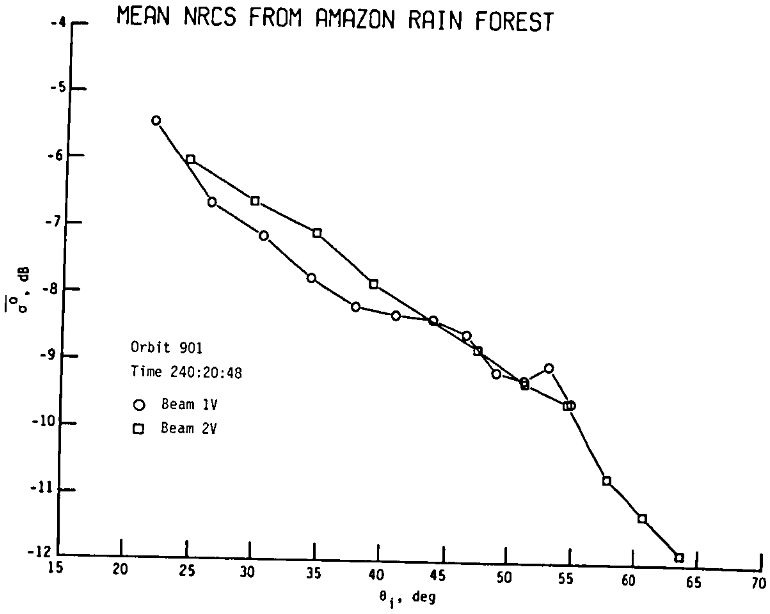
MEAN NRCS FROM AMAZON RAIN FOREST
$\overline{\sigma}^o$, dB
-4
-5
-6
-7
-8
-9
-10
-11
-12
15
20
25
30
35
40
45
50
55
60
65
70
θ_i, deg
Orbit 901
Time 240:20:48
○ Beam 1V
□ Beam 2V

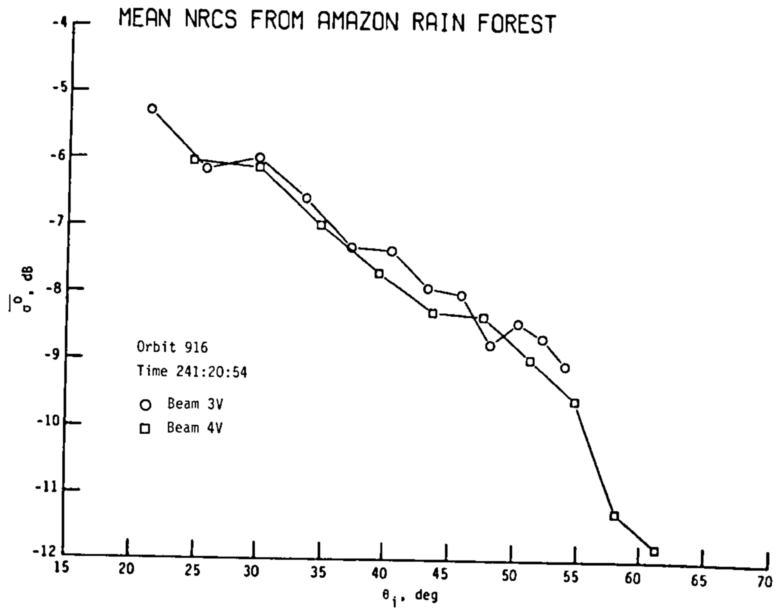
MEAN NRCS FROM AMAZON RAIN FOREST
$\overline{\sigma}^o$, dB
-4
-5
-6
-7
-8
-9
-10
-11
-12
15
20
25
30
35
40
45
50
55
60
65
70
θ_i, deg
Orbit 916
Time 241:20:54
○ Beam 3V
□ Beam 4V

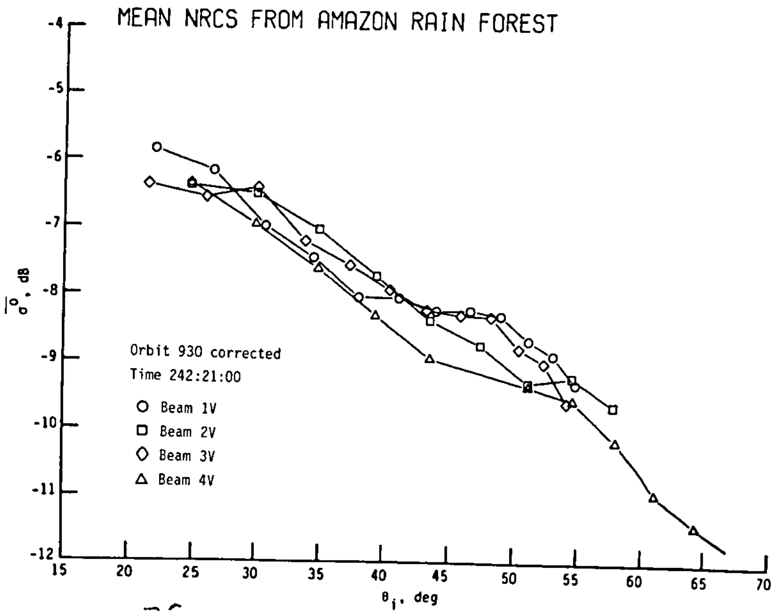
MEAN NRCS FROM AMAZON RAIN FOREST
$\overline{\sigma}^o$, dB
-4
-5
-6
-7
-8
-9
-10
-11
-12
15
20
25
30
35
40
45
50
55
60
65
70
θ_i, deg
Orbit 930 corrected
Time 242:21:00
○ Beam 1V
□ Beam 2V
◇ Beam 3V
△ Beam 4V

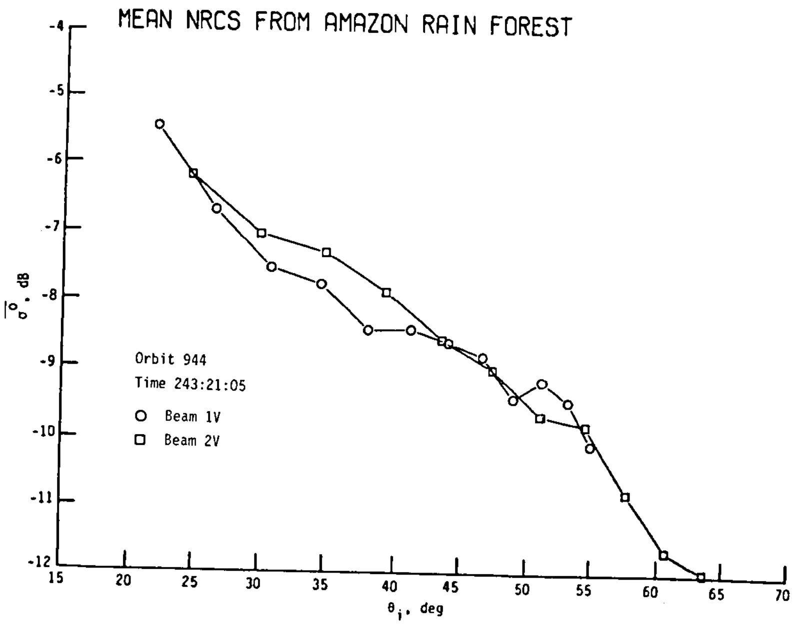
MEAN NRCS FROM AMAZON RAIN FOREST
$\overline{\sigma}^o$, dB
-4
-5
-6
-7
-8
-9
-10
-11
-12
15
20
25
30
35
40
45
50
55
60
65
70
θ_i, deg
Orbit 944
Time 243:21:05
○ Beam 1V
□ Beam 2V

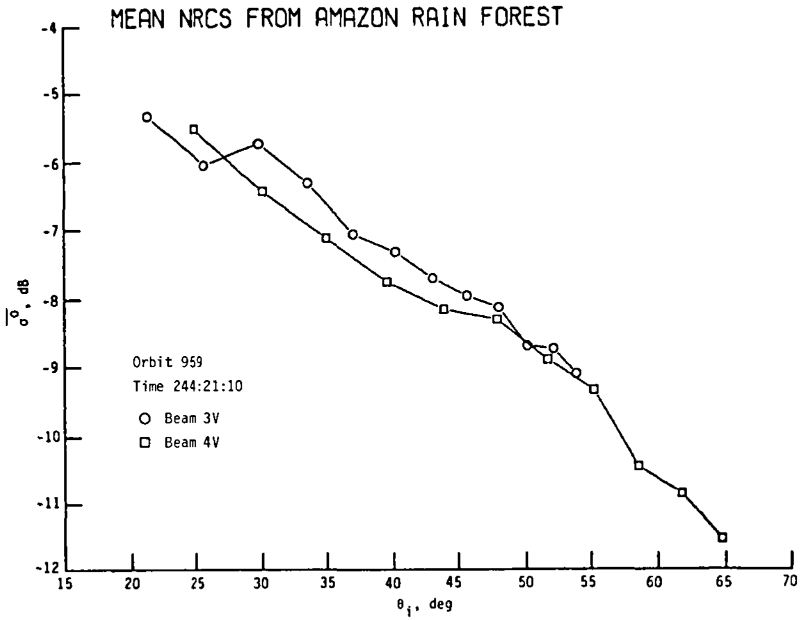
MEAN NRCS FROM AMAZON RAIN FOREST

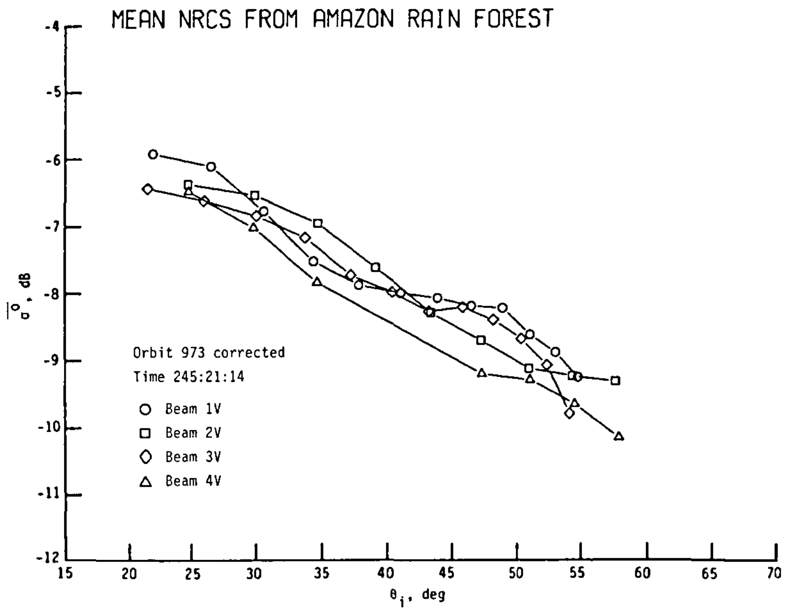
MEAN NRCS FROM AMAZON RAIN FOREST

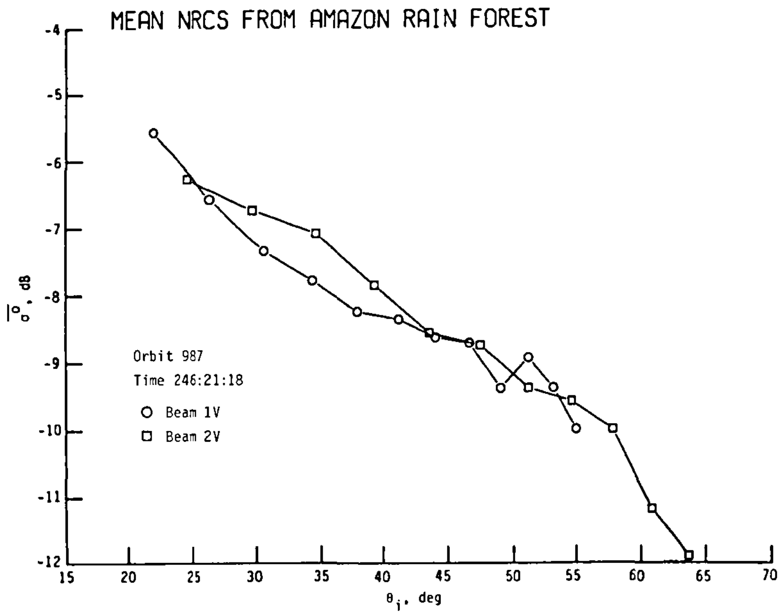
MEAN NRCS FROM AMAZON RAIN FOREST

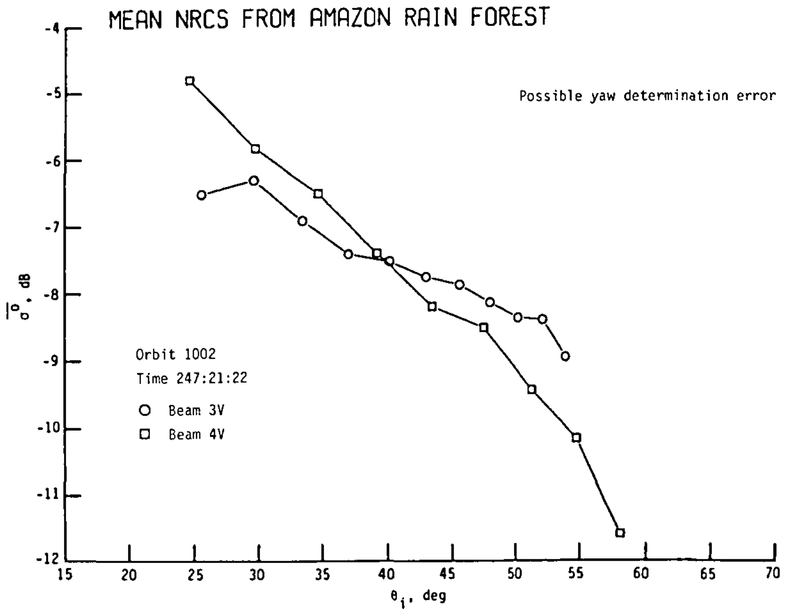
MEAN NRCS FROM AMAZON RAIN FOREST

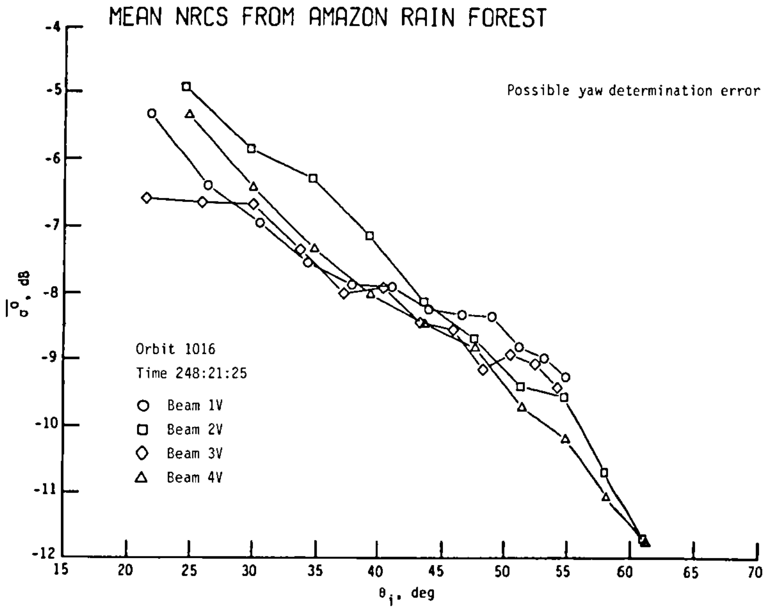
MEAN NRCS FROM AMAZON RAIN FOREST
Possible yaw determination error
-4
-5
-6
-7
-8
-9
-10
-11
-12
$\overline{\sigma}_o$, dB
15
20
25
30
35
40
45
50
55
60
65
70
θ_i, deg
Orbit 1016
Time 248:21:25
○ Beam 1V
□ Beam 2V
◇ Beam 3V
△ Beam 4V

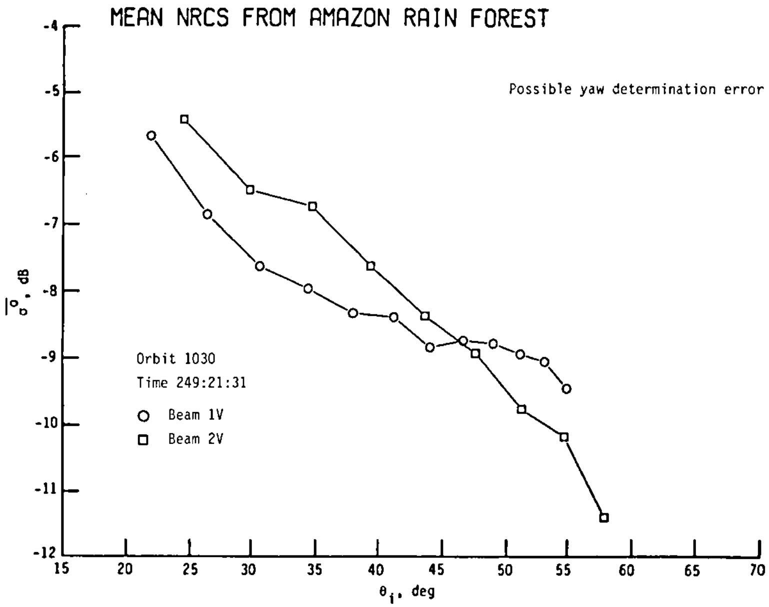
MEAN NRCS FROM AMAZON RAIN FOREST
Possible yaw determination error
-4
-5
-6
-7
-8
-9
-10
-11
-12
$\overline{\sigma}_o$, dB
15
20
25
30
35
40
45
50
55
60
65
70
θ_i, deg
Orbit 1030
Time 249:21:31
○ Beam 1V
□ Beam 2V

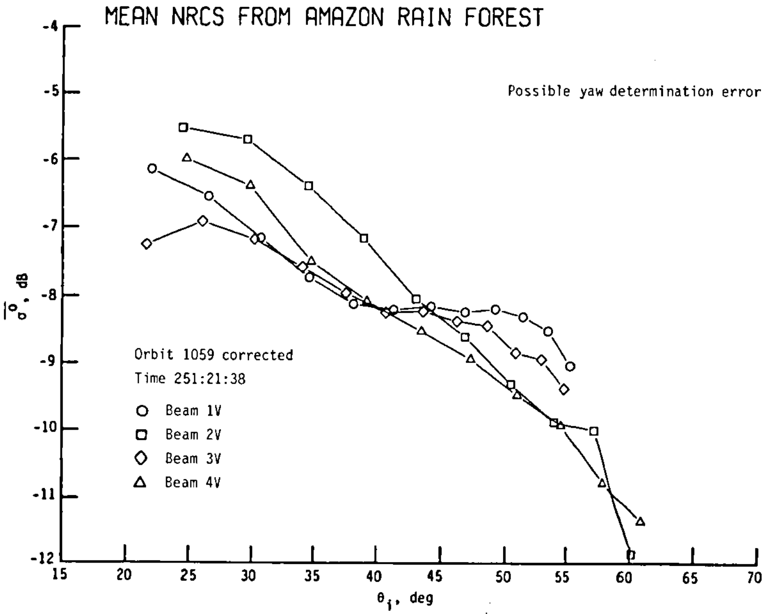
MEAN NRCS FROM AMAZON RAIN FOREST
Possible yaw determination error
-4
-5
-6
-7
-8
-9
-10
-11
-12
$\overline{\sigma}_o$, dB
15
20
25
30
35
40
45
50
55
60
65
70
θ_i, deg
Orbit 1059 corrected
Time 251:21:38
○ Beam 1V
□ Beam 2V
◇ Beam 3V
△ Beam 4V

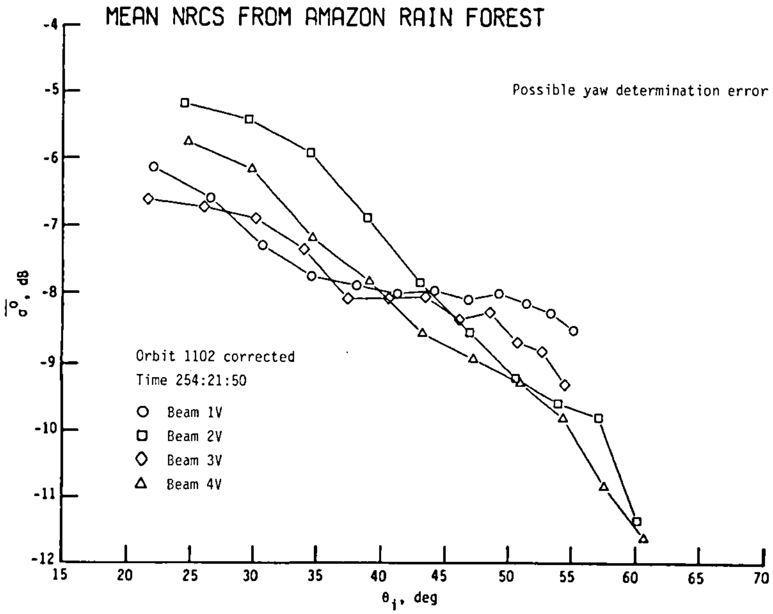
MEAN NRCS FROM AMAZON RAIN FOREST
Possible yaw determination error
-4
-5
-6
-7
-8
-9
-10
-11
-12
$\overline{\sigma}_o$, dB
15
20
25
30
35
40
45
50
55
60
65
70
θ_i, deg
Orbit 1102 corrected
Time 254:21:50
○ Beam 1V
□ Beam 2V
◇ Beam 3V
△ Beam 4V

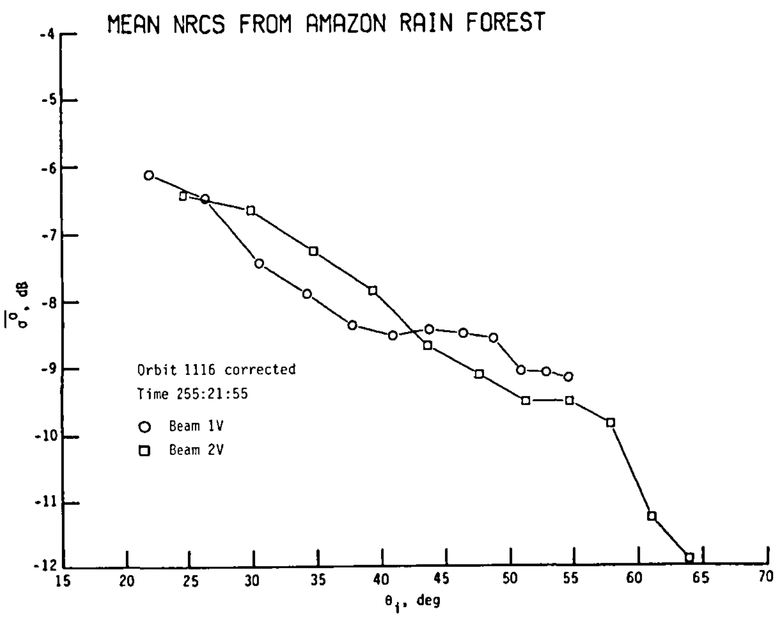

MEAN NRCS FROM AMAZON RAIN FOREST

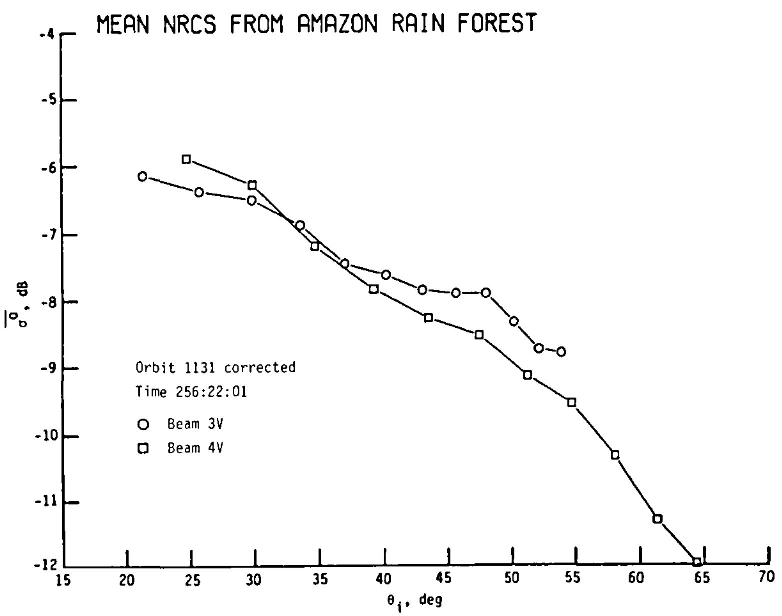

MEAN NRCS FROM AMAZON RAIN FOREST

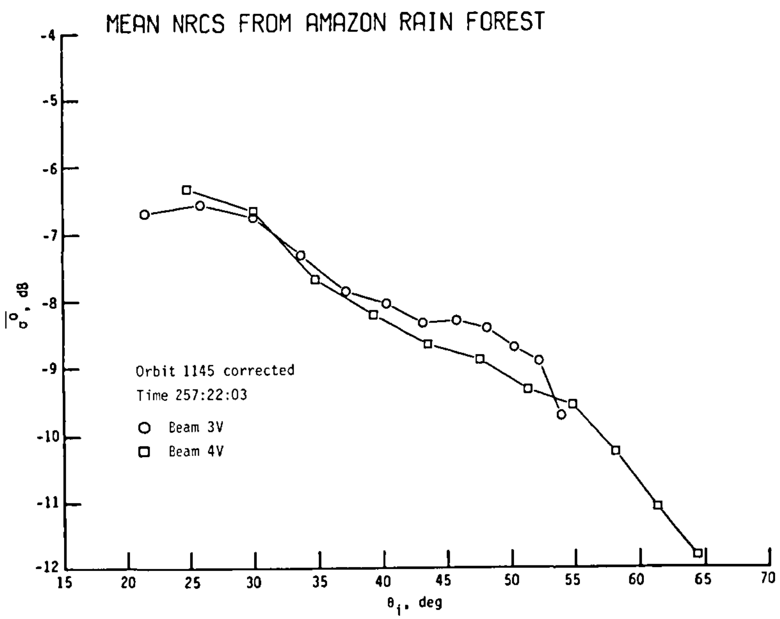

MEAN NRCS FROM AMAZON RAIN FOREST

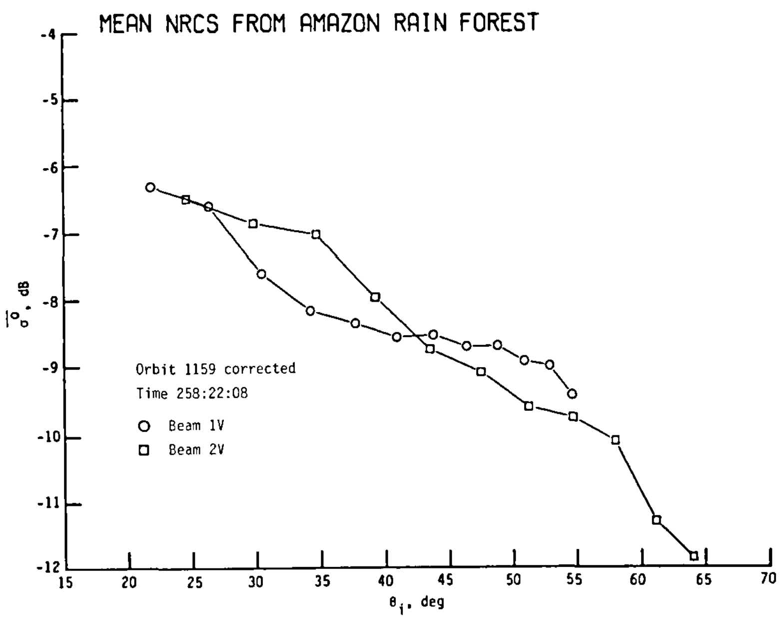

MEAN NRCS FROM AMAZON RAIN FOREST

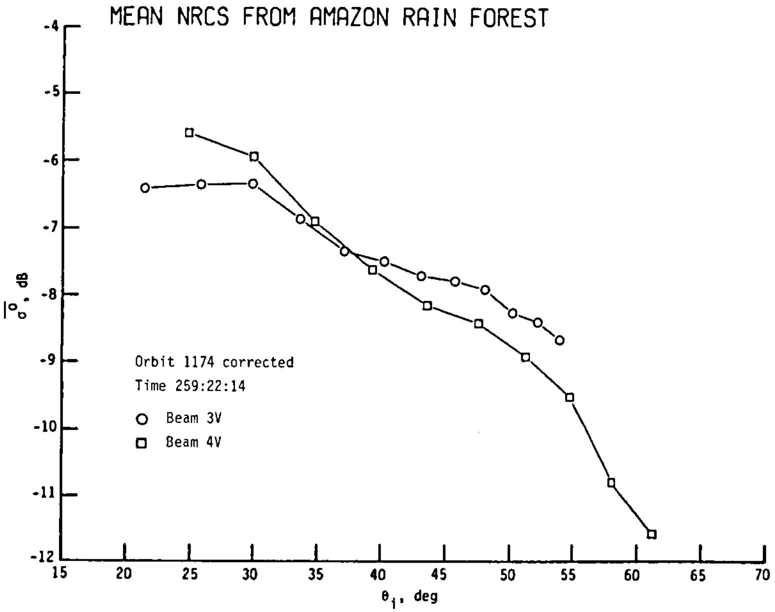
MEAN NRCS FROM AMAZON RAIN FOREST
$\overline{\sigma}^{o}$, dB
-4
-5
-6
-7
-8
-9
-10
-11
-12
15
20
25
30
35
40
45
50
55
60
65
70
θ_i, deg
Orbit 1174 corrected
Time 259:22:14
○ Beam 3V
□ Beam 4V

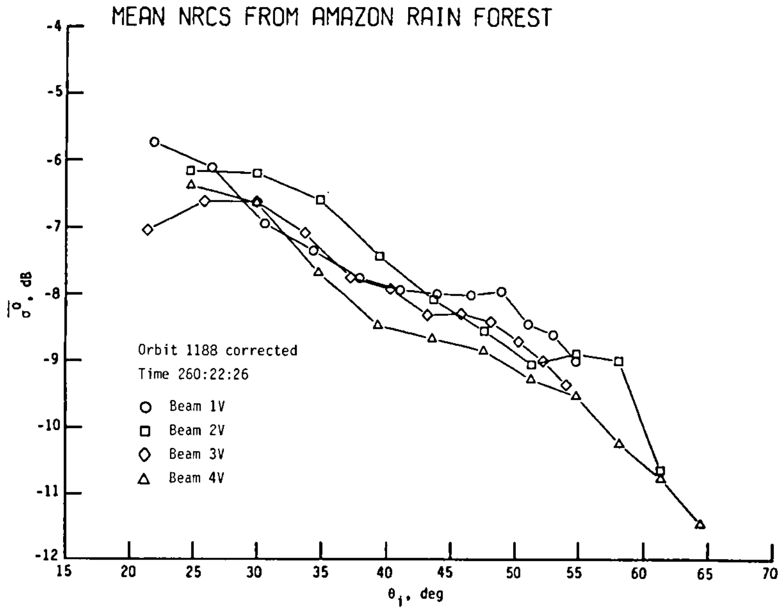
MEAN NRCS FROM AMAZON RAIN FOREST
$\overline{\sigma}^{o}$, dB
-4
-5
-6
-7
-8
-9
-10
-11
-12
15
20
25
30
35
40
45
50
55
60
65
70
θ_i, deg
Orbit 1188 corrected
Time 260:22:26
○ Beam 1V
□ Beam 2V
◇ Beam 3V
△ Beam 4V

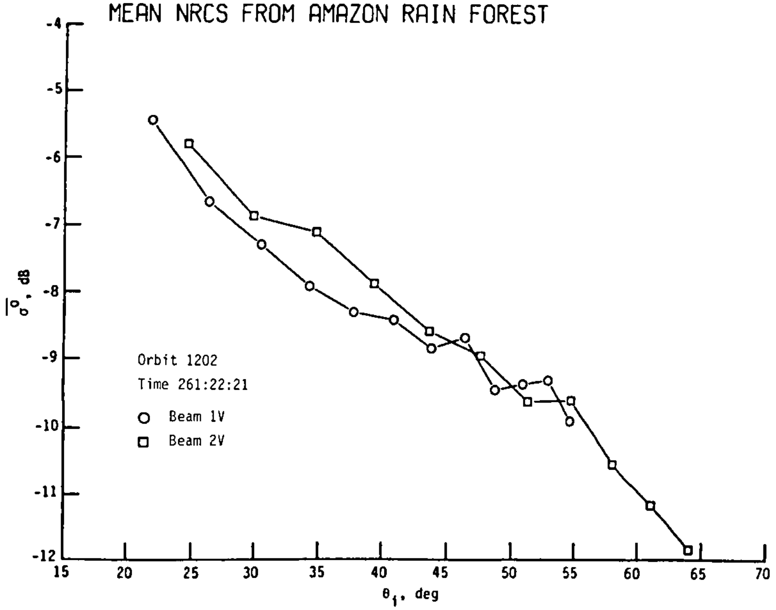
MEAN NRCS FROM AMAZON RAIN FOREST
$\overline{\sigma}^{o}$, dB
-4
-5
-6
-7
-8
-9
-10
-11
-12
15
20
25
30
35
40
45
50
55
60
65
70
θ_i, deg
Orbit 1202
Time 261:22:21
○ Beam 1V
□ Beam 2V

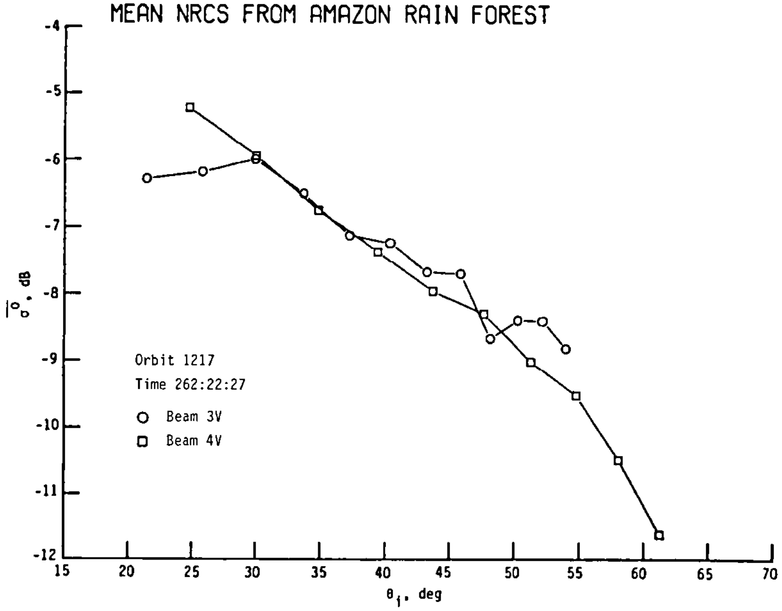
MEAN NRCS FROM AMAZON RAIN FOREST
$\overline{\sigma}^{o}$, dB
-4
-5
-6
-7
-8
-9
-10
-11
-12
15
20
25
30
35
40
45
50
55
60
65
70
θ_i, deg
Orbit 1217
Time 262:22:27
○ Beam 3V
□ Beam 4V

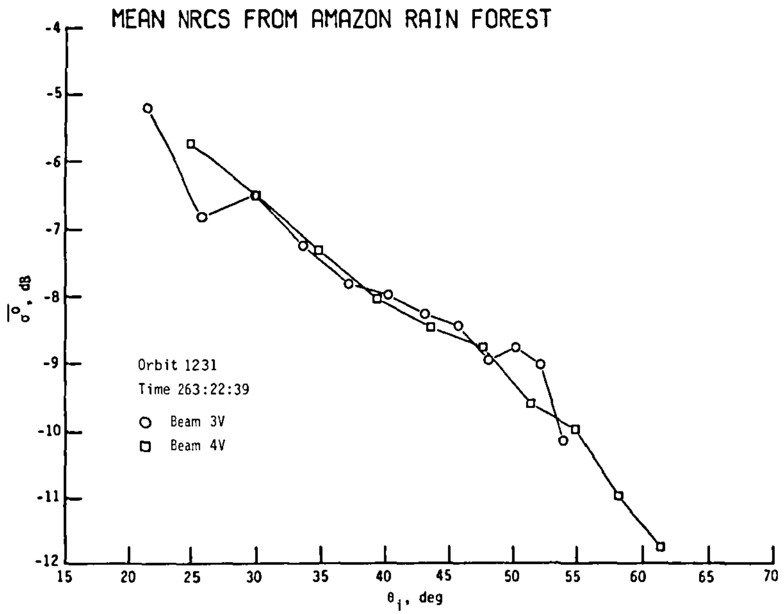
MEAN NRCS FROM AMAZON RAIN FOREST
$\overline{\sigma}_o$, dB
-4
-5
-6
-7
-8
-9
-10
-11
-12
15
20
25
30
35
40
45
50
55
60
65
70
θ_i, deg
Orbit 1231
Time 263:22:39
○ Beam 3V
□ Beam 4V

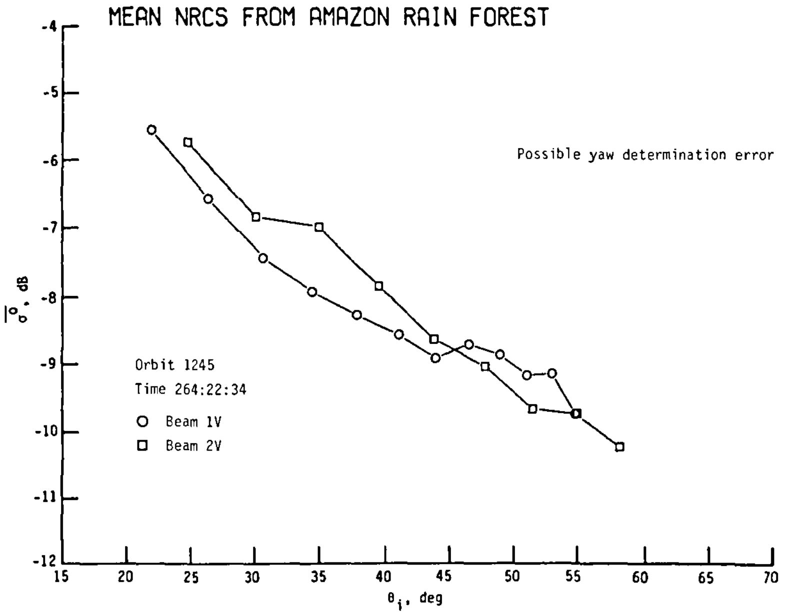
MEAN NRCS FROM AMAZON RAIN FOREST
Possible yaw determination error
$\overline{\sigma}_o$, dB
-4
-5
-6
-7
-8
-9
-10
-11
-12
15
20
25
30
35
40
45
50
55
60
65
70
θ_i, deg
Orbit 1245
Time 264:22:34
○ Beam 1V
□ Beam 2V

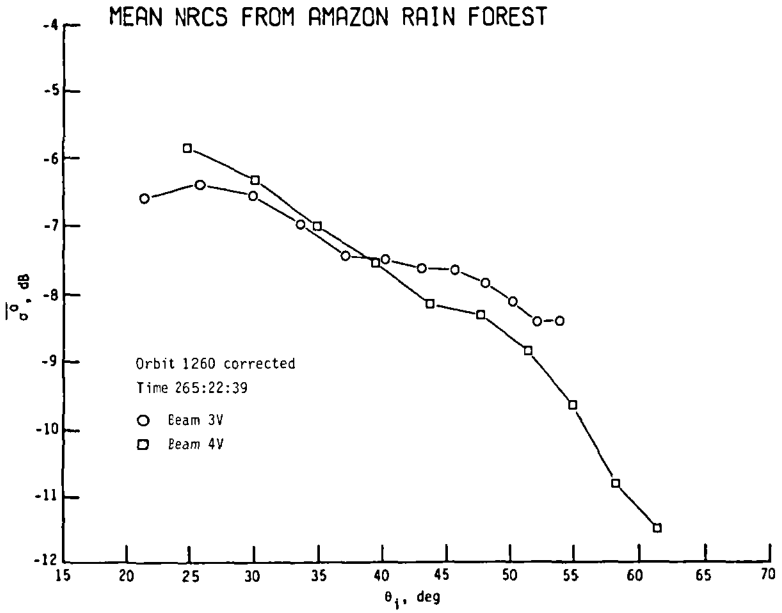
MEAN NRCS FROM AMAZON RAIN FOREST
$\overline{\sigma}_o$, dB
-4
-5
-6
-7
-8
-9
-10
-11
-12
15
20
25
30
35
40
45
50
55
60
65
70
θ_i, deg
Orbit 1260 corrected
Time 265:22:39
○ Beam 3V
□ Beam 4V

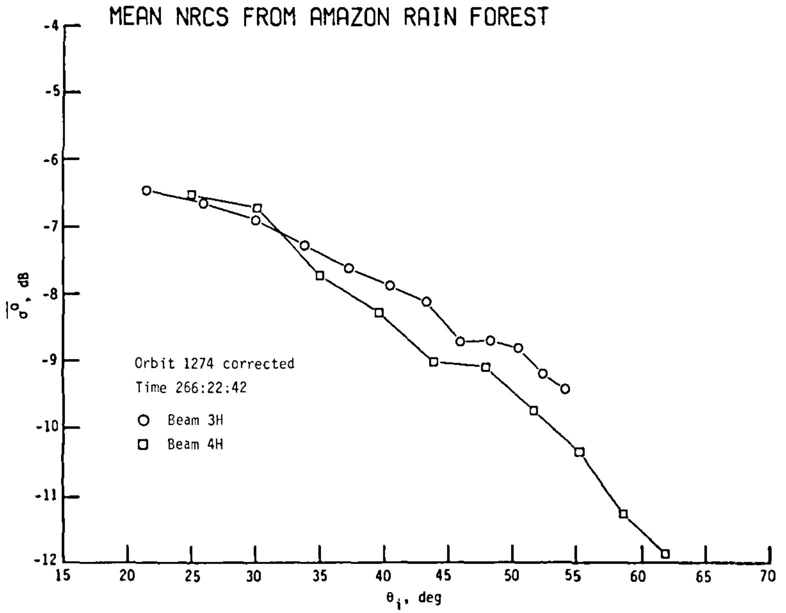
MEAN NRCS FROM AMAZON RAIN FOREST
$\overline{\sigma}_o$, dB
-4
-5
-6
-7
-8
-9
-10
-11
-12
15
20
25
30
35
40
45
50
55
60
65
70
θ_i, deg
Orbit 1274 corrected
Time 266:22:42
○ Beam 3H
□ Beam 4H

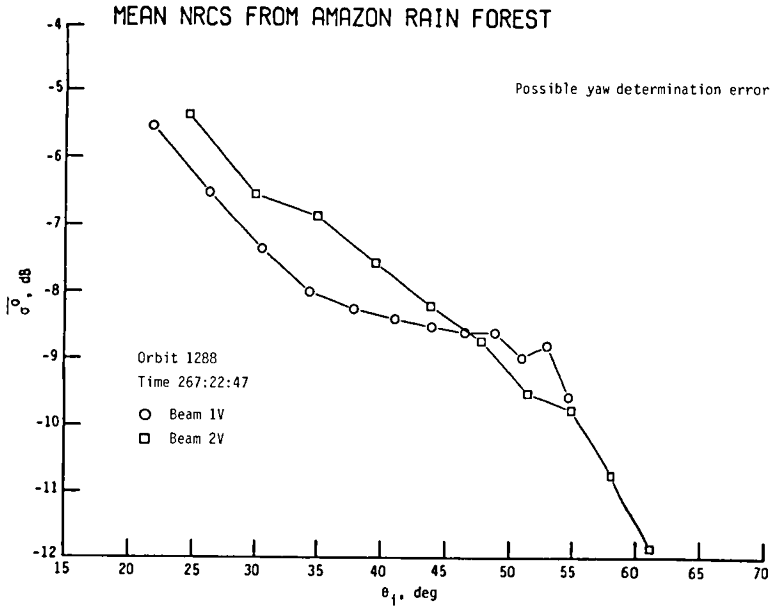

MEAN NRCS FROM AMAZON RAIN FOREST

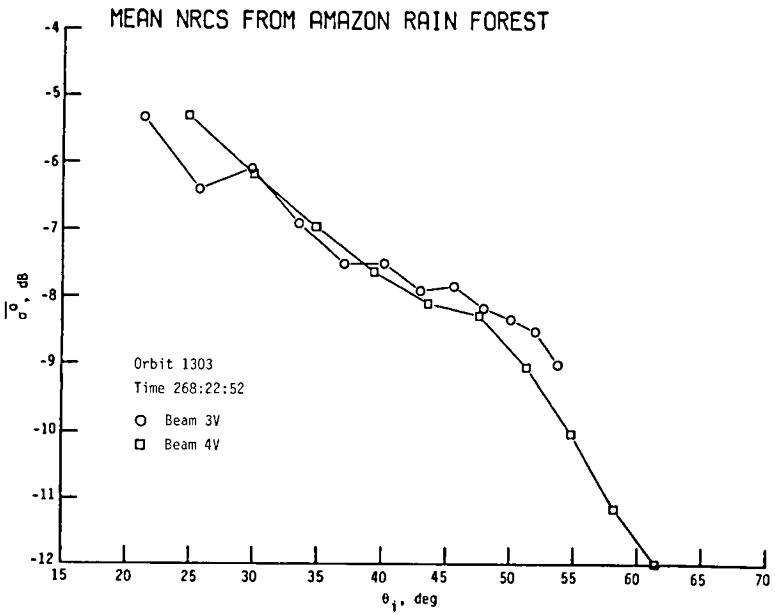

MEAN NRCS FROM AMAZON RAIN FOREST

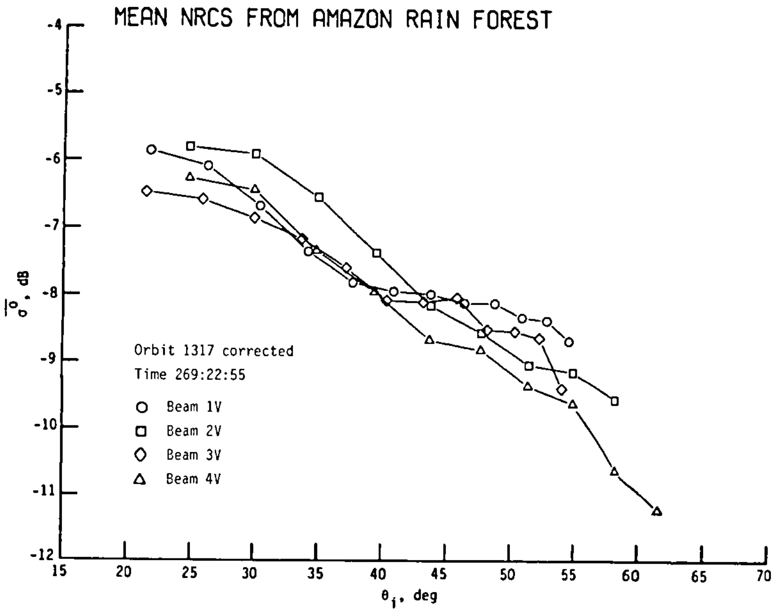

MEAN NRCS FROM AMAZON RAIN FOREST

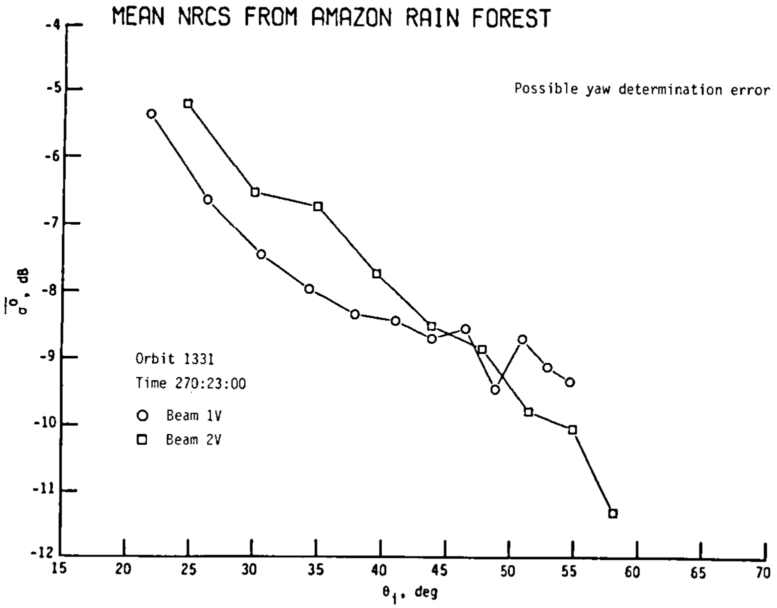

MEAN NRCS FROM AMAZON RAIN FOREST

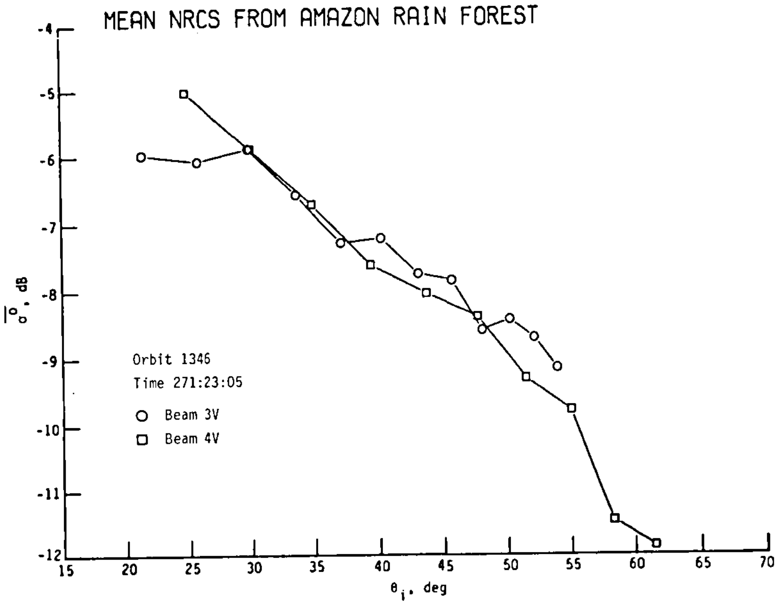
MEAN NRCS FROM AMAZON RAIN FOREST
$\overline{\sigma_o}$, dB
-4
-5
-6
-7
-8
-9
-10
-11
-12
15
20
25
30
35
40
45
50
55
60
65
70
θ_i, deg
Orbit 1346
Time 271:23:05
○ Beam 3V
□ Beam 4V

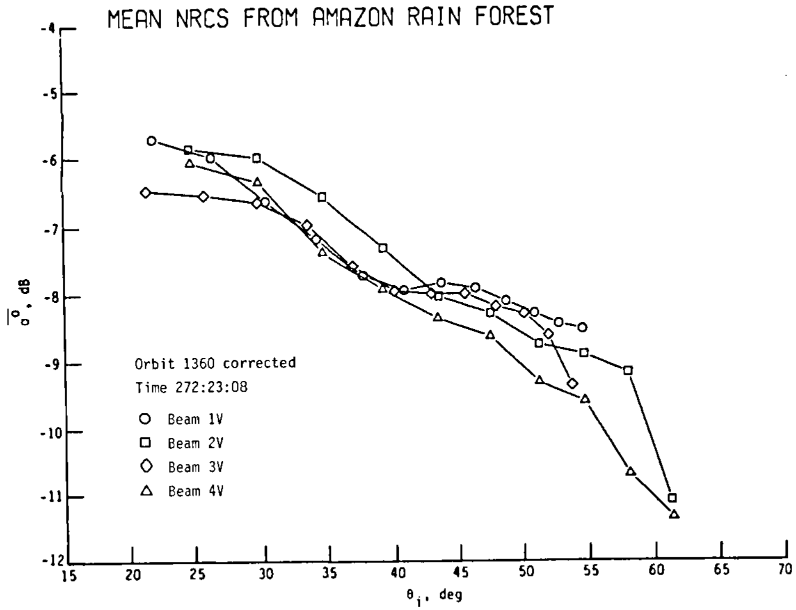
MEAN NRCS FROM AMAZON RAIN FOREST
$\overline{\sigma_o}$, dB
-4
-5
-6
-7
-8
-9
-10
-11
-12
15
20
25
30
35
40
45
50
55
60
65
70
θ_i, deg
Orbit 1360 corrected
Time 272:23:08
○ Beam 1V
□ Beam 2V
◇ Beam 3V
△ Beam 4V

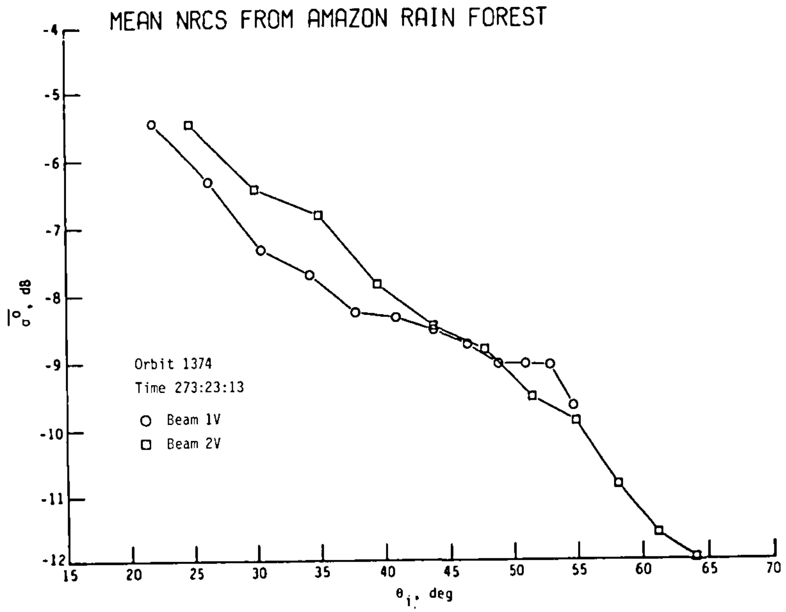
MEAN NRCS FROM AMAZON RAIN FOREST
$\overline{\sigma_o}$, dB
-4
-5
-6
-7
-8
-9
-10
-11
-12
15
20
25
30
35
40
45
50
55
60
65
70
θ_i, deg
Orbit 1374
Time 273:23:13
○ Beam 1V
□ Beam 2V

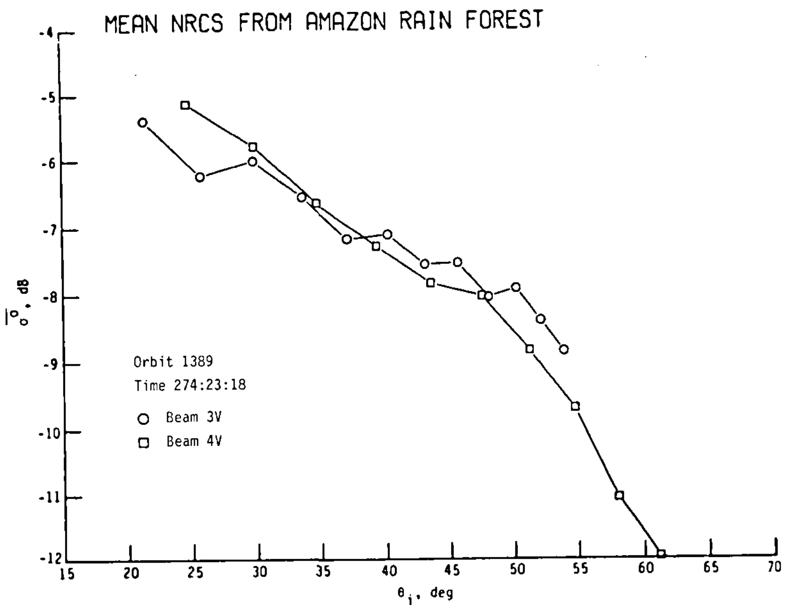
MEAN NRCS FROM AMAZON RAIN FOREST
$\overline{\sigma_o}$, dB
-4
-5
-6
-7
-8
-9
-10
-11
-12
15
20
25
30
35
40
45
50
55
60
65
70
θ_i, deg
Orbit 1389
Time 274:23:18
○ Beam 3V
□ Beam 4V

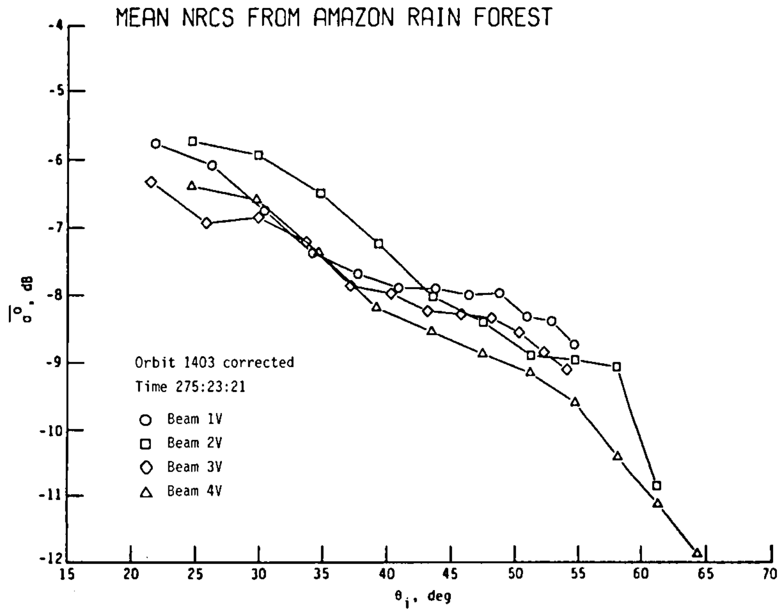
MEAN NRCS FROM AMAZON RAIN FOREST
Orbit 1403 corrected
Time 275:23:21
○ Beam 1V
□ Beam 2V
◇ Beam 3V
△ Beam 4V
$\overline{\sigma}^o$, dB
-4
-5
-6
-7
-8
-9
-10
-11
-12
15
20
25
30
35
40
45
50
55
60
65
70
θ_i, deg

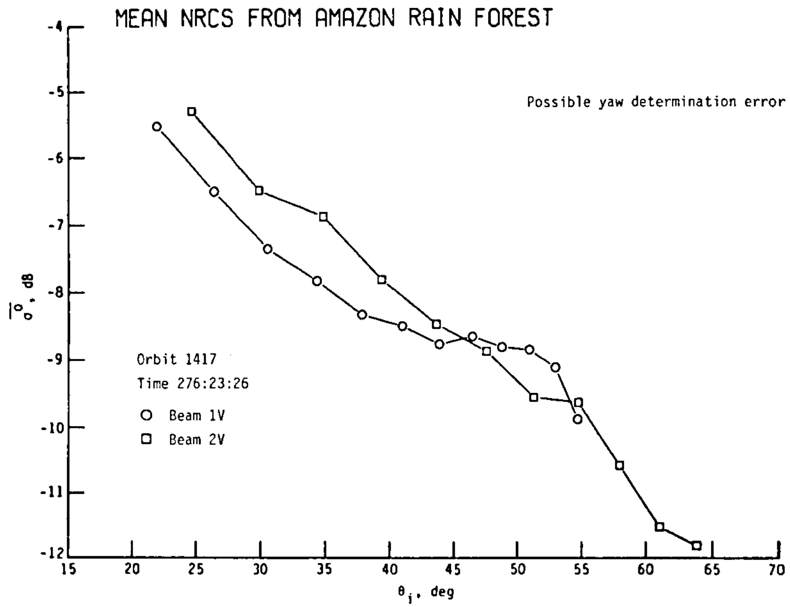
MEAN NRCS FROM AMAZON RAIN FOREST
Possible yaw determination error
Orbit 1417
Time 276:23:26
○ Beam 1V
□ Beam 2V
$\overline{\sigma}^o$, dB
-4
-5
-6
-7
-8
-9
-10
-11
-12
15
20
25
30
35
40
45
50
55
60
65
70
θ_i, deg

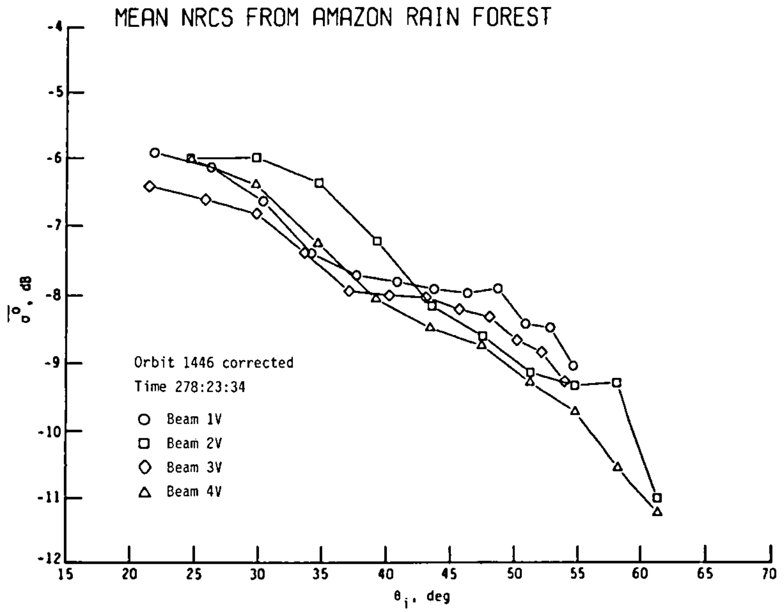
MEAN NRCS FROM AMAZON RAIN FOREST
Orbit 1446 corrected
Time 278:23:34
○ Beam 1V
□ Beam 2V
◇ Beam 3V
△ Beam 4V
$\overline{\sigma}^o$, dB
-4
-5
-6
-7
-8
-9
-10
-11
-12
15
20
25
30
35
40
45
50
55
60
65
70
θ_i, deg

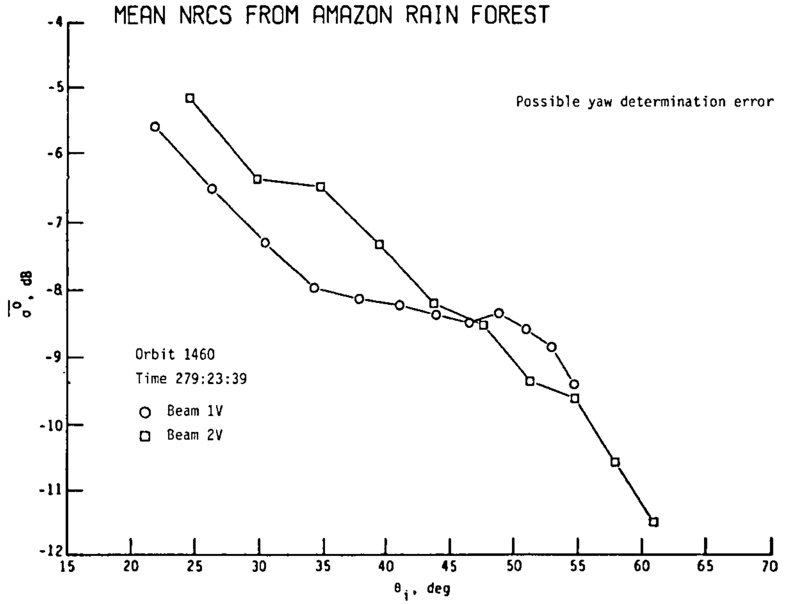
MEAN NRCS FROM AMAZON RAIN FOREST
Possible yaw determination error
Orbit 1460
Time 279:23:39
○ Beam 1V
□ Beam 2V
$\overline{\sigma}^o$, dB
-4
-5
-6
-7
-8
-9
-10
-11
-12
15
20
25
30
35
40
45
50
55
60
65
70
θ_i, deg

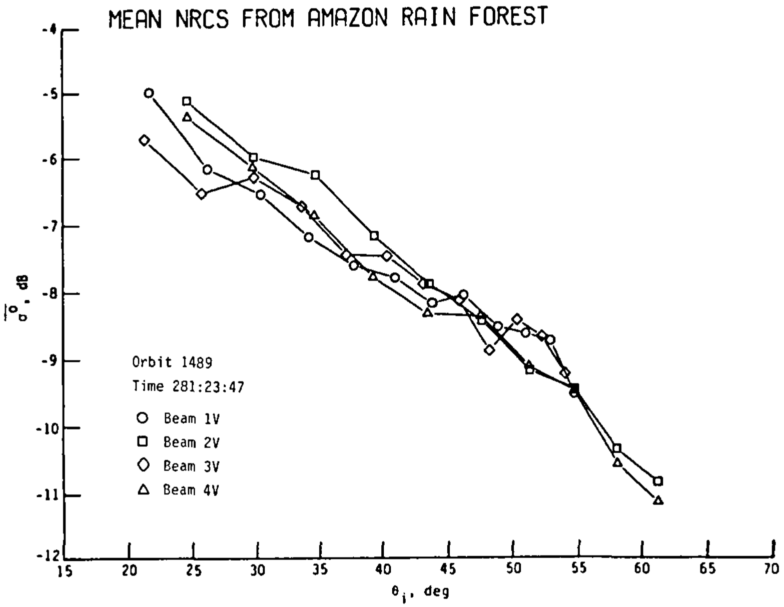
MEAN NRCS FROM AMAZON RAIN FOREST
Orbit 1489
Time 281:23:47
○ Beam 1V
□ Beam 2V
◇ Beam 3V
△ Beam 4V
$\overline{\sigma}^{o}$, dB
-4
-5
-6
-7
-8
-9
-10
-11
-12
15
20
25
30
35
40
45
50
55
60
65
70
θ_i, deg

APPENDIX C

DESCRIPTION OF σ^o CORRECTION ALGORITHM

A brief description of the equations and procedures used for correcting σ^o, with the use of some elements of computer programming notation, is presented in this appendix. The procedure incorporates the calculation of the mean noise spectral density determined from summing across all channels as a means for determining a more accurate measurement of the channel noise power which is subtracted from the measured signal plus noise power. This improved noise power measurement also provides a means for correcting small instrument gain biases. After the channel noise power and the corrected instrument gain are determined, the correct signal power is determined by the same procedure used in the original JPL σ^o algorithm. The difference between the signal power originally calculated and the corrected version of the signal power is then subtracted from the original value of σ^o to get a corrected value of σ^o. This correction algorithm can be applied to the final σ^o data provided in the Geophysical Data Record (GDR) produced by the Jet Propulsion Laboratory.

Step I: Calculate mean system noise temperature:

The TEV values for channels 13, 14, and 15 are first multiplied by the ratio (TN+TGC)/(TN+TG) listed in table 9 to correct for the error in TG (range-gate period). The mean equivalent system noise temperature (TEVM) is calculated by averaging the individual channel system noise temperature (TEV) listed in the GDR:

$$\mathrm{TEVM} = \frac{1}{N} \sum_{I=1}^{N} \mathrm{TEV(I)} \tag{1}$$

where N is the number of channel TEV values used in the summation of equation (1), normally equal to 15. If TEV(I) < 1100 or TEV(I) > 1500, do not include this value in equation (1). TEVM is the mean system noise temperature.

Step II: Calculate correct noise power and instrument gain for each channel:

The corrected channel noise power and instrument gain are determined as follows:

$$\mathrm{NPC(I) = K{*}TEVM{*}BN(I)} \tag{2}$$

where

K	Boltzmann constant
BN(I)	channel noise bandwidth
NPC(I)	channel noise power, W
I	channel number, 1 to 15

$$\mathrm{NPCDB(I) = 10{*}log(NPC(I))\quad dB} \tag{3}$$

$$\mathrm{GDB(I) = NPCDB(I)-NPDB(I)\quad dB} \tag{4}$$

where NPDB(I) is the original noise power for each channel listed in GDR, and GDB(I) is the instrument gain bias error.

(If TEV(I) < 1100 or TEV(I) > 1500, set GDB(I) = 0.)

$$\mathrm{GSNCDB(I)} = \mathrm{GSNDB(I)} - \mathrm{GDB(I)}\ \ \mathrm{dB} \tag{5}$$

where GSNDB(I) is the channel instrument gain for the signal plus noise measurement listed in the GDR, and GSNCDB(I) is the corrected instrument gain for the signal plus noise measurement.

Step III: Calculate correct signal power and corrected value of σ^{o}:

With a similar set of equations as those used in the original JPL σ^{o} algorithm, the received signal power is calculated as follows:

$$\mathrm{VSN(I)} = \mathrm{VSPN(I)} - (\mathrm{TG} - \mathrm{TS})/\mathrm{TN} * \mathrm{VN(I)} \tag{6}$$

where

VSPN(I)	signal plus noise voltage measured during period TG and listed in GDR for each channel
VN(I)	noise voltage listed in GDR for each channel
TG,TN	range-gate period and noise integration period, respectively, as listed in table 6; note that for channels 13, 14, and 15, the corrected values of TG in table 9 are used
TS	signal integration period, 0.2928 sec
VSN(I)	signal plus noise voltage corresponding to TS

$$\mathrm{GSNC(I)} = 10{*}{*}\mathrm{GSNCDB(I)}/10 \tag{7}$$

$$\mathrm{PSN(I)} = \mathrm{VSN(I)}/(\mathrm{GSNC(I)} * \mathrm{GASR} * \mathrm{TS}) \tag{8}$$

where GASR is the antenna switching matrix gain listed in the GDR, and PSN(I) is the signal plus noise power in watts.

$$\mathrm{PRRC(I)} = \mathrm{PSN(I)} - \mathrm{NPC(I)} \tag{9}$$

where PRRC(I) is the corrected received power in watts.

$$\mathrm{PRRCDB(I)} = 10 * \log(\mathrm{PRRC(I)})\ \ \mathrm{dBW} \tag{10}$$

The difference in dB between the original value of received power (PRRDB(I)) and the correct value (PRRCDB(I)), is the error in σ^{o} in dB. This value is subtracted from the final value of σ^{o} (CSGZDB(I)) listed in GDR. That is,

$$\mathrm{SGZCDB(I)} = \mathrm{CSGZDB(I)} - (\mathrm{PRRDB(I)} - \mathrm{PRRCDB(I)}) \tag{11}$$

where SGZCDB(I) is the corrected value of σ^{o} in dB.

APPENDIX C

A new value of the total normalized standard deviation (TNSD) of the measurement of σ^{o} must be computed since the signal-to-noise ratio (PRRC/NPC) is different. The following equations are used for this computation:

FAC = (1+TG(I)/(N*TN))*TG(I)/TS (12)

where N is the number of channels used in the summation of equation (1).

KPC(I) = sqrt(1/(BN(I)*TS)*(1+2/SNRC(I)+1/(SNRC(I)**2)*FAC)) (13)

where SNRC(I) = PRRC(I)/NPC(I), and KPC(I) is the normalized standard deviation (NSD) caused by communication noise.

DELSIG = 5*(10**(DSIGZ(I)/10-10**(-DSIGZ(I)/10)) (14)

where DSIGZ(I) is the error on σ^{o} due to attitude uncertainty errors in dB.

TNSDC(I) = sqrt(KPC(I)**2+DELSIG**2+5.3E-4)*100 (15)

where 5.3E-4 is the square of the random instrument error and TNSDC(I) is the corrected total normalized standard deviation in percent.

Note that if PRRC(I) is negative in equation (9) then equations (10), (11), (13), and (15) cannot be calculated. The value of σ^{o} (CSGZDB(I)) is left unchanged and PRRCDB(I),KPC(I), and TNSDC(I) are set to default values.

REFERENCES

1. Schroeder, Lyle C.; Boggs, Dale H.; Dome, George; Halberstam, Isadore M.; Jones, W. Linwood; Pierson, Willard J.; and Wentz, Frank J.: The Relationship Between Wind Vector and Normalized Radar Cross Section Used To Derive SEASAT-A Satellite Scatterometer Winds. J. Geophys. Res., vol. 87, no. C5, Apr. 30, 1982, pp. 3318-3336.

2. Bracalente, Emedio M.; Boggs, Dale H.; Grantham, William L.; and Sweet, Jon L.: The SASS Scattering Coefficient σ^o Algorithm. IEEE J. Oceanic Eng., vol. OE-5, no. 2, Apr. 1980, pp. 145-154.

3. Birrer, I. J.; Dome, G. J.; Sweet, J.; Berthold, G.; and Moore, R. K.: Off-Nadir Antenna Bias Correction Using Amazon Rain Forest σ^o Data. NASA CR-165921, 1982.

4. Birrer, I. J.; Bracalente, E. M.; Dome, G. J.; Sweet, J.; and Berthold, G.: σ^o Signature of the Amazon Rain Forest Obtained From the Seasat Scatterometer. IEEE Trans. Geosci. & Remote Sens., vol. GE-20, no. 1, Jan. 1982, pp. 11-17.

5. Treder, Alfred J.: Seasat Final Report. Volume IV: Attitude Determination. Publ. 80-38, Vol. IV (Contract NAS7-100), Jet Propul. Lab., California Inst. Technol., 1980. (Available as NASA CR-163943.)

6. Ulaby, Fawwaz T.; Moore, Richard K.; and Fung, Adrian K.: Microwave Remote Sensing - Active and Passive. Volume II: Radar Remote Sensing and Surface Scattering and Emission Theory. Addison-Wesley Pub. Co., Inc. 1982, pp. 816-847.

TABLE 1.- CODES USED FOR VEGETATION MAP

Code	Description
0	Outside Brazilian rain forest
1	Humid upper Amazon
2	Humid firm land
3	Humid floodlands
4	Humid plains
5	Mountainous regions
6	Savannah
7	Combinations of 1, 4
8	Combinations of 2, 4
9	Combinations of 1, 2, 4
10	Combinations of 1, 2
11	Combinations of 2, 6
12	Combinations of 2, 4, 6
13	Combinations of 1, 2, 3, 6
14	Combinations of 1, 6
15	Combinations of 2, 3, 6
16	Combinations of 2, 3
17	Combinations of 1, 2, 3
18	Combinations of 1, 3
19	Combinations of 2, 5
20	Combinations of 2, 5, 6

TABLE 2.- SCATTEROMETER OPERATING MODE SEQUENCE

Mode	Antenna sequence (a)
1	4V, 1V, 3V, 2V
2	4H, 1H, 3H, 2H
3	4V, 4H, 3V, 3H
4	1V, 1H, 2V, 2H
5	4V, 4V, 3V, 3V
6	1V, 1V, 2V, 2V
7	4H, 4H, 3H, 3H
8	1H, 1H, 2H, 2H
9	Continuous calibration
10	Standby, transmitter off, receiver operating in mode 5

[a] V is vertical polarization; H is horizontal polarization.

TABLE 3.- ASCENDING ORBITS PROCESSED

Orbit	Beam/pol (a)	Longitude of equator crossing (node), deg	Local time, day:hour:min	Comments
162	1&2/V&H	289.0	189:05:12	
176	1&2/V&H	297.9	190:05:16	
205	1&2/V&H	290.5	192:05:26	
248	1,2,3&4/V	291.9	195:05:37	
291	1,2,3&4/V	293.3	198:05:50	
305	1,2,3&4/V	302.2	199:05:55	
334	1&2/VV	294.8	201:06:02	
377	1&2/VV	296.3	204:06:18	
406	1&2/H	288.8	206:06:24	
420	3&4/H	297.7	207:06:28	
434	3&4/VV	306.5	208:06:34	
449	3&4/HH	290.3	209:06:40	
463	3&4/HH	299.1	210:06:51	
492	1&2/V	291.8	212:06:50	
535	1,2,3&4/V	293.2	215:06:53	
549	3&4/V	302.0	216:07:05	
564	1&2/V	285.8	217:07:11	
578	1,2,3&4/V	294.6	218:07:15	
592	1,2,3&4/V	303.5	219:07:20	
607	1&2/V	287.2	220:07:23	Large yaw determination error
621	1,2,3&4/V	296.1	221:07:27	
635	3&4/V	304.9	222:07:30	
650	1&2/V	288.7	223:07:35	Large yaw angle
664	1,2,3&4/V	297.5	224:07:40	Large yaw angle
678	3&4/V	306.3	225:07:45	
693	1&2/V	290.1	226:07:50	
707	1,2,3&4/V	298.9	227:07:54	
721	3&4/V	307.9	228:07:56	
736	1,2,3&4/V	291.7	229:08:04	
750	1,2,3&4/V	300.7	230:08:04	
765	1&2/V	284.6	231:08:11	
779	1,2,3&4/V	293.6	232:08:20	
793	1,2,3&4/V	302.7	233:08:20	
808	1&2/V	286.7	234:08:24	
822	1,2,3&4/V	295.7	235:08:28	
836	3&4/V	304.7	236:08:30	
851	1&2/V	288.6	277:08:36	
865	1,2,3&4/V	297.4	238:08:40	
879	3&4/V	305.8	239:08:46	
894	1&2/V	289.1	240:08:50	
908	1,2,3&4/V	297.5	241:08:53	
922	3&4/V	305.9	242:08:55	
937	1&2/V	289.2	243:09:04	
951	1,2,3&4/V	297.6	244:09:06	
965	3&4/V	306.0	245:09:10	
980	1&2/V	289.3	246:09:15	
994	1,2,3&4/V	297.7	247:09:18	
1008	3&4/V	306.6	248:09:25	
1037	1,2,3&4/V	297.8	250:09:32	
1051	3&4/V	306.2	251:09:36	
1066	1&2/V	289.5	252:09:42	
1080	1,2,3&4/V	297.9	253:09:48	Small yaw determination error
1094	3&4/V	306.3	254:09:49	
1109	1&2/V	289.5	255:09:55	
1123	1,2,3&4/V	297.9	256:10:01	
1137	3&4/V	306.2	257:10:03	
1152	1&2/V	289.5	258:10:08	
1166	1,2,3&4/V	297.9	259:10:14	Small yaw determination error
1180	3&4/V	306.2	260:10:15	
1195	1&2/V	289.5	261:10:21	Small yaw determination error
1209	1,2,3&4/V	297.9	262:10:23	
1223	3&4/V	306.2	263:10:28	
1238	1&2/V	289.5	264:10:34	Small yaw determination error
1252	1,2,3&4/V	297.5	265:10:37	
1266	3&4/V	306.2	266:10:41	
1281	1&2/V	289.5	267:10:47	
1295	1,2,3&4/V	297.8	268:10:50	
1309	3&4/V	306.2	269:10:54	
1324	1&2/V	289.5	270:11:00	
1338	1,2,3&4/V	297.8	271:11:03	
1352	3&4/V	306.2	272:11:07	
1367	1&2/V	289.2	273:11:13	
1381	1,2,3&4/V	297.8	274:11:16	
1395	3&4/V	306.2	275:11:20	
1410	1&2/V	289.2	276:11:26	
1424	1,2,3&4/V	297.8	277:11:29	
1453	1&2/V	289.5	279:11:39	Repeated frames of data on beam 1
1481	3&4/V	306.2	281:11:46	
1496	1&2/V	289.5	282:11:52	

[a] V is vertical polarization; H is horizontal polarization; VV is vertical polarization one-side mode; HH is horizontal polarization one-side mode.

TABLE 4.- DESCENDING ORBITS PROCESSED

Orbit	Beam/pol (a)	Longitude of equator crossing (node), deg	Local time, day:hour:min	Comments
155	1&2/V&H	297.2	188:17:10	
212	1&2/V&H	307.4	192:17:27	
241	1&2/V&H	299.9	194:17:36	
284	1,2,3&4/V	301.5	197:17:48	
327	1&2/VV	302.9	200:18:01	
356	1&2/VV	295.5	202:18:10	
399	1,2,3&4/H	296.9	205:18:22	
413	1&2/H	305.8	206:18:25	
428	3&4/V&H	289.6	207:18:32	
442	3&4/VV	298.4	208:18:35	
485	1&2/HH	299.8	211:18:47	
499	1&2/V	308.7	212:18:50	
514	3&4/V	292.4	213:18:55	
528	1,2,3&4/V	301.3	214:19:00	
557	1,2,3&4/V	293.9	216:19:08	
571	1,2,3&4/V	302.8	217:19:13	
614	1,2,3&4/V	304.2	220:19:25	
643	1,2,3&4/V	296.8	222:19:35	
657	1&2/V	305.7	223:19:40	
686	1,2,3&4/V	298.3	225:19:48	
700	1&2/V	307.1	226:19:52	
715	3&4/V	290.9	227:19:55	
729	1,2,3&4/V	299.8	228:20:00	
758	3&4/V	292.7	230:20:10	
772	1,2,3&4/V	301.7	231:20:14	
801	1,2,3&4/V	294.7	233:20:13	
815	1&2/V	303.8	234:20:24	
830	3&4/V	287.7	235:20:30	Small yaw determination error
844	1,2,3&4/V	296.7	236:20:34	
858	1&2/V	305.6	237:20:38	
873	3&4/V	289.1	238:20:44	
887	1,2,3&4/V	297.5	239:20:46	
901	1&2/V	305.2	240:20:48	
916	3&4/V	289.0	241:20:54	
930	1,2,3&4/V	297.6	242:21:00	
944	1&2/V	306.0	243:21:05	
959	3&4/V	289.3	244:21:10	
973	1,2,3&4/V	297.7	245:21:14	
987	1&2/V	306.1	246:21:18	
1002	3&4/V	289.4	247:21:22	Yaw determination error
1016	1,2,3&4/V	297.8	248:21:26	Yaw determination error
1030	1&2/V	306.2	249:21:31	Yaw determination error
1059	1,2,3&4/V	297.9	251:21:38	Yaw determination error
1102	1,2,3&4/V	297.9	254:21:50	Yaw determination error
1116	1&2/V	306.3	255:21:55	
1131	3&4/V	289.6	256:22:01	
1145	3&4/VV	297.9	257:22:03	
1159	1&2/V	306.3	258:22:08	
1174	3&4/V	289.6	259:22:14	
1188	1,2,3&4/V	297.9	260:22:26	
1202	1&2/V	306.3	261:22:21	
1217	3&4/V	289.6	262:22:27	
1231	3&4/VV	297.9	263:22:39	
1245	1&2/V	306.3	264:22:34	Yaw determination error
1260	3&4/VV	289.6	265:22:39	
1274	3&4/HH	297.9	266:22:42	
1288	1&2/V	306.3	267:22:47	Yaw determination error
1303	3&4/V	289.6	268:22:52	
1317	1,2,3&4/V	297.9	269:22:55	
1331	1&2/V	306.3	270:23:00	Yaw determination error
1346	3&4/V	289.6	271:23:05	
1360	1,2,3&4/V	297.9	272:23:08	
1374	1&2/V	306.3	273:23:13	Yaw determination error
1389	3&4/V	289.6	274:23:18	
1403	1,2,3&4/V	297.9	275:23:21	
1417	1&2/V	306.3	276:23:26	Yaw determination error
1446	1,2,3&4/V	297.9	278:23:34	
1460	1&2/V	306.3	279:23:39	Yaw determination error
1489	1,2,3&4/V	297.9	281:23:47	

[a] V is vertical polarization; H is horizontal polarization; VV is vertical polarization one-side mode; HH is horizontal polarization one-side mode.

TABLE 5.- σ° ERROR SENSITIVITY TO YAW DETERMINATION ERROR

Incidence angle, deg	σ° error sensitivity, dB/(deg yaw angle), for -			
	Beams 1 and 3		Beams 2 and 4	
	Ascending orbit	Descending orbit	Ascending orbit	Descending orbit
20	0.91	0.62	-0.62	-0.91
25	.84	.64	-.64	-.84
30	.77	.59	-.59	-.77
35	.63	.50	-.50	-.63
40	.44	.33	-.33	-.44
45	.10	.12	-.12	.10
50	-.18	-.13	.13	.18
55	-.62	-.45	.45	.62
60	-1.12	-.81	.81	1.12
65	-1.72			1.72

TABLE 6.- CHANNEL NOISE BANDWIDTH, INTEGRATION PERIODS, AND NSD FOR EACH INTEGRATION PERIOD

Channel	Bandwidth B_N, Hz	Noise integration period, T_N, sec	NSD, $\frac{100}{\sqrt{B_N T_N}}$, percent	Signal + noise integration period (range gate), T_G, sec	NSD, $\frac{100}{\sqrt{B_N T_G}}$, percent
1	27 373	0.48175	0.87	0.37752	0.98
2	24 490		.92	.38962	1.02
3	21 389		.99	.40484	1.07
4	19 043		1.04	.42280	1.11
5	15 368		1.16	.44662	1.21
6	12 588		1.28	.47551	1.29
7	9 992		1.44	.51103	1.40
8	8 247		1.59	.55632	1.48
9	6 493		1.79	.61254	1.59
10	5 317		1.98	.68827	1.65
11	4 478		2.15	.69023	1.80
12	3 869		2.32	.68125	1.95
13	27 904		.86	.35175	1.02
14	27 896		.86	.34746	1.04
15	27 759		.86	.34511	1.04
1 to 12			0.36		0.37
1 to 15			.29		.32

TABLE 7.- STATISTICS OF MEASURED NOISE POWER DURING ONE SEQUENCE OF 124 SCIENCE FRAMES OVER WATER FOR ORBIT 986

[Standby mode; approximate time period, -15 sec to 4 min past ascending node]

Cell	Number of samples	PSN		SNKT[a] mean, dBW	NP		NKT[b] mean, dBW	DPN, dB		DG, dB				RR		TEV[c], K		TA[d] mean, K
		Mean, dBW	NSD, %		Mean, dBW	NSD, %		Mean	SD	Mean	SD	Min	Max	Mean	SD	Mean	SD	
Beam 3V																		
1	62	-153.205	0.72	-197.578	-153.187	0.89	-197.560	0.018	0.05	-0.069	0.04	-0.178	0.050	1.004	0.01	1270.31	11.34	205.72
2	62	-153.733	.84	-197.623	-153.715	.84	-197.605	.018	.05	-.024	.04	-.117	.066	1.004	.01	1257.27	10.53	192.68
3	62	-154.295	1.22	-197.597	-154.283	1.07	-197.585	.012	.07	-.044	.05	-.158	.049	1.003	.01	1263.17	13.52	198.58
4	62	-154.865	1.01	-197.662	-154.848	.80	-197.645	.017	.06	.016	.04	-.057	.130	1.004	.01	1245.68	9.94	181.08
5	62	-155.751	1.06	-197.617	-155.759	1.13	-197.625	-.008	.07	-.004	.05	-.100	.101	.998	.02	1251.41	14.18	186.82
6	62	-156.593	1.19	-197.592	-156.588	1.07	-197.587	.005	.06	-.042	.04	-.140	.039	1.001	.01	1262.39	13.52	197.79
7	62	-157.674	1.47	-197.671	-157.664	1.27	-197.661	.010	.08	.032	.06	-.100	.222	1.003	.02	1241.17	15.79	176.58
8	62	-158.485	1.22	-197.648	-158.475	1.51	-197.638	.010	.08	.009	.06	-.114	.178	1.003	.02	1247.86	18.78	183.26
9	62	-159.562	1.71	-197.686	-159.543	1.74	-197.668	.018	.09	.039	.07	-.095	.183	1.004	.02	1239.23	21.52	174.63
10	62	-160.437	1.58	-197.694	-160.478	1.96	-197.735	-.041	.10	.106	.09	-.060	.266	.991	.02	1220.29	23.94	155.69
11	62	-161.174	1.73	-197.685	-161.159	2.09	-197.670	.015	.13	.041	.09	-.183	.259	1.004	.03	1238.69	25.94	174.10
12	62	-161.757	2.03	-197.633	-161.778	2.08	-197.654	-.020	.13	.025	.09	-.194	.297	.996	.03	1243.29	25.87	178.70
13	62	-153.249	1.02	-197.705	-153.146	.77	-197.603	.103	.05	-.026	.04	-.124	.072	1.024	.01	1257.87	9.74	193.27
14	62	-153.181	.79	-197.637	-153.068	.83	-197.524	.113	.05	-.106	.04	-.181	.012	1.025	.01	1281.03	10.64	216.44
15	62	-153.233	.90	-197.667	-153.098	.73	-197.532	.134	.04	-.097	.03	-.159	-.008	1.029	.01	1278.46	9.37	213.87
Beam 4V																		
1	62	-153.203	1.04	-197.577	-153.188	0.87	-197.561	0.016	0.05	0.009	0.04	-0.086	0.071	1.003	0.01	1270.12	11.00	174.46
2	62	-153.649	.84	-197.539	-153.640	.94	-197.530	.009	.06	-.022	.04	-.122	.072	1.002	.01	1279.22	11.99	183.56
3	62	-154.254	1.00	-197.556	-154.246	.76	-197.548	.008	.06	-.004	.04	-.108	.086	1.002	.01	1273.87	9.66	178.21
4	62	-154.783	1.03	-197.580	-154.761	1.13	-197.558	.022	.07	.007	.05	-.076	.095	1.005	.02	1270.88	14.42	175.21
5	62	-155.665	.97	-197.531	-155.683	1.17	-197.549	-.018	.06	-.003	.05	-.119	.104	.996	.01	1273.60	14.87	177.94
6	62	-156.605	1.09	-197.604	-156.607	1.17	-197.607	-.003	.06	.055	.05	-.068	.142	.999	.01	1256.75	14.75	161.09
7	62	-157.600	1.58	-197.596	-157.594	1.34	-197.591	.006	.09	.040	.06	-.066	.211	1.001	.02	1261.32	16.88	165.66
8	62	-158.310	1.58	-197.473	-158.312	1.30	-197.475	-.001	.10	-.077	.06	-.216	.045	1.000	.02	1295.51	16.85	199.84
9	62	-159.417	1.38	-197.541	-159.438	2.04	-197.562	-.022	.11	.011	.08	-.155	.197	.995	.02	1269.66	25.84	173.99
10	62	-160.294	1.40	-197.551	-160.310	2.15	-197.566	-.016	.10	.015	.09	-.221	.226	.997	.02	1268.51	27.25	172.85
11	62	-160.973	1.66	-197.483	-160.961	2.15	-197.472	.011	.12	-.079	.09	-.294	.106	1.003	.03	1296.28	27.85	200.62
12	62	-161.742	2.02	-197.618	-161.733	2.30	-197.609	.009	.13	.058	.09	-.131	.271	1.003	.03	1256.24	28.89	160.58
13	62	-153.206	.81	-197.663	-153.073	.79	-197.529	.133	.05	-.022	.03	-.108	.093	1.029	.01	1279.32	10.08	183.66
14	62	-153.189	.98	-197.645	-153.067	.78	-197.523	.122	.06	-.029	.04	-.101	.053	1.028	.01	1281.33	10.04	185.66
15	62	-153.153	1.01	-197.587	-153.029	.81	-197.463	.124	.05	-.089	.03	-.162	-.009	1.027	.01	1299.04	10.49	203.38

[a] For beam 3V: AV SNKT (Cells 1 to 12) = -197.639 dBW, NSD = 0.401%.
For beam 4V: AV SNKT (Cells 1 to 12) = -197.554 dBW, NSD = 0.397%.

[b] For beam 3V: AV NKT (Cells 1 to 12) = -197.629 dBW, NSD = 0.382%.
For beam 4V: AV NKT (Cells 1 to 12) = -197.552 dBW, NSD = 0.408%.

[c] For beam 3V: TEVM (Cells 1 to 12) = 1250.25 K, NSD = 0.38%.
For beam 4V: TEVM (Cells 1 to 12) = 1272.77 K, NSD = 0.41%.

[d] For beam 3V: TAM (Cells 1 to 12) = 185.65 K, NSD = 2.58%.
For beam 4V: TAM (Cells 1 to 12) = 177.10 K, NSD = 2.93%.

TABLE 8.- STATISTICS OF MEASURED NOISE POWER DURING ONE SEQUENCE OF 124 SCIENCE FRAMES OVER LAND FOR ORBIT 686

[Standby mode; approximate time period, 12 to 16 min past ascending node]

Cell	Number of samples	PSN		SNKT[a] mean, dBW	NP		NKT[b] mean, dBW	DPN, dB		DG, dB				RR		TEV[c], K		TA[d] mean, K
		Mean, dBW	NSD, %		Mean, dBW	NSD, %		Mean	SD	Mean	SD	Min	Max	Mean	SD	Mean	SD	
Beam 3V																		
1	62	-153.046	1.31	-197.419	-153.030	1.58	-197.404	0.015	0.06	0.007	0.07	-0.448	0.105	1.003	0.01	1316.90	20.83	251.94
2	62	-153.517	1.02	-197.407	-153.516	.85	-197.406	.001	.06	.009	.04	-.079	.095	1.000	.01	1316.27	11.19	251.31
3	62	-154.097	1.01	-197.399	-154.085	.75	-197.387	.012	.06	-.010	.03	-.081	.052	1.003	.01	1322.00	9.94	257.05
4	62	-154.617	1.15	-197.414	-154.610	.99	-197.408	.007	.06	.011	.05	-.078	.150	1.002	.01	1315.73	13.08	250.77
5	62	-155.514	1.28	-197.380	-155.497	1.09	-197.363	.017	.08	-.034	.05	-.150	.051	1.004	.02	1329.27	14.52	264.31
6	62	-156.339	1.25	-197.339	-156.333	1.30	-197.332	.007	.09	-.064	.05	-.209	.048	1.002	.02	1338.70	17.41	273.74
7	62	-157.405	1.40	-197.401	-157.406	1.25	-197.403	-.001	.09	.006	.06	-.159	.145	1.000	.02	1317.12	16.45	252.16
8	62	-158.204	1.32	-197.367	-158.209	1.56	-197.372	-.005	.07	-.025	.06	-.189	.126	.999	.02	1326.69	20.64	261.73
9	62	-159.311	1.50	-197.435	-159.314	1.86	-197.438	-.003	.10	.042	.08	-.118	.205	1.000	.02	1306.46	24.30	241.50
10	62	-160.118	1.43	-197.375	-160.153	1.80	-197.410	-.035	.10	.014	.07	-.125	.139	.992	.02	1314.97	23.68	250.01
11	62	-160.976	1.68	-197.487	-160.960	2.05	-197.470	.016	.12	.074	.08	-.177	.267	1.004	.03	1296.81	26.63	231.85
12	62	-161.506	1.78	-197.382	-161.490	2.67	-197.366	.015	.13	-.030	.11	-.240	.255	1.004	.03	1328.38	35.48	263.42
13	62	-153.000	1.02	-197.456	-152.903	.87	-197.360	.096	.05	-.037	.04	-.143	.066	1.022	.01	1330.20	11.52	265.24
14	62	-152.989	1.00	-197.444	-152.859	.85	-197.315	.130	.05	-.082	.04	-.180	.002	1.029	.01	1344.21	11.41	279.25
15	62	-153.051	1.08	-197.485	-152.909	.68	-197.343	.142	.06	-.054	.04	-.133	.030	1.031	.01	1335.55	9.05	270.59
Beam 4V																		
1	62	-152.923	0.90	-197.296	-152.909	0.93	-197.282	0.013	0.05	-0.039	0.04	-0.111	0.076	1.003	0.01	1354.22	12.62	258.16
2	62	-153.398	.92	-197.288	-153.385	.88	-197.275	.013	.06	-.046	.04	-.125	.040	1.003	.01	1356.43	11.96	260.37
3	62	-154.029	1.10	-197.331	-154.011	.83	-197.313	.018	.06	-.008	.04	-.106	.104	1.004	.01	1344.62	11.17	248.56
4	62	-154.518	1.01	-197.315	-154.509	.91	-197.306	.009	.06	-.015	.04	-.127	.096	1.002	.01	1346.83	12.19	250.77
5	62	-155.449	1.04	-197.315	-155.454	1.09	-197.321	-.005	.06	-.001	.05	-.127	.101	.999	.01	1342.35	14.58	246.28
6	62	-156.337	1.21	-197.336	-156.315	1.21	-197.315	.021	.07	-.007	.05	-.143	.086	1.005	.02	1344.18	16.22	248.12
7	62	-157.383	1.37	-197.380	-157.387	1.20	-197.383	-.003	.08	.062	.05	-.039	.173	.999	.02	1323.14	15.90	227.08
8	62	-158.131	1.53	-197.294	-158.114	1.64	-197.277	.017	.09	-.044	.07	-.236	.141	1.004	.02	1355.93	22.29	259.87
9	62	-159.314	1.32	-197.438	-159.312	1.79	-197.436	.001	.09	.115	.07	-.082	.238	1.001	.02	1307.06	23.45	211.00
10	62	-160.053	1.49	-197.309	-160.084	1.77	-197.340	-.031	.10	.020	.07	-.146	.209	.993	.02	1336.25	23.72	240.19
11	32	-160.852	1.93	-197.363	-160.841	2.04	-197.352	.011	.12	.031	.08	-.164	.226	1.003	.03	1332.80	27.21	236.74
12	62	-161.315	1.63	-197.191	-161.334	2.04	-197.210	-.019	.12	-.111	.09	-.319	.098	.996	.03	1377.01	28.03	280.95
13	62	-153.010	.90	-197.467	-152.890	.81	-197.347	.120	.05	.026	.04	-.059	.104	1.027	.01	1334.23	10.84	238.17
14	62	-152.933	1.03	-197.388	-152.804	.89	-197.259	.130	.06	-.062	.04	-.154	.031	1.030	.01	1361.53	12.11	265.47
15	62	-152.939	1.17	-197.373	-152.815	.70	-197.249	.125	.07	-.072	.04	-.160	.013	1.027	.02	1364.66	9.56	268.60

[a] For beam 3V: AV SNKT (Cells 1 to 12) = -197.401 dBW, NSD = 0.438%.
For beam 4V: AV SNKT (Cells 1 to 12) = -197.323 dBW, NSD = 0.440%.

[b] For beam 3V: AV NKT (Cells 1 to 12) = -197.397 dBW, NSD = 0.503%.
For beam 4V: AV NKT (Cells 1 to 12) = -197.321 dBW, NSD = 0.427%.

[c] For beam 3V: TEVM (Cells 1 to 12) = 1318.92 K, NSD = 0.50%.
For beam 4V: TEVM (Cells 1 to 12) = 1342.08 K, NSD = 0.43%.

[d] For beam 3V: TAM (Cells 1 to 12) = 253.96 K, NSD = 2.61%.
For beam 4V: TAM (Cells 1 to 12) = 246.02 K, NSD = 2.33%

TABLE 9.- CORRECTED RANGE-GATE PERIOD AND ASSOCIATED PARAMETERS

Cell	Number of samples	RR	T_{GC}, sec	$\frac{T_G}{T_{GC}}$, dB	$\frac{T_N + T_{GC}}{T_N + T_G}$
13	2169	1.02571	0.34293	0.110	0.98942
14	2169	1.02788	.33804	.119	.98864
15	2169	1.02785	.33576	.119	.98869

TABLE 10.- LOCATION OF OUTLIER POINTS ON FIVE REPEAT ORBITS

Beam/cell	Orbit	Latitude, deg	Longitude, deg	σ^o, dB
1V/8	1209	1.69	304.05	-13.2
1V/8	1252	1.49	304.13	-12.7
1V/8	1295	1.61	304.06	-12.6
1V/8	1338	1.48	304.15	-12.1
1V/8	1381	1.43	304.10	-11.5
2V/12	1209	-3.28	304.82	-11.4
2V/12	1252	-3.48	304.90	-10.7
2V/12	1295	-3.35	304.83	-12.7
2V/12	1338	-3.50	304.87	-10.3
2V/12	1381	-3.51	304.92	-11.0

TABLE 11.- STATISTICS OF σ^o RESPONSE OVER AMAZON RAIN FOREST FOR ORBIT 205

[Sunrise pass (0500 to 0730)]

Cell	Number of samples	$\bar{\theta}_i$, deg	σ^o Mean, dB	σ^o SD, dB	σ^o Sample NSD, %	Estimated NSD for each sample, %	σ^o, dB Min	σ^o, dB Max
Beam 1H								
1	13	24.4	-5.07	0.32	7.4	9.2	-5.70	-4.47
2	15	29.6	-5.24	.24	5.5	6.8	-5.63	-4.95
3	10	34.4	-6.40	.23	5.3	5.0	-6.72	-6.01
4	12	38.9	-7.05	.39	8.7	3.7	-7.94	-6.45
5	8	43.1	-7.38	.33	7.5	3.0	-7.87	-6.96
6	8	47.0	-7.67	.29	6.4	3.0	-8.21	-7.43
7	9	50.6	-8.08	.45	10.3	3.7	-8.76	-7.47
8	12	53.9	-8.72	.51	11.6	4.7	-9.68	-8.04
9	10	57.0	-9.35	.70	15.4	6.0	-10.66	-8.60
10	8	59.8	-10.51	.74	15.2	7.4	-12.25	-9.72
11	9	62.7	-11.10	.38	8.7	9.0	-11.72	-10.53
12	9	65.3	-11.49	.26	5.9	11.0	-11.92	-11.19
Beam 1V								
1	12	24.6	-5.02	0.30	7.0	8.8	-5.48	-4.46
2	12	29.8	-5.75	.23	5.2	6.8	-6.27	-5.48
3	11	34.7	-6.65	.22	5.1	4.9	-6.93	-6.31
4	12	39.2	-7.22	.50	10.8	3.7	-8.47	-6.64
5	8	43.4	-7.61	.24	5.3	2.9	-8.08	-7.28
6	8	47.3	-7.67	.35	8.0	3.0	-8.33	-7.14
7	9	50.9	-8.27	.84	16.8	3.7	-10.30	-7.55
8	14	54.3	-8.85	.46	10.5	4.7	-9.72	-8.17
9	6	57.5	-9.74	.49	10.4	6.1	-10.72	-9.37
10	9	60.3	-10.34	.64	14.4	7.6	-11.59	-9.44
11	9	63.2	-11.05	.39	9.1	9.9	-11.60	-10.51
12	9	65.8	-11.74	.91	23.7	14.1	-12.61	-9.89
Beam 2H								
1	18	21.5	-6.00	0.52	12.1	10.7	-6.96	-5.00
2	13	26.0	-5.84	.46	10.8	7.5	-6.68	-5.12
3	11	30.2	-5.98	.26	5.9	5.9	-6.53	-5.60
4	14	34.0	-6.60	.37	8.4	4.9	-7.49	-6.03
5	10	37.5	-6.94	.30	6.8	4.0	-7.41	-6.61
6	11	40.7	-7.21	.29	6.6	3.4	-7.86	-6.78
7	9	43.6	-7.40	.41	9.3	3.2	-8.19	-6.74
8	7	46.3	-7.56	.40	9.0	3.2	-8.20	-7.07
9	9	48.6	-7.97	.38	8.4	3.5	-8.81	-7.52
10	7	50.8	-8.29	.54	12.1	3.9	-9.23	-7.58
11	9	52.7	-8.69	.72	15.3	4.4	-10.06	-8.02
12	8	54.5	-9.52	.50	11.5	4.9	-10.34	-8.80
Beam 2V								
1	18	21.6	-5.90	0.72	16.6	12.6	-6.91	-4.79
2	15	26.2	-5.85	.43	9.8	7.6	-6.66	-5.28
3	12	30.4	-6.04	.26	5.8	5.9	-6.64	-5.74
4	12	34.2	-6.38	.35	8.1	4.8	-6.99	-5.86
5	12	37.7	-6.75	.23	5.3	4.0	-7.14	-6.35
6	10	40.9	-7.36	.33	7.5	3.3	-7.91	-6.93
7	10	43.9	-7.32	.35	7.8	3.1	-8.10	-6.89
8	9	46.5	-7.93	.37	8.6	3.2	-8.46	-7.38
9	8	48.9	-8.03	.53	12.2	3.4	-8.85	-7.22
10	7	51.1	-8.42	.26	6.2	3.8	-8.70	-8.02
11	7	53.1	-8.59	.74	15.5	4.3	-10.14	-7.88
12	12	54.9	-9.07	.91	17.4	4.8	-11.70	-8.41

TABLE 12.- STATISTICS OF σ^o RESPONSE OVER AMAZON RAIN FOREST FOR ORBIT 212

[Evening pass (1730 to 2330)]

Cell	Number of samples	$\bar{\theta}_i$, deg	σ^o			Estimated NSD for each sample, %	σ^o, dB	
			Mean, dB	SD, dB	Sample NSD, %		Min	Max
			Beam 1H					
1	8	21.1	-6.47	0.86	17.3	11.9	-8.44	-5.62
2	12	25.5	-6.19	.44	9.7	7.5	-7.19	-5.64
3	17	29.5	-6.43	.21	5.0	5.5	-6.81	-6.05
4	18	33.2	-7.03	.15	3.6	4.5	-7.28	-6.60
5	14	36.5	-7.64	.26	5.9	3.7	-8.28	-7.33
6	13	39.6	-7.86	.22	5.0	3.3	-8.45	-7.55
7	9	42.3	-8.07	.50	10.9	3.2	-9.22	-7.49
8	6	44.8	-8.18	.27	6.2	3.2	-8.59	-7.90
9	8	47.0	-8.42	.36	8.2	3.5	-8.94	-7.96
10	7	49.1	-8.30	.28	6.3	3.9	-8.83	-8.00
11	7	50.9	-9.15	.42	10.3	4.3	-9.53	-8.31
12	9	52.5	-9.65	.17	3.8	4.8	-9.98	-9.42
			Beam 1V					
1	8	21.3	-6.09	0.12	2.8	8.7	-6.24	-5.92
2	13	25.6	-6.06	.35	7.5	6.7	-7.11	-5.76
3	17	29.7	-6.90	.25	5.6	5.4	-7.50	-6.43
4	18	33.4	-7.29	.21	4.7	4.4	-7.92	-6.93
5	16	36.7	-7.78	.21	4.8	3.7	-8.30	-7.44
6	15	39.8	-8.05	.15	3.5	3.2	-8.28	-7.76
7	8	42.5	-8.56	.69	14.5	3.1	-10.00	-8.06
8	6	45.0	-8.45	.06	1.5	3.2	-8.56	-8.38
9	8	47.3	-8.51	.21	4.9	3.5	-8.87	-8.16
10	7	49.3	-8.46	.33	7.6	3.8	-8.82	-8.02
11	8	51.1	-8.88	.77	18.1	4.2	-9.72	-7.97
12	7	52.8	-9.75	.17	3.8	4.7	-10.07	-9.59
			Beam 2H					
1	17	25.4	-6.52	0.29	6.3	8.6	-7.33	-6.22
2	14	30.8	-6.86	.39	8.4	6.3	-7.73	-6.44
3	12	35.9	-7.52	.34	7.2	4.6	-8.46	-7.24
4	8	40.7	-8.21	.31	6.9	3.5	-8.76	-7.95
5	7	45.3	-8.61	.15	3.4	2.9	-8.78	-8.40
6	8	49.4	-9.27	.18	4.0	3.0	-9.66	-9.11
7	7	53.3	-9.71	.21	4.7	3.6	-9.98	-9.46
8	11	56.9	-10.21	.40	8.7	4.5	-11.05	-9.75
9	8	60.4	-10.87	.20	4.7	5.6	-11.14	-10.61
10	7	63.7	-11.53	.39	8.7	7.0	-12.23	-11.14
11	13	66.8	-12.26	.59	12.8	9.1	-13.50	-11.59
12	18	70.0	-12.82	.62	13.9	13.1	-14.15	-11.75
			Beam 2V					
1	15	25.7	-6.41	0.41	9.3	8.6	-7.22	-5.85
2	15	31.1	-6.69	.23	5.1	6.2	-7.19	-6.43
3	13	36.2	-7.31	.45	9.3	4.6	-8.66	-6.89
4	10	41.0	-8.26	.33	7.2	3.4	-9.11	-8.00
5	7	45.6	-8.62	.15	3.5	2.9	-8.83	-8.43
6	9	49.7	-9.38	.34	7.7	3.0	-10.06	-8.82
7	7	53.7	-9.50	.14	3.4	3.6	-9.65	-9.23
8	8	57.4	-9.53	.41	9.1	4.4	-10.32	-9.11
9	9	60.7	-10.72	.22	5.0	5.6	-11.22	-10.48
10	8	64.2	-11.42	.64	14.0	7.1	-12.66	-10.68
11	13	67.3	-11.83	.51	11.6	9.1	-12.78	-11.12
12	17	70.7	-12.23	.43	10.2	13.1	-13.02	-11.31

TABLE 13.- STATISTICS OF σ^o RESPONSE OVER AMAZON RAIN FOREST FOR ORBIT 420

[Sunrise pass (0500 to 0730)]

Cell	Number of samples	$\bar{\theta}_i$, deg	σ^o			Estimated NSD for each sample, %	σ^o, dB	
			Mean, dB	SD, dB	Sample NSD, %		Min	Max
Beam 3H								
1	9	25.2	-5.41	0.31	7.0	8.3	-6.09	-5.04
2	5	30.4	-5.35	.19	4.3	6.4	-5.62	-5.17
3	9	35.4	-6.48	.23	5.4	4.6	-6.82	-6.13
4	13	40.1	-6.84	.24	5.5	3.4	-7.23	-6.34
5	15	44.5	-7.53	.15	3.5	2.9	-7.78	-7.25
6	17	48.6	-7.85	.25	6.0	3.0	-8.31	-7.33
7	19	52.5	-8.38	.29	6.7	3.6	-8.91	-7.91
8	18	56.2	-8.77	.40	9.1	4.5	-9.69	-8.07
9	13	59.7	-9.28	.15	3.5	5.6	-9.46	-8.99
10	11	63.2	-10.45	.27	6.1	6.9	-10.85	-10.09
11	11	66.5	-10.86	.26	6.0	8.6	-11.39	-10.57
12	12	69.8	-11.41	.65	14.1	12.1	-13.01	-10.42
Beam 3V								
1	10	24.9	-5.41	0.43	9.5	8.7	-6.38	-4.91
2	5	30.2	-5.07	.40	8.6	6.4	-5.77	-4.78
3	11	35.2	-6.17	.23	5.5	4.6	-6.42	-5.75
4	13	39.8	-6.68	.32	7.6	3.4	-7.19	-6.11
5	12	44.2	-7.38	.26	5.9	2.9	-7.76	-6.97
6	17	48.2	-7.59	.26	6.1	3.0	-7.93	-7.11
7	20	52.1	-8.00	.34	7.8	3.5	-8.55	-7.40
8	20	55.8	-8.43	.35	8.3	4.4	-9.07	-7.75
9	14	59.3	-8.87	.20	4.7	5.5	-9.28	-8.49
10	14	62.6	-9.93	.21	4.7	6.8	-10.23	-9.56
11	11	65.9	-10.37	.27	6.2	8.1	-10.92	-9.93
12	11	69.1	-11.10	.26	5.9	10.1	-11.60	-10.77
Beam 4H								
1	7	21.7	-5.88	0.49	11.2	8.8	-6.73	-5.09
2	11	26.1	-5.62	.34	7.8	6.8	-6.28	-5.16
3	9	30.2	-5.80	.21	4.8	5.4	-6.10	-5.48
4	8	33.9	-6.34	.37	8.2	4.4	-7.13	-5.87
5	10	37.3	-6.79	.19	4.4	3.6	-7.02	-6.44
6	10	40.4	-7.07	.24	5.4	3.2	-7.52	-6.78
7	12	43.3	-7.16	.23	5.3	3.1	-7.58	-6.69
8	15	45.9	-7.40	.19	4.4	3.2	-7.67	-7.06
9	11	48.2	-7.51	.25	5.7	3.5	-7.96	-7.10
10	13	50.3	-8.13	.26	5.9	3.9	-8.57	-7.79
11	16	52.3	-8.63	.46	11.0	4.3	-9.25	-7.62
12	17	54.0	-9.17	.24	5.7	4.8	-9.51	-8.64
Beam 4V								
1	9	21.5	-4.96	0.35	7.9	8.6	-5.55	-4.58
2	10	25.9	-5.18	.40	9.4	6.7	-5.77	-4.49
3	8	30.0	-5.50	.24	5.6	5.4	-5.81	-5.16
4	10	33.7	-6.14	.33	7.4	4.4	-6.78	-5.64
5	11	37.1	-6.69	.21	4.9	3.7	-7.01	-6.32
6	11	40.2	-6.86	.25	5.7	3.2	-7.17	-6.54
7	11	43.1	-6.97	.22	5.1	3.1	-7.38	-6.61
8	15	45.6	-7.05	.25	5.9	3.2	-7.45	-6.50
9	12	47.9	-7.16	.28	6.7	3.4	-7.48	-6.50
10	11	50.1	-7.59	.26	6.0	3.8	-8.08	-7.13
11	17	52.0	-7.70	.40	9.2	4.2	-8.35	-6.93
12	15	53.7	-8.18	.50	11.4	4.7	-9.17	-7.45

TABLE 14.- STATISTICS OF σ^o RESPONSE OVER AMAZON RAIN FOREST FOR ORBIT 428

[Evening pass (1730 to 2330)]

Cell	Number of samples	$\bar{\theta}_i$, deg	σ^o			Estimated NSD for each sample, %	σ^o, dB	
			Mean, dB	SD, dB	Sample NSD, %		Min	Max
Beam 3H								
1	16	21.2	-5.84	0.50	11.0	10.3	-7.08	-5.00
2	20	25.6	-6.08	.26	5.8	7.3	-6.75	-5.70
3	21	29.7	-6.36	.26	6.0	5.9	-6.78	-5.84
4	19	33.4	-6.79	.27	6.3	4.6	-7.24	-6.25
5	21	36.9	-7.25	.30	6.9	3.8	-7.93	-6.72
6	20	40.0	-7.30	.26	6.0	3.3	-7.79	-6.69
7	19	42.9	-7.66	.32	7.7	3.1	-8.13	-6.77
8	16	45.5	-8.07	.21	5.0	3.2	-8.34	-7.62
9	18	47.8	-8.10	.34	7.7	3.5	-8.86	-7.48
10	18	49.9	-8.55	.27	6.2	3.9	-9.07	-8.05
11	19	51.9	-8.82	.46	9.8	4.4	-10.26	-8.05
12	17	53.7	-8.90	.61	13.6	4.8	-10.23	-7.96
Beam 3V								
1	9	21.0	-5.73	0.46	10.8	14.4	-6.30	-5.01
2	20	25.4	-6.03	.31	7.2	7.8	-6.52	-5.36
3	21	29.5	-5.99	.23	5.4	5.9	-6.29	-5.46
4	21	33.2	-6.53	.28	6.4	4.6	-7.21	-6.10
5	18	36.7	-7.14	.23	5.2	3.8	-7.76	-6.84
6	20	39.8	-7.31	.24	5.7	3.3	-7.70	-6.82
7	17	42.6	-7.63	.24	5.6	3.1	-8.04	-7.12
8	19	45.2	-7.68	.31	7.3	3.2	-8.11	-7.07
9	18	47.5	-7.99	.39	9.1	3.4	-8.80	-7.16
10	17	49.7	-8.14	.62	12.9	3.8	-10.11	-7.22
11	19	51.6	-8.58	.35	8.2	4.3	-9.11	-7.82
12	12	53.4	-8.71	.54	11.7	4.7	-10.02	-7.94
Beam 4H								
1	22	24.6	-6.07	0.25	5.6	8.9	-6.60	-5.72
2	20	29.7	-6.53	.37	7.6	6.6	-7.93	-6.15
3	22	34.6	-7.21	.15	3.4	5.0	-7.55	-6.89
4	18	39.1	-7.90	.22	5.0	3.6	-8.26	-7.41
5	20	43.4	-8.44	.28	6.7	2.9	-8.95	-7.82
6	20	47.4	-8.59	.51	13.3	3.0	-9.26	-6.87
7	14	51.1	-9.36	.22	5.0	3.7	-9.73	-8.92
8	17	54.6	-9.89	.33	7.8	4.8	-10.30	-9.11
9	15	57.9	-11.24	.28	6.5	6.2	-11.73	-10.78
10	14	61.2	-11.78	.64	14.8	7.9	-13.16	-10.62
11	6	64.2	-12.40	.39	8.9	10.5	-13.01	-11.94
12	10	67.2	-13.31	.94	22.4	15.8	-14.67	-11.93
Beam 4V								
1	21	24.3	-5.80	0.22	5.0	8.9	-6.29	-5.50
2	23	29.5	-6.22	.30	6.3	6.6	-7.36	-5.83
3	21	34.3	-7.25	.22	5.0	5.0	-7.91	-6.84
4	15	38.8	-7.68	.25	6.0	3.6	-7.99	-7.23
5	17	43.1	-8.18	.33	8.1	2.9	-8.62	-7.20
6	18	47.0	-8.15	.71	19.0	3.0	-8.84	-6.12
7	16	50.8	-8.90	.31	7.4	3.7	-9.35	-8.34
8	16	54.2	-9.26	.38	8.8	4.8	-9.84	-8.52
9	15	57.4	-10.26	.36	8.4	6.0	-10.89	-9.52
10	17	60.6	-11.08	.40	9.4	7.6	-12.00	-10.08
11	4	63.8	-11.43	.16	3.6	9.9	-11.64	-11.26
12	6	66.6	-11.93	1.03	23.9	14.0	-13.58	-10.48

TABLE 15.- STATISTICS OF σ^o RESPONSE OVER AMAZON RAIN FOREST FOR ORBIT 1080

[Morning pass (0800 to 1145)]

Cell	Number of samples	$\bar{\theta}_i$, deg	σ^o Mean, dB	SD, dB	Sample NSD, %	Estimated NSD for each sample, %	σ^o, dB Min	Max
Beam 1V								
1	11	24.8	-5.45	0.13	3.0	10.1	-5.64	-5.29
2	8	29.9	-6.10	.19	4.4	8.1	-6.36	-5.80
3	15	34.8	-7.12	.19	4.5	6.1	-7.44	-6.85
4	10	39.4	-7.85	.21	4.8	4.6	-8.07	-7.50
5	12	43.6	-8.49	.22	5.1	3.2	-8.95	-8.13
6	7	47.5	-8.71	.15	3.5	3.0	-8.98	-8.52
7	10	51.1	-9.43	.11	2.5	4.1	-9.58	-9.23
8	6	54.6	-10.28	.18	4.1	6.1	-10.52	-10.02
9	5	57.9	-11.16	.52	12.0	8.4	-11.67	-10.53
10	4	60.9	-11.91	.20	4.7	11.2	-12.11	-11.64
11	0	.0	.00	.00	.0	.0	99.00	-99.00
12	0	.0	.00	.00	.0	.0	99.00	-99.00
Beam 2V								
1	7	21.7	-6.75	1.27	27.9	15.2	-8.62	-5.45
2	14	26.2	-6.65	.35	7.9	8.8	-7.46	-6.24
3	9	30.4	-7.08	.18	4.1	6.9	-7.35	-6.73
4	12	34.2	-7.36	.23	5.4	5.6	-7.70	-6.87
5	17	37.8	-7.66	.12	2.8	4.7	-7.85	-7.37
6	8	40.9	-8.09	.19	4.4	3.9	-8.31	-7.83
7	9	43.9	-8.27	.19	4.3	3.3	-8.51	-7.99
8	13	46.5	-8.53	.24	5.6	3.2	-8.84	-8.07
9	11	48.9	-8.72	.21	4.9	3.5	-9.13	-8.40
10	10	51.0	-9.12	.35	7.7	4.0	-9.89	-8.77
11	4	53.0	-9.16	.64	14.1	4.7	-10.11	-8.62
12	9	54.7	-8.94	.58	13.6	5.5	-10.09	-7.82
Beam 3V								
1	10	24.3	-6.17	0.49	11.0	11.1	-7.15	-5.57
2	10	29.4	-5.90	.35	8.0	8.2	-6.54	-5.33
3	10	34.2	-6.77	.47	11.3	6.2	-7.38	-5.88
4	12	38.7	-7.41	.36	8.2	4.6	-7.97	-6.89
5	15	42.9	-8.06	.28	6.5	3.2	-8.53	-7.63
6	13	46.8	-8.27	.27	6.3	3.0	-8.69	-7.89
7	15	50.5	-8.77	.22	5.0	4.1	-9.41	-8.51
8	19	54.0	-9.33	.39	8.7	6.0	-10.30	-8.74
9	16	57.2	-9.84	.29	6.5	8.3	-10.41	-9.40
10	14	60.3	-10.77	.57	13.5	10.8	-11.67	-9.74
11	13	63.3	-11.63	.35	7.9	13.6	-12.34	-11.13
12	11	66.2	-11.88	.39	8.8	16.4	-12.71	-11.51
Beam 4V								
1	7	21.8	-5.98	0.34	7.9	9.9	-6.48	-5.58
2	8	26.2	-6.08	.34	8.1	8.2	-6.50	-5.41
3	9	30.3	-6.66	.44	9.7	6.8	-7.50	-6.12
4	10	34.1	-7.22	.70	14.7	5.6	-8.92	-6.45
5	8	37.6	-7.62	.65	15.5	4.7	-8.31	-6.63
6	10	40.8	-7.89	.40	9.1	3.9	-8.46	-7.34
7	11	43.7	-7.96	.39	9.0	3.4	-8.67	-7.31
8	16	46.3	-8.06	.32	7.4	3.2	-8.67	-7.65
9	12	48.7	-8.10	.31	7.0	3.5	-8.68	-7.68
10	12	50.9	-8.45	.46	10.5	4.1	-9.38	-7.79
11	16	52.9	-8.71	.39	8.9	4.8	-9.29	-8.11
12	17	54.7	-9.43	.54	13.3	5.6	-10.21	-8.22

TABLE 16.- STATISTICS OF σ^o RESPONSE OVER AMAZON RAIN FOREST FOR ORBIT 1360

[Evening pass (1730 to 2330)]

Cell	Number of samples	$\bar{\theta}_i$, deg	σ^o			Estimated NSD for each sample, %	σ^o, dB	
			Mean, dB	SD, dB	Sample NSD, %		Min	Max
Beam 1H								
1	17	21.9	-5.71	0.38	8.6	9.5	-6.69	-5.09
2	18	26.4	-5.98	.38	8.7	8.2	-6.79	-5.28
3	16	30.5	-6.63	.28	6.6	6.8	-7.15	-6.01
4	21	34.3	-7.19	.26	6.0	5.6	-7.69	-6.54
5	18	37.8	-7.72	.31	7.1	4.6	-8.25	-7.02
6	19	41.0	-7.94	.39	8.7	3.9	-8.85	-7.23
7	20	43.9	-7.84	.40	8.8	3.3	-8.94	-7.27
8	19	46.5	-7.91	.24	5.6	3.2	-8.29	-7.45
9	22	48.9	-8.11	.33	7.4	3.5	-9.00	-7.71
10	19	51.0	-8.29	.34	8.0	4.0	-8.82	-7.51
11	24	53.0	-8.44	.41	9.4	4.7	-9.33	-7.80
12	19	54.7	-8.52	.69	15.6	5.5	-9.68	-7.50
Beam 2V								
1	18	24.7	-5.85	0.38	8.5	10.7	-6.56	-5.22
2	17	29.9	-5.98	.36	8.5	8.1	-6.60	-5.21
3	19	34.8	-6.56	.31	7.1	6.2	-7.32	-6.07
4	19	39.4	-7.31	.39	8.7	4.6	-8.49	-6.64
5	20	43.7	-8.03	.24	5.6	3.2	-8.49	-7.57
6	19	47.6	-8.29	.34	7.7	3.0	-8.85	-7.70
7	21	51.4	-8.75	.40	9.2	4.1	-9.50	-8.15
8	14	54.8	-8.90	.37	8.3	6.0	-9.45	-8.45
9	10	58.1	-9.17	.50	11.7	8.2	-9.84	-8.38
10	3	61.3	-11.08	.28	6.6	10.8	-11.32	-10.77
11	0	.0	.00	.00	.0	.0	99.00	-99.00
12	0	.0	.00	.00	.0	.0	99.00	-99.00
Beam 3V								
1	6	21.4	-6.47	0.46	10.6	16.6	-7.12	-5.92
2	6	25.8	-6.54	.34	7.6	8.9	-7.12	-6.20
3	11	29.9	-6.64	.30	6.7	7.0	-7.23	-6.20
4	10	33.6	-6.98	.23	5.4	5.6	-7.45	-6.58
5	4	37.1	-7.58	.12	2.8	4.7	-7.70	-7.42
6	8	40.2	-7.95	.20	4.7	3.9	-8.17	-7.66
7	6	43.1	-7.99	.32	7.3	3.3	-8.44	-7.64
8	8	45.7	-8.00	.28	6.4	3.2	-8.43	-7.63
9	7	48.1	-8.19	.23	5.3	3.5	-8.51	-7.87
10	7	50.2	-8.29	.21	4.9	4.0	-8.54	-8.02
11	7	52.2	-8.62	.31	7.1	4.7	-9.09	-8.30
12	8	53.9	-9.36	1.92	33.9	5.5	-13.35	-8.18
Beam 4V								
1	9	24.8	-6.06	0.39	8.5	10.2	-6.89	-5.71
2	11	30.0	-6.35	.24	5.5	8.1	-6.75	-6.00
3	6	34.8	-7.39	.14	3.1	6.2	-7.61	-7.28
4	6	39.3	-7.93	.13	2.9	4.6	-8.15	-7.77
5	6	43.6	-8.36	.11	2.4	3.2	-8.48	-8.18
6	8	47.6	-8.64	.30	6.8	3.0	-9.00	-8.32
7	13	51.4	-9.32	.31	6.8	4.1	-10.14	-8.95
8	18	54.9	-9.60	.17	3.8	6.0	-10.03	-9.36
9	15	58.2	-10.68	.59	13.1	8.4	-12.09	-9.75
10	6	61.4	-11.34	.30	6.9	11.2	-11.84	-10.98
11	7	64.5	-12.09	1.01	20.8	14.9	-13.94	-11.29
12	5	67.5	-12.19	.49	11.9	19.5	-12.70	-11.40

TABLE 17.- COMBINED STATISTICS OF σ^o RESPONSE OVER AMAZON RAIN FOREST DURING SUNRISE PASSES

(a) Beams 1H, 1V, 2H, and 2V

Cell	Number of samples	$\bar{\theta}_i$, deg	σ^o			Estimated NSD for each sample, %	σ^o, dB	
			Mean, dB	SD, dB	Sample NSD, %		Min	Max
Beam 1H								
1	54	25.5	-5.20	0.31	7.1	9.0	-5.99	-4.47
2	60	30.9	-5.62	41	9.4	6.7	-6.51	-4.93
3	42	36.0	-6.59	.33	7.5	4.8	-7.35	-6.01
4	44	40.8	-7.18	.39	8.8	3.7	-8.12	-6.45
5	35	45.4	-7.52	.40	8.8	2.9	-8.70	-6.96
6	32	49.5	-8.02	.49	11.4	3.0	-8.92	-7.08
7	27	53.2	-8.57	.77	16.6	3.7	-11.05	-7.47
8	39	56.9	-9.28	.72	16.2	4.8	-11.00	-8.04
9	23	58.9	-9.75	.78	18.0	6.0	-11.22	-8.60
10	25	63.5	-11.04	.86	19.2	8.1	-12.59	-9.72
11	28	66.8	-11.92	1.13	24.6	12.0	-14.52	-10.28
12	25	69.5	-12.97	2.20	40.7	23.4	-18.81	-11.19
Beam 1V								
1	155	25.5	-5.29	0.48	10.9	8.5	-7.09	-4.28
2	132	30.9	-6.05	.45	9.9	6.6	-7.63	-5.04
3	139	35.9	-6.81	.43	9.6	4.9	-8.52	-5.96
4	136	40.6	-7.24	.46	11.0	3.6	-8.81	-5.68
5	165	45.0	-7.81	.42	9.5	2.9	-9.25	-6.92
6	141	49.1	-8.01	.45	10.3	3.0	-9.25	-7.01
7	151	52.9	-8.57	.60	13.2	3.7	-10.39	-7.36
8	134	56.6	-9.13	.79	16.4	4.7	-11.65	-7.87
9	124	59.7	-10.17	.62	13.5	6.0	-12.75	-9.05
10	113	63.1	-10.89	.81	17.2	8.5	-14.53	-9.26
11	108	66.0	-11.59	.88	18.7	12.8	-14.58	-10.19
12	77	69.0	-12.33	1.75	26.9	27.4	-22.09	-9.89
Beam 2H								
1	55	20.8	-6.16	0.68	14.7	11.9	-8.34	-4.97
2	52	25.2	-6.01	.45	10.3	7.9	-7.18	-5.12
3	44	29.2	-6.08	.31	7.1	6.1	-6.73	-5.51
4	53	32.9	-6.60	.33	7.3	4.8	-7.52	-6.03
5	46	36.2	-6.79	.28	6.3	4.0	-7.41	-6.28
6	53	39.1	-6.94	.30	7.0	3.4	-7.86	-6.32
7	47	41.9	-7.23	.34	7.9	3.2	-8.19	-6.49
8	36	44.4	-7.44	.45	9.7	3.2	-9.12	-6.73
9	34	46.8	-7.60	.45	10.3	3.5	-8.81	-6.80
10	38	48.5	-7.78	.51	11.4	3.9	-9.23	-6.88
11	40	50.4	-8.27	.78	17.2	4.3	-10.06	-7.00
12	37	52.2	-8.93	.77	17.4	4.8	-10.80	-7.69
Beam 2V								
1	151	21.2	-5.70	0.75	16.7	13.6	-7.84	-4.23
2	161	25.6	-5.83	.51	11.7	7.7	-7.21	-4.51
3	155	29.7	-6.12	.51	11.1	5.9	-8.27	-5.12
4	129	33.4	-6.25	.49	10.3	4.7	-8.42	-5.49
5	147	36.9	-6.70	.51	11.2	3.9	-8.65	-5.63
6	164	40.0	-7.04	.42	9.5	3.3	-8.36	-6.21
7	144	42.8	-7.35	.39	8.7	3.1	-8.73	-6.43
8	139	45.4	-7.61	.42	9.7	3.2	-8.84	-6.53
9	147	47.7	-7.83	.56	12.7	3.4	-9.62	-6.64
10	161	49.8	-8.25	.51	11.6	3.8	-10.72	-6.65
11	169	51.7	-8.39	.52	11.9	4.3	-10.14	-7.03
12	157	53.4	-8.53	.67	14.7	4.7	-11.70	-7.23

TABLE 17.- Concluded

(b) Beams 3H, 3V, 4H, and 4V

Cell	Number of samples	$\bar{\theta}_i$, deg	σ^o			Estimated NSD for each sample, %	σ^o, dB	
			Mean, dB	SD, dB	Sample NSD, %		Min	Max
				Beam 3H				
1	62	25.1	-5.75	0.46	9.8	8.4	-7.91	-5.04
2	46	30.4	-5.67	.37	8.4	6.3	-6.50	-5.11
3	52	35.4	-6.49	.37	8.5	4.6	-7.31	-5.88
4	54	40.0	-6.78	.32	7.3	3.4	-7.45	-6.23
5	50	44.5	-7.52	.33	7.6	2.9	-8.09	-6.85
6	51	48.6	-7.84	.26	6.1	3.0	-8.34	-7.29
7	49	52.6	-8.48	.28	6.4	3.6	-9.06	-7.91
8	50	56.3	-8.96	.52	10.5	4.4	-11.62	-8.07
9	42	59.9	-9.50	.32	7.2	5.5	-10.42	-8.99
10	43	63.3	-10.76	.44	9.8	6.9	-11.76	-10.09
11	37	66.7	-11.40	.53	12.1	8.9	-12.41	-10.57
12	33	70.0	-11.84	.77	17.5	12.8	-13.78	-10.42
				Beam 3V				
1	140	24.8	-5.75	0.52	12.1	9.0	-7.07	-4.54
2	121	30.0	-5.45	.56	12.8	6.4	-6.66	-4.35
3	143	35.0	-6.38	.54	12.6	4.7	-7.68	-5.02
4	132	39.5	-6.97	.46	10.7	3.5	-8.03	-5.87
5	130	43.8	-7.61	.45	10.4	2.9	-8.74	-6.54
6	134	48.0	-7.62	.44	10.0	3.0	-9.05	-6.70
7	141	51.7	-8.03	.61	12.3	3.6	-11.51	-7.03
8	120	55.3	-8.43	.49	11.1	4.7	-9.73	-7.51
9	104	58.7	-8.83	.45	10.6	5.8	-9.75	-7.82
10	87	61.9	-9.90	.62	14.9	7.1	-11.01	-8.08
11	74	65.1	-10.68	.64	15.8	8.8	-12.14	-8.86
12	46	68.1	-11.41	.92	21.8	11.2	-12.98	-9.14
				Beam 4H				
1	57	21.7	-6.11	0.42	9.6	8.9	-7.22	-5.09
2	64	26.1	-5.75	.39	8.7	6.8	-6.78	-5.07
3	58	30.2	-6.03	.45	9.3	5.4	-7.95	-5.48
4	49	33.9	-6.45	.32	7.3	4.4	-7.17	-5.87
5	52	37.3	-6.82	.36	7.8	3.6	-8.25	-6.33
6	53	40.4	-7.03	.32	7.3	3.2	-7.62	-6.36
7	49	43.3	-7.18	.36	8.3	3.1	-8.06	-6.39
8	52	45.9	-7.37	.37	8.2	3.2	-8.63	-6.79
9	47	48.2	-7.66	.45	10.2	3.5	-8.64	-6.72
10	46	50.3	-8.12	.38	8.2	3.9	-9.62	-7.48
11	46	52.2	-8.56	.46	10.8	4.3	-9.43	-7.62
12	45	54.0	-9.26	.31	7.0	4.8	-10.22	-8.64
				Beam 4V				
1	123	21.5	-5.38	0.71	15.4	8.8	-8.82	-3.92
2	139	25.9	-5.43	0.52	12.0	6.8	-7.52	-4.11
3	130	30.0	-5.87	.45	10.5	5.5	-6.91	-4.78
4	138	33.7	-6.48	.52	11.8	4.5	-8.43	-5.20
5	132	37.1	-6.94	.42	9.8	3.7	-7.89	-5.85
6	142	40.3	-7.05	.42	9.6	3.3	-8.25	-5.97
7	133	43.0	-7.22	.45	10.1	3.2	-8.91	-6.12
8	136	45.6	-7.31	.43	9.8	3.2	-8.56	-6.21
9	145	48.0	-7.49	.45	10.5	3.5	-8.52	-6.00
10	140	50.1	-7.77	.48	11.1	3.9	-8.86	-6.62
11	149	52.0	-8.00	.59	13.3	4.3	-10.32	-6.65
12	134	53.7	-8.48	.66	15.0	4.8	-10.52	-6.80

TABLE 18.- COMBINED STATISTICS OF σ^o RESPONSE OVER AMAZON RAIN FOREST DURING MORNING PASSES

Cell	Number of samples	$\bar{\theta}_i$, deg	σ^o			Estimated NSD for each sample, %	σ^o, dB	
			Mean, dB	SD, dB	Sample NSD, %		Min	Max
Beam 1V								
1	460	24.8	-5.62	0.39	8.7	9.5	-7.57	-4.83
2	434	30.0	-6.32	.34	7.6	7.5	-7.49	-5.53
3	429	35.0	-7.26	.33	7.3	5.7	-9.27	-6.34
4	359	39.5	-7.88	.36	8.1	4.2	-10.63	-6.06
5	394	43.8	-8.48	.33	7.6	3.1	-9.99	-7.41
6	277	47.6	-8.71	.43	9.2	3.0	-12.62	-7.59
7	294	51.4	-9.24	.42	9.9	4.0	-11.16	-7.81
8	278	54.9	-9.84	.61	13.9	5.5	-12.52	-8.33
9	288	58.1	-10.85	.91	22.3	7.6	-12.67	-8.59
10	193	60.8	-11.60	.88	20.1	9.7	-14.19	-9.75
11	168	63.9	-12.86	1.25	28.3	14.5	-16.42	-10.71
12	173	66.5	-13.03	1.69	33.2	22.2	-21.90	-10.69
Beam 2V								
1	421	21.6	-6.68	0.79	17.3	14.6	-10.82	-4.70
2	504	26.1	-6.44	.44	9.8	8.3	-8.52	-5.18
3	516	30.2	-6.85	.40	9.0	6.6	-8.95	-5.72
4	454	34.0	-7.00	.33	7.6	5.3	-8.71	-5.99
5	490	37.5	-7.43	.34	7.6	4.4	-9.39	-6.49
6	423	40.7	-7.85	.33	7.3	3.7	-9.21	-6.92
7	380	43.6	-8.15	.38	8.5	3.3	-11.06	-7.32
8	392	46.2	-8.42	.36	8.3	3.2	-9.76	-7.55
9	406	48.5	-8.74	.40	9.0	3.5	-11.16	-7.76
10	359	50.7	-9.06	.46	10.6	4.0	-10.62	-7.69
11	321	52.6	-9.20	.53	11.5	4.6	-13.16	-7.91
12	277	54.4	-9.24	.80	16.8	5.2	-12.67	-7.82
Beam 3V								
1	497	24.5	-6.42	0.58	13.0	10.4	-9.37	-4.95
2	426	29.7	-6.00	.50	10.8	7.7	-9.45	-4.81
3	568	34.6	-6.86	.41	9.4	5.8	-8.24	-5.53
4	456	39.1	-7.49	.36	8.5	4.3	-8.90	-5.65
5	445	43.4	-8.13	.31	7.1	3.2	-9.79	-7.17
6	405	47.4	-8.28	.35	8.1	3.0	-9.99	-7.08
7	448	51.1	-8.76	.36	8.1	4.0	-10.48	-7.60
8	422	54.6	-9.28	.45	10.1	5.6	-12.50	-8.00
9	445	58.0	-9.70	.51	11.6	7.7	-13.24	-8.16
10	366	61.1	-10.77	.64	16.1	9.7	-12.29	-8.42
11	373	64.2	-11.39	.57	13.4	12.2	-12.90	-9.62
12	317	67.0	-11.91	.75	17.7	14.8	-14.14	-9.78
Beam 4V								
1	399	21.7	-6.03	0.64	14.5	9.6	-8.52	-4.44
2	461	26.1	-6.19	.51	11.7	7.8	-8.39	-4.75
3	446	30.2	-6.63	.49	11.1	6.5	-8.47	-5.31
4	467	34.0	-7.20	.47	10.7	5.3	-10.07	-5.72
5	514	37.4	-7.62	.40	9.1	4.5	-8.85	-6.47
6	504	40.6	-7.75	.37	8.6	3.8	-9.33	-6.71
7	462	43.5	-7.87	.36	8.3	3.3	-9.35	-6.87
8	466	46.1	-8.03	.41	9.0	3.2	-10.99	-7.09
9	478	48.5	-8.16	.37	8.4	3.5	-9.73	-7.09
10	472	50.6	-8.53	.52	10.6	4.0	-13.34	-7.40
11	447	52.6	-8.82	.57	12.6	4.7	-10.82	-7.68
12	464	54.4	-9.45	.60	14.2	5.4	-13.25	-7.69

TABLE 19.- COMBINED STATISTICS OF σ^o RESPONSE OVER AMAZON RAIN FOREST DURING EVENING PASSES

(a) Beams 1H, 1V, 2H, and 2V

Cell	Number of samples	$\bar{\theta}_i$, deg	σ^o			Estimated NSD for each sample, %	σ^o, dB	
			Mean, dB	SD, dB	Sample NSD, %		Min	Max
Beam 1H								
1	48	21.7	-6.57	0.59	13.0	11.3	-8.44	-5.62
2	83	26.2	-5.92	.56	11.5	7.4	-8.47	-4.96
3	91	30.2	-6.35	.35	8.1	5.7	-7.64	-5.49
4	98	34.0	-7.15	.41	9.2	4.6	-8.61	-6.09
5	86	37.5	-7.67	.48	9.4	3.8	-10.74	-7.01
6	91	40.7	-7.82	.49	9.8	3.3	-10.63	-7.11
7	91	43.6	-7.93	.46	9.6	3.2	-10.75	-7.11
8	89	46.3	-8.07	.49	10.5	3.2	-10.47	-7.20
9	79	48.5	-8.21	.67	13.2	3.5	-11.77	-7.22
10	93	50.7	-8.62	.63	13.0	3.9	-11.51	-7.59
11	91	52.6	-9.28	.57	13.1	4.4	-10.56	-7.93
12	86	54.2	-9.76	.40	9.2	4.9	-11.12	-8.65
Beam 1V								
1	493	21.9	-5.97	0.47	10.7	9.4	-7.82	-4.87
2	508	26.4	-6.20	.47	10.4	7.8	-9.16	-5.15
3	458	30.6	-6.95	.63	11.7	6.4	-14.47	-6.01
4	456	34.3	-7.51	.46	10.0	5.3	-10.46	-6.54
5	439	37.8	-7.96	.42	9.6	4.4	-9.46	-6.61
6	458	41.0	-8.08	.44	9.5	3.6	-11.49	-7.21
7	444	43.9	-8.20	.41	9.1	3.3	-10.00	-7.27
8	450	46.5	-8.29	.40	9.1	3.2	-9.70	-7.33
9	451	48.9	-8.40	.51	11.3	3.5	-11.94	-7.22
10	466	51.0	-8.75	.51	11.3	4.0	-11.30	-7.44
11	473	53.0	-9.02	.66	14.7	4.6	-11.96	-7.65
12	459	54.7	-9.50	.73	17.6	5.3	-12.40	-7.50
Beam 2H								
1	85	24.7	-6.49	0.50	10.9	9.1	-8.41	-5.52
2	88	29.8	-6.53	.41	9.3	6.6	-7.73	-5.46
3	86	34.7	-7.26	.45	9.5	4.9	-9.57	-6.30
4	93	39.1	-7.65	.53	10.4	3.6	-11.31	-7.02
5	87	43.2	-8.29	.59	11.6	3.0	-11.92	-7.30
6	100	47.1	-8.60	.48	10.4	3.0	-10.68	-7.66
7	93	50.7	-9.06	.38	8.9	3.7	-9.98	-8.13
8	82	54.3	-9.70	.37	8.3	4.6	-11.05	-8.85
9	74	57.3	-10.05	.44	10.1	5.8	-11.14	-8.62
10	55	60.4	-10.76	.54	12.1	7.2	-12.25	-9.77
11	68	63.6	-11.37	.63	13.6	8.7	-13.50	-10.13
12	56	67.0	-11.92	.81	17.9	11.2	-14.15	-10.76
Beam 2V								
1	526	24.7	-6.44	0.62	13.9	10.4	-9.01	-4.96
2	458	29.9	-6.60	.56	12.7	7.6	-9.06	-5.21
3	453	34.8	-7.03	.52	11.7	5.8	-9.60	-5.88
4	449	39.3	-7.70	.43	9.9	4.2	-9.19	-6.64
5	447	43.6	-8.39	.39	8.9	3.1	-10.68	-7.48
6	504	47.5	-8.78	.46	10.1	3.0	-11.73	-7.56
7	492	51.2	-9.28	.44	10.0	3.9	-11.36	-8.15
8	431	54.6	-9.41	.43	9.8	5.4	-11.13	-8.29
9	397	57.8	-9.55	.48	10.8	7.1	-11.22	-8.31
10	293	60.7	-10.64	.51	11.9	8.8	-12.66	-9.07
11	346	63.6	-11.29	.52	11.7	11.1	-13.00	-10.18
12	350	66.4	-11.68	.62	13.9	13.6	-13.60	-10.08

TABLE 19.- Concluded

(b) Beams 3H, 3V, 4H, and 4V

Cell	Number of samples	$\bar{\theta}_i$, deg	σ^o			Estimated NSD for each sample, %	σ^o, dB	
			Mean, dB	SD, dB	Sample NSD, %		Min	Max
Beam 3H								
1	48	21.4	-6.14	0.75	15.1	10.8	-9.41	-5.00
2	50	25.8	-6.36	.54	10.8	7.7	-9.21	-5.70
3	54	29.9	-6.66	.48	10.3	6.3	-8.75	-5.84
4	49	33.7	-7.06	.35	8.0	5.1	-7.97	-6.25
5	44	37.1	-7.41	.30	6.9	4.1	-8.04	-6.72
6	48	40.2	-7.58	.36	8.3	3.5	-8.34	-6.69
7	37	43.1	-7.84	.36	8.4	3.2	-8.48	-6.77
8	37	45.7	-8.34	.49	10.5	3.2	-10.26	-7.62
9	40	48.0	-8.38	.42	9.6	3.5	-9.37	-7.48
10	44	50.2	-8.74	.43	9.5	4.0	-9.93	-8.05
11	41	52.1	-9.07	.68	14.0	4.5	-11.60	-8.05
12	48	54.0	-9.31	1.09	20.8	5.2	-13.08	-7.96
Beam 3V								
1	465	21.2	-6.35	0.86	19.0	16.2	-10.06	-4.43
2	535	25.6	-6.45	.47	10.5	8.6	-8.22	-5.17
3	585	29.7	-6.46	.40	9.1	6.7	-7.67	-5.46
4	570	33.5	-6.93	.41	9.1	5.4	-9.92	-6.05
5	491	37.0	-7.47	.34	7.7	4.5	-9.37	-6.50
6	495	40.1	-7.67	.37	8.4	3.7	-9.66	-6.82
7	475	43.0	-7.95	.37	8.4	3.3	-9.63	-7.08
8	450	45.6	-7.99	.41	9.4	3.2	-10.43	-6.72
9	462	47.9	-8.14	.44	10.3	3.5	-9.51	-6.64
10	447	50.1	-8.47	.50	11.2	4.0	-11.59	-7.22
11	433	52.0	-8.77	.59	12.1	4.6	-13.18	-7.60
12	429	53.8	-8.99	.93	18.0	5.3	-13.35	-7.34
Beam 4H								
1	55	24.8	-6.37	0.37	8.4	9.4	-7.41	-5.72
2	51	29.9	-6.69	.31	6.9	7.2	-7.93	-6.15
3	46	34.7	-7.48	.34	7.7	5.3	-8.26	-6.89
4	33	39.2	-8.07	.29	6.7	3.8	-8.72	-7.41
5	36	43.5	-8.66	.37	8.5	3.0	-9.49	-7.82
6	39	47.5	-8.85	.47	12.3	3.0	-9.54	-6.87
7	48	51.4	-9.59	.56	10.5	4.0	-12.12	-8.92
8	55	55.0	-10.20	.62	12.8	5.6	-12.73	-9.11
9	56	58.2	-11.21	.34	8.0	7.3	-11.97	-10.33
10	41	61.3	-11.78	.47	10.9	9.1	-13.16	-10.62
11	33	64.4	-12.59	.69	15.2	12.6	-14.40	-11.64
12	20	67.1	-13.04	.99	23.2	15.9	-14.67	-11.50
Beam 4V								
1	558	24.6	-6.14	0.52	11.7	9.9	-9.19	-5.06
2	550	29.7	-6.50	.48	10.9	7.8	-8.41	-5.38
3	479	34.6	-7.38	.44	9.9	5.8	-10.48	-6.44
4	441	39.1	-7.98	.43	9.7	4.3	-10.12	-6.96
5	424	43.3	-8.42	.39	9.1	3.2	-9.87	-7.20
6	427	47.3	-8.58	.45	10.5	3.0	-11.54	-6.12
7	467	51.1	-9.10	.39	8.8	4.1	-10.75	-8.10
8	507	54.6	-9.52	.39	8.9	5.8	-11.53	-8.46
9	440	57.9	-10.35	.69	15.4	7.9	-13.18	-8.56
10	319	61.0	-11.13	.49	11.2	10.3	-12.90	-9.70
11	245	64.0	-11.65	.71	16.0	13.4	-14.10	-10.13
12	193	67.0	-12.15	.91	20.4	18.4	-15.78	-9.97

TABLE 20.- REGRESSION PARAMETERS FOR $\overline{\sigma^o}$ VERSUS θ_i FOR EACH BEAM AND POLARIZATION FOR EACH TIME PERIOD

Spacecraft direction	Beam	Pol	Local time, hr	$\overline{\sigma^o}$ value at θ_i = 45°	a	b	R^2
Ascending	1	V	0500 to 0730	-7.70	-2.785	-0.109	-0.99
	2	V		-7.61	-2.745	-.108	.99
	3	V		-7.43	-2.261	-.115	.94
	4	V		-7.46	-3.571	-.084	.96
	1	H		-7.54	-1.966	-.124	.98
	2	H		-7.66	-2.988	-.104	.92
	3	H		-7.51	-2.042	-.121	.99
	4	H		-7.51	-2.901	.102	.96
Ascending	1	V	0800 to 1145	-8.48	-2.543	-0.132	0.98
	2	V		-8.34	-3.312	-.112	.99
	3	V		-8.10	-2.450	-.126	.98
	4	V		-8.05	-4.253	-.084	.96
Descending	1	V	1730 to 2330	-8.29	-4.747	-0.79	0.94
	2	V		-8.48	-2.622	-.130	.99
	3	V		-8.03	-3.811	-.094	.97
	4	V		-8.47	-3.310	-.115	.97
	1	H		-8.14	-3.449	-.104	.92
	2	H		-8.40	-3.061	-.119	.99
	3	H		-8.19	-3.515	-.104	.98
	4	H		-8.73	-2.968	-.128	.99

TABLE 21.- STATISTICS OF σ^o RESPONSE OVER AMAZON RAIN FOREST FOR NADIR CELLS

Cell	Number of samples	$\bar{\theta}_i$, deg	σ^o			Estimated NSD for each sample, %	σ^o, dB	
			Mean, dB	SD, dB	Sample NSD, %		Min	Max
Beam 1H								
13	126	7.9	-6.45	1.07	30.2	10.4	-9.71	-2.55
14	123	3.9	-5.41	1.61	80.5	9.4	-8.65	3.00
15	101	.3	12.52	6.04	665.3	4.8	-4.85	30.71
Beam 1V								
13	100	8.2	-5.29	4.02	76.5	178.2	-16.43	0.64
14	100	4.1	-3.76	3.87	72.3	143.2	-15.84	2.00
15	131	.2	9.74	7.28	252.3	62.0	-19.00	21.52
Beam 2H								
13	131	7.8	-6.66	1.52	33.7	27.1	-11.34	-3.17
14	113	3.8	-5.39	2.09	88.8	21.3	-9.87	2.49
15	100	.5	9.01	5.45	696.2	9.4	-7.29	27.43
Beam 2V								
13	69	7.8	1.35	5.20	80.7	408.8	-12.40	5.63
14	53	3.7	1.40	4.56	82.9	256.5	-12.60	6.96
15	82	.4	9.52	7.38	208.6	191.6	-16.52	20.51
Beam 3H								
13	57	8.7	-7.18	4.14	56.0	188.5	-20.63	-4.07
14	63	4.5	-4.22	4.12	289.7	92.8	-16.58	9.44
15	78	.4	4.50	5.90	408.1	53.7	-22.19	19.77
Beam 3V								
13	39	8.2	8.05	4.19	81.6	192.9	-3.55	13.49
14	22	4.2	6.42	4.70	71.9	300.1	-8.90	10.45
15	48	.2	9.84	6.15	156.8	178.3	-5.31	17.91
Beam 4H								
13	92	8.2	-6.44	0.91	23.5	10.4	-10.13	-2.91
14	86	4.4	-5.13	1.96	118.9	9.4	-8.57	5.13
15	79	.7	5.80	5.02	566.9	6.4	-7.19	22.82
Beam 4V								
13	108	8.2	-8.13	2.73	56.6	71.0	-20.32	-3.22
14	99	4.3	-6.66	3.27	74.1	69.2	-18.44	-.42
15	95	.5	3.30	5.52	272.7	27.3	-11.87	16.65

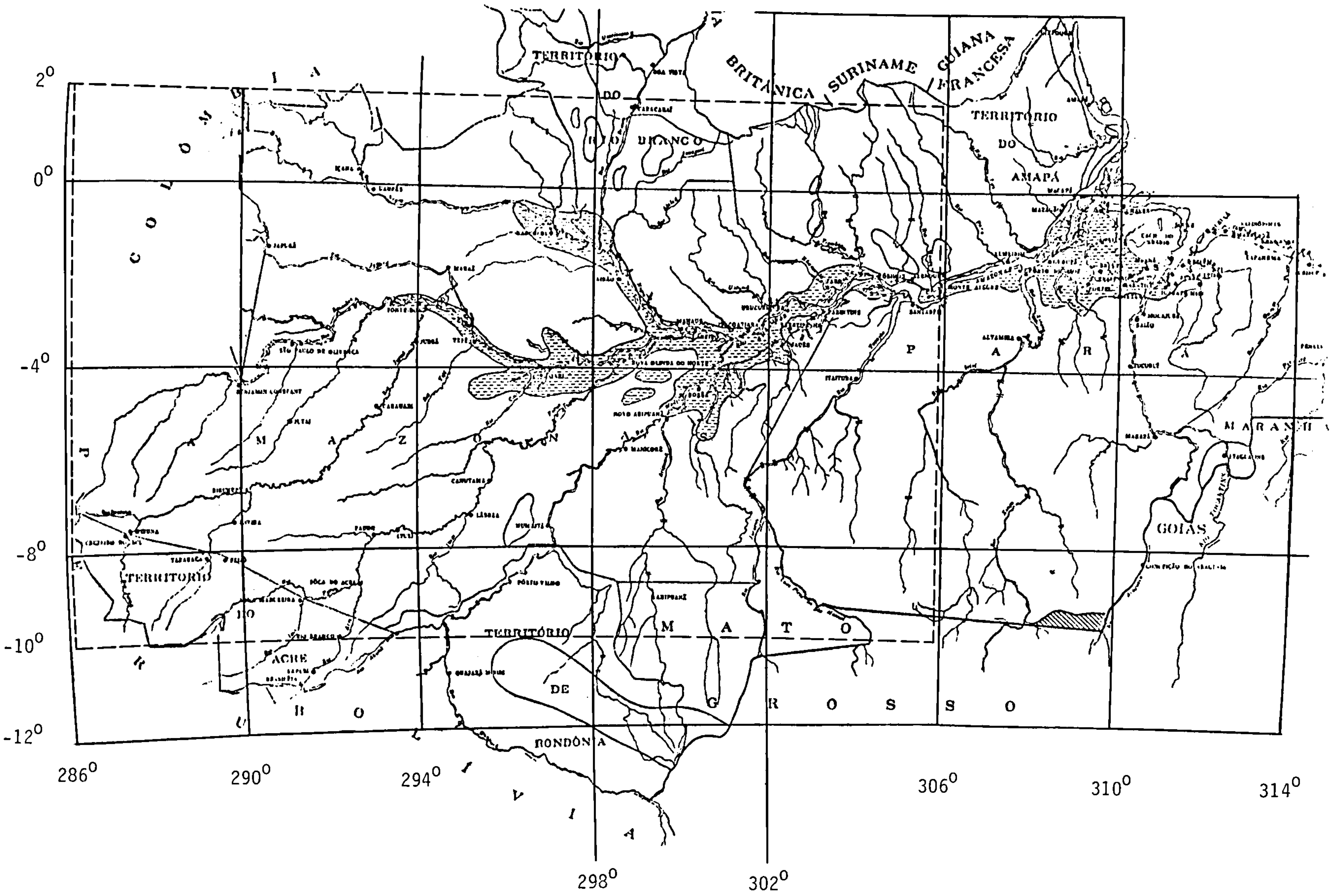

(a) Vegetation patterns.

Figure 1.- Maps of Amazon region. (Note: original maps had color shadings which distinguished vegetation types and geological regions.)

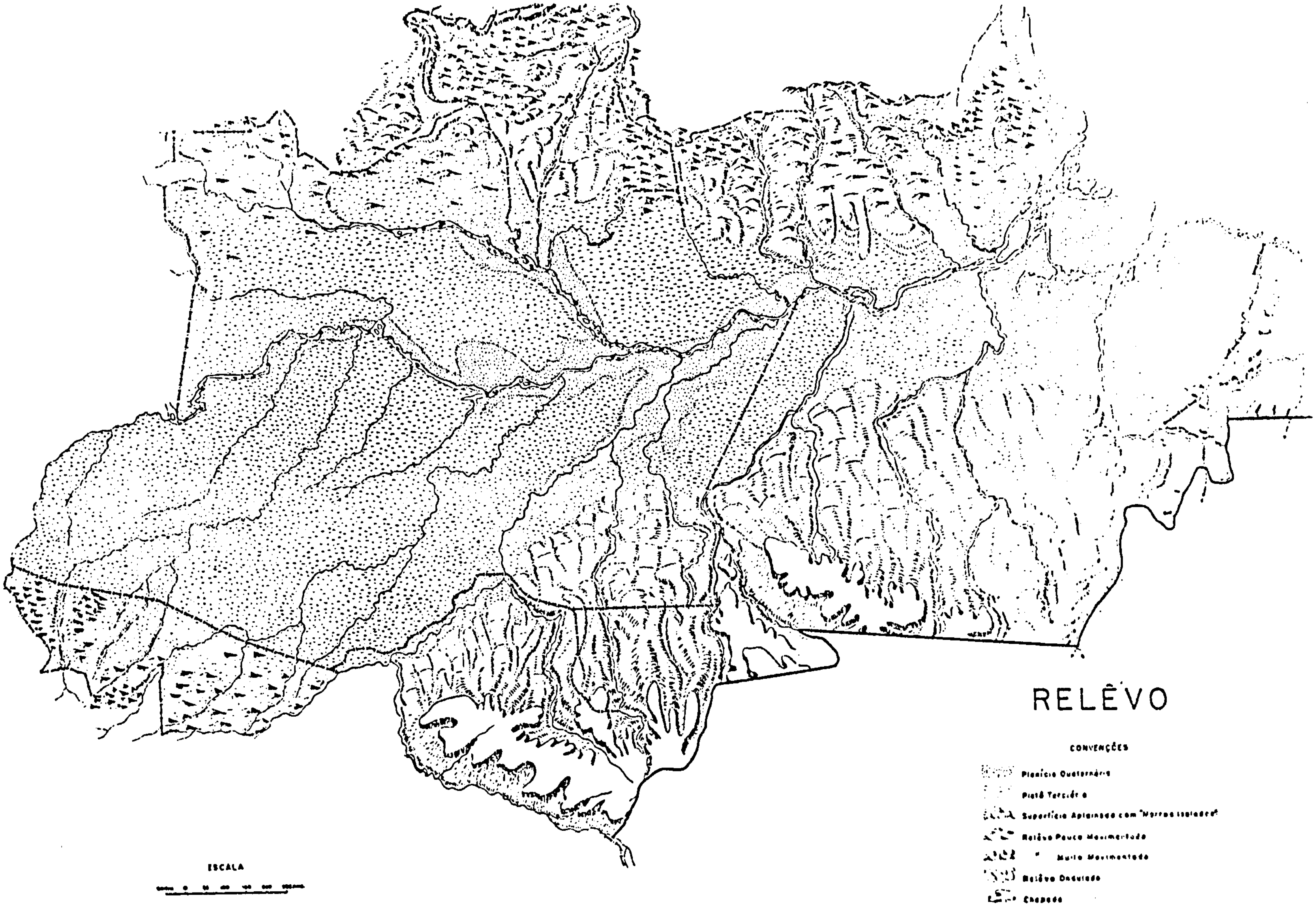

(b) Geological classification.

Figure 1.- Concluded.

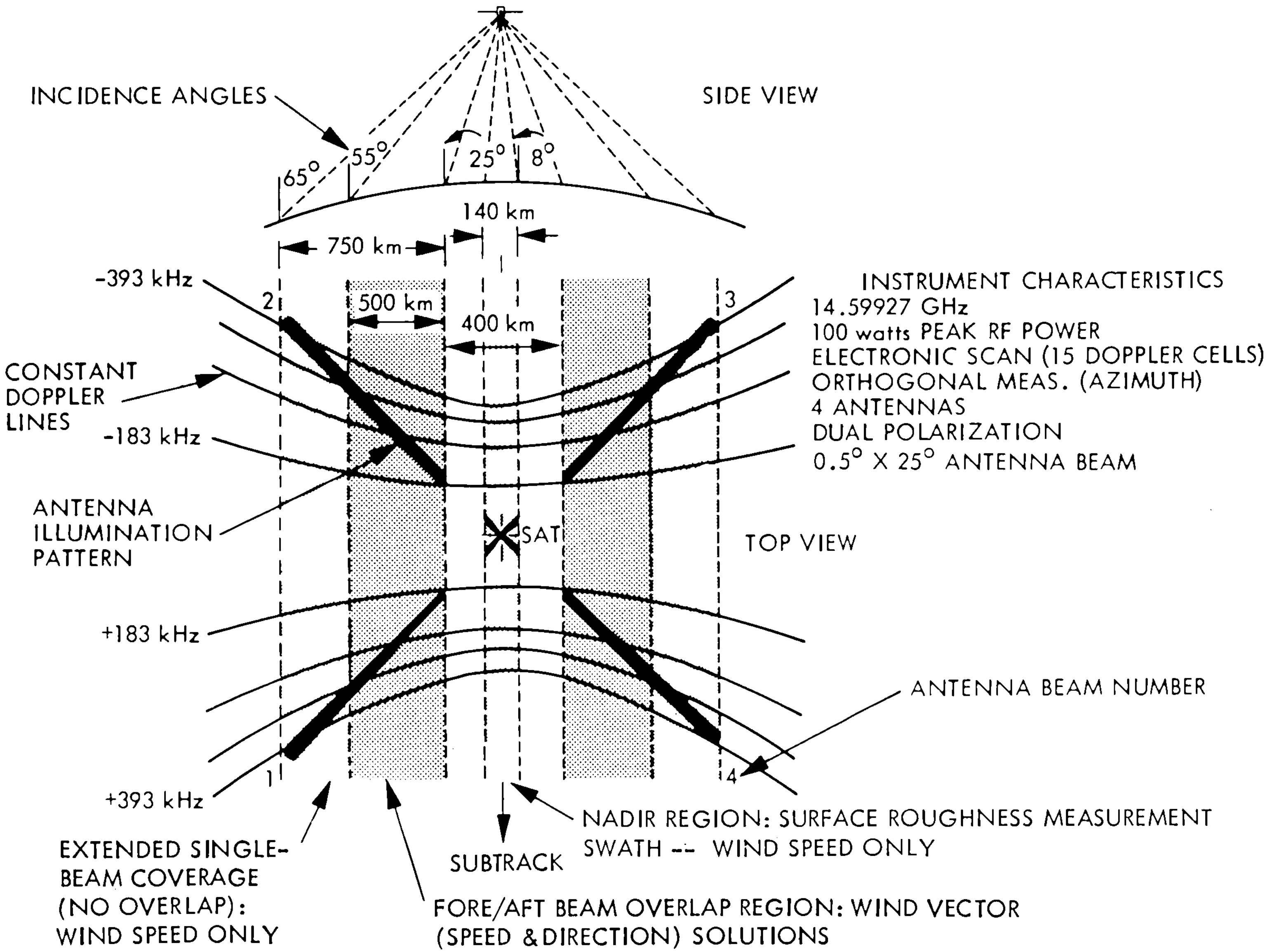

Figure 2.- Scatterometer measurement geometry.

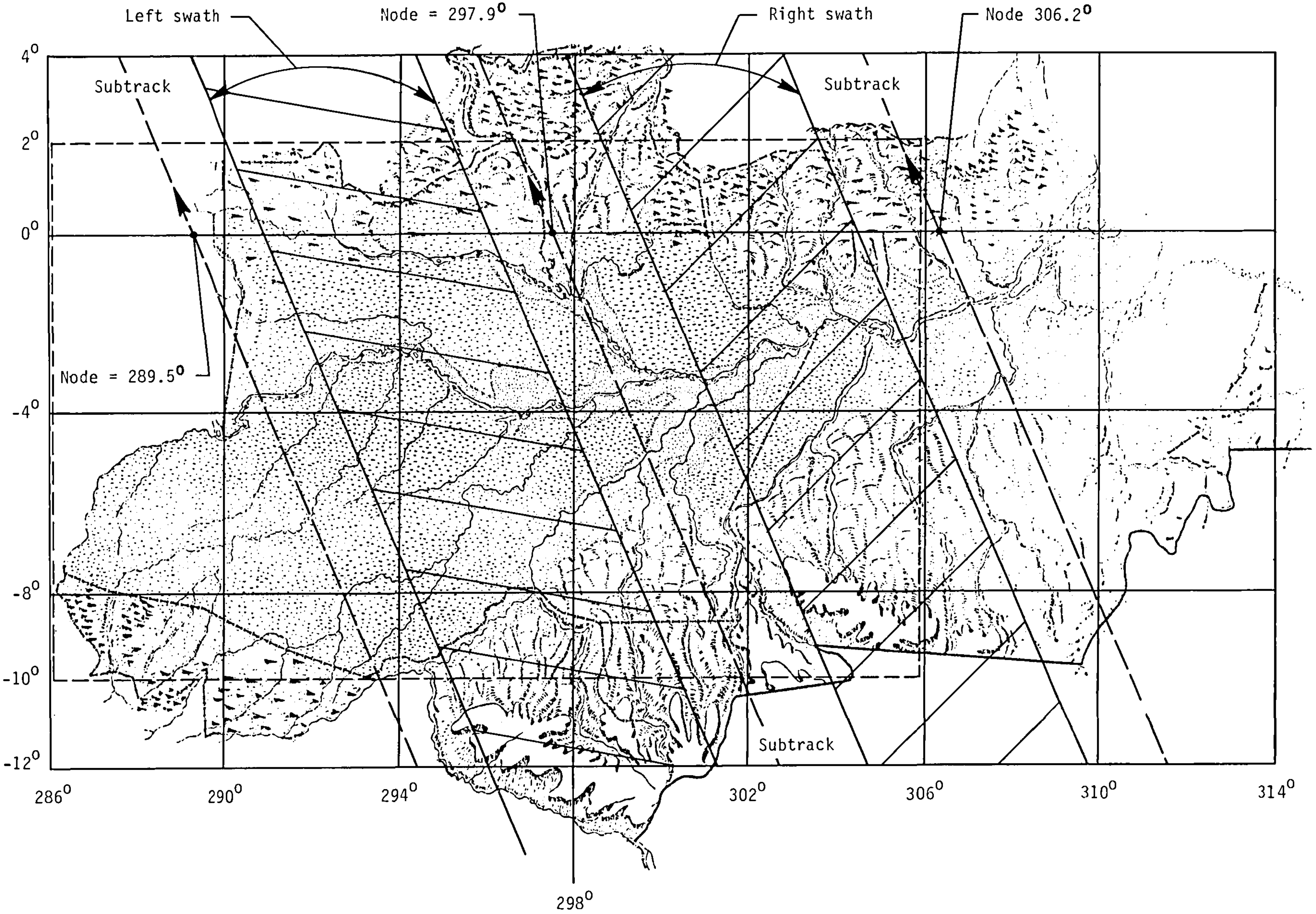

(a) Ascending passes.

Figure 3.- Map of Amazon region showing swath coverage.

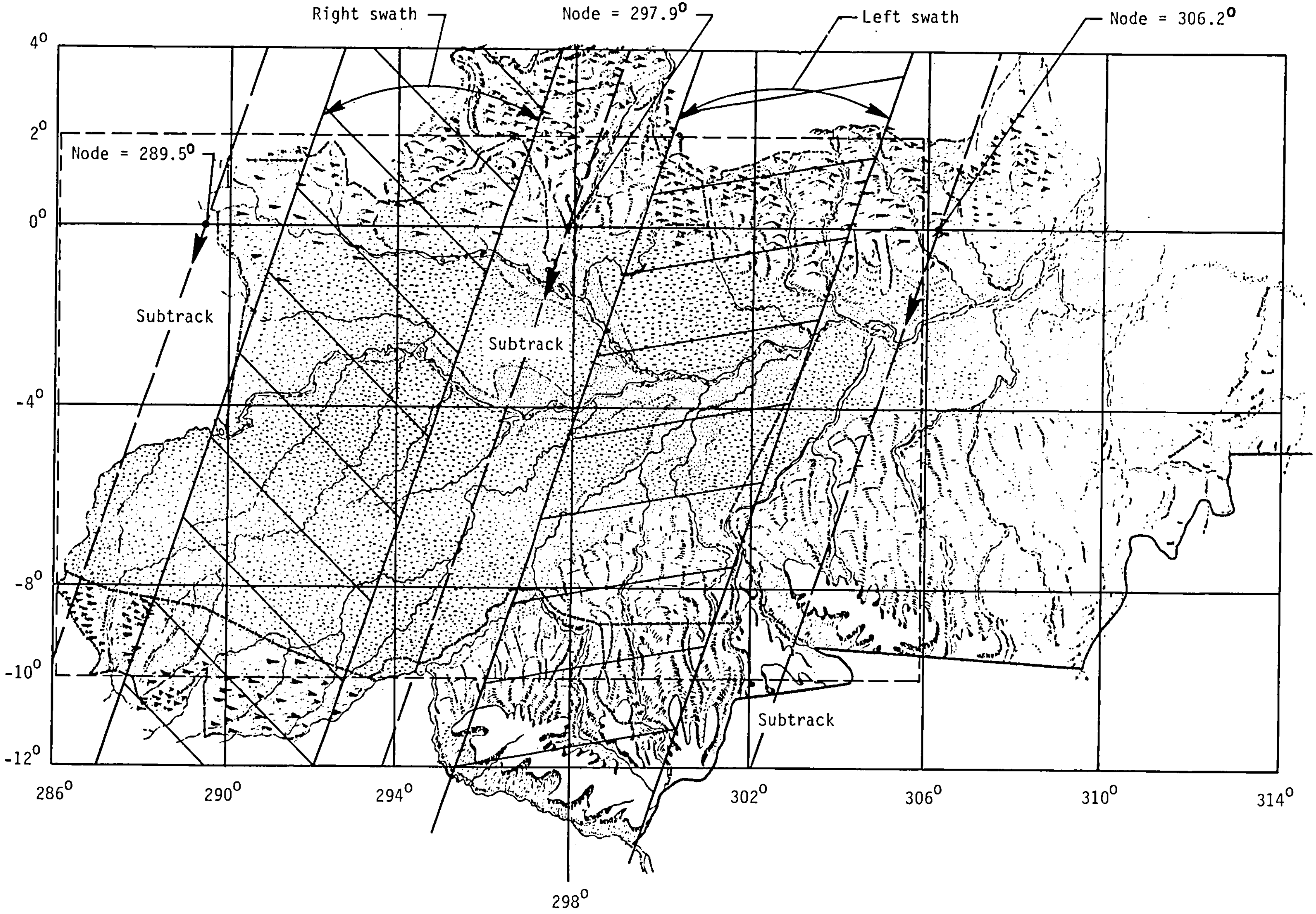

(b) Descending passes.

Figure 3.- Concluded.

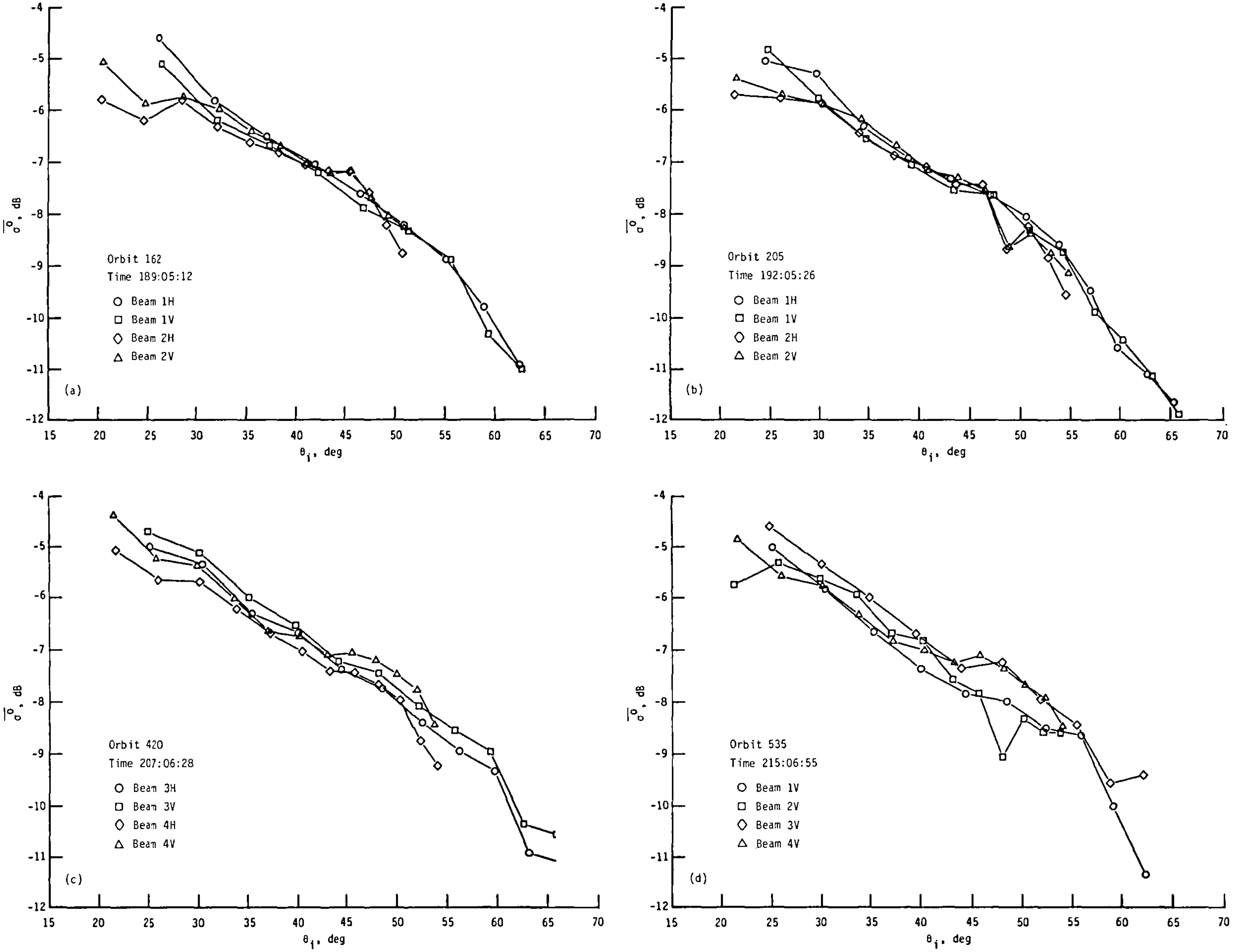

Figure 4.- Plots of $\overline{\sigma^o}$ against θ_i after initial processing for four orbits over Amazon rain forest during sunrise time period.

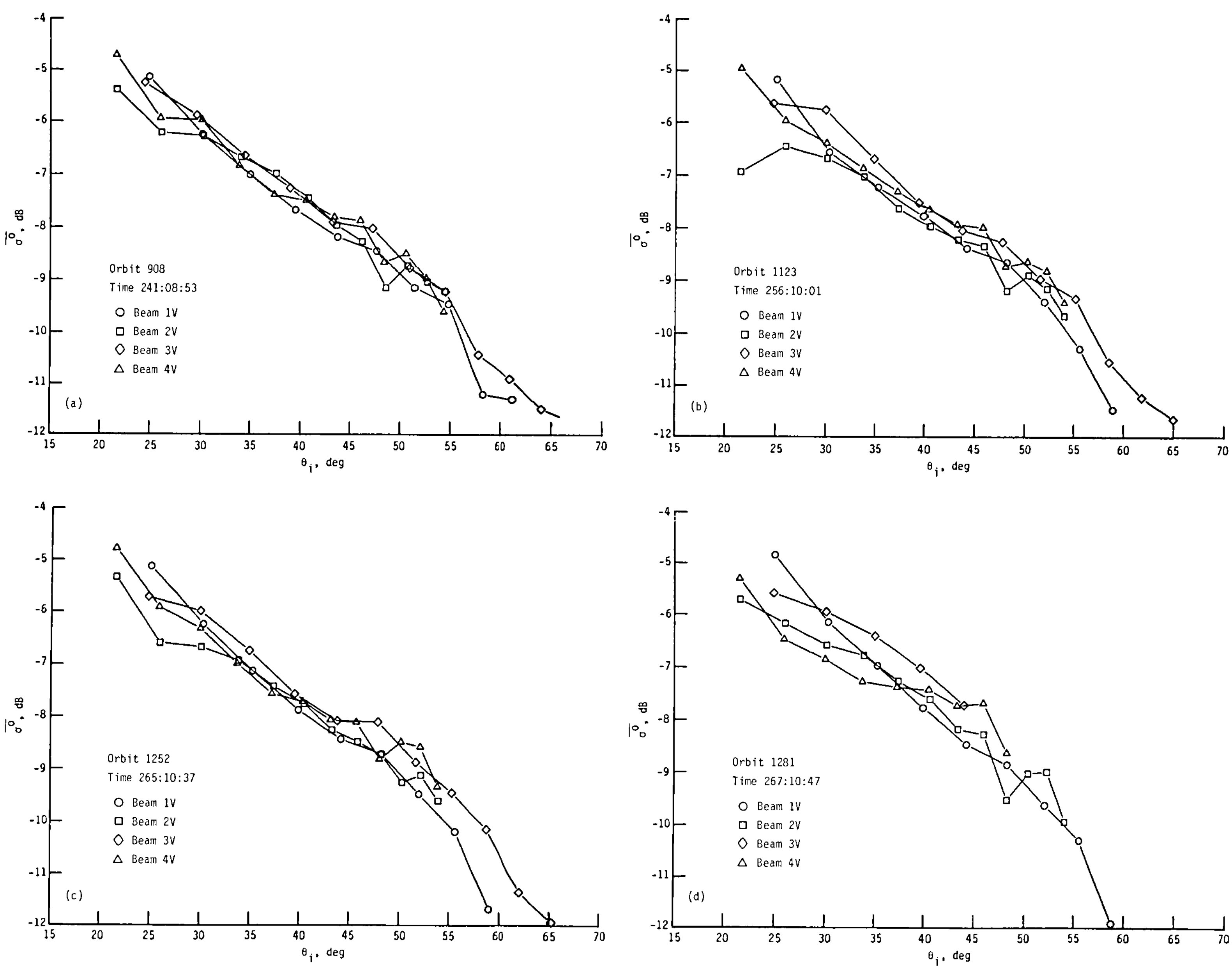

Figure 5.- Plots of $\overline{\sigma^o}$ against θ_i after initial processing for four orbits over Amazon rain forest during morning time period.

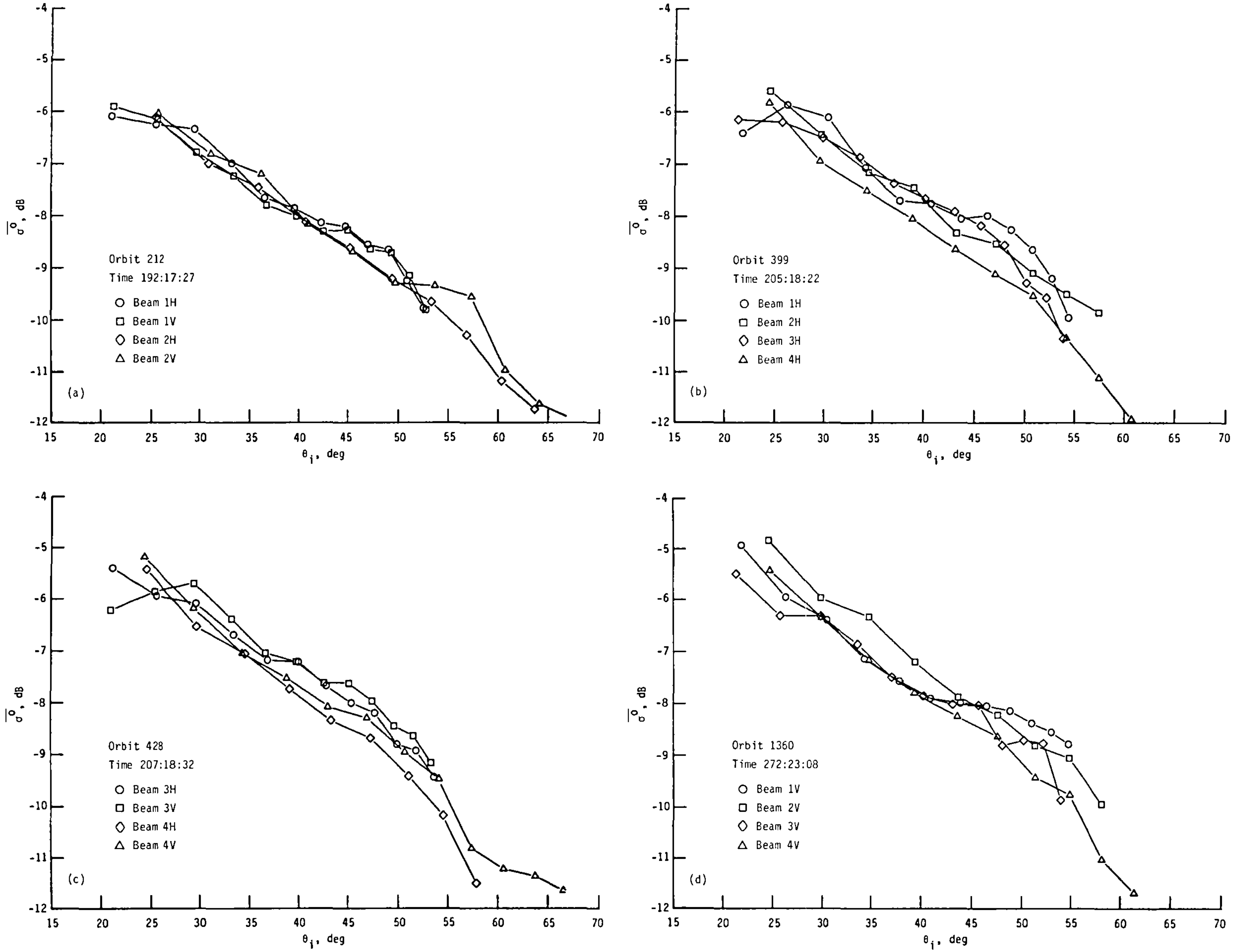

Figure 6.- Plots of $\overline{\sigma^o}$ against θ_i after initial processing for four orbits over Amazon rain forest during evening time period.

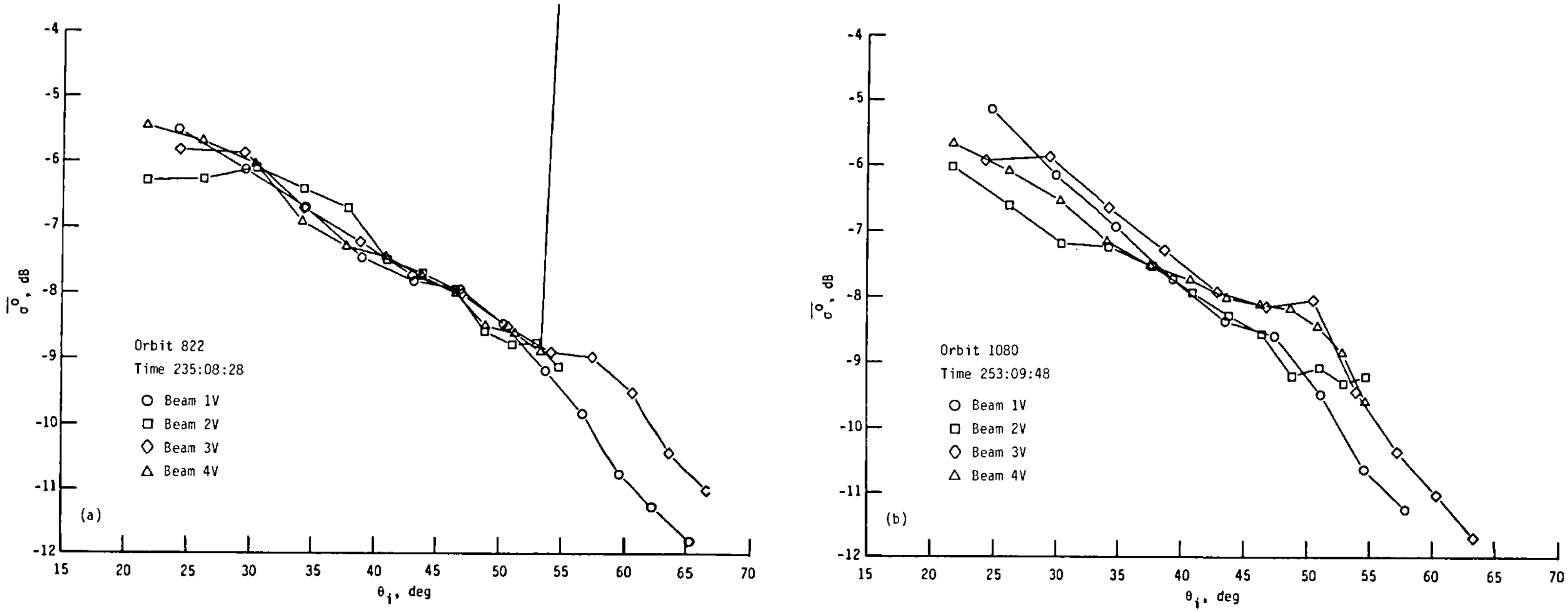

Figure 7.- Plots of $\overline{\sigma^o}$ against θ_i for orbit 822 over Amazon rain forest showing effects of bit error on cell 12 of beam 4 and for orbit 1080 showing effects of high value of V_{SN} due to bit error on cell 7 of beam 3.

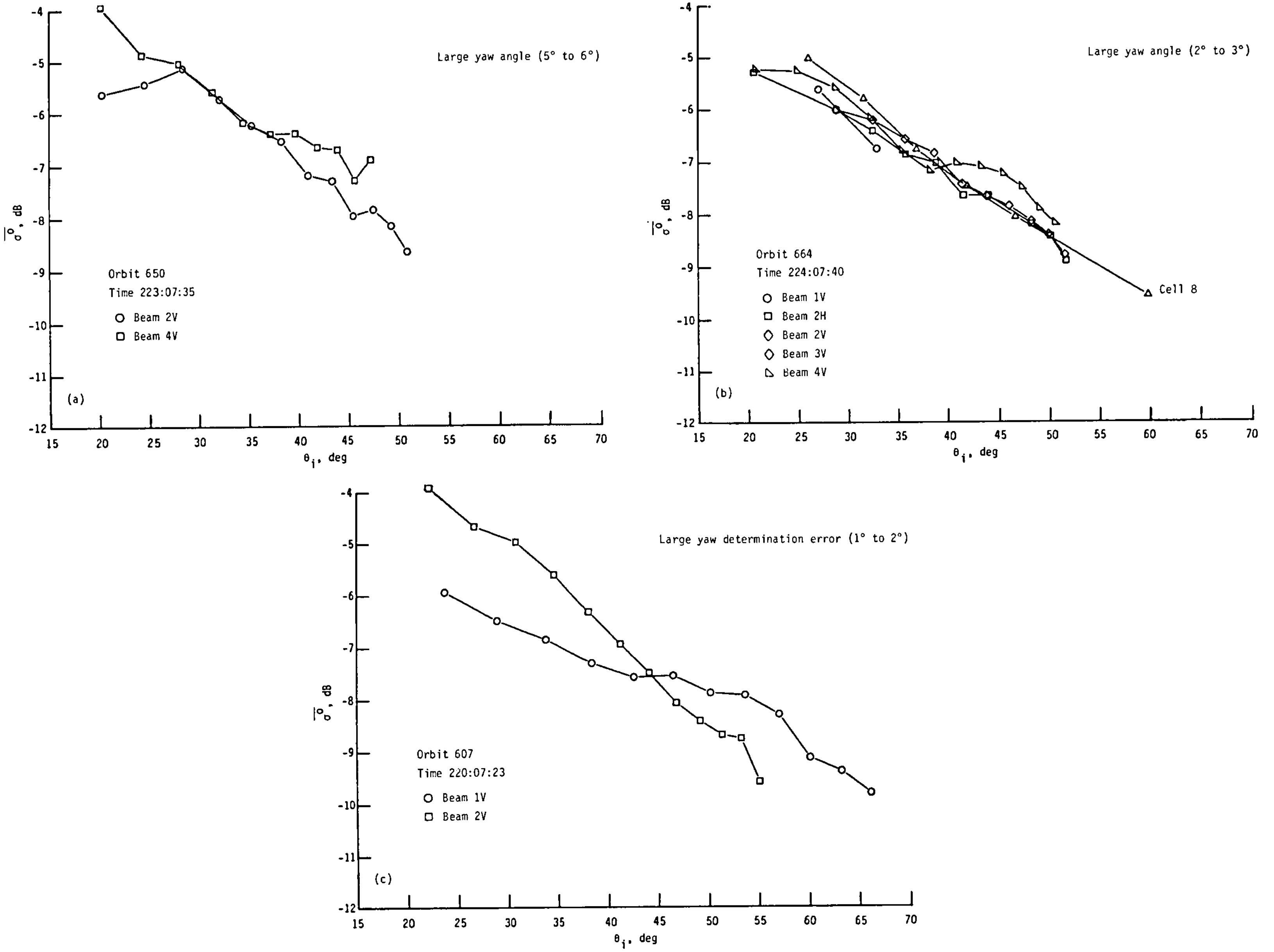

Figure 8.- Plots of $\overline{\sigma^o}$ against θ_i for orbits 650 and 664 over Amazon rain forest showing effects of large yaw angle and for orbit 607 showing effects of large yaw angle determination error.

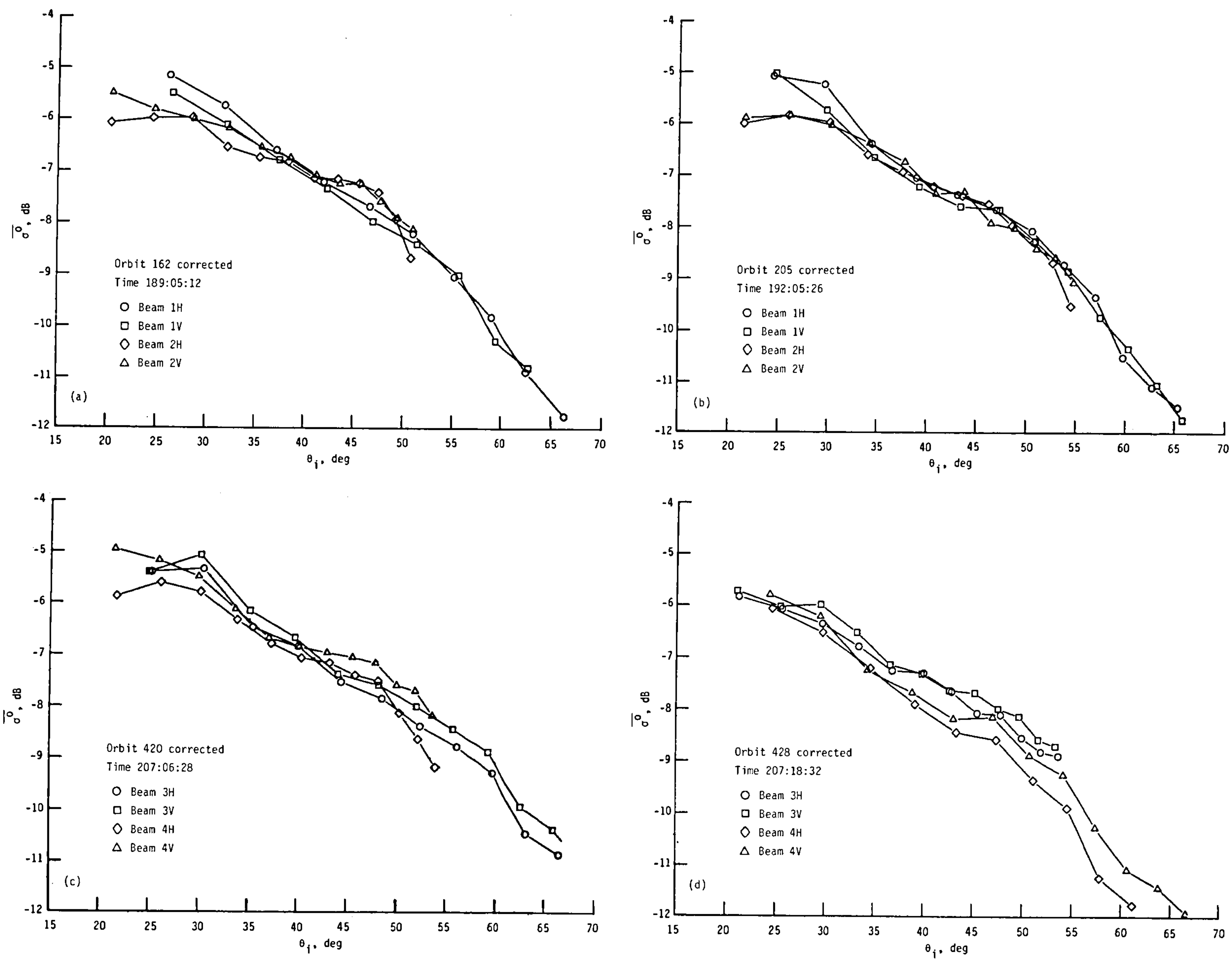

Figure 9.- Plots of $\overline{\sigma^o}$ against θ_i after reprocessing through σ^o correction algorithm for orbits 162, 205, 420, and 428 over Amazon rain forest.

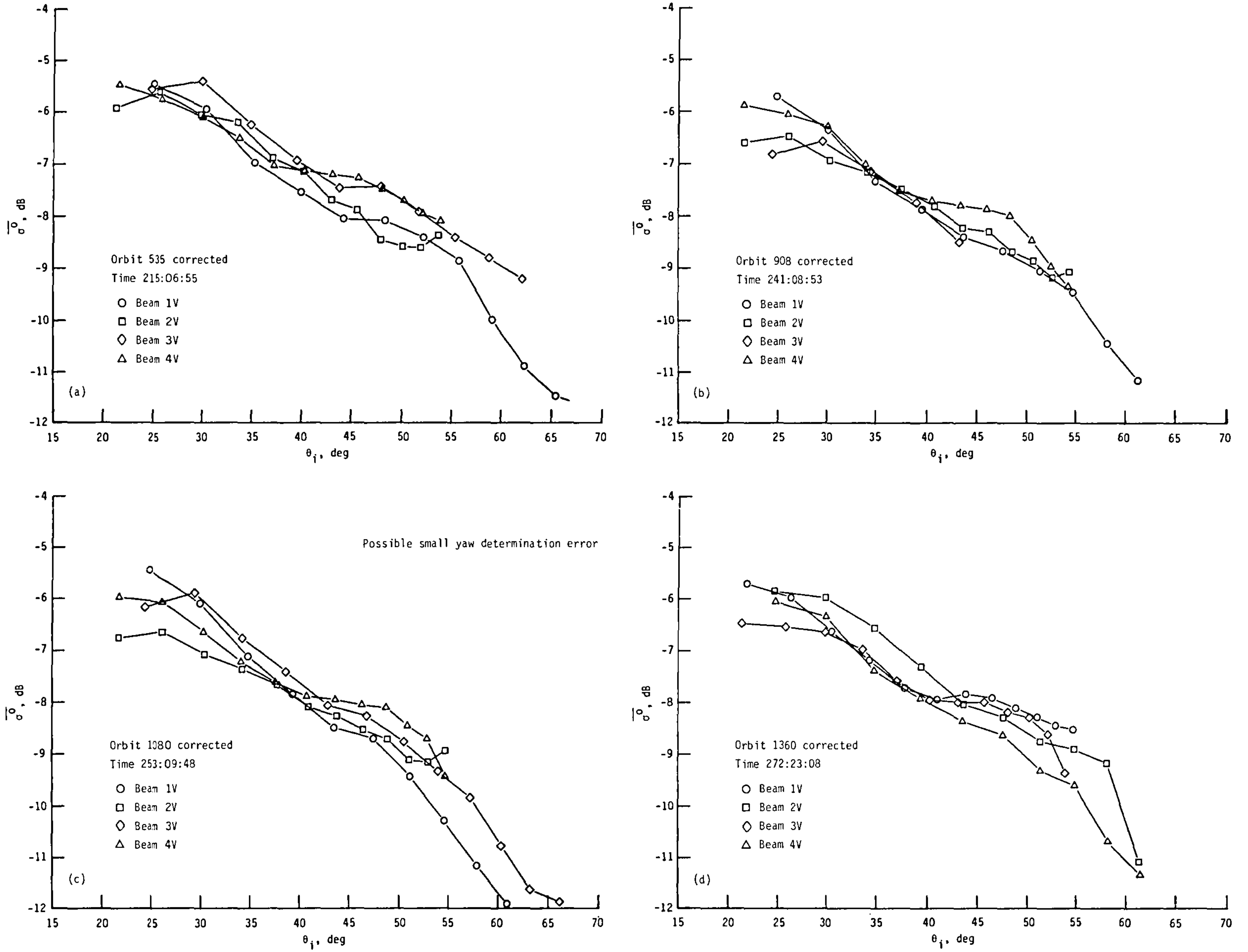

Figure 10.- Plots of $\overline{\sigma^o}$ against θ_i after reprocessing through σ^o correction algorithm for orbits 535, 908, 1080, and 1360 over Amazon rain forest.

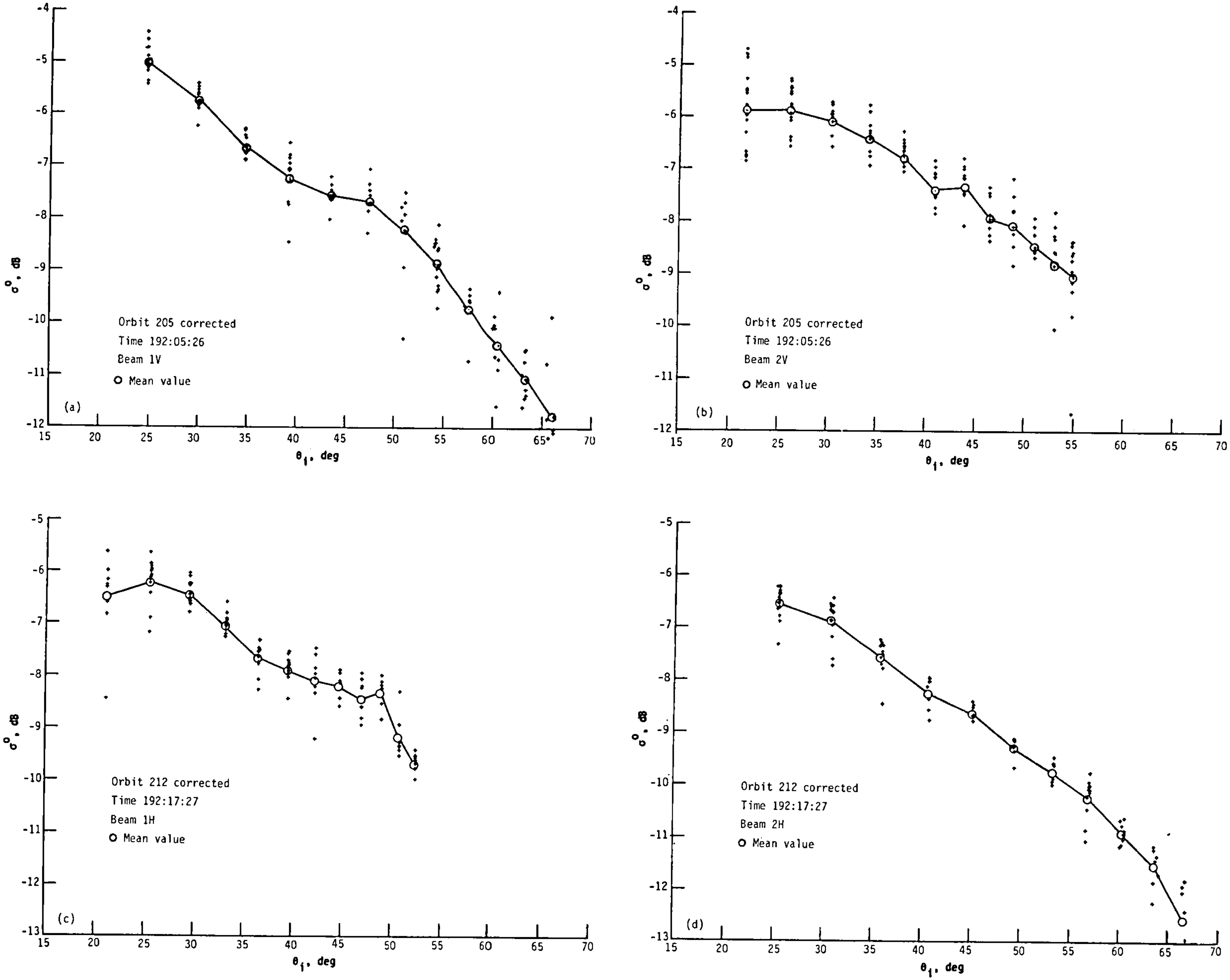

Figure 11.- Scatter plots of σ^o against θ_i for orbits 205, beams 1V and 2V, and 212, beams 1H and 2H, over Amazon rain forest.

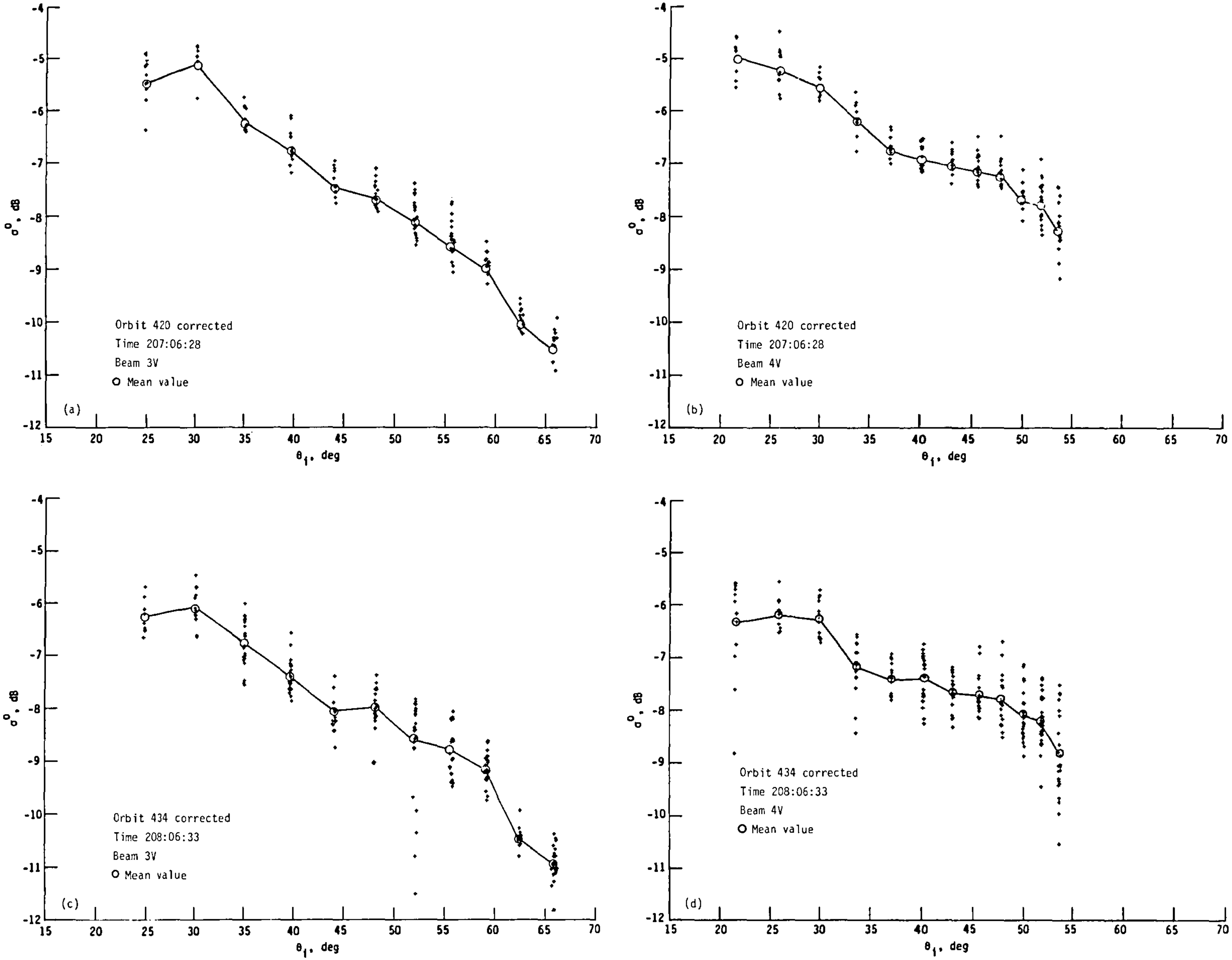

Figure 12.- Scatter plots of σ^o against θ_i for orbits 420, beams 3V and 4V, and 434, beams 3V and 4V, over Amazon rain forest.

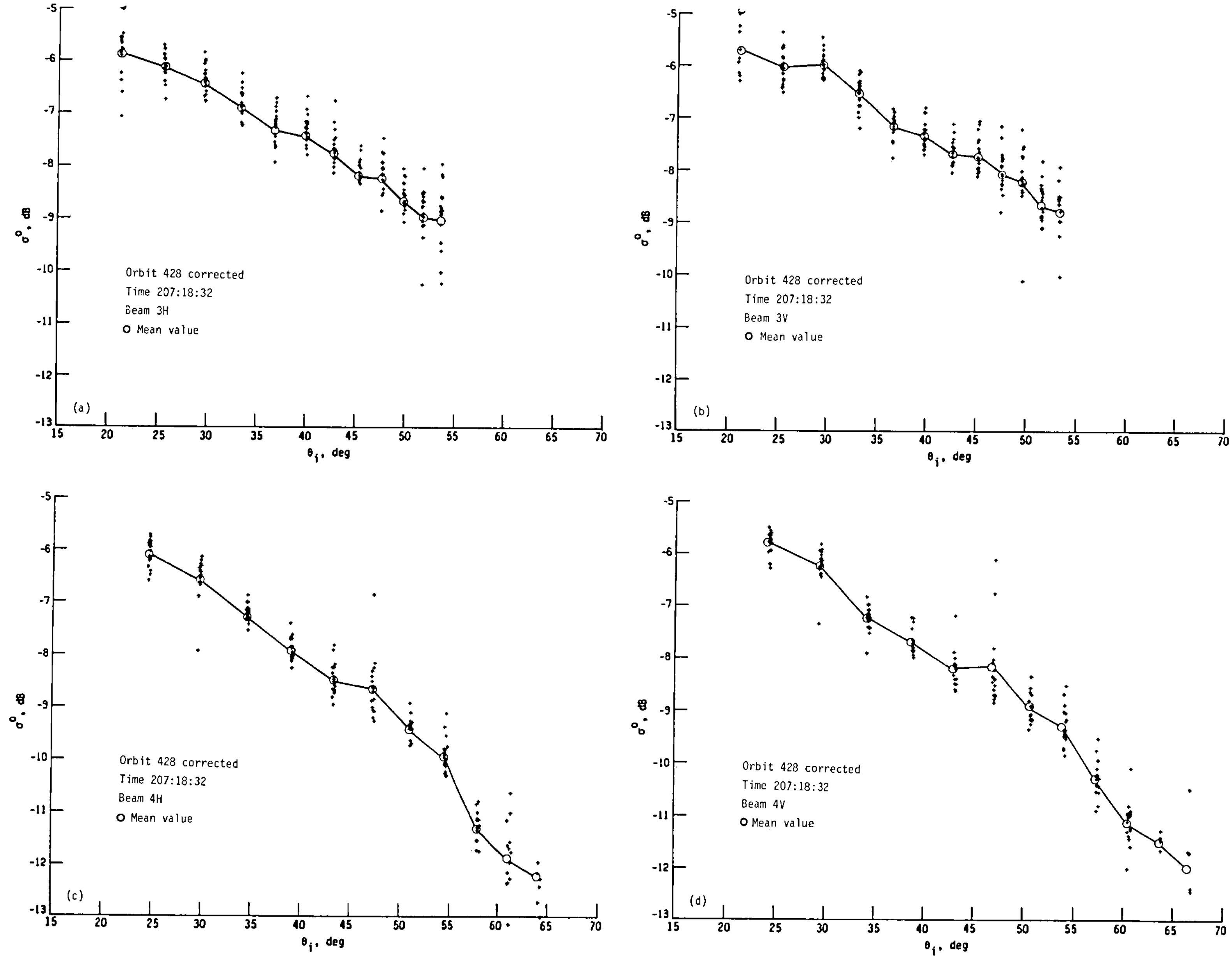

Figure 13.- Scatter plots of σ^o against θ_i for orbit 428, beams 3H, 3V, 4H, and 4V, over Amazon rain forest.

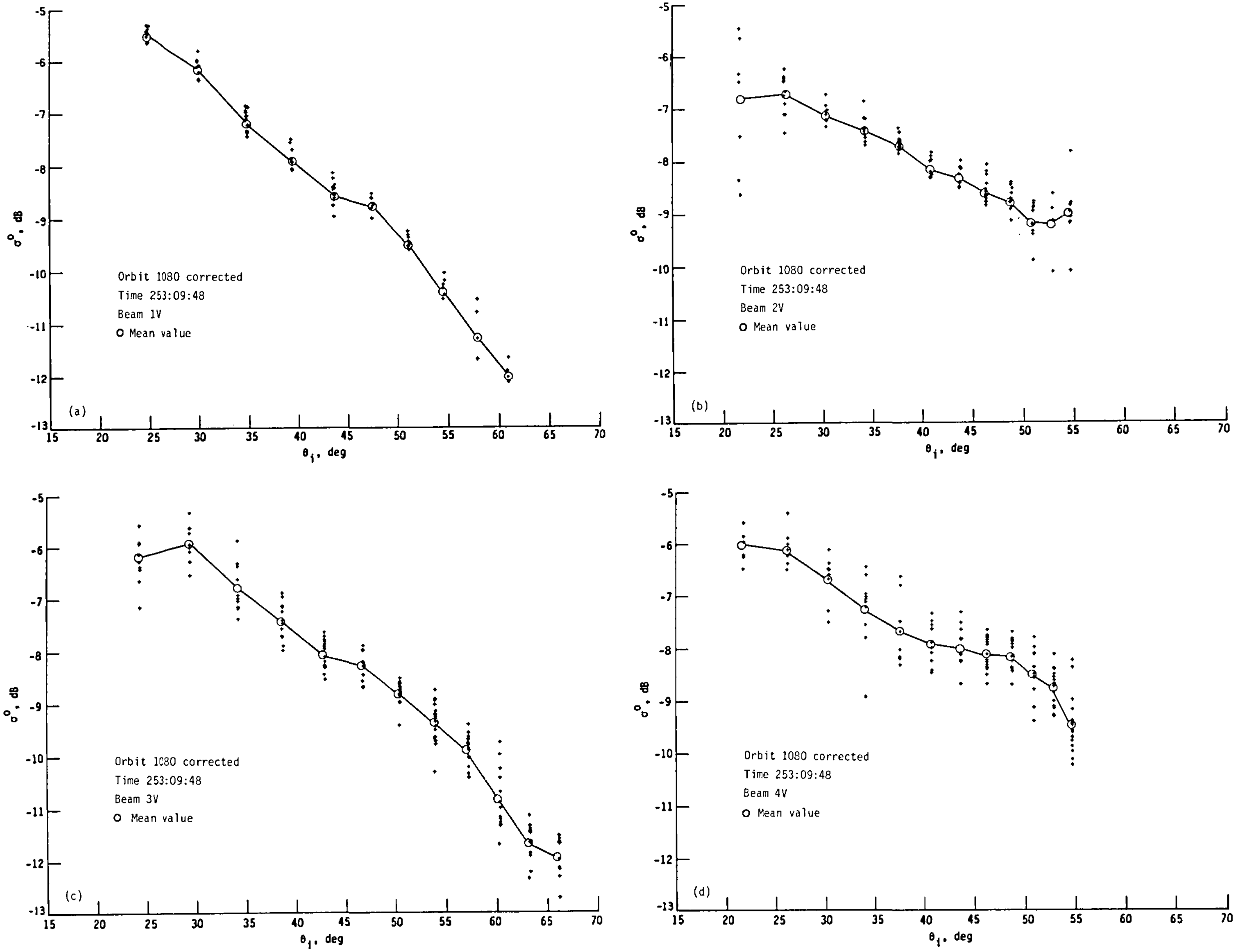

Figure 14.- Scatter plots of σ^o against θ_i for orbit 1080, beams 1V, 2V, 3V, and 4V, over Amazon rain forest.

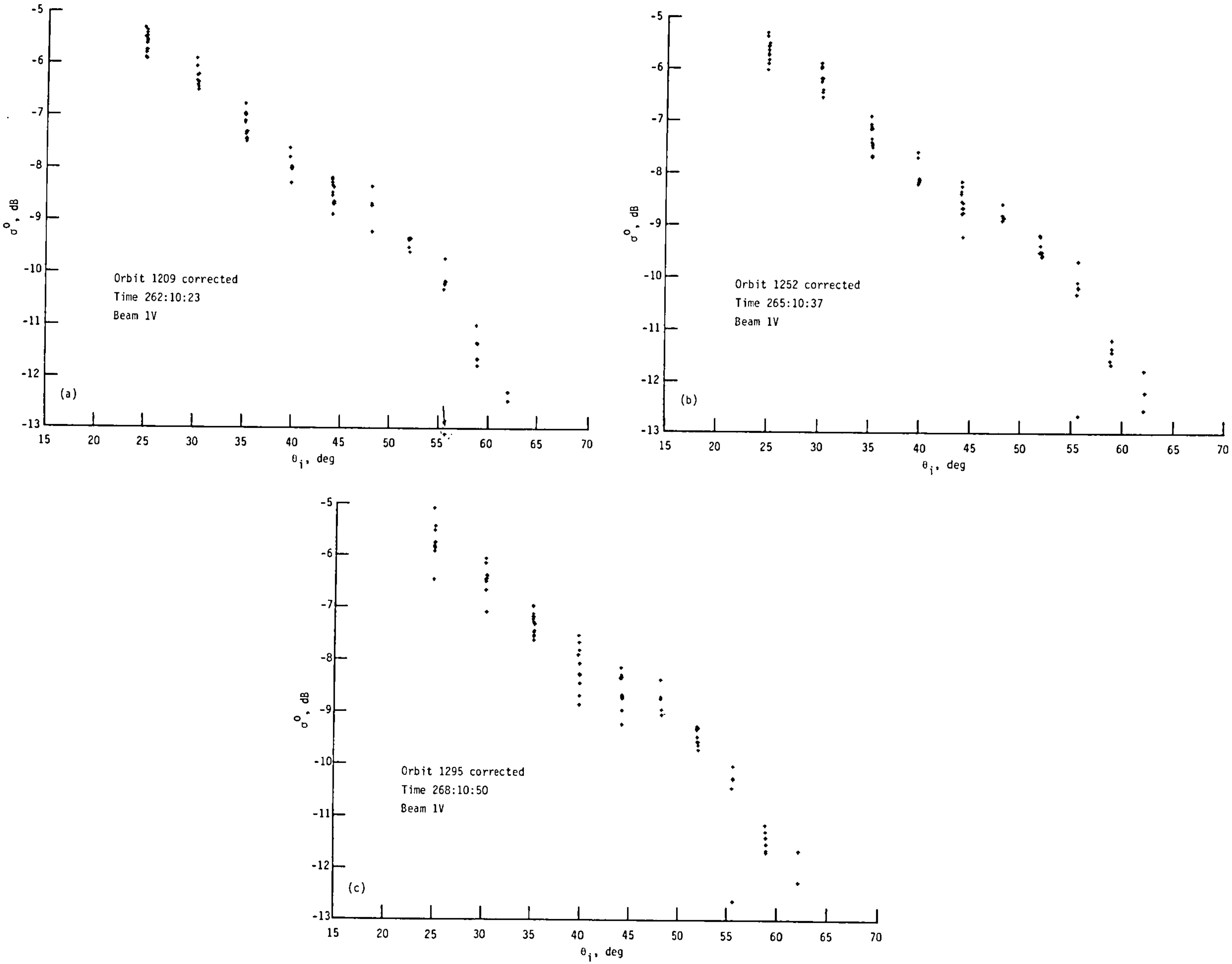

Figure 15.- Scatter plots of σ^o against θ_i for beam 1V of repeat orbits 1209, 1252, and 1295 over Amazon rain forest.

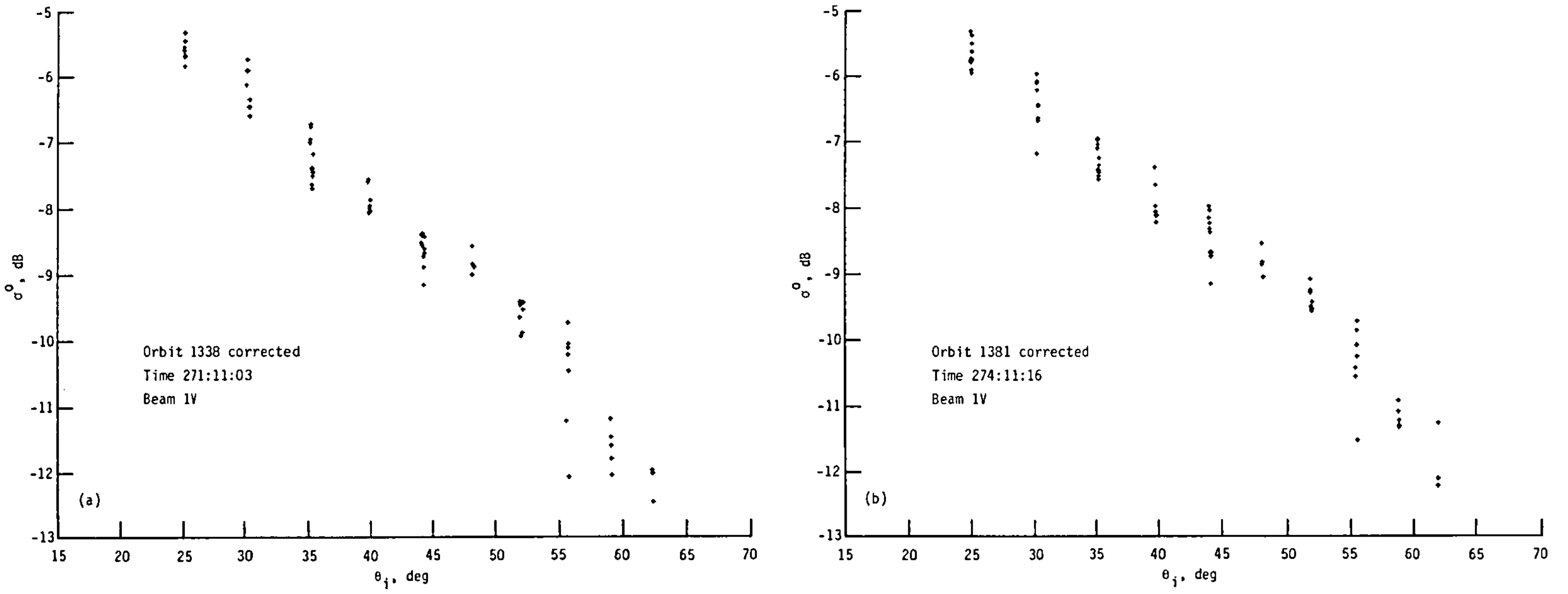

Figure 16.- Scatter plots of σ^o against θ_i for beam 1V of repeat orbits 1338 and 1381 over Amazon rain forest.

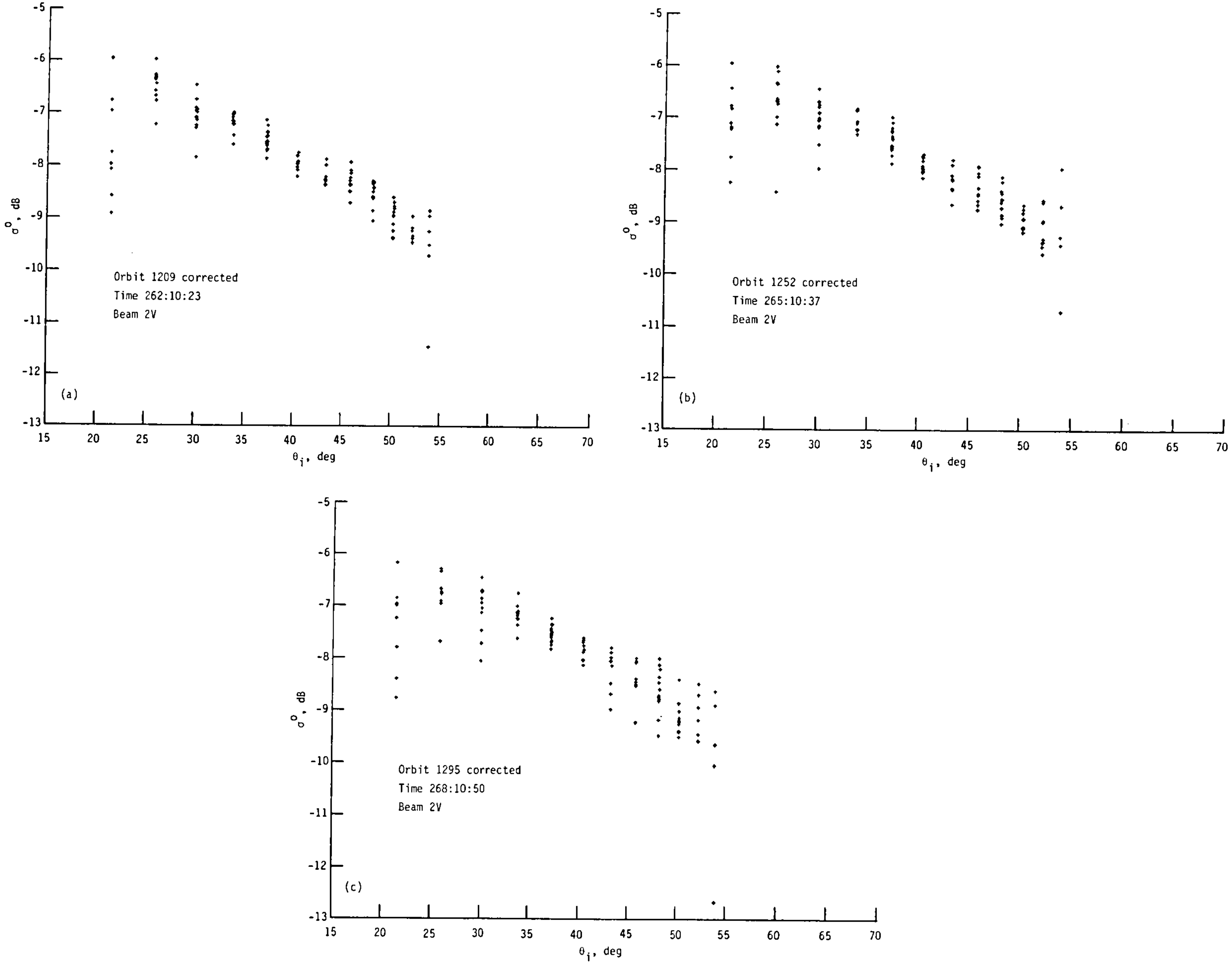

Figure 17.- Scatter plots of σ^o against θ_i for beam 2V of repeat orbits 1209, 1252, and 1295 over Amazon rain forest.

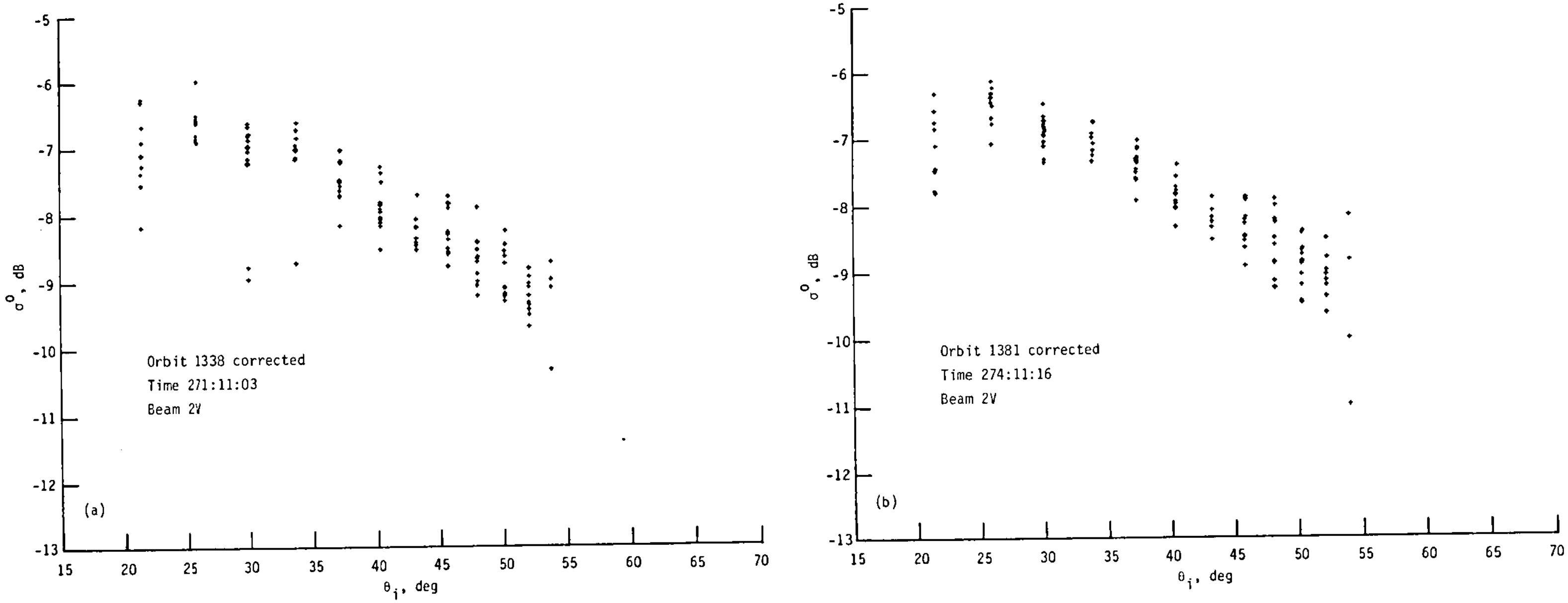

Figure 18.- Scatter plots of σ^o against θ_i for beam 2V of repeat orbits 1338 and 1381 over Amazon rain forest.

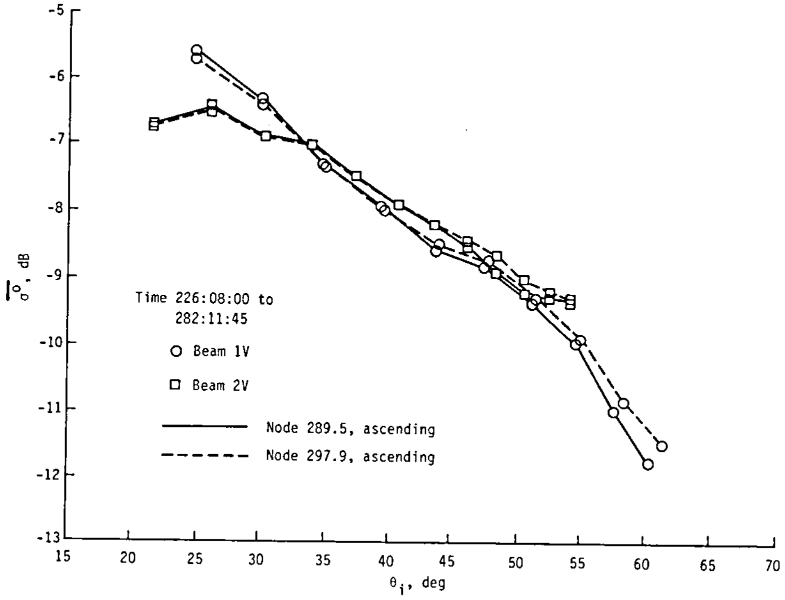

(a) Nodes 289.5 and 297.9, beams 1V and 2V.

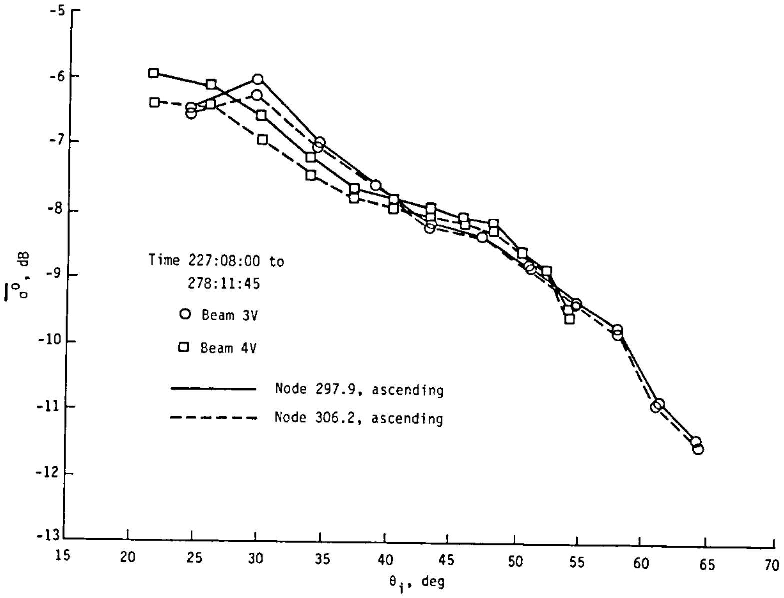

(b) Nodes 297.9 and 306.2, beams 3V and 4V.

Figure 19.- Comparison of response of $\overline{\sigma^o}$ against θ_i for ascending node passes over Amazon rain forest during morning time period.

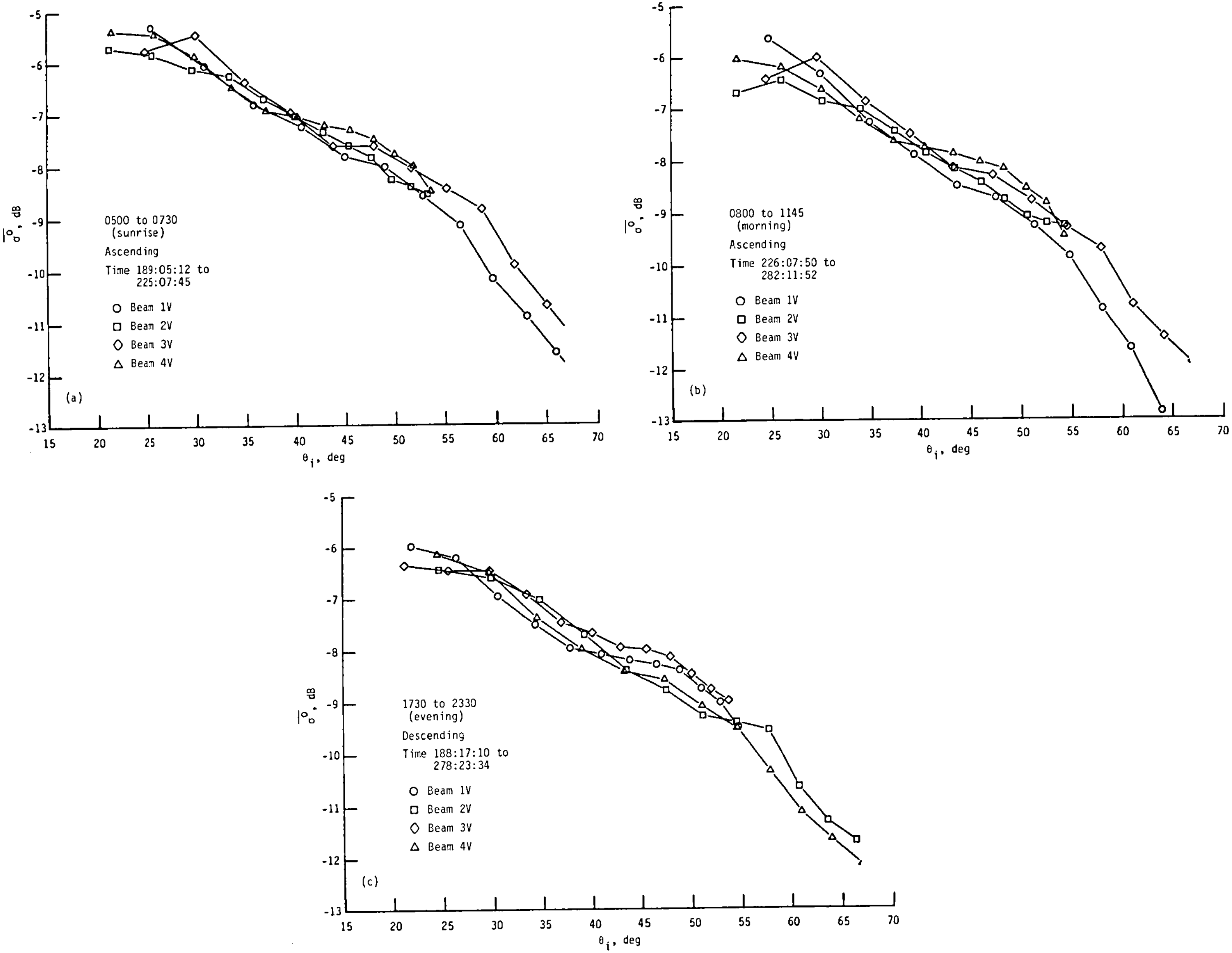

Figure 20.- Combined plots of $\overline{\sigma^o}$ against θ_i for each time period over Amazon rain forest for beams 1V, 2V, 3V, and 4V.

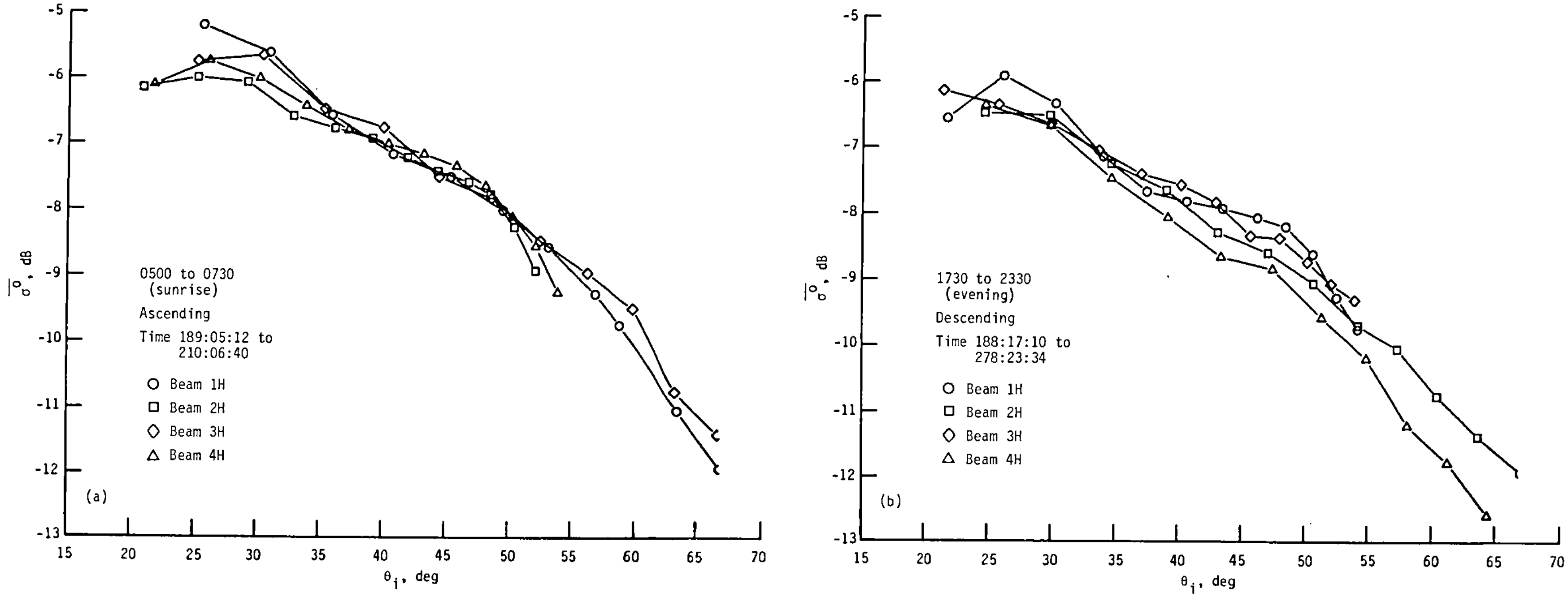

Figure 21.- Combined plots of $\overline{\sigma^o}$ against θ_i for sunrise and evening time periods over Amazon rain forest for beams 1H, 2H, 3H, and 4H.

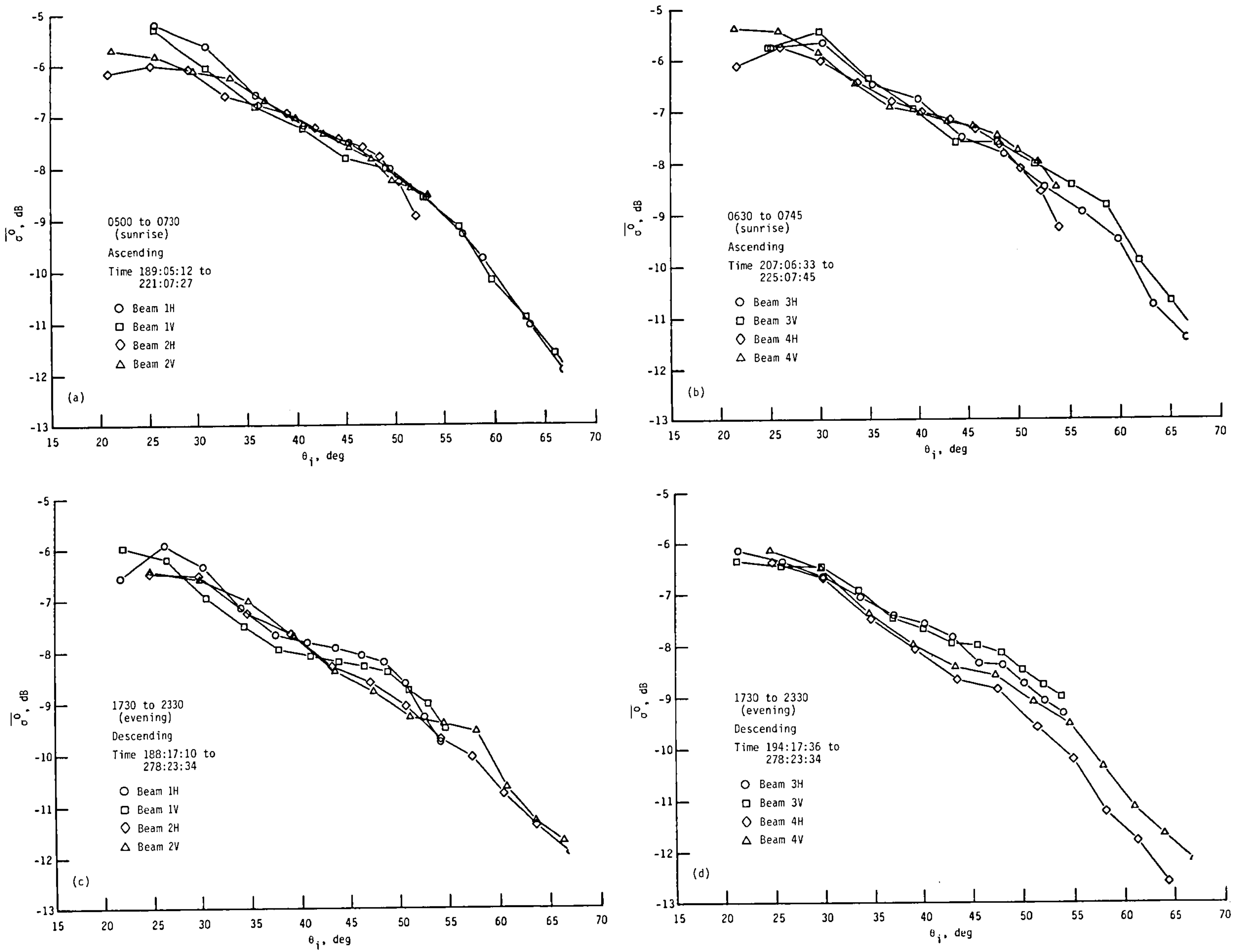

Figure 22.- Combined plots of $\overline{\sigma^o}$ against θ_i for sunrise and evening time periods over Amazon rain forest for all beams and polarizations.

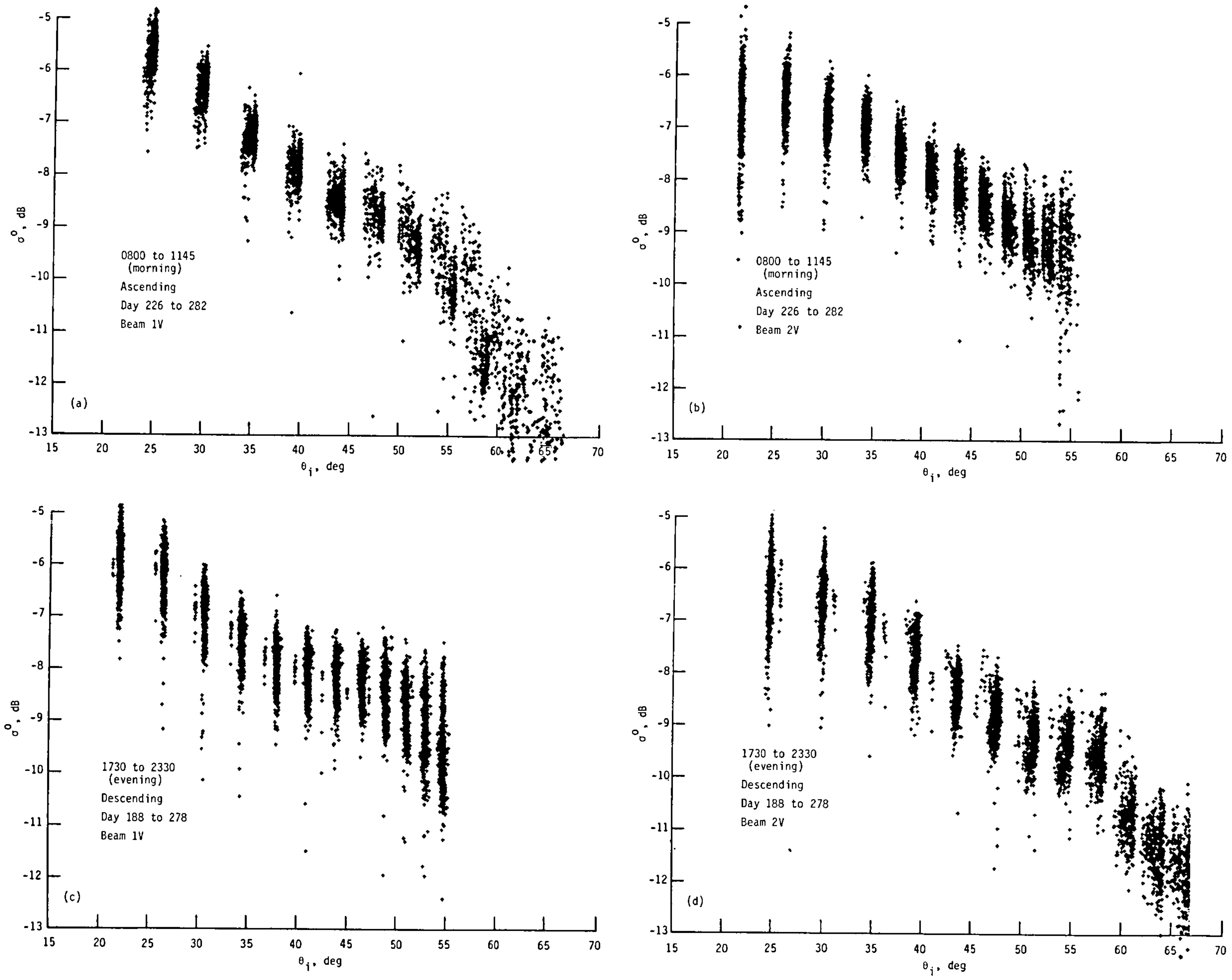

Figure 23.- Scatter plots of σ^o against θ_i for morning and evening passes over Amazon rain forest for beams 1V and 2V.

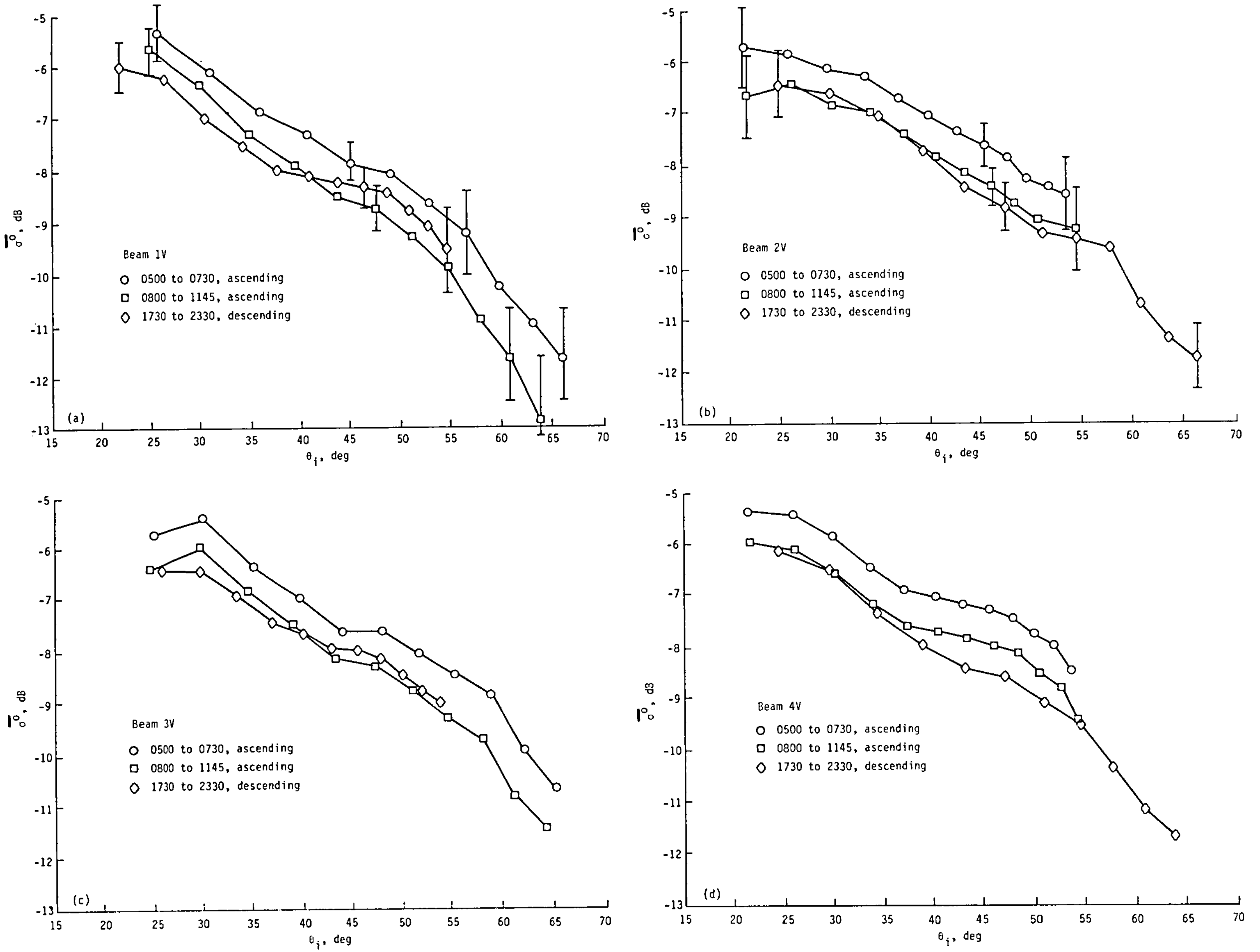

Figure 24.- Comparison of response of $\overline{\sigma^o}$ against θ_i for each time period over Amazon rain forest for beams 1V, 2V, 3V, and 4V.

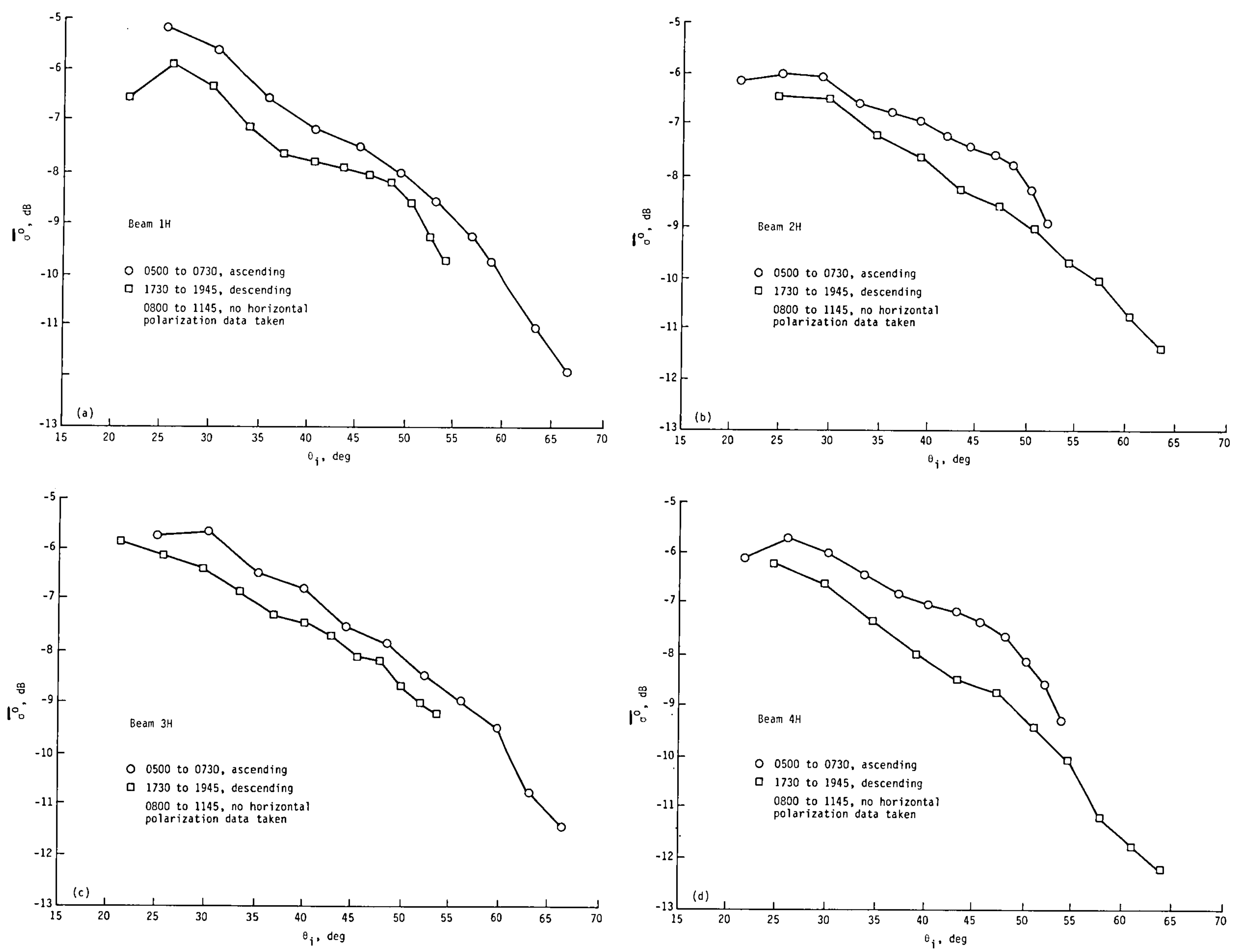

Figure 25.- Comparison of response of $\overline{\sigma^o}$ against θ_i for each time period over Amazon rain forest for beams 1H, 2H, 3H, and 4H.

1. Report No. NASA TM-85779	2. Government Accession No.	3. Recipient's Catalog No.

4. Title and Subtitle
ANALYSIS OF NORMALIZED RADAR CROSS SECTION (σ^o) SIGNATURE OF AMAZON RAIN FOREST USING SEASAT SCATTEROMETER DATA

5. Report Date
August 1984

6. Performing Organization Code
506-58-23-01

7. Author(s)
Emedio M. Bracalente and Jon L. Sweet

8. Performing Organization Report No.
L-15749

9. Performing Organization Name and Address

NASA Langley Research Center
Hampton, VA 23665

10. Work Unit No.

11. Contract or Grant No.

12. Sponsoring Agency Name and Address
National Aeronautics and Space Administration
Washington, DC 20546

13. Type of Report and Period Covered
Technical Memorandum

14. Sponsoring Agency Code

15. Supplementary Notes

Emedio M. Bracalente: Langley Research Center, Hampton, Virginia.
Jon L. Sweet: Kentron International, Inc., Hampton, Virginia.

16. Abstract

A detailed analysis of the normalized radar cross section σ^o signature of the Amazon rain forest was conducted by using Seasat scatterometer data. Statistics of the measured σ^o values were determined from multiple orbit passes for three local time periods. Plots of $\overline{\sigma^o}$ against incidence angle as a function of beam and polarization show that less than 0.3 dB relative bias exists between all beams over a range of incidence angle from 30° to 53°. The backscattered measurements analyzed show the Amazon rain forest to be relatively homogeneous, azimuthally isotropic and insensitive to polarization. The return from the rain forest target appears relatively consistent and stable, except for the small diurnal variation (0.75 dB) that occurs at sunrise. Because of the relative stability of the rain forest target and the scatterometer instrument, the response of $\overline{\sigma^o}$ versus incidence angle was able to detect errors in the estimated yaw attitude angle. Also, small instrument gain biases in some of the processing channels were detected. This led to the development of an improved σ^o algorithm, which uses a more accurate method for estimating the system noise power. The study of the Amazon rain forest backscatter signature shows that it is a suitable target for calibrating spaceborne scatterometers.

17. Key Words (Suggested by Author(s))
Amazon rain forest radar response
Scattering coefficient (σ^o)
Scatterometer calibration
Antenna bias correction

18. Distribution Statement
Unclassified - Unlimited

Subject Category 43

19. Security Classif. (of this report) Unclassified	20. Security Classif. (of this page) Unclassified	21. No. of Pages 115	22. Price A06

For sale by the National Technical Information Service, Springfield, Virginia 22161

NASA-Langley, 1984

National Aeronautics and
Space Administration

Washington, D.C.
20546

Official Business
Penalty for Private Use, $300

THIRD-CLASS BULK RATE

Postage and Fees Paid
National Aeronautics and
Space Administration
NASA-451

U.S.MAIL

NASA

POSTMASTER: If Undeliverable (Section 158
Postal Manual) Do Not Return